# REMOVAL OF ORGANIC COMPONENTS AND BACTERIA FROM WATER BY ELECTROCHEMICAL COMBUSTION

M Cronje • PGL Baker •JH Knoetze •
RD Sanderson • AM Crouch

WRC Report No. 1196/1/04

Water Research Commission

# REMOVAL OF ORGANIC COMPONENTS AND BACTERIA FROM WATER BY ELECTROCHEMICAL COMBUSTION

**Report to the**
**WATER RESEARCH COMMISSION**

**by**

M CRONJE, P G L BAKER,
J H KNOETZE, R D SANDERSON
AND A M CROUCH

University of Stellenbosch

**WRC Report No 1196/1/04**
**ISBN No 1-77005-335-2**

**JULY 2005**

**Disclaimer**

This report emanates from a project financed by the Water Research Commission (WRC) and is approved for publication. Approval does not signify that the contents necessarily reflect the views and policies of the WRC or the members of the project steering committee, nor does mention of trade names or commercial products constitute endorsement or recommendation for use.

Printed By Sidwaa Printers 012 804 1164

# Executive Summary

Recent years have seen the development of various treatment methods for the purification of industrial wastewaters due to the increased demand for reducing pollution loads in effluents. Aqueous waste streams containing toxic organic compounds are of special interest, since conventional treatment methods such as biological waste treatment can not always be used. Other popular treatment methods are often ineffective. The catalytic oxidation of water containing organic waste has been investigated since the 1960s with varying degrees of success. A major problem associated with this method is the high temperatures and pressures required to improve the activation energies involved. According to the literature, electrochemical oxidation has become a popular method for treating these wastes, since the applied voltage determines the activation energy and, therefore, the process can often be performed under ambient conditions.

The main objectives of the project were the following:

- Development of a multi-family water-treatment system that sterilises water and removes undesirable organics.
- Obtaining a water treatment system that should also be capable of treating industrial effluents.
- Investigation of different types of cell designs as alternatives to current cell design for efficiency improvements.

This led to the investigation of a unique reactor system for the treatment of such wastes. The reactor utilises proton-exchange membrane technology to eliminate the requirement of conductivity in wastewater streams to be treated; thus the membrane serves as a solid electrolyte. The reactor system is therefore referred to as a solid-polymer-electrolyte (SPE) reactor. Novel metal oxide anodes are responsible for the oxidation of the organic molecules. Metal oxide catalysts are useful in the treatment of a wide variety of organic wastes.

Mixed metal oxide stannates were prepared by the sol-gel method and coated onto solid titanium substrates as thin films, using spin and dip coating methods. Metal oxides such as $Sb_2O_5$, $ZrO_2$, CuO, $MnO_x$ and $PdO_2$ were introduced into a $SnO_2$ host matrix using the sol-gel technique. Dopants were added to the catalyst to improve properties such as catalytic activity and conductivity and to produce dimensionally stable electrocatalyst materials. These mixed metal oxides were cast as thin film electrodes, then characterised by a range of spectroscopic techniques to establish surface morphology. They were also characterised by electrochemical techniques for elucidation of electrocatalytic ability. A $SnO_2$ catalyst doped with $ZrO_2$ was used as anode in this study.

Experimental data were obtained by operating the reactor in two different modes of operation. Phenol was selected as model contaminant due to its resistance to oxidation. Galvanostatic operation (constant current) was used to test the influence of flow rate, current density and membrane-electrode-assembly (MEA) compression factor. The effect of separating the electrolytes in the two compartments of the reactor was also investigated in this mode.

Potentiostatic operation (constant voltage) was employed to compare the current efficiencies of the two different modes of operation. According to reports from the literature, fouling via the formation of a polymeric film may have a detrimental influence on the oxidation efficiency. The polarity of the electrodes was reversed in order to remove such films during operation. These experiments were also performed under potentiostatic operation.

In addition, nickel-plated aluminium and titanium current collectors were tested. The nickel-plated aluminium current collectors were significantly cheaper than the titanium current collectors. Typical reactor lengths were calculated for 99% phenol combustion using the experimental data. The results are summarised in Table 1.

The results showed that the phenol oxidation reaction rate depended on both the flow rate and the current density. It was found that some optimum current density existed at each flow rate (Reynolds number) that was investigated. This optimum corresponded to a maximum reaction rate for low flow rates, but in the case of high flow rates the optimum current density corresponded to a minimum reaction rate. Separation of the two compartments of the reactor had a noticeable effect on the efficiency of the reactor. This was attributed to the reversible reaction between hydroquinone and *p*-benzoquinone, two breakdown products of phenol. The MEA compression factor was found not to influence the oxidation reaction rate in the range of values investigated.

Table 1: Reactor lengths and current efficiencies for 99% conversion of phenol

| Re | I [mA] | Separated | L [m] | ε [%] |
|---|---|---|---|---|
| Nickel-plated current collectors | | | | |
| 650 | 20 | No | 6159 | 6.23 |
| 650 | 35 | No | 2878 | 10.04 |
| 650 | 50 | No | 3606 | 5.76 |
| 650 | 50 | Yes | 1803 | 10.13 |
| 1516 | 50 | Yes | 3011 | 13.97 |
| Titanium current collectors | | | | |
| 796 | 20 | No | 6124 | 48.82 |
| 1784 | 20 | No | 2945 | 59.84 |
| 1784 | 30 | No | 4067 | 30.50 |
| 1784 | 40 | No | 3994 | 34.28 |
| 1784 | 50 | No | 2987 | 48.71 |
| 2583 | 20 | No | 1160 | 30.08 |

Typical indicator organisms (*Enterococcus faecallis*, *Escherishia coli* and *Salmonella*) were used to determine the reactor's disinfection capability. After four hours of electrolysis, complete destruction of all microorganisms was observed. This was verified by allowing a 24-hour period after each experiment, in which no regrowth was observed.

A requirement of the study was the accurate determination of the various oxidation breakdown products of phenol. This led to the refinement of an HPLC analytical method in order to quantitatively determine these products.

A basic cost analysis was performed for a typical reactor system treating 186 *l*/h. This would relate to a daily allowance of 20 *l* per person per day (200 persons), the minimum recommended quantity as specified by the World Health Organisation. This cost amounted to approximately R2.50 per day (R75 per month). The water provided as such would be completely disinfected with up to 75% removal of organic content.

A detailed sensitivity analysis was performed to determine the influence of the major parameters on the phenol conversion in the reactor. It was found that the internal surface area of the catalyst substrate as well as the reaction rate constant was the most important factors. It was also found that the recycle ratio did not influence the conversion greatly.

An analysis was performed to determine the actual physical requirements of the system to make it competitive with existing water treatment technologies. These requirements were compared with improvements that were physically possible. It was found that the required improvements were physically impossible to attain with present technology.

The following major conclusions were drawn from the results of the study:

- The SPE reactor system is only partially successful in removing organic materials from waste water. It does however, completely destroy all living organisms.
- Due to the complex interactions between the various parameters in the reactor system, the experimental data could not give any indication as to what the limiting process was. A theoretical evaluation of the system in chapter 6 indicated however that internal mass transfer was the limiting factor regarding the reaction rate.
- Despite the higher current efficiencies observed under potentiostatic control, it was found that galvanostatic control, due to the much higher rate of charge transfer, was the better choice for the mode of operation of the reactor. Reductions in the length of the reactor of up to an order of magnitude were obtained.
- The reactor system, using the current catalyst and reactor set-up, is not economically viable for treating contaminated water due to high costs of materials and operation.
- The required length for the reactor can be reduced by up to an order of a magnitude when treating waste streams that are only contaminated with micro-organisms.
- Titanium must be used for the current collectors. Nickel-plated current collectors showed corrosion, even after the first run. Although nickel may be cheaper initially, more frequent maintenance will be needed. The presence of nickel ions in the effluent is also undesirable.
- The HPLC analytical method that was developed for the quantitative detection of phenol and its breakdown products was accurate and successful. However, there is still much information that needs to be obtained regarding the exact breakdown products. Only a few of these products have been identified to date.
- The system developed to date is not economical compared to other water treatment technologies. Also, the projected improvements recommended in the various properties of the reactor, such as catalyst substrate, reaction rate constant and mass transfer coefficients are physically impossible. For example, the rate of the limiting step in the process needs to be improved from the current value of approximately $1.1\times10^{-7}$ m/s to at least $5\times10^{-4}$ m/s.

The following recommendations are made for future work in this field of research:

- High overpotentials are observed for the electrode reactions. One of the main reasons for the high overpotential may be the contact between the electrode and the membrane. If the catalyst and membrane can be combined into one part, then two contacting surfaces would be removed.
- It is not possible to identify and quantitatively analyse all of the intermediates of phenol oxidation. Accurate measurement of the oxygen and carbon dioxide generated in the reaction will however give an indication of the selectivity and extent of the oxidation reaction. If reliable methods can be obtained to measure the concentrations of these gases, more accurate assumptions can be made about the oxidation reaction mechanisms involved.
- When considering future work, the results in chapter 6 should be taken into account. The types of improvements that are necessary before this type of technology (electrochemical combustion of organics) would be feasible are recommended and discussed.

# Contents


Executive Summary ..... i
Contents ..... iv
List of Tables ..... vii
List of Figures ..... viii
Nomenclature ..... x
Glossary ..... xii

1 Introduction ..... 1
1.1 Water Treatment Techniques ..... 1
1.2 Electrochemical Oxidation ..... 1
1.3 Problem Statement ..... 2
1.4 Objectives ..... 3
1.5 Realising the Objectives ..... 3
1.6 Scope of the Report ..... 4

2 Electrochemical Oxidation of Organic Molecules ..... 5
2.1 Introduction ..... 5
2.2 Reaction Mechanics ..... 5
2.2.1 Overview of reaction mechanism ..... 5
2.2.2 Phenol oxidation ..... 6
2.2.3 Electrode passivation ..... 8
2.3 Principles of the SPE Reactor ..... 9
2.4 Review of Previous Work ..... 12
2.4.1 Grimm's research ..... 12
2.4.2 Other research ..... 12
2.4.3 Analysis of literature review ..... 14

3 Phenol Oxidation ..... 16
3.1 Introduction ..... 16
3.2 Experimental ..... 16
3.2.1 Instruments and specifications ..... 16
3.2.2 Experimental reactor ..... 17
3.2.3 Analysis of phenol and breakdown products ..... 18
3.3 Results and Discussion ..... 21
3.3.1 Determination of apparent reaction rate constants ..... 21
3.3.2 Results — galvanostatic operation ..... 22
3.3.3 Results – potentiostatic ..... 27
3.3.4 Results – titanium current collectors ..... 32
3.4 Conclusions ..... 36

4 Disinfection ..... 37
4.1 Introduction ..... 37
4.2 Experimental ..... 37
4.2.1 Pathogen selection ..... 37
4.2.2 Experimental method ..... 37

4.3 Results ..... 38
4.3.1 High–concentration experiments ..... 39
4.3.2 Low–concentration experiments ..... 39
4.4 Conclusions ..... 42

5 Application of Experimental Data ..... 43
5.1 Introduction ..... 43
5.2 Discussion of Experimental Work ..... 43
5.3 Scale-up Calculations ..... 45
5.4 Economic Evaluation ..... 47
5.5 Conclusions ..... 49

6 System Requirements for Future Applications ..... 51
6.1 Introduction ..... 51
6.2 Sensitivity Analysis ..... 51
6.2.1 Reactor model revisited ..... 51
6.2.2 Effect of parameters ..... 51
6.2.3 Mass transfer effects ..... 56
6.3 Requirements for a Practical Application ..... 60
6.3.1 Reactor specifications ..... 60
6.3.2 Reactor capability ..... 64
6.4 Conclusions ..... 64

7 Overall Conclusions and Recommendations ..... 65
7.1 Conclusions ..... 65
7.2 Recommendations ..... 65

References ..... 67

A Additional Theory and Literature ..... 70
A.1 Electrochemical Reactors ..... 70
A.1.1 Electrochemical Reaction Rates ..... 71
A.1.2 Cell Potential ..... 73
A.1.3 Electrode Kinetics ..... 77
A.1.4 Electrode Mass Transfer Phenomena ..... 79
A.1.5 Analogy to Chemical Kinetics ..... 80
A.2 Electrode Preparation ..... 83
A.2.1 Spray Pyrolysis ..... 83
A.2.2 Thermal Decomposition ..... 83
A.2.3 Sol-gel Dip-coating ..... 83

B Catalyst Development ..... 86
B.1 Preparation of Mixed Metal Oxide Catalysts ..... 86
B.1.1 Sol-gel preparation of mixed metal oxide electrodes ..... 86
B.1.2 Preparation of thin-film electrodes ..... 87

B.2 Characterisation of catalysts ..... 88
B.2.1 Experimental ..... 88
B.2.2 Results and discussion ..... 89
B.2.3 X-ray methods ..... 91
B.3 Conclusions and Recommendations ..... 97

C Model derivations ..... 99
C.1 Reactor Model ..... 99
C.2 Scale-up Calculation ..... 101
C.3 Economic Evaluation ..... 103
C.4 Sensitivity Analysis ..... 105
C.5 Internal Mass Transfer ..... 107

D Miscellaneous Calculations ..... 109
D.1 Reaction Rate Constants ..... 109
D.2 Differential Method of Rate Analysis ..... 109
D.3 Reactor Cost ..... 110

E Initial Work ..... 112
E.1 Introduction ..... 112
E.2 Experimental ..... 112
E.2.1 Instruments and specifications ..... 112
E.2.2 Experimental reactor ..... 113
E.2.3 Analysis ..... 114
E.2.4 Method ..... 114
E.3 Results and Discussion ..... 114
E.4 Conclusions ..... 117

F Growth Curves ..... 118

G Technical Drawings ..... 120

# List of Tables


| | | |
|---|---|---|
| 1. | Typical reactor lengths and current efficiencies for 99% conversion of phenol | iv |
| 3.1 | Toxicity of phenol and the main breakdown products | 19 |
| 3.2 | HPLC retention times for the phenolic compounds | 19 |
| 3.3 | Retention times for the aliphatic acids | 20 |
| 3.4 | Experimental parameters for current density experiments | 22 |
| 3.5 | Reaction rate constants for current experiments | 23 |
| 3.6 | Experimental parameters for flow rate experiments | 24 |
| 3.7 | Reaction rate constants for flow rate experiments | 24 |
| 3.8 | Experimental parameters for MEA compression experiment | 25 |
| 3.9 | Reaction rate constants for stack pressure experiments | 26 |
| 3.10 | Reaction rate constants for separated electrolytes | 27 |
| 3.11 | Reaction rate constants for potentiostatic experiments — with and without polarity change | 32 |
| 3.12 | Typical potential values for different currents | 33 |
| 3.13 | Reaction orders determined from the differential method | 35 |
| 4.1 | Reaction rate constants for microbiological experiments | 40 |
| 5.1 | Comparison of experimental reaction rate constants for different experiments | 43 |
| 5.2 | Calculated reactor lengths – nickel-plated current collectors | 45 |
| 5.3 | Calculated reactor lengths – titanium current collectors | 45 |
| 5.4 | Calculated reactor lengths – potentiostatic and microbiological experiments | 46 |
| 5.5 | Estimated capital costs of reactor per meter length (June 2003) | 48 |
| 6.1 | Major parameters for sensitivity analysis | 51 |
| 6.2 | Constant values used to determine other parameters (effect of apparent reaction rate constant) | 52 |
| 6.3 | Constant values for other parameters (effect of specific surface area) | 54 |
| 6.4 | Constant values for other parameters (effect of recycle ratio) | 55 |
| 6.5 | Practical vs. theoretical reaction rate coefficients | 59 |
| 6.6 | Typical values for the effective diffusivity | 60 |
| 6.7 | Typical values for the resistance to mass transfer in the reactor | 63 |
| 6.8 | Expected improvements in the various parameter values | 64 |
| A.1 | Summary of method for determining reaction order | 82 |
| B.1 | Doping ratios for mixed metal tin oxides | 87 |
| B.2 | Band gap energy values of the mixed metal tin oxide gels prepared | 90 |
| B.3 | Typical compositional analysis of mixed metal tin oxide thin films (% composition based on ppm analysis) as determined by PIXE/RBS | 97 |
| D.1 | Data for the derivation of reaction orders (60 ppm) | 109 |
| D.2 | Statistical data for polynomial fits | 110 |
| E.1 | Experimental parameter values for initial experiments | 115 |
| E.2 | Rate constants for initial experiments | 117 |

# List of Figures


| | | |
|---|---|---|
| 2.1 | Proposed phenol oxidation to carbon dioxide and water | 7 |
| 2.2 | Phenol oxidation and polymerisation pathways | 9 |
| 2.3 | Parts of an SPE reactor | 10 |
| 2.4 | Normalised experimental data reported from the literature | 14 |
| 3.1 | Experimental set-up used for the laboratory-scale experiments | 17 |
| 3.2 | Photographs of the laboratory-scale electrochemical cell | 18 |
| 3.3 | HPLC chromatogram of the standards for phenolic compounds | 19 |
| 3.4 | HPLC chromatogram of acid standards | 20 |
| 3.5 | HPLC chromatogram of initial acid sample (example 1) | 20 |
| 3.6 | HPLC chromatogram of initial acid sample (example 2) | 21 |
| 3.7 | HPLC chromatogram of final acid sample | 21 |
| 3.8 | Effect of current density on reaction rate | 23 |
| 3.9 | Effect of flow rate on reaction rate | 24 |
| 3.10 | Effect of MEA compression on reaction rate | 26 |
| 3.11 | Effect of electrolyte separation on reaction rate | 27 |
| 3.12 | Results of potentiostatic experiments | 28 |
| 3.13 | Normalised potentiostatic experimental results | 29 |
| 3.14 | Theoretical vs. practical conversion | 29 |
| 3.15 | Potentiostatic breakdown curve (polarity changed) | 30 |
| 3.16 | Normalised potentiostatic breakdown curve (polarity changed) | 30 |
| 3.17 | Theoretical vs practical conversion (polarity changed) | 32 |
| 3.18 | Concentration vs time curves for a flow rate of 11.5 *l*/h using titanium current collectors | 33 |
| 3.19 | Concentration vs time curves for a flow rate of 25.7 *l*/h using titanium current collectors | 34 |
| 3.20 | Concentration vs time curves for a flow rate of 37.2 *l*/h using titanium current collectors | 34 |
| 4.1 | Disinfection of high concentration samples | 39 |
| 4.2 | Disinfection of various micro-organisms | 40 |
| 4.3 | Disinfection of *Salmonella* | 41 |
| 4.4 | Disinfection of *E. faecallis* | 41 |
| 5.1 | Reaction rate constants for titanium and nickel-plated current collectors | 44 |
| 5.2 | Proposed flow diagram for pilot plant | 47 |
| 5.3 | Reactor length vs recycle ratio for $X = 0.75$ | 48 |
| 5.4 | Costs of various parts of a typical reactor (June 2003) | 49 |
| 6.1 | Effect of reaction rate constant on conversion | 52 |
| 6.2 | Effect of specific surface area on conversion | 54 |
| 6.3 | Effect of recycle ratio on conversion | 55 |
| 6.4 | Effect of recycle ratio on conversion (importance of reaction rate constant) | 56 |
| 6.5 | Schematic representation of reactor for mass transfer study | 56 |
| 6.6 | Effect of recycle ration on reactor capital cost | 61 |
| 6.7 | Effect of product flow rate on reactor capital cost | 62 |
| 6.8 | Analogy of mass transfer resistance to electrical systems | 62 |
| A.1 | Parts of an electrochemical cell | 70 |
| A.2 | Voltage components in an electrochemical cell | 74 |
| A.3 | Semi-logarithmic plot for determination of $i_0$ and the Tafel slope | 79 |
| A.4 | Determination of reaction rate constants for different reaction orders | 82 |
| B.1 | Schematic of the sol–gel process | 86 |
| B.2 | Design of mixed metal tin oxide coated electrode | 87 |
| B.3 | TGA of metal oxide doped tin oxide gels | 89 |
| B.4 | An example of how band gap energy was measured for $ZrO_2/SnO_2$ | 90 |
| B.5 | The effect of ageing on $SnO_2/ZrO_2$ | 91 |

| | | |
|---|---|---|
| B.6 | ZRD pattern for Zr-$SnO_2$ powder showing only the characteristic peaks for $SnO_2$ | 92 |
| B.7 | Scanning electron micrographs of mixed metal oxides | 92 |
| B.8 | Atomic force microscopy of mixed metal oxides | 93 |
| B.9 | RBS of Zr/$SnO_2$ dip coated surfaces and the fit spectrum by RUMP | 95 |
| B.10 | RBS of Zr/$SnO_2$ spin coated surfaces and the fit spectrum by RUMP | 96 |
| C.1 | Nomenclature used in model derivation | 99 |
| C.2 | Nomenclature used for reactor | 100 |
| C.3 | Reactor conversion versus reactor length | 103 |
| D.1 | Determination of reaction order – example | 110 |
| E.1 | Reactor flow system used in the initial work | 112 |
| E.2 | Breakdown curve for 500 *l*/h experiment | 115 |
| E.3 | Breakdown curve for 600 *l*/h experiment | 116 |
| E.4 | Breakdown curve for 700 *l*/h experiment | 116 |
| F.1 | Growth curve for *E. faecallis*: Absorbence and cell count | 118 |
| F.2 | Growth curve for *E. faecallis* at various TSB concentrations | 118 |
| F.3 | Growth curve for *Salmonella* at various TSB concentrations | 119 |
| F.4 | Growth curve for *E. coli* at various TSB concentrations | 119 |
| G.1 | Technical drawing showing initial reactor current collector | 120 |
| G.2 | Technical drawing of initial reactor anodic frame | 121 |
| G.3 | Technical drawing of initial reactor cathodic frame | 122 |
| G.4 | Technical drawing showing all parts of the laboratory reactor | 123 |
| G.5 | Technical drawing of laboratory reactor current collector | 124 |
| G.6 | Technical drawing of laboratory reactor current collector frame | 125 |

# Nomenclature
## General

| Symbol | Description | Units |
|---|---|---|
| $A$ | activity coefficient | [kmol/m$^3$] |
| $a(t)$ | catalytic activity | |
| $A$ | surface area | [m$^2$] |
| $C$ | Concentration | [kmol/m$^3$] |
| $d_e$ | equivalent diameter | [m] |
| $D$ | Diffusivity | [m$^2$/s] |
| $e_0$ | charge of single electron | [C] |
| $f$ | friction factor | |
| $F$ | Faraday's constant | [C/mol] |
| $G$ | free energy | [kJ/kmol] |
| $i$ | current density | [A/cm$^2$] |
| $I$ | total current | [A] |
| $k$ | reaction rate constant | varies[1] |
| $k_m$ | mass transfer coefficient | [m/s] |
| $L$ | Length | [m] |
| $m$ | Mass | [kg] |
| $M_R$ | molecular mass | [kg/kmol] |
| $n$ | number of moles | [kmol] |
| $N_A$ | Avogadro's number | [mol$^{-1}$] |
| $p$ | Pressure | [Pa] |
| $Q$ | charge passed | [C] |
| $r$ | reaction rate | [kmol/s.m$^3$] |
| $\bar{r}$ | reaction rate per unit electrode area | [kmol/s.m$^2$] |
| $R$ | Universal gas constant | [kJ/kmol.K] |
| Re | Reynolds number | |
| $S_a$ | Specific surface area | [kg cat./m$^3$] |
| Sc | Schmidt number | |
| Sh | Sherwood number | |
| $t$ | Time | [s] |
| $T$ | Temperature | [K] |
| $V$ | Potential | [V] |
| $\dot{V}$ | flow rate per unit area | [m$^3$/m$^2$.s] |
| $v$ | volumetric flow rate | [m$^3$/s] |
| $X$ | Conversion | |

[1] Depends on the reaction order and type of reaction

**Greek Symbols**

| Symbol | Description | Units |
|---|---|---|
| $\alpha$ | charge transfer coefficient | |
| $\beta$ | curve-fitting coefficient | [1/s] |
| $\gamma$ | aspect ratio | [m/m] |
| $\delta$ | substrate thickness | [m] |
| $\varepsilon$ | current efficiency | |
| $\eta$ | Overpotential | [V] |
| $\Theta$ | electrode bubble coverage fraction | |
| $\mu$ | chemical potential | [kJ/kmol] |
| $\nu_e$ | stoichiometric number of electrons | [mol $e^-$/mol] |
| $\rho$ | Density | [kg/m$^3$] |
| $\tau$ | residence time | [s] |

**Subscripts**

| Symbol | Description | Units |
|---|---|---|
| 0 | initial value | |
| a | anode | |
| b | bubble | |
| c | cathode | |
| e | electrode | |
| i | internal (with reference to substrate material) | |
| in | inlet, reactor | |
| j | specific reaction | |
| out | outlet, reactor | |
| p | product | |
| Ph | phenol | |
| R | reactor | |
| r | reactant, recycle | |
| s | substrate | |
| t | value at time *t* | |
| T | total | |

**Glossary**

| | |
|---|---|
| AFM | Atomic force microscopy |
| emf | Electro-motive force |
| EOI | Electrochemical oxidation index |
| HPLC | High-pressure liquid chromatography |
| MEA | Membrane-electrode assembly |
| PEM | Proton exchange membrane |
| PEMFC | Proton exchange membrane fuel cell |
| PIXE | Particle-induced X-ray emission |
| RBS | Rutherford backscattering |
| SEM | Scanning electron microscopy |
| SPE | Solid-polymer-electrolyte |
| TGA | Thermogravimetric analysis |
| TOC | Total organic carbon |
| TSB | Tryptone soy broth |
| UV | Ultra-violet |

# 1 Introduction

The need for reduced or zero-pollutant effluents from chemical and petrochemical industries has increased in the last few decades due to increasingly stringent legislation and pressure from environmental groups. Many of these industries have effluent streams containing quantities of organic compounds that are too low in concentration to recover economically, but high enough in concentration to be harmful to the environment. Thus, the need for a reliable system for the removal of such organics has resulted in much research focussing on water purification, especially in the electrocatalytic oxidation of organics in dilute aqueous solutions.

## 1.1 Water Treatment Techniques

Various methods of oxidative water treatment techniques have been developed with different levels of success. The most popular techniques used for both organic oxidation and disinfection includes the following [0]:

- Ozone treatment
- Wet-air oxidation
- Catalytic oxidation
- Oxidation with high-frequency ultrasound
- Ultraviolet radiation
- Adsorption on activated carbon
- Activated sludge
- Coagulation
- Flocculation

Electrochemical treatment methods can also be used. This technique is discussed in more detail in the next section.

## 1.2 Electrochemical Oxidation

Electrochemical oxidation utilizes specific electrodes that show activity towards the oxidation of organic molecules. Electricity is provided as the driving force for the oxidation reaction that would under normal circumstances not take place at the conditions present in the electrochemical reactor (low temperature).

In the last two to three decades significant advances have been made in the field of electrocatalysts [2, 3, 4] — they are used as catalysts in electrochemical oxidation; a popular treatment method for the oxidation of dilute aqueous organic wastes.

In electrocatalysis the success of the process seems to depend largely on the type of catalyst that is used. Therefore a wide variety of catalysts have been tested in other studies in an attempt to improve the catalytic activity. Traditional catalysts, such as the noble metals Pt, Pd and Ir, show limited use for the oxidation of aromatic compounds (see section 2.2), since they promote the reaction only up to the formation of quinones. These metals have thus been used as substrate materials for the more exotic metal oxide films that show a much higher selectivity toward the complete combustion of organic molecules. Due to the cost of these noble metals, they are often substituted by titanium substrates. Titanium is known as a valve-metal, which, among other things, provide the required properties for good catalyst adhesion.

Tin dioxide is a very popular metal oxide catalyst [5, 6, 7, 8], since it shows promise in the complete breakdown of organic molecules to carbon dioxide and water (the desired final products of combustion). Additional reasons for the use of tin dioxide are as follows [9]:

- high chemical and electrochemical stability
- high electric conductivity when combined with selected dopants
- high overpotential for the oxygen evolution reaction

Lead dioxide has shown similar activity [10, 11, 12], but the possible leaching of toxic lead ions into treated drinking or natural water makes it an unfavourable choice. It has been shown that adding dopants as metal oxides can improve the catalytic activity of the catalyst film [13]. $SnO_2$ powders doped with a wide variety of dopants such as Cu [14], Ir, Mb [15], Mn [16], Pd, Rh, Ru, Sb [17] and Zr [14] have been produced and tested for their catalytic activity.

The present study follows on from the work of Grimm, who used $Ti/SnO_2/Sb_2O_5$ electrodes [13]. A parallel study was carried out by Baker [18] to address issues regarding the electrochemical properties of a variety of electrocatalysts. It was found that the $Ti/SnO_2/ZrO_2$ system showed the best catalytic activity and was therefore chosen as the catalyst for use in this project.

The need for reducing energy cost requirements was an important consideration in the development of these novel metal oxide catalysts, since they show promise in lowering the activation energies. Therefore, the total energy expenditure of converting a toxic molecule to either less toxic molecules, or completely destroying the molecule to carbon dioxide, would require significantly less energy. A related disadvantage is however the high cost of some of the precursors needed to prepare these metal oxides.

## 1.3 Problem Statement

Ever-increasing demands on water resources as well as environmental legislation require water of very high quality. Organic molecules, especially toxic cyclic organic molecules, tend to act as biocide, preventing the successful application of biological treatment methods. Biological methods of treatment must sometimes be combined with chemical treatment methods to provide water of the necessary quality. In the case of small rural communities in remote areas, the need for a municipal water treatment system does not outweigh the economical aspects associated with the cost and operation of such a plant.

Therefore, it would be ideal if a system could be developed that is capable of both disinfection and unwanted organic content removal. Low cost and low maintenance requirements are vital aspects of such a reactor system for such communities. Industrial applications of such a system would be the post-treatment of process streams for the removal of toxic organic molecules that are harmful to the environment and show resistance to treatment by conventional means.

The objectives of the present project, based on the statements made in the above paragraphs, are the following.

## 1.4 Objectives

The main objectives of the project were:

1. Development of a multi-family water-treatment system that sterilises waters and removes undesirable organics.
2. Obtaining a water treatment system that should also be capable of treating industrial effluents.
3. Investigation of different types of cell designs as alternatives to current cell design for efficiency improvements.

More specifically, the following were addressed:

1. As a limited amount of information is available on the exact kinetics of the electrochemical oxidation process, additional data regarding this aspect of electrochemical combustion were required. The necessary model parameters could then be extracted from this data.
2. As reported on in the literature, only current density and catalyst type have been investigated as process variables to date, the effect of other important parameters such as flow rate, necessary for a robust model needed to be determined.
3. A simple kinetic model for the breakdown of typical organic contaminants was to be formulated. This would then be incorporated into the reactor model.
4. A typical water treatment unit for both the industrial and sterilisation applications, based on the model, was to be designed.
5. A full economical evaluation to determine the feasibility of this type of reactor system was to be performed.

## 1.5 Realising the Objectives

Most of the work that was done with these electrocatalysts to date was based on systems that contained supporting electrolytes, either in the form of altered pH or salinity [4, 5, 19]. The main problem associated with a practical implementation of electrochemical water treatment technologies requiring a supporting electrolyte, is the requirement of regular maintenance to resupply the reactor system with fresh electrolyte. It would be ideal if a system could be designed that does not require post-treatment to restore the original pH and salinity conditions.

Therefore, a new system was developed in which the requirement of the supporting electrolyte was eliminated and substituted with a solid polymer electrolyte (SPE) that served as conductive medium for proton transfer. A disadvantage of these systems is however the contacting of the electrodes to the membrane in order to obtain an evenly distributed current density. Some work has been done (especially in the development of fuel cells) on impregnating the membrane with catalyst particles, although catalyst loading then becomes a factor, as well as the lifetime of the membrane-catalyst assembly.

The work reported here focuses mainly on the investigation of such a system to determine its feasibility in two fields of water treatment. The primary focus was, as explained above, the removal of unwanted organic compounds from water. Phenol, or some substituted form of phenol, has almost exclusively been used as model contaminant in all the literature to date and will also be used here. Since the active agent in the breakdown of the organic molecules is a hydroxyl radical, it was realised that this system could potentially be used in the disinfection of especially rural water sources in disadvantaged communities. The secondary focus of this project therefore deals with disinfection.

As mentioned, this research follows on from the work of Grimm [13], whose research focused mainly on the electrochemical aspects of the metal oxide catalysts. Principally, the same reactor was used for this research — with the exception of the flow channels. Grimm's work showed promise in the removal of high concentrations of phenol, but the experiments that were described showed only the concentration-time data. No additional analyses were performed and therefore no information was given about the actual rates of combustion. These values are considered to be critical in the accurate design of larger reactors and were therefore addressed in this report.

## 1.6 Scope of the Report

In this report, the use of novel metal oxide catalysts in electrochemical reactors is investigated for the removal of organic materials from water. Chapter 2 provides a discussion of electrochemical reactors in general and the accepted mechanism of electrochemical oxidation of organic molecules. Chapters 3 and 4 contain the information gained from the experimental testing and engineering analysis of the catalyst performance. In an attempt to compare the economic viability of systems employing these catalysts, chapter 5 presents the results of an economical analysis of our system. In chapter 6 the actual requirements of our reactor system and what would be required of the system to make it economically feasible. The chapter also considers the actual limiting process at the electrode. Finally, the conclusions drawn from the research, together with suggestions on future improvements of the technology, are supplied in chapter 7.

An expanded appendix is added to the report, containing additional information. This information includes relevant theory, the initial work preceding the work discussed in chapter 3, and typical calculations performed. Appendix B describes the research performed by P.G.L. Baker regarding the development of metal oxide catalysts. Other appendices include growth curves for the indicator organisms measured during the experimental work regarding disinfection and detailed technical drawings of the reactors used during the project.

# 2 Electrochemical Oxidation of Organic Molecules

## 2.1 Introduction

A reasonable amount of work has been done in the area of electrochemical combustion of organic molecules. This chapter is subdivided into two parts addressing the most important research taken from the literature as well as a discussion on the general principles involved in SPE reactors.

The accepted reaction mechanism of the oxidation reaction is discussed in section 2.2. Comninellis [2] suggested a general reaction mechanism where two reaction pathways were discussed. A summary of this mechanism is provided in section 2.2.1. The research carried out in the present project however, required additional information on the actual breakdown products formed during oxidation. This additional information is presented in sections 2.2.2 and 2.2.3.

A brief discussion of the processes that take place in the SPE reactor as well as the major parts of such a reactor are described in section 0. The importance of the PEM is also explained, together with some of the advantages and disadvantages associated with its use.

During the past few decades a fair amount of research into the electrochemical oxidation of organic molecules has been done utilising a variety of metal oxides catalysts. The most important research, according to the author, is summarised in section 2.4. This summary includes the work of Grimm, who was the principal researcher in the project, WRC Project \# 852, from which the present one follows on. In conclusion, all of the researchers' work is discussed and compared (section 2.4.3).

## 2.2 Reaction Mechanics

### 2.2.1 Overview of reaction mechanism

According to Comninellis [2], there are two main reaction pathways for the oxidation of phenol that are dependent only on the type of catalyst chosen as anode. In the electrochemical conversion method, cyclic organic molecules are converted by ring opening to aliphatic acids, which can be treated using biological methods for further purification. This method requires post-treatment to completely remove all organic carbon. Electrode materials that have a high selectivity towards organic ring opening but a low selectivity towards reaction with the formed aliphatic acids are preferable. Typical electrode materials are Pt, Ti/$IrO_2$ and Ti/$RuO_2$.

The electrochemical combustion reaction on the other hand completely oxidises the organic molecules into carbon dioxide and water. Electrode materials must have high catalytic activity towards the combustion of all organic molecules to $CO_2$. Comninellis found that Ti/$SnO_2$ gives the best results for this type of reaction. It also shows higher current efficiencies than the previously mentioned electrode materials.

The first and most important step in the oxidation reaction pathway is the formation of the active site on the catalyst surface. The active site is formed by discharge of a water molecule on the catalyst surface to produce an adsorbed hydroxyl radical as shown in equation 2.1.

$$MO_x + H_2O \rightarrow MO_x(^{\bullet}OH) + H^+ + e^- \qquad (2.1)$$

This may or may not be followed by the interaction of the hydroxyl radical with the oxygen in the metal oxide lattice. The hydroxyl radical absorbs into the lattice to form a higher oxide:

$$MO_x(^{\bullet}OH) \rightarrow MO_{x+1} + H^+ + e^- \quad (2.2)$$

This is only possible if the metal has higher oxidation states. Therefore the "active oxygen" can take two forms: physisorbed "active oxygen" (hydroxyl radicals, $^{\bullet}OH$) and chemisorbed "active oxygen" (lattice oxygen, $MO_{x+1}$). If an organic molecule is available when a reaction site is formed, the following oxygen transfer reactions can take place:

$$R + MO_x(^{\bullet}OH)_z \rightarrow nCO_2 + zH^+ + ze^- + MO_x \quad (2.3)$$

$$R + MO_{x+1} \rightarrow RO + MO_x \quad (2.4)$$

where $n$ is dependent on the number of carbon atoms in the original organic molecule and $z$, to a certain extent, is dependant on the breakdown pathway that is followed. The corresponding acid formed in reaction 2.4 is normally treated by biological methods to convert it to carbon dioxide.

$$RO \xrightarrow{BIO} CO_2 \quad (2.5)$$

In the absence of an organic molecule, oxygen is formed as a side reaction:

$$MO_{x+1} \rightarrow MO_x + \frac{1}{2}O_2 \quad (2.6)$$

$$MO_x(^{\bullet}OH) \rightarrow \frac{1}{2}O_2 + H^+ + e^- + MO_x \quad (2.7)$$

If the potential of the reaction is kept below the potential for oxygen evolution by hydrolysis, equation (2.7) represents the only competing side reaction.

### 2.2.2 Phenol oxidation

Equation (2.3) offers a very simplified view of the overall reaction mechanism. In reality, several intermediate steps take place before the phenol molecule is completely converted to carbon dioxide and water. The most complete reaction pathway reported for the oxidation of phenol has been sourced from work pertaining to the wet-air oxidation of phenol [20]. Although the process does not operate with electrodes, it still uses a catalyst and is believed to follow a free radical mechanism. The reaction scheme is presented in Figure 2.1.

Researchers examining the use of electrodes for the combustion of organic molecules observed some of the breakdown products given in the reaction scheme. Using Ti/$SnO_2$ electrodes, Comninellis [5, 7] found the aromatic dihydroxy-benzenes and *p*-benzoquinone. *o*-Benzoquinone may have been present, but no standards for analysis could be obtained due to its instability. Maleic, oxalic and formic acid were also found in the reaction mixture, together with some unidentified intermediates. With Ti/$IrO_2$ electrodes, Comninellis *et al.* [21] found only the aromatic intermediates. Sharifian and Kirk [11], and Tahar and Savall [12], detected benzoquinone and maleic acid as intermediate products.

In Figure 2.1 only the breakdown products are shown, with no information on the formation of the hydroxyl radical intermediates or the number of electrons involved. In the literature, both Comninellis *et al.* [5, 21] and Petrov *et al.* [6] found that the complete combustion of phenol requires a total of 28 electrons and the discharge of 11 water molecules.

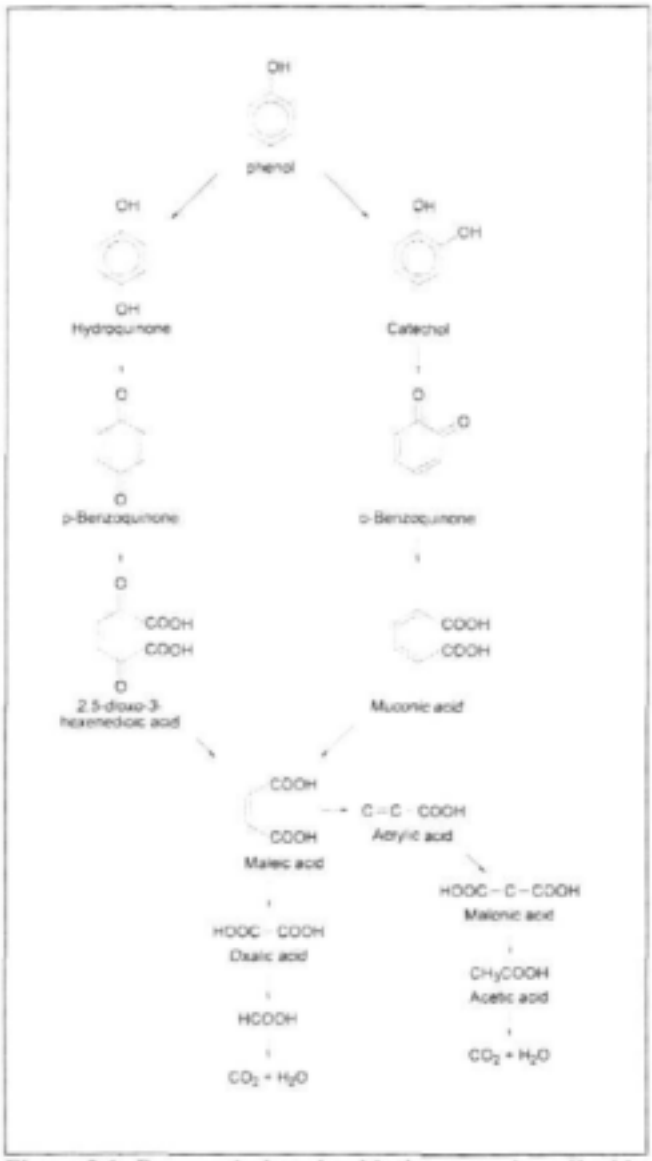


**Figure 2.1: Proposed phenol oxidation to carbon dioxide and water (ref. [20]).**

Thus, the total hydroxyl formation reaction can be written as

$$MO_x + 11H_2O \rightarrow MO_x\left(^{\bullet}OH\right)_{11} + 11H^+ + 11e^- \qquad (2.8)$$

The reaction for the oxidation of phenol to carbon dioxide and water may then be written as

$$C_6H_5OH + MO_x\left(^{\bullet}OH\right)_{11} \rightarrow 6CO_2 + 17H^+ + 17e^- + MO_x \qquad (2.9)$$

Combining (2.8) and (2.9) the overall reaction for the breakdown of phenol can be obtained:

$$C_6H_6O + 11H_2O \rightarrow 6CO_2 + 28H^+ + 28e^- \qquad (2.10)$$

It must be noted that the reactions of 1,2- and 1,4-dihydroxybenzene to form *o*- and *p*-benzoquinone are reversible reactions and take place without the requirement of active oxygen:

$$C_6H_6O_2 \Leftrightarrow C_6H_4O_2 + 2H^+ + 2e^- \qquad (2.11)$$

### 2.2.3 Electrode passivation

According to Gattrell and Kirk [22, 23], passivation of an electrode is the decrease in the activity of an electrode caused by the formation of an unreactive, impermeable film on the electrode surface. In some of the initial work regarding the catalysed combustion of organic molecules it was found that in some cases the catalyst became poisoned, causing the catalyst to rapidly lose activity. The first report of this poisoning was on the combustion of cumene using $Fe_2O_3$ as catalyst [24]. It was found that phenol was the poison, it being one of the breakdown products.

Gattrell and Kirk oxidised phenol using platinum electrodes. They observed the formation of a strongly adhering, defect-free polymeric film on the surface of the anode. The passive film is the result of the formation of organic tars through electropolymerisation. These tars are characterised by their low rate of oxidation, low permeability and strong adhesion properties.

In Figure 2.2 the reaction pathway is shown for both the polymerisation reaction as well as the first steps of the oxidation reaction. The phenoxy-radical intermediate was found to be the key intermediate — it interacted with other phenoxy-radicals to form dimers.

These dimers could in turn form radicals and interact with the phenoxy radical or other dimeric radicals, forming higher molecular weight materials. Gattrell and Kirk determined that the product distribution and reaction pathways were dependent on several factors, such as phenol concentration, the electrode material, reactant adsorption characteristics, pH, current density and potential.

Gattrell and Kirk [25] suggested that an oxide-coated electrode could be used to prevent the formation of the passivating film at higher potentials, at which hydroxyl radicals and peroxide intermediates are formed. Due to the oxygen evolution reaction a fraction of the applied current will be wasted, causing a reduction in observed current efficiencies. Koile and Johnson [26] determined the effect of this oxygen evolution on the passivating film and found that significant rupturing of the film did not result in recovery of the electrode surface. However, this proved the strong adsorption characteristics of the film.

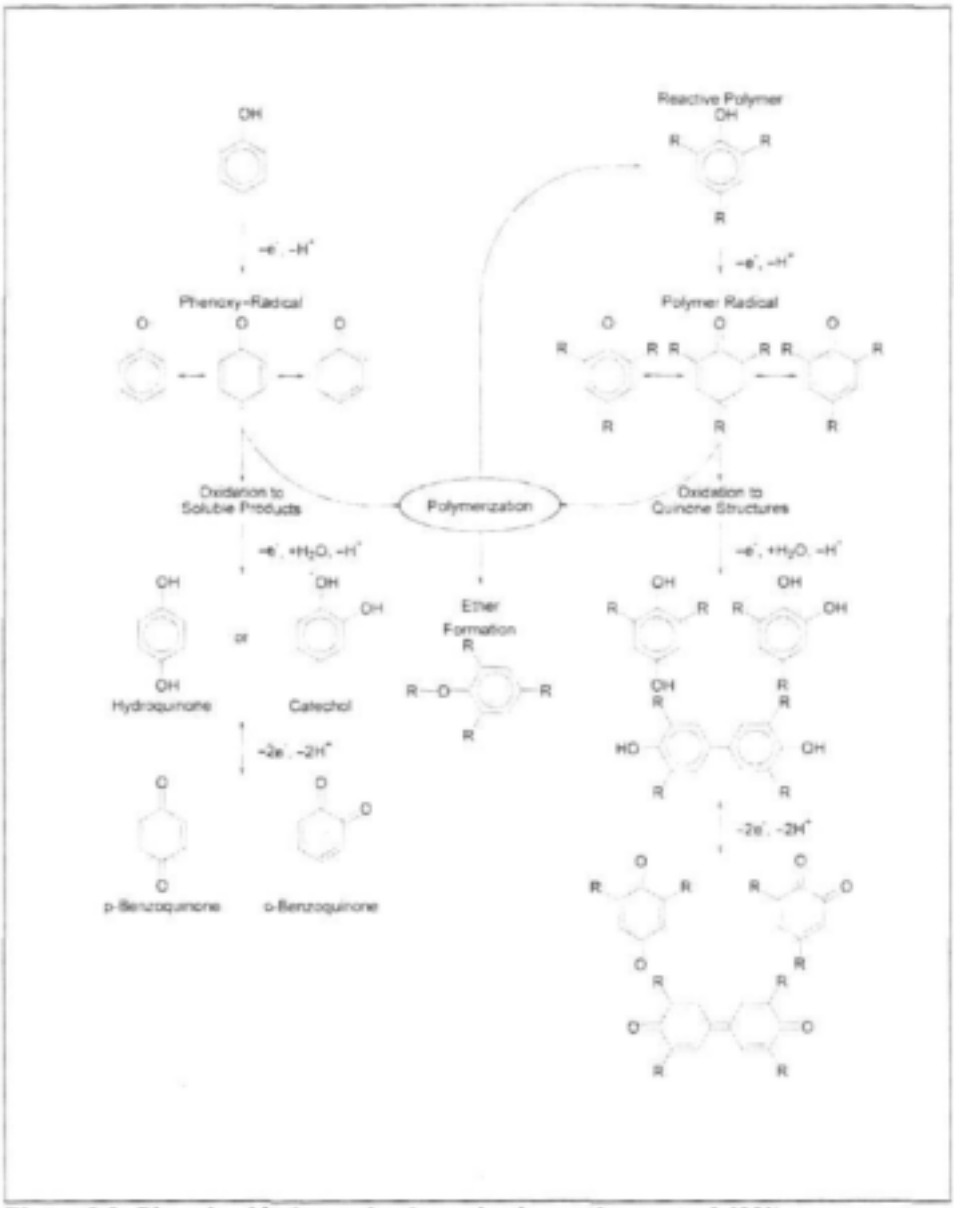


**Figure 2.2: Phenol oxidation and polymerisation pathways (ref. [23]).**

According to Comninellis, the metal oxide catalysts, especially the $SnO_2$ and doped $SnO_2$ films, are resistant to the formation of this passivating film. This theory has however not been proven yet. For instance, in this study, the phenol concentration was found to decrease with time, but none of the aliphatic acid intermediates were detected. This could imply the removal of phenol by the formation of a polymeric film.

## 2.3 Principles of the SPE Reactor

A simplified representation of a typical SPE reactor is given in Figure 2.3. A cross-section of the membrane-electrode assembly and the top current collector is shown to give a view of the flow channels.

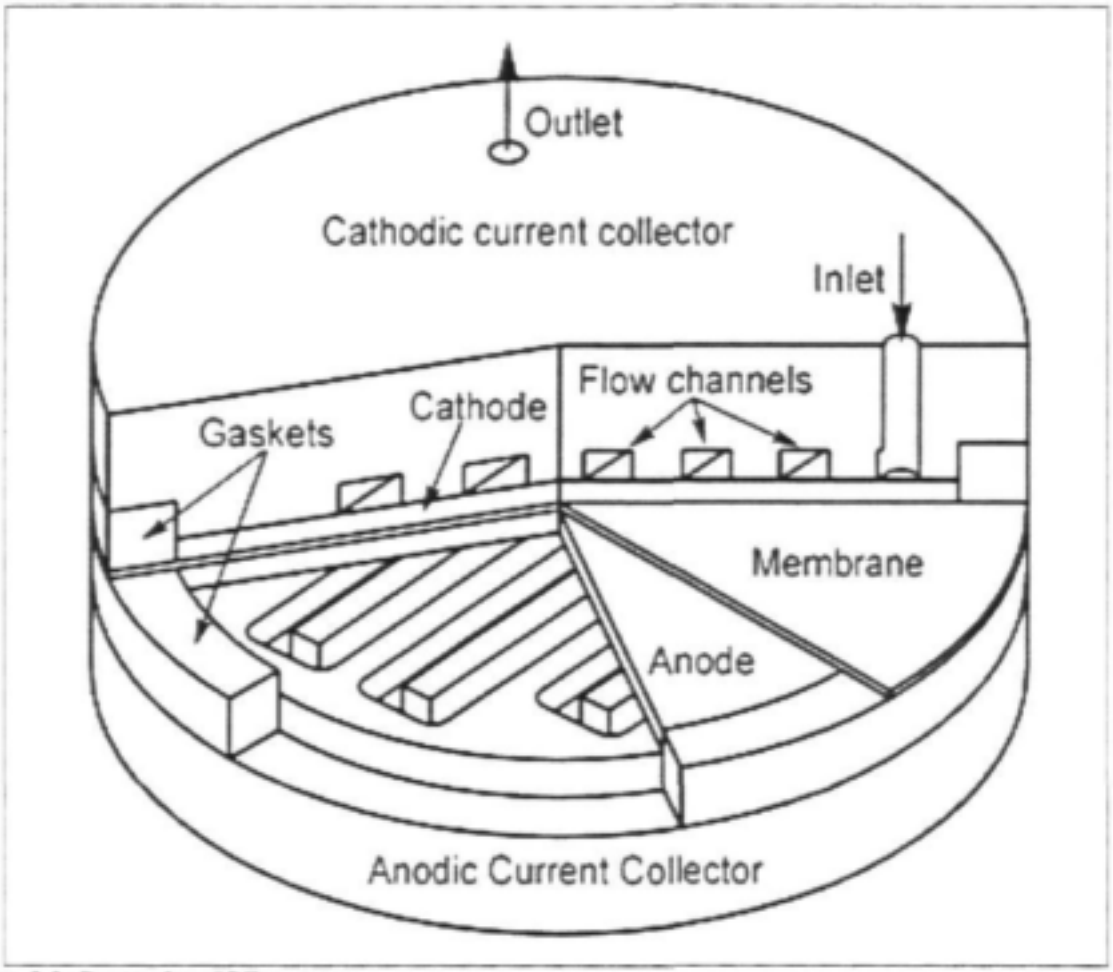


**Figure 2.3: Parts of an SPE reactor.**

The most important part of the reactor is the membrane-electrode-assembly (MEA). This is the structure in the reactor where all of the half-reactions take place. It consists of the proton-exchange-membrane (PEM) sandwiched between the two electrodes. According to the literature, Nafion is the first choice of material for use as the proton exchange membrane for the SPE reactors. Nafion (a trademark of E.I. du Pont de Nemours Company) is a copolymer of tetrafluoroethylene and sulphonyl fluoride vinyl ether. Hence, Nafion contains functional $SO_3^{2-}$ groups that interact with the protons and allows for the proton conductivity. The characteristics that make Nafion such a good choice for the PEM are summarised below:

- high ionic conductivity
- outstanding chemical and thermal stability
- good mechanical strength.

Usually the Nafion membrane is used in the $H^+$-ionic form, although it can also be used in other ionic forms such as $K^+$ and $Na^+$.

As mentioned in chapter 1, the reactor system needs to operate without the need for any additional electrolytes. Typically, some form of ionising compound (in the form of acidity, salinity or alkalinity) is added to the water to improve the conductivity of the system. This has been done in almost all of the cases in the literature that have been studied [19, 10, 8, 27]. The addition of such compounds to the system, although they would eliminate the need for the PEM, would lead to the requirement for regular maintenance of practical electrochemical reactors. This can be undesirable in cases where the reactor system is used in water purification, for a number of reasons:

- poor accessibility to remote areas, which can prevent scheduled maintenance checks of the treatment reactors, resulting in the reactor not being operational for periods of time
- the potential hazard to the environment and residents in the area in the case of a reactor leak
- the cost involved in periodically resupplying a reactor with the appropriate chemicals.

The use of a PEM membrane eliminates the possible dangers and expenses involved with any of the above issues. The one disadvantage of the PEM membrane is however the relatively high cost, but this is balanced against the stability and long lifetimes of these membranes.

As mentioned, protons and water molecules travel through the PEM. In this way it basically serves as a solid electrolyte, hence the name SPE. In this case, protons are generated at the anode according to the reactions given in equation (2.1) and equation (2.3). These protons then migrate into the membrane and interact with the functional $SO_3^{2-}$ groups. The protons in the membrane at the cathode are consumed in the cathodic reaction which, in this case, is the hydrogen evolution reaction.

$$2H^+ + 2e^- \rightarrow H_2 \qquad (2.12)$$

Electrons pass through the external circuit as they are generated at the anode and are consumed at the cathode.

One of the problems with the Nafion membrane is that impurities present in the electrolyte can have a negative influence on the functioning of the membrane. Metal ions such as $Mg^{2+}$ and $Ca^{2+}$ ions may replace the $H^+$-ions in the polymer, thus changing the morphology and functionality of the membrane. These ions bond permanently with the Nafion membrane, thus reducing its capacity for protons and increasing the specific resistance of the membrane. While the electrochemical cell is operational, the membrane absorbs protons in favour of the other heavier ions. It is only when no potential is applied on the cell that any of the ions can interact with the membrane. It has also been observed that the Nafion membrane absorbs organic molecules. This may have a significant influence on the efficiency of the membrane.

Another limitation of the membrane is the maximum current density. It has been found that high current densities can dehydrate the membrane, thereby reducing the proton conductivity and increasing the resistance to charge transfer. Very high current densities can even cause the membrane to burn, causing permanent and irreversible damage. This only occurs at very high current densities, in the order of 1000 A/cm$^2$.

The reactions take place close to or at the membrane-electrode interface. Therefore, good contacting between the membrane and electrode is vital for uniform current distribution. This is normally accomplished by bolting the two current collectors together. They are then connected to the power source via an external circuit. The cathode is connected to the negative terminal and the anode to the positive terminal.

The flow channels are machined into the current collectors. The contaminated water flows in through the inlet in the current collector, travels through the reactor, and leaves by the outlet. In this way the liquid in the cathodic and anodic sides of the reactor can be separated if desired. The water in the flow channel diffuses through the electrode to the membrane-electrode interface where the reaction will take place.

## 2.4 Review of Previous Work

Several researchers have done a significant amount of work using metal oxide electrocatalysts for the oxidation of phenol. A fair variety of catalysts (and model contaminants) have been tested for their activity towards the oxidation reaction. This section will be subdivided into two parts. The first is a detailed description of work carried out by Grimm, since all of the work in the present study is based on his findings. The second section is a short overview of the most important research done by other authors in the field of electrocatalytic oxidation of organics. In most cases $SnO_2$, $PbO_2$ or $IrO_2$ were used, sometimes with the addition of dopants. Several researchers employed the solid-polymer-electrolyte system, as used in this study, but with the addition of supporting electrolytes for improved conductivity.

### 2.4.1 Grimm's research

A detailed account of the oxidation results reported by Grimm will be given first (all of the facts in this section were taken from his PhD thesis [13]).

As in the present study, one of the major hurdles was the determination of the phenol and intermediate concentrations. Grimm chose a simple and easy-to-use method for the determination of these compounds (it is described in section E.2.3). The method entails the reaction of phenols with 4-aminoantipyridine to form a coloured antipyrine dye that can be analysed spectrophotometrically at 510 nm. In effect, a phenol index is obtained that is a comparative measure of the content of the phenolic compounds. Mention is made of the inherent problems in this method of analysis, since several distillation steps are required to ensure that only phenolic and substituted phenolic compounds are detected. Also, no differentiation can be made between different phenolic compounds. Several other types of interference can also affect the obtained phenol index.

The electrochemical cell utilised was identical to the one used in the laboratory-scale work in this study, with the exception of the flow channels. Grimm's reactor was initially used for water hydrolysis and therefore the current collectors were machined to optimise the hydrogen and oxygen yields. The problem with the shape of these current collectors was that it was very difficult to characterise the flow without the use of computational methods.

Grimm conducted experiments at two different phenol concentrations. The first experiment used a very high phenol concentration (1 g/*l*) while the second used a very low concentration of phenol (1 mg/*l*). This corresponded with molar concentrations of 10.6 and 0.011 mM phenol. He used two different reaction volumes for the different experiments. In the high concentration experiment, only 100 m*l* was used and in the low concentration experiment, 500 m*l* was used.

The analysis of the results showed that for the high concentration experiment the concentration was reduced from 1 g/*l* to 0.22 g/*l* after 960 minutes of electrolysis. This reaction time corresponded with a specific charge of 320 Ah/dm$^3$ and a conversion of 78%. With the low concentration experiments the phenol concentration was reduced to 0.02 mg/*l* after 240 minutes of electrolysis. This corresponds with a specific charge of 8 Ah/dm$^3$. He also observed very low current efficiencies, ranging from 22.3% to 2%.

### 2.4.2 Other research

Some of the first work done in the field of electrochemical oxidation of cyclic organic molecules was by Kirk *et al.* [10], using a packed bed reactor. Lead particles were converted to $PbO_2$ to act as anodic material and a stainless steel plate served as cathode. Analine was

chosen as model contaminant. As a result, a 98% conversion of analine after the passage of 25 $Ah/dm^3$ was obtained. Sulphuric acid (pH 2) was used as supporting electrolyte. The cell was operated at a current density of about 9 $mA/cm^2$ and current efficiencies in the range of 42 to 18% were obtained.

They also tested the reactor system in the electrolysis of phenol [11] and obtained a 98.4% conversion of the phenol to intermediates after the passage of 25 $Ah/dm^3$. The supporting electrolyte was 1.0 M sulphuric acid.

Stucki *et al.* [4] studied the performance of high overpotential anodes in the treatment of waste waters. A wide variety of organic compounds were evaluated. These compounds were dissolved in a base electrolyte of 0.5 M $Na_2SO_4$ and adjusted to the desired pH by addition of either NaOH or $H_2SO_4$. It was found that after the passage of a specific charge of 74.7 $Ah/dm^3$ all of the TOC carbon was removed. The model contaminant in this specific case was benzoic acid. An electrochemical oxidation index (EOI), which is a measure of the reactivity of a particular compound with regards to oxidation by electrogenerated hydroxyl radicals, was calculated for each compound. Comninellis defined this EOI as [27]:

$$EOI = \frac{1}{\tau}\int_0^{\tau} \frac{\dot{v} - \dot{v}_{org}}{\dot{v}} d\tau \qquad (2.13)$$

The EOI is determined by the measurement of the evolved oxygen ($\dot{v}$) during an experiment in the presence and absence of the organic compound. They observed the highest EOI value for benzoic acid (EOI = 0.79). The next lowest value for the EOI was 0.8 for nitrobenzene, while the lowest EOI value was 0.02, which was obtained for triaminotriazin.

Murphy *et al.* [28] performed similar experiments using a PEM as electrolyte in an electrochemical cell. The anode (with a geometric surface area of 6.25 $cm^2$) consisted of a platinum-10% iridium mesh that was pressed onto the Nafion 117 PEM. This membrane mesh assembly was then sandwiched between two titanium current collectors coated with platinum. Experiments were conducted on a mixture of 12 organic compounds that was being circulated through the reactor at 3 *l*/h. These experiments showed that at a current density of 1.2 $A/cm^2$, 97.3% of the TOC present in the solution was completely removed after the passage of a specific charge of 3703 $Ah/dm^3$. The long times required for TOC removal may be due solely to the resistance that some organic molecules have to electrochemical oxidation, especially acetic acid — which had the highest TOC concentration. In these studies, using wet-air oxidation, acetic acid has been shown to be particularly resistant to oxidation [20].

Petrov *et al.* [6] prepared anodes by hot-pressing Teflon bonded (10 wt%) $SnO_2$ onto a fine titanium mesh. The membrane/electrode assembly was prepared using a technique employed in proton-exchange-membrane fuel cell (PEMFC) technology. This enhanced the energy efficiencies and power densities. The electrodes were then impregnated with Nafion solution (0.6 $mg/cm^2$) and hot pressed to the Nafion membrane at 130°C, which is slightly above the glass transition temperature of Nafion. The cathode material was platinum gauze. The electrodes were tested on the same cocktail of organics as used by Murphy *et al.* [28]. All of the total organic carbon was removed after the passage of 1050 to 2100 $Ah/dm^3$, depending on experimental conditions.

Comninellis and co-workers used a two-compartment cell for the oxidation of organics. In the initial work [5, 7], $SnO_2$ coated titanium was used as anode and a platinum spiral was used as cathode. Oxidation of phenol was carried out in the reactor at a current density of 50 to 57 $mA/cm^2$, a temperature of 70°C and pH 2. The initial concentration of the phenol was 21 mM. The removal of the phenol, as well as the TOC in the solution, was measured and compared.

The analysis showed that after 25 to 30 Ah/dm$^3$ (3.125 to 3.75 h), complete elimination of phenol had occurred. Longer oxidation times were necessary to reduce the TOC to 10% of the original value (50 Ah/dm$^3$ or 6.25 h).

The effect of NaCl on the rate of removal of organics was also tested [19]. Using Ti/$IrO_2$ electrodes they observed an improvement in the removal rate in the presence of $Cl^-$. Cell conditions were the following: current density 100 mA/cm$^2$, pH 12.2 and temperature 50°C. After 20 Ah/dm$^3$, using only $Na_2SO_4$ as electrolyte, a 40% conversion of the phenol was obtained. For solutions with both $Na_2SO_4$ and NaCl, 95% conversions were obtained. The removal rate seemed independent of the $Cl^-$ concentration (which was 433, 85 and 17 mM respectively).

Final experiments [21] involved the testing of the Ti/$IrO_2$ system for conventional aromatic removal. Phenol was used as model pollutant in a solution with a pH of 2. The temperature of the solution was 50°C and current densities of between 2.5 and 28 mA/cm$^2$ were maintained. Full conversion of the phenol to intermediate molecules was obtained after the passage of 35 Ah/dm$^3$.

Tahar and Savall [12] prepared $PbO_2$ electrodes on a tantalum surface for the oxidation of phenol. They prepared the lead dioxide by oxidation of a lead nitrate solution. They are some of the few researchers that mention the possibility of the formation of polymeric oligomers. They also used sulphuric acid (pH 2) to increase the conductivity of the solution. The oxidation experiments were performed at temperatures ranging from 60 to 90°C and they managed to convert all of the phenol to intermediates after the passage of between 31.6 and 15.2 Ah/dm$^3$ respectively. However, only 93.1% of the TOC carbon was removed after 100 Ah/dm$^3$ (initial TOC = 1500 ppm). It was found that maleic acid was difficult to oxidise to breakdown products.

Polcaro *et al.* [8] also used a parallel plate reactor with a $SnO_2$ coated sheet of titanium as anode. They used $Na_2HPO_4$ and $H_3PO_4$ as supporting electrolyte at different pH values (7 and 3). 2-chlorophenol was used as organic pollutant. In some of the experiments chlorides were added to investigate their effect on the combustion of the chlorophenols. It was found that 98.1% of the chlorophenol was removed after the passage of 2.13 Ah/dm$^3$.

### 2.4.3 Analysis of literature review

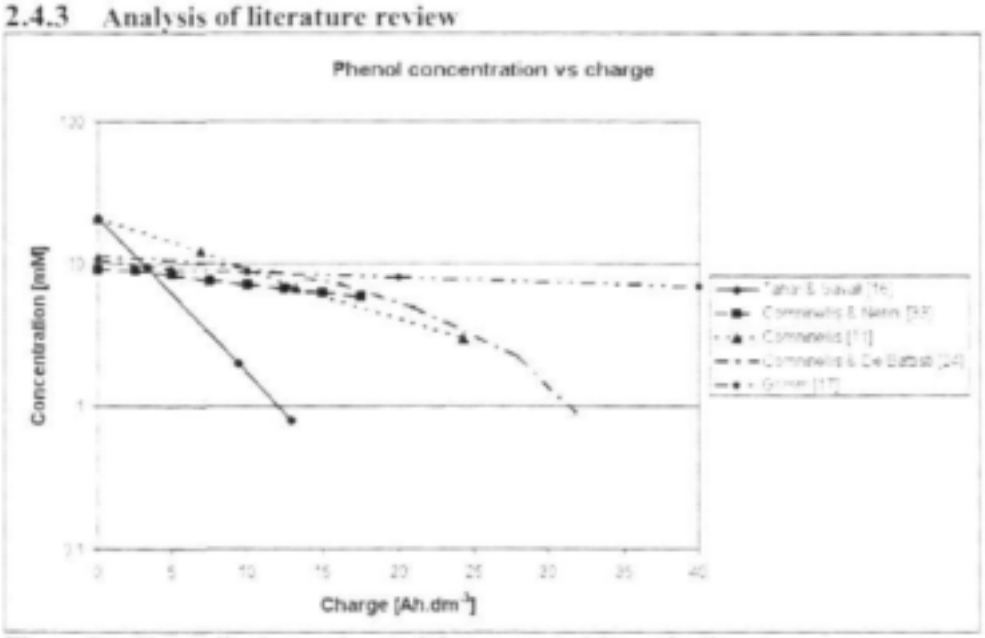


**Figure 2.4: Normalised experimental data reported from the literature.**

To shed some perspective on all of the data given in this section, the experimental data of some of the researchers mentioned has been converted into a normalised form and plotted. The researchers are indicated in the key of the graph. This data is presented in Figure 2.4.

The $x$-axis of the plot is given in terms of specific charge ($Ah/dm^3$), as the extent of an electrochemical reaction is normally proportional to the amount of charge passed according to equation 2.14.

$$n = \frac{Q}{\nu_e F} = \frac{It}{\nu_e F} \tag{2.14}$$

Also, since the number of moles of reactant present in the solution determines the required charge, the charge is divided by the volume of the solution. All of the curves given in Figure 2.4 are based on phenol concentration. Therefore, the number of moles of electrons that are required for the combustion of one mole of phenol is constant for all of the cases ($\nu_e = 28$).

An efficient oxidation reaction will be one represented by a sharp gradient. On the other hand, lines with low gradients will represent an inefficient reaction. This can be explained by the specific charge. An efficient reaction will ensure that a larger fraction of the applied current is applied towards the oxidation reaction. This will in effect reduce the nominator of equation 2.14 since a smaller total current needs to be applied.

Another way of looking at an efficient process is by examining the number of moles of reactant that can be converted for the applied charge. If a larger fraction of the applied current is spent on converting phenol, more moles of phenol can be converted, corresponding to either a higher concentration of solution or a larger volume of solution with the same initial concentration. This in effect increases the denominator of the specific charge, leading to smaller values of the specific charge for higher conversions.

# 3 Phenol Oxidation

## 3.1 Introduction

Initially, the present project was supposed to immediately scale-up the reactor based on the results of Grimm [13] and bench-scale experiments were to be performed in order for a pilot plant to be built. This scale-up reactor was bigger than the laboratory-scale size that Grimm used (reaction volume 50 *l* vs 1 *l*). The reactor did not work due to very low conversions obtained. Major shortcomings in the reactor system were the small surface-area-to-volume ratio as well as the high initial concentration used. These critical parameters were subsequently adjusted and additional laboratory-scale experiments were performed. The details of the initial work are described in appendix E.

A number of researchers have used Nafion as proton-exchange membrane in conjunction with various catalysts in different forms. Gatrell and Kirk used lead and lead dioxide pellets in the oxidation of phenol. They did however use sulphuric acid as supporting electrolyte. Murphy et al. [28] also employed a PEM in their reactor but used no supporting electrolyte in their feed solutions.

## 3.2 Experimental

### 3.2.1 Instruments and specifications

The experimental set-up used the same reaction volume as that used by Grimm [13]. The reservoir consisted of a 1*l* glass bottle that could be sealed to prevent the relatively volatile organics from escaping into the atmosphere. Flow control was maintained by a ball valve, since only three flow rates were chosen for the experimental work. The experimental set-up is shown in Figure 3.1.

Preliminary work on the laboratory-scale reactor was done using a peristaltic pump (with a maximum flow rate of 21.8 *l*/h). Later a small, magnetically driven centrifugal pump with a maximum flow rate of 37.2 *l*/h was used (Schmitt-Kreisel, 7505). This did not correspond with the maximum flow rate capacity of the pump due to the high pressure drop through the reactor. Since the pH measurements in the initial experiments remained constant over the duration of the experiments, the pH measurements were abandoned and only the phenol concentration was measured. In later experiments, pH, conductivity and temperature were measured.

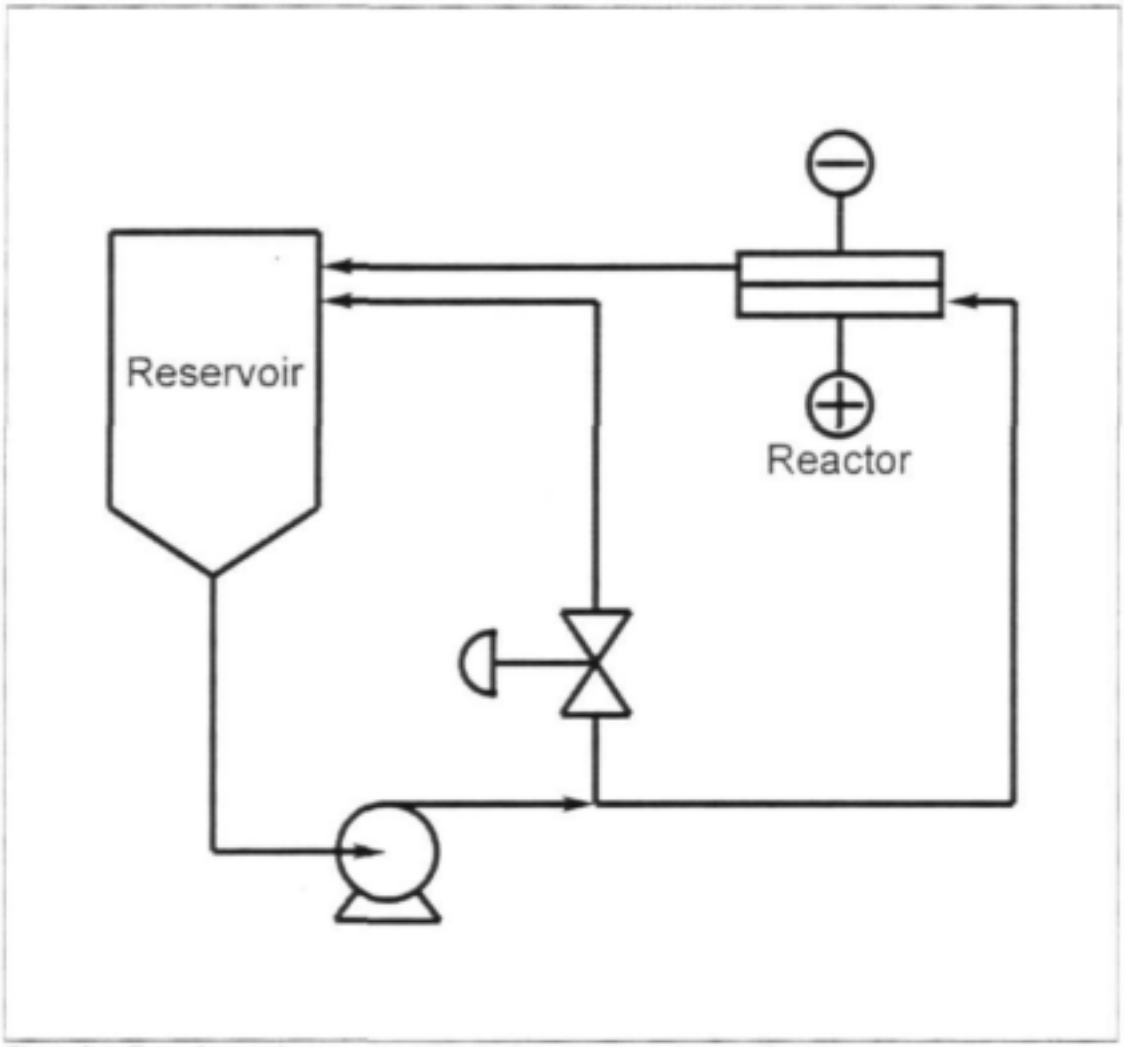


**Figure3.1: Experimental set-up used for the laboratory-scale experiments.**

The pH and temperature were measured on-line using a +GF+ Signet 2714 pH electrode obtained from Indecx, South Africa. The pH probe was connected to a pre-amplifier (+GF+ Signet 2720) and the readings were displayed with a +GF+ Signet 8750-1 transmitter. The conductivity was measured using a Genway 4071 conductivity meter.

### 3.2.2 Experimental reactor

The materials of construction chosen for the current collectors in the laboratory-scale reactor were also chosen for their relative corrosion resistance. Since the initial experiments showed that the pH of the solution leaving the reactor remained virtually constant (pH ≈ 4.5), it was decided that nickel, which has good corrosion resistance to mild acidic solutions, could be used as current collector material. Nickel, although possessing a relatively good electronic conductivity, has a resistance three times greater than titanium and about six times greater than aluminium.

Aluminium, upon exposure, forms an oxide layer that acts as electric insulator and could therefore not be used in pure form as current collector material. One advantage of using aluminium was its relatively easy machinability. Therefore aluminium discs were obtained (Non-ferrous Metals, Cape Town, South Africa), upon which a single flow channel of length 548 mm was machined (see schematic in Appendix G). The inlet and the outlet of each current collector were situated in the back of each current collector. Stainless steel 316 flow nozzles ($^1/_8$", West Beach Instrumentation, Cape Town, South Africa) were used to provide

connections to the external fluid circuit. The aluminium current collectors were then electroplated with nickel to provide adequate electric conductivity and corrosion resistance. The electroplating was done by Metana Surface Coatings cc, Cape Town, South Africa.

Four nickel-plated aluminium pins attached to the back of the current collectors supplied electrical contact. On the edges of each current collector, facing the opposite current collector a lip was machined. On the edges of each current collector facing the opposite current collector, a lip was machined. A Viton gasket was placed onto this edge to provide a seal for the reactor. The current collectors were once again housed in a PVC frame, which was fastened with eight M8 mild steel bolts. The nuts for these bolts were fastened using a torque meter to ensure that the stack pressure was constant for each experiment. Detailed drawings of the laboratory-scale reactor are given in Appendix G. Photographs of the various parts of the reactor are given in Figure 3.2 (a) to (d).

Although the cost of this experimental set-up was significantly less than the equivalent titanium reactor (approximately 10 times), it was found that some corrosion still took place. Most of the corrosion was believed to take place due to the anodic oxidation of the nickel to nickel oxide, since very high potentials (between 20 and 30 V) were required to obtain the working current densities. Another reason for the use of nickel was to ensure that sufficient funds remained for the construction of a pilot plant if the need arose.

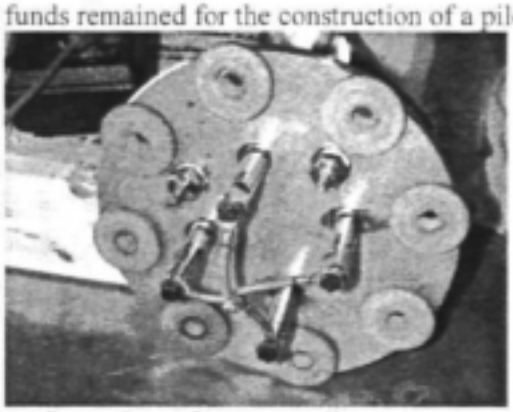

(a) Rear view of current-collector

(b) Top view of current collector

(c) Assembly of electrochemical cell

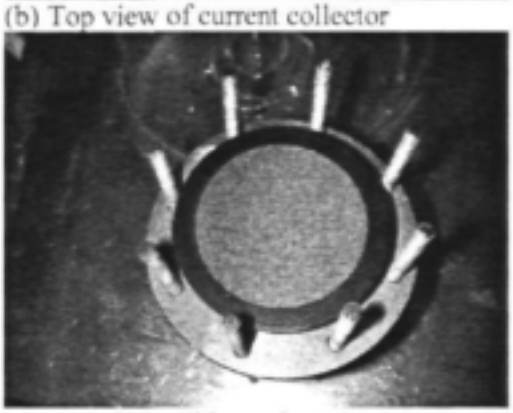

(d) Assembly with anode

**Figure3.2: Photographs of the laboratory-scale electrochemical cell.**

Once it was found that the process was not economically viable (see chapter 5), a titanium reactor was constructed to see if this would have any significant effect on the observed reaction rates.

### 3.2.3 Analysis of phenol and breakdown products

Since the use of total organic carbon (TOC) analysis of the samples required a large sample volume (20m *l*) relative to the reactor volume (1 *l*), the use of high-pressure liquid

chromatography (HPLC) for the determination of the breakdown products was investigated. It was later determined that the method used by the CSIR (Stellenbosch) for TOC determination was inadequate for the determination of the TOC for the phenolic samples. The method used was ideal for TOC determination of natural water sources, but due to the refractory characteristics of phenol and phenolic compounds, inaccurate results were obtained. Using HPLC, it was found that two different columns were required for the quantitative analysis of the suspected breakdown products.

The column used for the determination of the phenolic compounds was a conventional C18 column (Phenomenex, LUNA 5$\mu$ C18(2) 150×4.6 mm). The column used for the determination of the aliphatic acids was a PL Hi-Plex H Ligand Exchange Column (300×7.7 mm). The separation and analysis were performed using a Thermo Separation SpectraSystem HPLC with an UV-detector.

10 $\mu l$ of the samples containing phenolic compounds were injected, using 50% methanol/50% water as mobile phase. The detector was set at a wavelength of 280 nm for these compounds. A chromatogram of the phenolic standards is shown in Figure 3.3 and the retention times for the various compounds are given in Table 3.2.

An important fact to note is the toxicity of phenol compared to the toxicities of the breakdown products. The following table summarises the lethal dose for oral ingestion of phenol and the two main breakdown products, *p*-benzoquinone and hydroquinone. The tests were performed on rats.

**Table 3.1: Toxicity of phenol and the main breakdown products [29]**

| Compound | LD50 [mg/kg] |
|---|---|
| Phenol | 414 |
| *p*-Benzoquinone | 130 |
| Hydroquinone | 320 |

These values imply that the breakdown products formed by the oxidation reaction have greater toxicity than phenol (lower lethal dose). Therefore, if the oxidation reaction produced these products, albeit in lower concentrations, the product stream would have a similar level of toxicity.

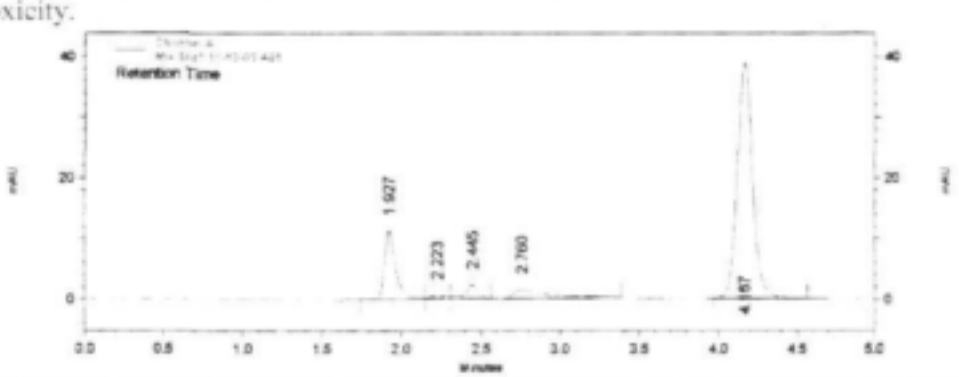


**Figure 3.3: HPLC chromatogram of the standards for phenolic compounds (mobile phase: 50% MeOH/50% $H_2O$, Detector: 280 nm).**

**Table 3.2: HPLC retention times for the phenolic compounds (see Figure 3.3)**

| Compound | Retention Time [min] |
|---|---|
| Hydroquinone | 1.927 |
| Resorcinol | 2.223 |
| Benzoquinone | 2.445 |
| Catechol | 2.760 |
| Phenol | 4.167 |

For the analysis of the organic acids, a 0.01 N $H_2SO_4$ mobile phase was used. Detection of the acid peaks was done at 210 nm. The chromatograms produced in the analysis of the organic acid standards showed tailing on all of the peaks, but these peaks were still usable. A chromatogram of the organic acid standards is given below in Figure 3.4. The acids tested were maleic, fumaric and oxalic acid. Formic acid was also tested, but did not show a well-defined peak. The residence times of the individual acids are given in Table 3.3.

The samples taken during the experiments were analysed with both columns. Examples of the chromatograms of initial and final samples are given in Figure 3.5 to Figure 3.7.

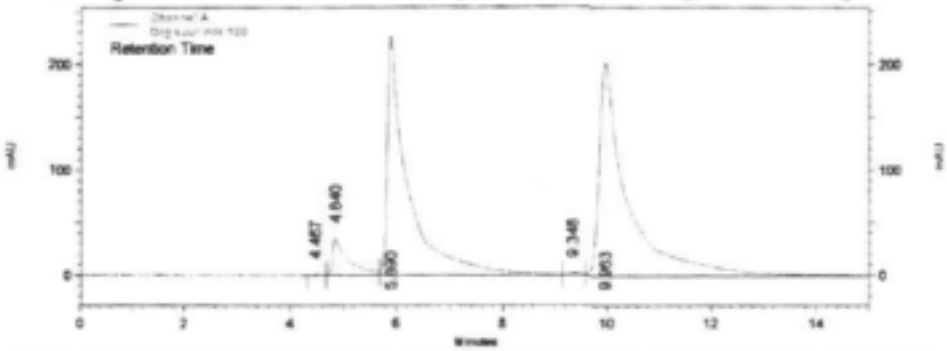


**Figure 3.4: HPLC Chromatogram of acid standards (mobile phase: 0.01 N $H_2SO_4$, Detector: 210 nm).**

**Table 3.3: Retention times for the aliphatic acids**

| Compound | Retention Time [min] |
|---|---|
| Formic acid | 4.467 and 9.348 |
| Oxalic acid | 4.840 |
| Maleic acid | 5.890 |
| Fumaric acid | 9.963 |

Two strange peaks were noted in the chromatograms obtained with the column used for the aliphatic acids, Figure 3.7. The initial sample was taken before the solution was pumped through the reactor and therefore should only have contained phenol as contaminant. Thus, the peak observed could be due to the presence of phenol in the sample. However, as the experiment progressed, an additional peak was observed before the 'phenol' peak.

One possible explanation for the strange peaks is the formation of aliphatic organic intermediates with other functional groups, such as alcohols and ketones. This is possible since the reaction involves the formation of the highly reactive hydroxyl intermediate, which can react with organic molecules in any number of ways. Note however, that none of the aliphatic intermediates that are popularly believed to be formed (oxalic, maleic and fumaric acid) were present in the samples.

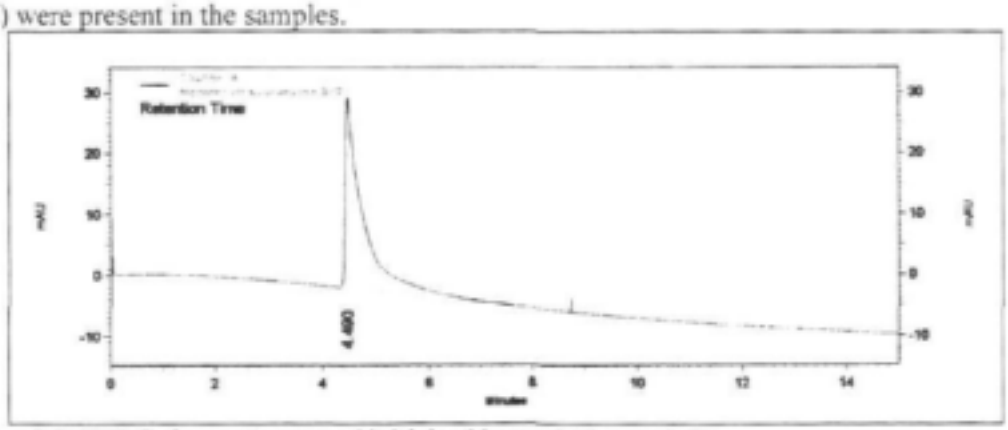


**Figure 3.5: HPLC chromatogram of initial acid sample (example 1).**

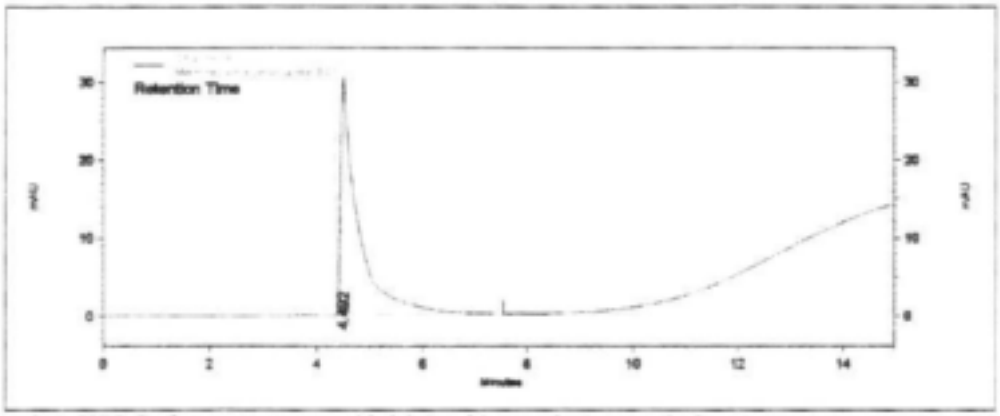


**Figure 3.6: HPLC chromatogram of initial acid sample (example 2).**

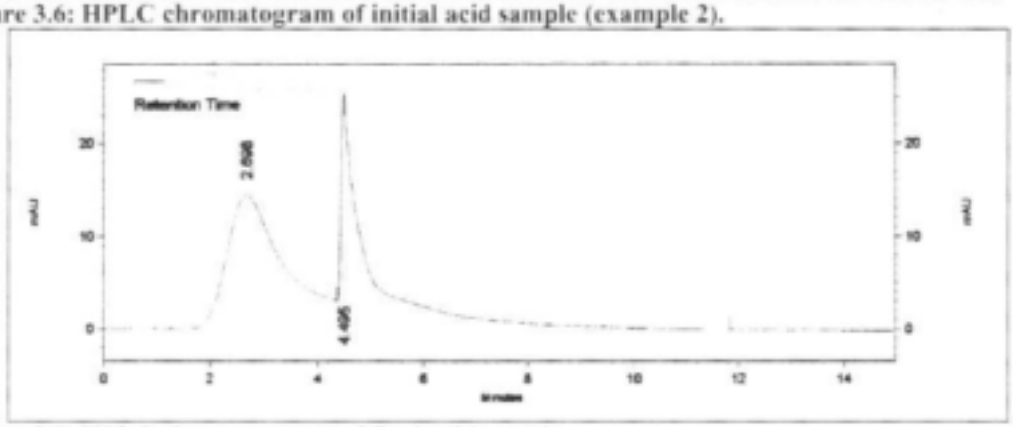


**Figure 3.7: HPLC chromatogram of final acid sample.**

Therefore, the samples could be accurately analysed by HPLC for the phenolic compounds, but total organic carbon analysis must still be used to account for the contribution of the aliphatic intermediates.

## 3.3 Results and Discussion

### 3.3.1 Determination of apparent reaction rate constants

The following sections discuss the results of the experiments. The discussion is mostly based on the apparent reaction rate constant which is obtained from a linear regression fitted to the experimental data. This section discusses the procedure followed to extract the apparent reaction rate constant.

In all of the experiments, the concentration-time data is measured. Thus, we have an expression of the form:

$$C_{Ph,t} = C_{Ph,0} e^{\beta t} \tag{3.1}$$

Thus, $\beta$ is the one coefficient of regression. An exponential curve was chosen because first-order kinetics was assumed in the model derivation. The final form of the reactor model, expressing the final concentration in terms of the initial concentration, is:

$$C_{Ph,t} = C_{Ph,0} \exp\left(\frac{t}{\tau}\left\{\exp\left(-\frac{kWL}{v_R}\right)-1\right\}\right) \tag{3.2}$$

The detailed derivation of equation 3.2 is provided in section C.1 in the appendices. The relationship between the regression coefficient, $\beta$, and the apparent reaction rate constant, $k$, can be obtained from equations 3.1 and 3.2 after some mathematical manipulation:

$$k = -\frac{v_R}{WL}\ln(\beta\tau + 1) \tag{3.3}$$

where $v_R$ is the flow rate through the reactor
W is the width of the flow channel
L Is the length of the reactor
$\tau$ Is the residence time of the solution in the reservoir.

This expression was used to determine $k$ in all of the experimental work.

### 3.3.2 Results — galvanostatic operation

#### Effect of current density

The choice of current densities to be tested depended on the power supply used. Due to the high overpotential at the electrode, only relatively low current densities could be maintained without pushing the operating potential above the maximum for the power supply. Therefore, currents of between 20 and 50 mA were selected. The exact parameters, including the calculated current densities of the current experiments are given in Table 3.4. The conversion in the table is based on the complete combustion of phenol.

Table 3.4: Experimental parameters for current density experiments

| Applied current | | Flow Rate | $C_{Ph,0}$ | Volume | Conversion |
|---|---|---|---|---|---|
| I [mA] | i [A/cm$^2$] | [l/h] | [ppm Ph] | [l] | (phenol) |
| 20 | 0.352 | 9.36 | 50 | 1.0 | 0.0623 |
| 35 | 0.617 | 9.36 | 50 | 1.0 | 0.100 |
| 50 | 0.881 | 9.36 | 50 | 1.0 | 0.0577 |

The breakdown curves for the three currents are presented in Figure 3.8. From the graph it can be seen that the intermediate current value results in the highest reaction rate compared to both the low and high current densities. The values for the are shown in Table 3.5. In all cases the experimental values were lower than the theoretical values. These theoretical values were obtained from the mass transfer correlation given by equation A.46 (see appendix A).

This correlation was set up for solid duct walls, while in the experiments the electrode was porous. The correlation was therefore only an estimation of the external mass transfer to the surface of the electrode. It nonetheless provided a measure against which the experimental values could be compared.

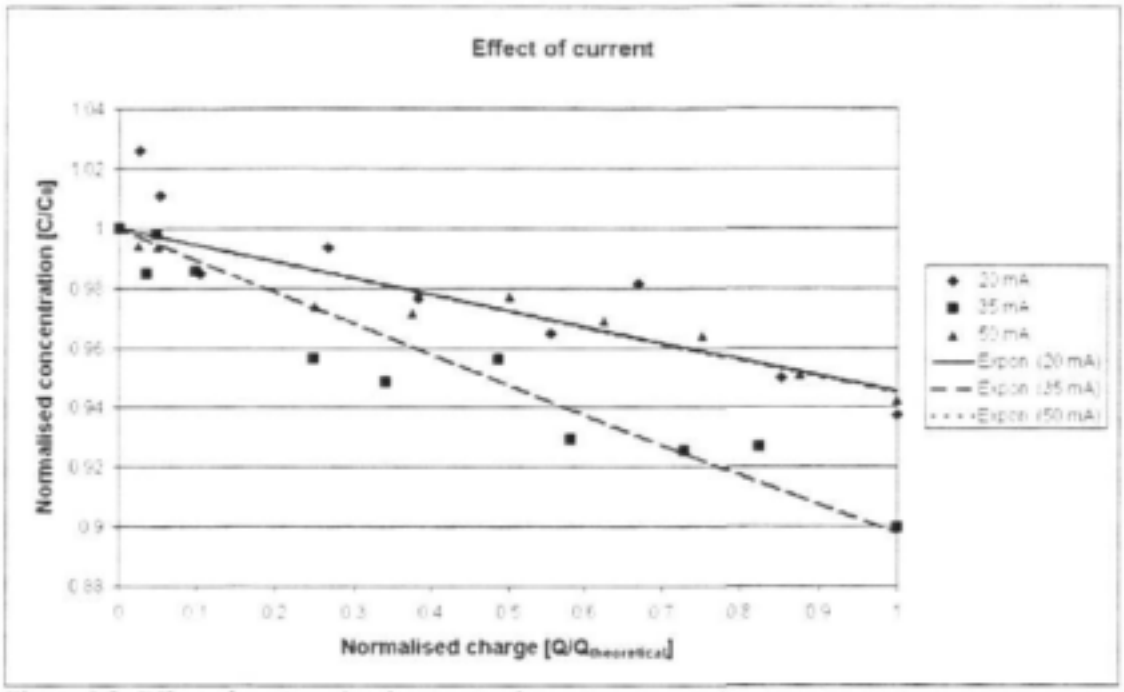


**Figure 3.8: Effect of current density on reaction rate.**

One of the side effects of the phenol oxidation reaction is oxygen evolution, whether by water electrolysis or by the reaction, as shown in equation 2.7. This means that if the process is externally mass-transfer limited, higher experimental rate constants than the theoretical values shown in Table 3.5 would be observed (as explained in section A.1.4). Therefore, based on these results, one would assume that the process could not be externally mass-transfer limited. More information is required to make a better judgement of the exact limiting conditions prevalent in the reactor. Therefore, the results of both the current and flow rate experiments will be discussed in the next section.

**Table 3.5: Reaction rate constants for current experiments**

| Current [mA] | $-\beta$ [$s^{-1}$] | $k_{m,experimental}$ [m/s] | $k_{m,theoretical}$ [m/s] | $R^2$ % | 95% conf. interval |
|---|---|---|---|---|---|
| 20 | $8.62 \times 10^{-7}$ | $3.93 \times 10^{-7}$ | $5.92 \times 10^{-6}$ | 77.2 | $4.57 \times 10^{-7}$ |
| 35 | $2.54 \times 10^{-6}$ | $1.16 \times 10^{-6}$ | $5.92 \times 10^{-6}$ | 91.0 | $5.43 \times 10^{-7}$ |
| 50 | $2.03 \times 10^{-6}$ | $9.26 \times 10^{-7}$ | $5.92 \times 10^{-6}$ | 90.3 | $4.80 \times 10^{-7}$ |

Also note that, because of gas formation increasing the mass transfer, the Reynolds number as calculated is only a quantification of the flow and not necessarily a good characterisation of the flow.

The intermediate current value of 35 mA corresponded with the highest reaction rate constant. The reaction rate should be proportional to the applied current and therefore it is expected that the highest reaction rate constant would be associated with the highest current (50 mA).

This effect could partly be explained by the covering effect, caused by the formation of gas bubbles on the surface and in the pores of the catalyst. This phenomenon effectively reduces the fraction of the electrode surface available for reaction. Low current densities may force the selectivity of the reaction to be closer to the oxidation reaction due to lower applied potentials, but also causes the reaction to take place more slowly due to a lower current density.

The high current density on the other hand speeds up the oxidation reaction, but also causes a larger fraction of the electrode surface to be covered, resulting in a lower overall oxidation

rate. Some intermediate value of the current therefore maximises the oxidation rate whilst minimising the formation of gas bubbles, resulting in a high overall reaction rate.

**Effect of flow rate**

Experiments to determine the effect of mass transfer were conducted at two different flow rates, both being in the laminar region of flow due to the limitations of the pumps available. The pressure drop in the reactor was very high because of the small equivalent diameter ($d_e$ = 4 mm), thus limiting the maximum flow rate. The values for the experimental parameters are given in Table 3.6. The normalised concentration-charge data are presented in Figure 3.9.

**Table 3.6: Experimental parameters for flow rate experiments**

| Flow rate | | Flow Rate | $C_{Pb,0}$ | Volume | Conversion |
|---|---|---|---|---|---|
| [l/h] | Re | I [mA] | [ppm Pb] | [l] | (phenol) |
| 9.36 | 650 | 50 | 50 | 1.0 | 0.101 |
| 21.8 | 1516 | 50 | 50 | 1.0 | 0.140 |

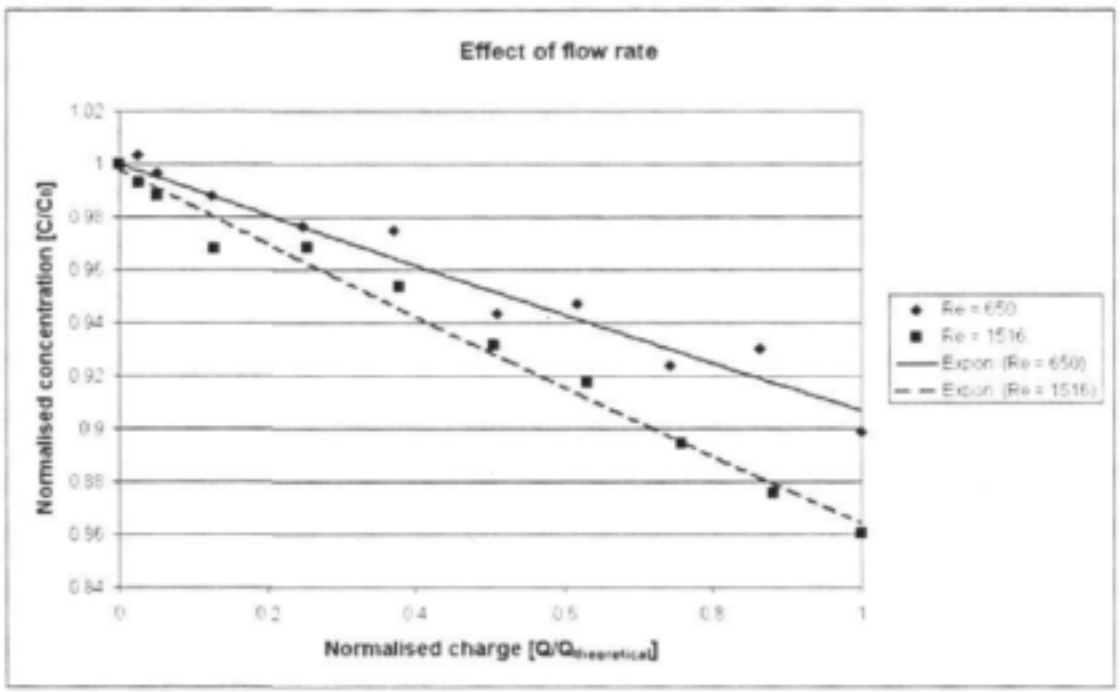


**Figure 3.9: Effect of flow rate on reaction rate.**

The reaction rate constants were calculated for both of the flow rates and are given in the table below.

Table 3.7: Reaction rate constants for flow rate experiments

| Re | $-\beta$ [$s^{-1}$] | $k_{m,experimental}$ [m/s] | $k_{m,theoretical}$ [m/s] | $R^2$ % | 95% conf. interval |
|---|---|---|---|---|---|
| 650 | $3.50 \times 10^{-6}$ | $1.59 \times 10^{-6}$ | $5.92 \times 10^{-6}$ | 96.1 | $5.66 \times 10^{-7}$ |
| 1516 | $5.50 \times 10^{-6}$ | $2.51 \times 10^{-6}$ | $7.85 \times 10^{-6}$ | 98.6 | $4.96 \times 10^{-7}$ |

In both cases the experimental rate constants were lower than the theoretical rate constants. However, it must be noted that the ratio between the values for the high and low flow rate were almost the same (1.32 for the theoretical and 1.49 for the experimental values). The same applies in these experiments as for the current experiments. The gas evolution would cause the mass transfer to be higher than theoretically predicted if external mass-transfer conditions limited the reaction.

It is realistic to assume that an increase in flow rate will cause a decrease in covering effect due to an increase in the bubble removal rate. From the experimental results presented in this section and the previous section, due to the dependency of the reaction rate on both the current density and the flow rate, it seems that the reaction is in some intermediate limiting regime. This is entirely possible for electrochemical reactions and can be accounted for in the Butler-Volmer equation according to Wendt and Kreysa [30].

This of course complicates the extraction of the experimental parameters significantly, especially since very little information is available on the exact current density-potential relationships. In this case, the best approach would probably be to assume that the kinetics are similar to those encountered in chemical kinetics, assume a reaction order and obtain at least a reasonable estimation of the reaction order and reaction rate constants, as discussed in section A.1.5.

**Effect of the MEA compression factor**

Due to the design of the reactor, the quality of the electrode-membrane contact plays an important role in the current distribution. If the reactor is not fastened tightly enough, high local current densities can exist, thereby changing the overpotential and thus the reaction. Therefore two different stack pressures were tested to observe the effect of this parameter. The values for the experimental parameters are given in Table 3.8 and the breakdown curves for the two experiments are given in Figure 3.10.

**Table 3.8: Experimental parameters for MEA compression experiments**

| Torque [lb-in] | Flow rate Re | Applied current I [mA] | $C_{Ph,0}$ [ppm Ph] | Volume [l] | Conversion (phenol) |
|---|---|---|---|---|---|
| 15 | 650 | 50 | 50 | 1.0 | 0.0577 |
| 25 | 650 | 50 | 50 | 1.0 | 0.0533 |

The reaction rate constants for the two different stack pressures are given below. They are given in terms of torque applied to the nuts used to fasten the frame of the reactor. The constants obtained for the two experiments were similar, differing by 15%, but with the lower rate constant associated with the higher stack pressure. This was unexpected, but the $R^2$ value of the second exponential fit was only 86% and may cause the constant to be slightly inaccurate. It was observed in the experimental work that lower potentials were obtained, for higher compression factors. This would imply a better distribution of current across the electrode. Since no real conclusive information could be extracted from this experiment, it was decided to at least keep the stack pressure constant for all the other experiments in order to eliminate any additional effects.

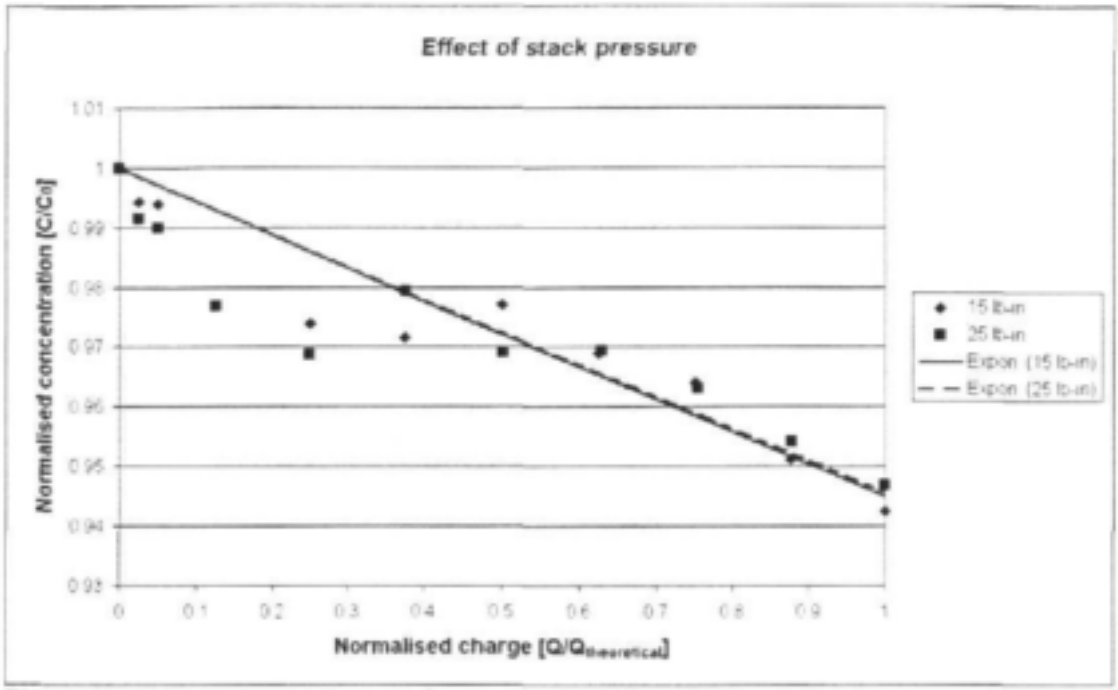


**Figure 3.10: Effect of MEA compression on reaction rate.**

**Table 3.9: Reaction rate constants for stack pressure experiments**

| Torque [lb-in] | $-\beta$ [$s^{-1}$] | $k_{m,experimental}$ [m/s] | $R^2$ % | 95% conf. interval |
|---|---|---|---|---|
| 15 | $2.03 \times 10^{-6}$ | $9.26 \times 10^{-7}$ | 90.3 | $4.80 \times 10^{-7}$ |
| 25 | $2.06 \times 10^{-6}$ | $9.40 \times 10^{-7}$ | 72.4 | $6.85 \times 10^{-7}$ |

### Anolyte-catholyte separation

One of the intermediate steps in the oxidation of phenol is the reversible reaction between *o*- and *p*-benzoquinone and their respective dihydroxybenzene structures. Therefore, the following can be expected: if the reverse reaction is somehow suppressed, an increase in the reaction rate should be observed. For the reverse reaction to take place, benzoquinone must be reduced — a reaction that takes place at the cathode. Thus, the easiest way of preventing the reverse reaction from taking place, is by the separation of the catholyte and the anolyte.

In these experiments, peristaltic pumps were still used to pump the phenol solution through the reactor. An identical peristaltic pump was obtained and used to pump distilled water through the cathodic side of the reactor. As a result, the phenol solution was only pumped through the anodic side of the reactor. The results obtained for this are presented in Figure 3.11 in normalised form and the calculated rate constants are given in Table 3.10.

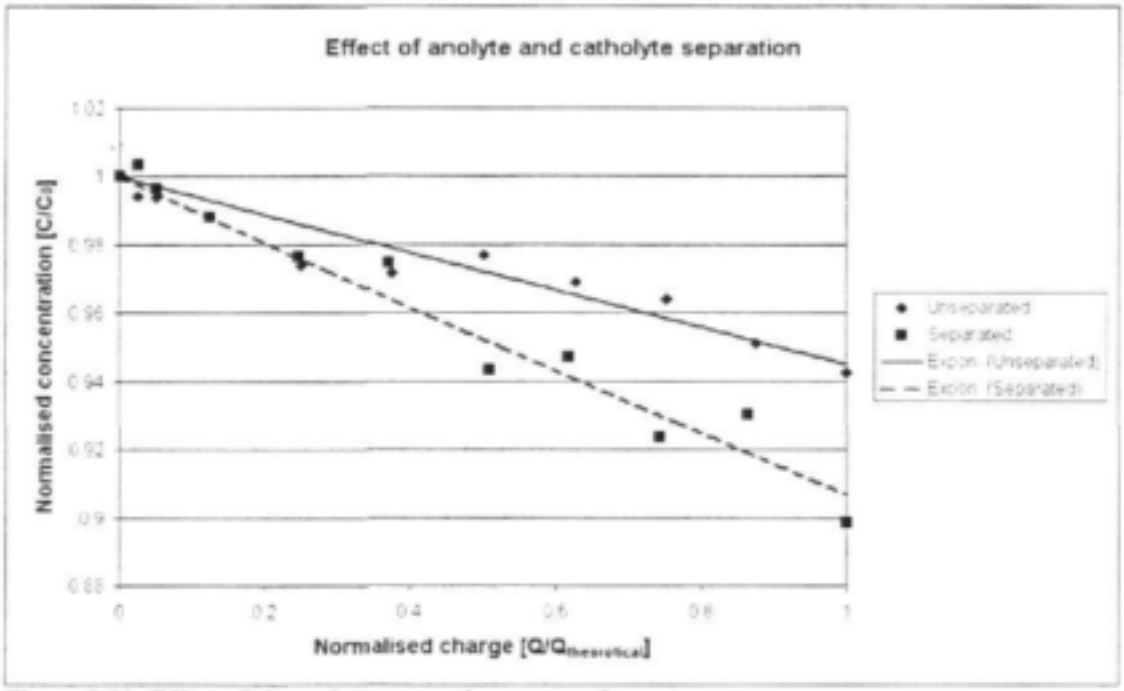


**Figure 3.11: Effect of electrolyte separation on reaction rate.**

**Table 3.10: Reaction rate constants for separated electrolytes**

| | $-\beta$ [$s^{-1}$] | $k_{m,experimental}$ [m s] | $R^2$ % | 95% conf. interval |
|---|---|---|---|---|
| Unseparated | $2.03 \times 10^{-6}$ | $9.26 \times 10^{-7}$ | 90.3 | $4.80 \times 10^{-7}$ |
| Separated | $3.50 \times 10^{-6}$ | $1.60 \times 10^{-6}$ | 96.1 | $5.66 \times 10^{-7}$ |

It can be seen that the rate constant for the case where the electrolytes were separated is two times greater than that for the unseparated case. This will have a marked influence in the final design of the reactor. The cost of having an additional system responsible for pumping the catholyte must therefore be weighed up against the improvement in reaction rate. The remainder of the experiments, especially those done in the reactor using titanium current collectors, were done unseparated (no additional pumps were available). The effect of separating the catholyte and anolyte is compared economically in chapter 5.

### 3.3.3 Results – potentiostatic

Due to the low conversions obtained in the galvanostatic experiments, it was decided to perform experiments in which the potential was kept at a constant value, below that required for the side reaction but above the potential required for the oxidation of the phenol. The theoretical potential that corresponds with this value is about 1.4 V, whereas the ohmic losses due to the membrane and current collectors must still be accounted for. The phenol oxidation potential and the water hydrolysis reaction differ by 0.3 V (water hydrolysis being 1.7 V) and therefore a fixed potential value of 2.0 V was chosen. The potential for the hydrogen evolution reaction is between -0.2 to -0.4 V. Thus, the chosen potential, including the potential drop across the membrane, will be sufficient for the phenol oxidation but still less than the oxygen evolution potential.

The graph in Figure 3.12 shows the concentration versus time profiles of phenol, and some of the identified breakdown products. The phenol concentration is read off the left-hand axis and the concentrations of the breakdown products are read off the right-hand axis. Figure 3.13 shows the same concentration profiles, but uses normalised charge as the x-axis. This was done to show the theoretical extent of the reaction at the different sampling points. Note that

after 55 hours of reaction, almost 80% of the theoretical charge had been supplied to the system, with only 23% conversion of the phenol.

The breakdown products that were analysed were *p*-benzoquinone and hydroquinone. These breakdown products formed quickly (before the first sample point) and then seemed to reach an equilibrium concentration. The concentrations were still very low and, in some instances, the analytical method used was not sensitive enough to discern between the corresponding peak and the baseline, especially in the case of *p*-benzoquinone. Typical concentrations obtained were below 1.8 ppm. Since none of the acid intermediates were detected (section 3.2.3), it was assumed that they were either broken down preferentially or not even formed.

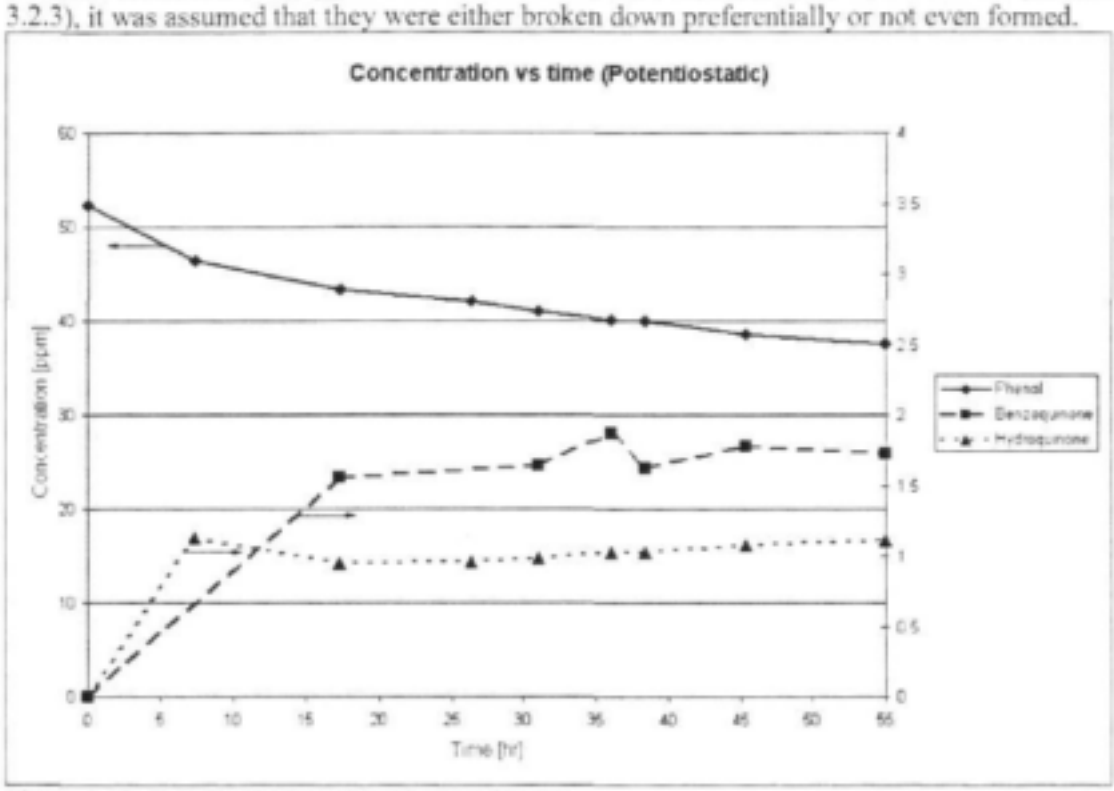


**Figure 3.12: Results of potentiostatic experiments.**

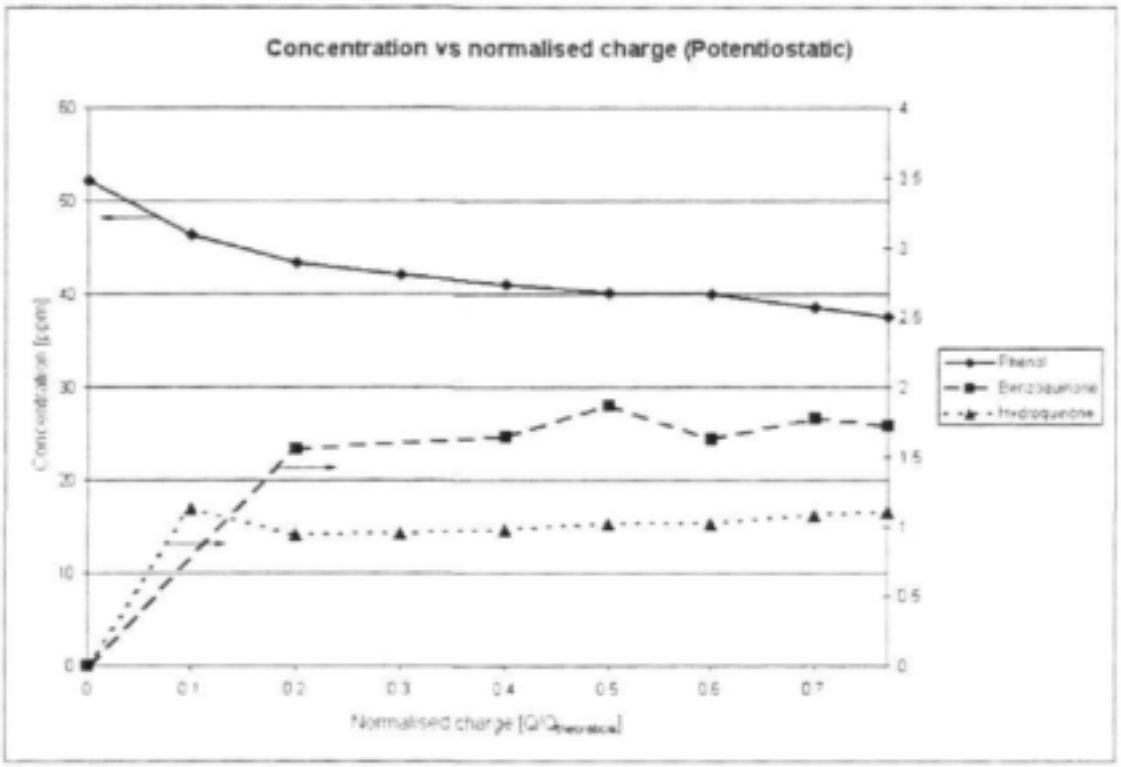


**Figure 3.13: Normalised potentiostatic experimental results.**

The obtained conversions were compared to the theoretical conversions as calculated with Faraday's law. The total organic carbon was calculated based on the concentrations of the compounds in the samples and compared to the theoretical conversion (Figure 3.14). Notice that after approximately 30% of the required charge was supplied to the system, the conversion slowed down significantly.

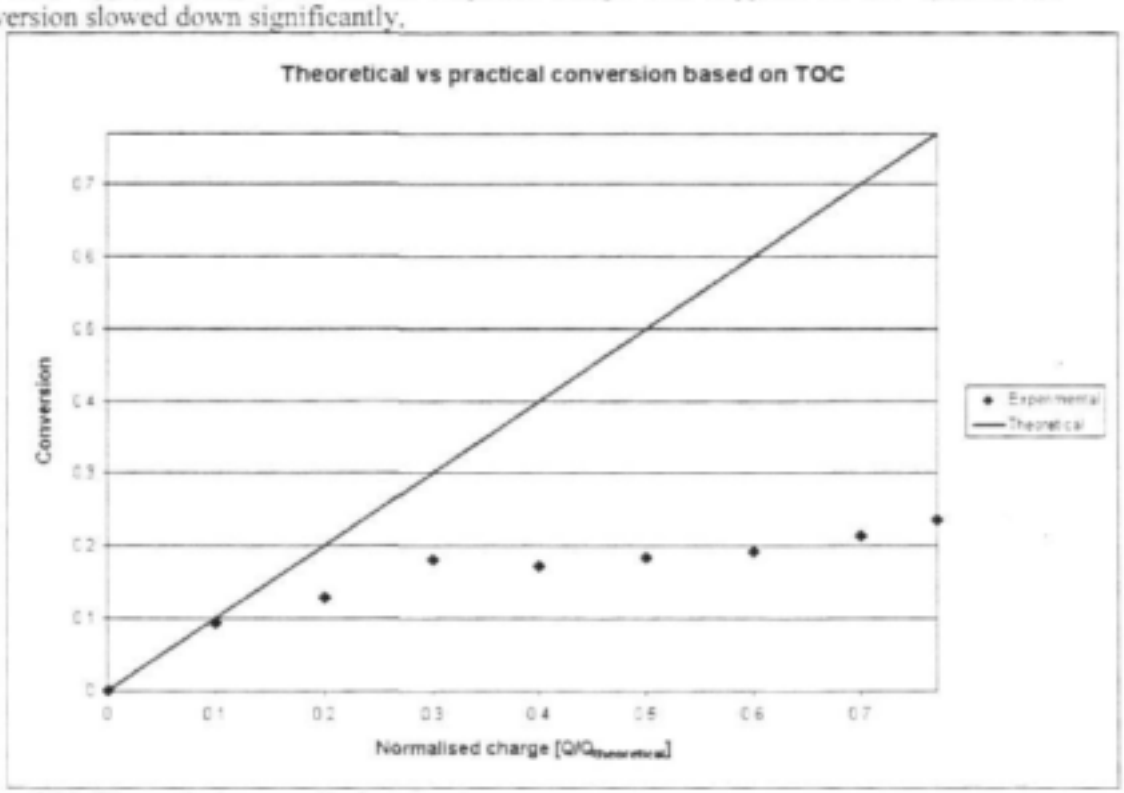


**Figure 3.14: Theoretical vs practical conversion.**

Due to a suspicion that a polymeric film of polyphenol might be forming, an experiment was carried out in which both the anode and the cathode were a titanium electrode coated with the $SnO_2/ZrO_2$ catalyst. The experiment was run for a set period of time (8 hours) after which the polarity was changed. This was done in an attempt to remove the polymeric film, a process that could take place in a couple of ways:

- by reversing the polymeric reaction, or
- by regenerating the catalyst surface by breaking up the film due to hydrogen evolution.

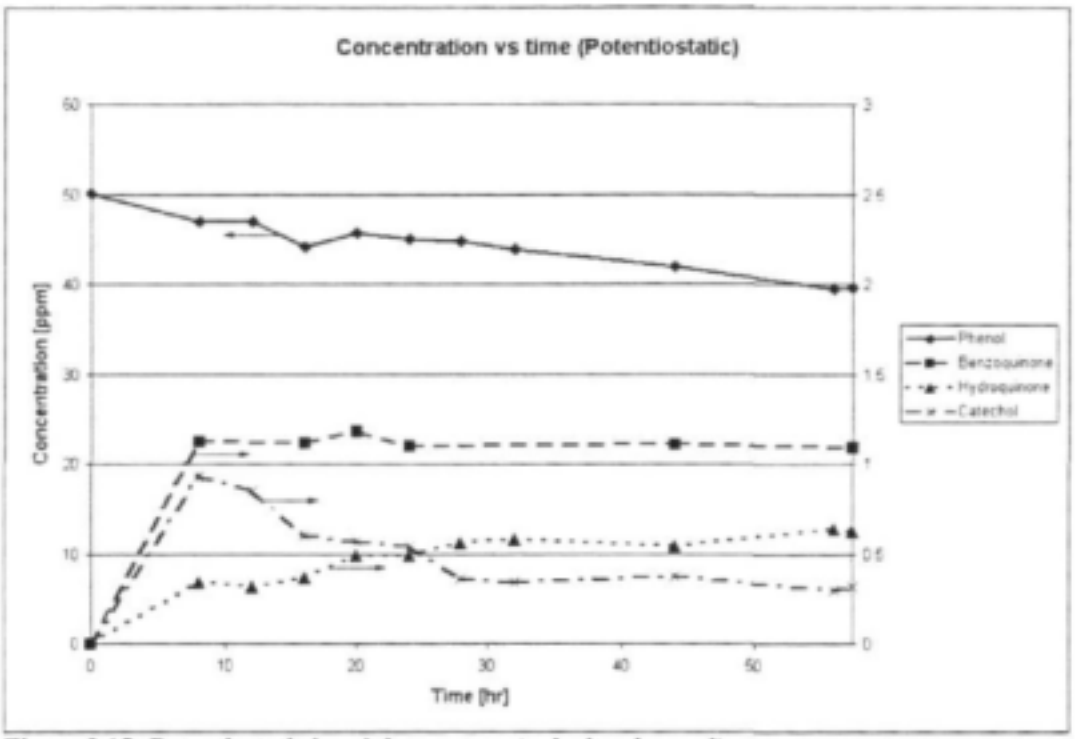


Figure 3.15: Potentiostatic breakdown curve (polarity changed).

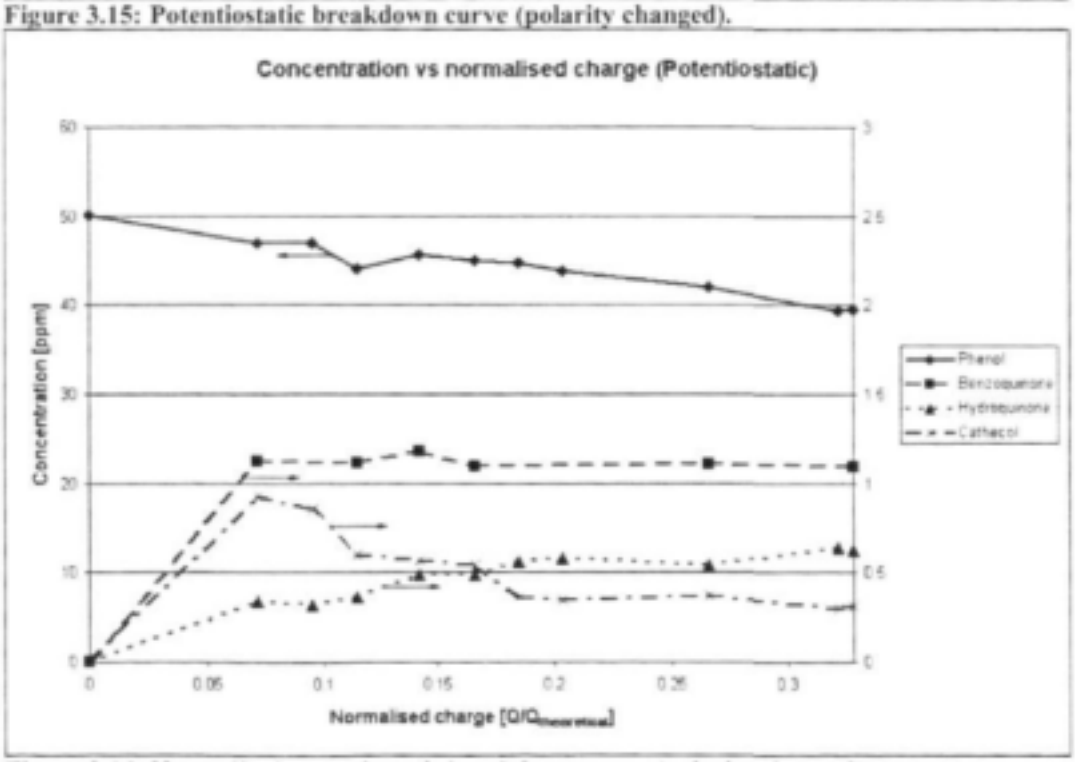


Figure 3.16: Normalised potentiostatic breakdown curve (polarity changed).

Because no analytical methods for determining the presence of a polymeric film were available, at this stage it could not be said which one of these two phenomena were responsible for film removal, or even whether the film was removed. The concentration-time profiles for these experiments are given in Figure 3.15. The normalised graph is given in Figure 3.16.

Despite an experiment duration of 60 hours, only 33% of the theoretical charge was supplied, with a conversion of 21% with respect to phenol. This was only 1% more than the experiments without the polarity change — except that here the current, and hence the charge transfer, was considerably lower. If the two graphs are compared at the same normalised charge however, it could be seen that similar phenol conversion was obtained. Therefore, these experiments need to be repeated for a longer period of time to be able to see if the same trend is followed, as is the case of the experiments without the polarity changes. If, even with the lower rate of charge transfer, some regeneration of the surface takes place, then this mode of operation may be used in a practical reactor to eliminate the need for electrode maintenance.

From the graphs it was seen that the concentration of the breakdown products remained below 2 ppm. It was also seen that certain cyclic intermediates reacted more favourably than others, i.e. catechol (1,2-dihydroxy-benzene) reached its apparent maximum concentration much earlier than hydroquinone (1,4-dihydroxy-benzene) did. The benzoquinone concentration seemed to reach a constant value at 1.1 ppm. This could be explained by examining the reactions in Figure 2.2. The first reaction was the formation of the dihydroxy compounds, followed by a reversible reaction in which these dihydroxy compounds alternated between their hydrogenated and non-hydrogenated forms. Therefore, the benzoquinone reached some equilibrium concentration. In the experiments where the polarity was changed, the benzoquinone only reached a maximum of 1.1 ppm compared to 1.8 ppm in the first experiment. This could simply mean that the catalyst as cathode had a higher potential for the reverse reaction.

The total organic carbon values for phenol and the individual breakdown products were calculated and the conversion based on this was plotted versus time (see Figure 3.17). From this graph, the overall current efficiency was calculated to be just below 55%. This is a great improvement on the current efficiencies observed in the galvanostatic experiments — which averaged between 6 and 14%.

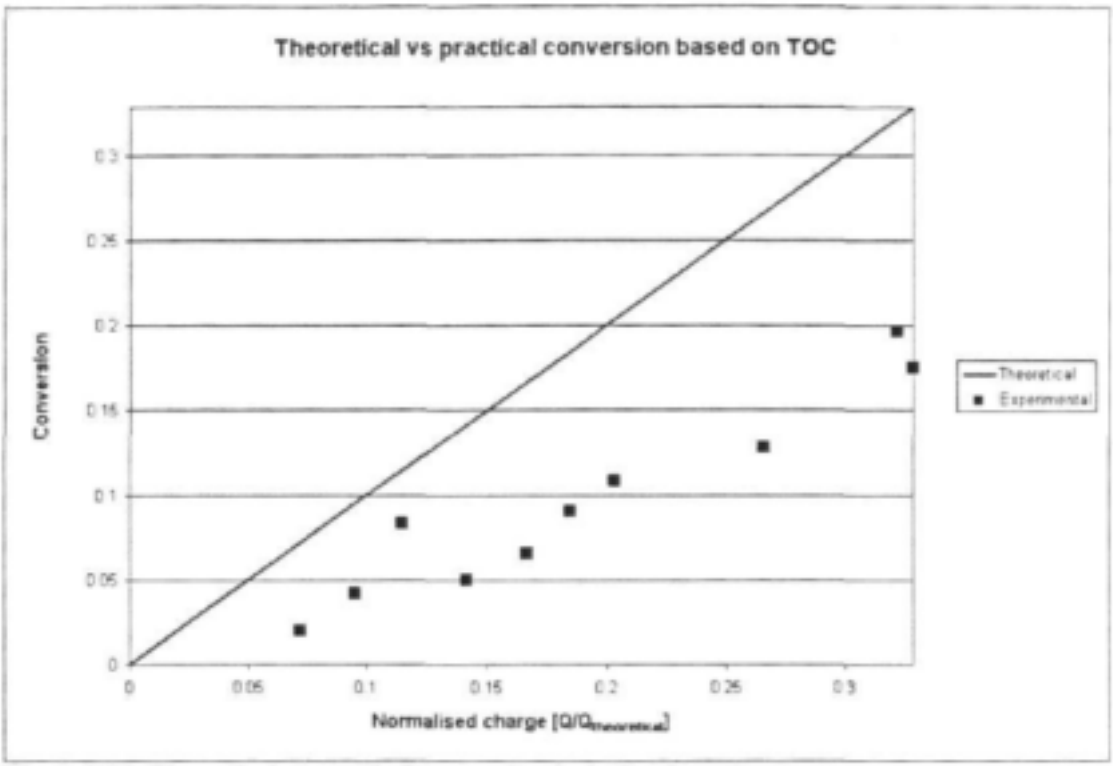


**Figure 3.17: Theoretical vs practical conversion (polarity change)**

Whereas the experiments conducted under galvanostatic operation normally ranged from about 8 hours (50 mA) to 20 hours (20 mA) for 100% theoretical charge applied, these experiments took place at a much slower rate (60 hours) — with anything from 35 to 80% charge applied. This could however, be justified with the much higher current efficiencies obtained. A full analysis of the data should prove which mode of operation would be the best.

**Table 3.11: Reaction rate constants for potentiostatic experiments — with and without polarity change**

| | $-\beta$ [$s^{-1}$] | $k_{m,experimental}$ [m/s] | $R^2$ % | 95% conf. interval |
|---|---|---|---|---|
| No polarity change | $1.53 \times 10^{-6}$ | $6.98 \times 10^{-7}$ | 92.4 | $3.91 \times 10^{-7}$ |
| Polarity change | $1.08 \times 10^{-6}$ | $4.93 \times 10^{-6}$ | 98.5 | $1.08 \times 10^{-7}$ |

The reaction rate constants calculated for the two separate experiments are given in Table 3.11. The $R^2$ values indicate that the experimental values are predicted reasonably well with the exponential curve. In both cases, the initial point deviated significantly from the exponential curve. This could again imply the rapid initial deactivation of the catalyst to some steady-state value.

### 3.3.4 Results – titanium current collectors

Despite the precautions taken, it was still found that some of the nickel leached into the solution, thereby altering the conductivity of the water and also the subsequent reaction rates. From the analysis of the results (see chapter 5), it was still determined that the phenol oxidation process would not be economically viable. Therefore, titanium current collectors were constructed to determine whether current efficiency could be improved, since they would not corrode in the same way.

Three sets of experiments were conducted at different flow rates. Each set was carried out at four different current values of 20, 30, 40 and 50 mA. No real differences between the

potential-current values for the nickel-plated and titanium current-collectors were observed. Although the potential was not constant during an experimental run, values for both the nickel-plated and titanium current collectors are nonetheless shown in Table 3.12.

**Table 3.12: Typical potential values for different currents**

| Current [mA] | Potential (nickel) [V] | Potential (titanium) [V] |
|---|---|---|
| 20 | 18 | 14 |
| 50 | 22 | 24 |

If these potential values are broken down into the separate contributions, as discussed in the additional theory equation A.33a) in appendix A, then it is seen that most of the potential is attributed to the overpotential and ohmic losses. As mentioned in section 3.3.3, the value of *Vmin* was approximately 1.4 V. If the potential drop in the current collectors and external circuit is assumed to be negligible, this means that most of the potential is required in the overpotential to drive the reaction.

This would then suggest that the kinetics of the reaction must be hindered causing high overpotentials. Hindered kinetics such as these would mean that if the process was operated galvanostatically, a limited fraction of the applied current would be used in the oxidation reaction — with the rest of the current wasted on side reactions. One solution to this is having very high aspect ratio flow channels, thereby increasing the electrode area to flow rate ratio.

Each experiment conducted with the titanium current collectors was run for a total of four hours. Using Faraday's law, this experimental time did not correspond with a 100% theoretical conversion time but had to be chosen due to time constraints. For the current values of 20 and 50 mA, this corresponded with a theoretical conversion of 20.1 and 50.2% respectively. Samples were taken every 15 minutes, to obtain accurate information closer to the start of the experiment when most of the deactivation was assumed to take place.

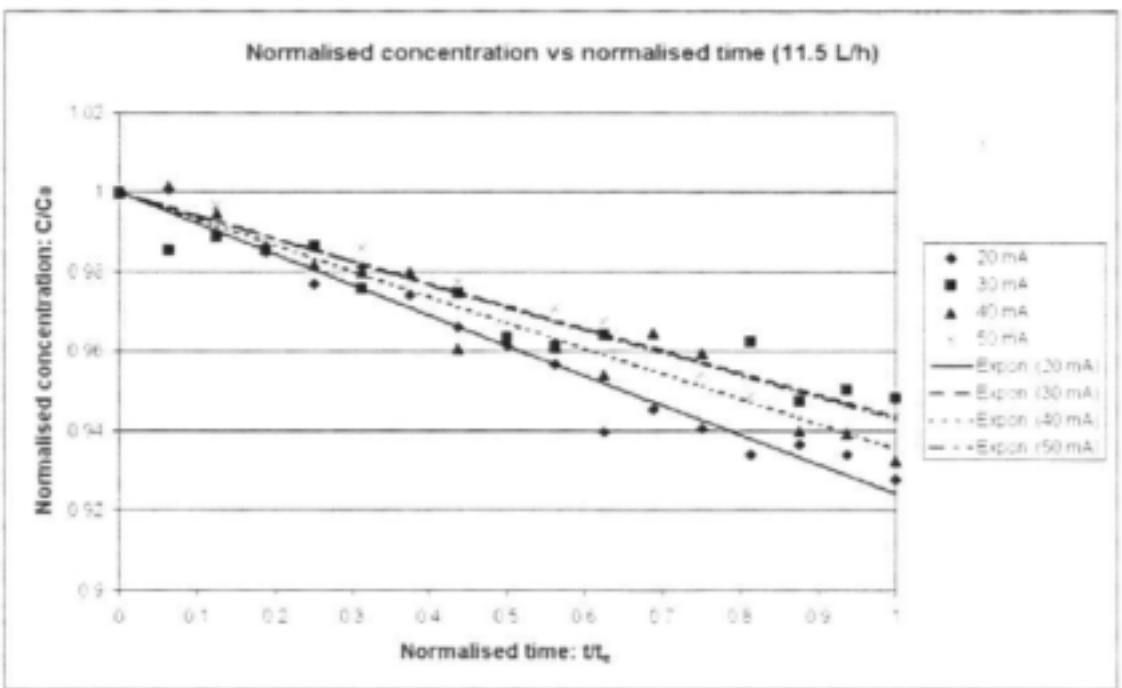


**Figure 3.18: Concentration vs time curves for a flow rate of 11.5 l/h using titanium current collectors.**

The breakdown curves for each set of experiments are given in Figures 3.18 to 3.20. Only the phenol concentrations were measured, since it was found in the previous analysis (section 3.3.3) that the quinones and dihydroxy-benzenes were present in very low concentrations. Also, the conversions in these experiments were much lower due to the short reaction times. As explained in section 3.2.3, for very low concentrations of the intermediate products, especially benzoquinone, inaccurate concentration values were measured. Therefore, it was not deemed useful to analyse the intermediates, since the accuracy of the measured concentrations could not be accepted as meaningful.

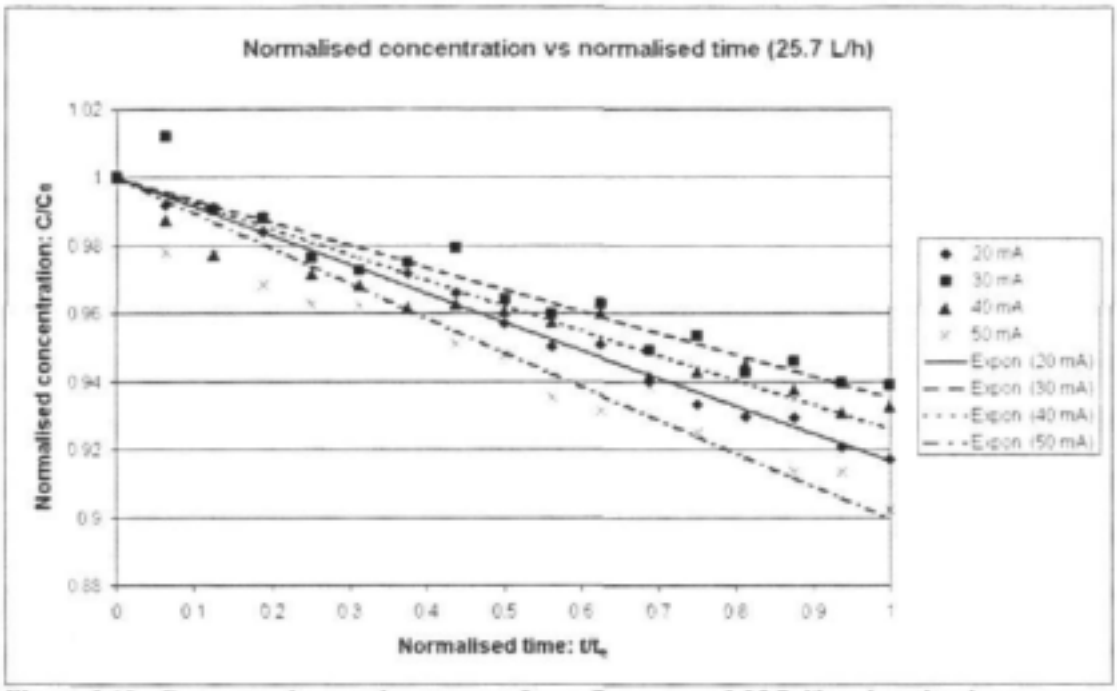


**Figure 3.19: Concentration vs time curves for a flow rate of 25.7 *l*/h using titanium current collectors.**

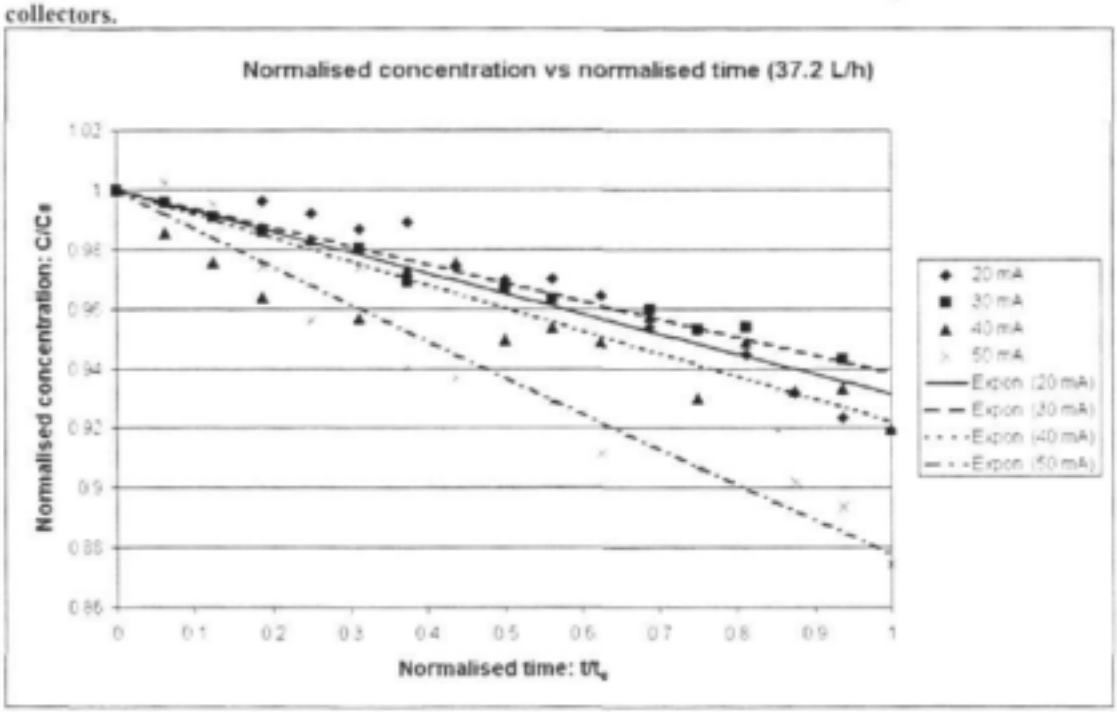


**Figure 3.20: Concentration vs time curves for a flow rate of 37.2 *l*/h using titanium current collectors.**

For all of these curves the reaction model was fitted and the appropriate reaction rate constants extracted. Once this was done some empirical correlation for the value of the reaction rate constants could be obtained. This could then be used in design equations for larger scale reactors (chapter 5).

**Reaction order experiments**

Notwithstanding all the experimental results obtained to date, still very little was known about what processes took place and their relative kinetics. Therefore more information needed to be gathered to attempt to answer these questions. The reaction order can sometimes give a clear indication of the limiting step in a reaction. For instance, if a reaction order other than unity is obtained, one can normally assume that the reaction is not mass-transfer limited.

The method of numerically differentiating the concentration versus time data is used for the extraction of the reaction orders of constant volume systems as explained in section A.1.5. The system in this application is not exactly a batch reactor, but the conversion per pass is very low — hence one can assume that it is similar to a batch reactor. The exact derivation of the method, using a numerical example, is given in Appendix D.

The experiments were conducted with initial concentrations of 40, 50 and 60 ppm phenol. The concentrations were kept relatively close together to prevent any passivation effects from influencing the results. An applied current of 50 mA was chosen, because high conversions were expected with this current value, and thus an improvement in the accuracy of the results. Both a 2nd and 3rd-order polynomial was fitted to the concentration time data, differentiated, and evaluated according to the differential method in order to determine the reaction orders. The results obtained are summarised in Table 3.13.

The reaction orders obtained in this fashion varied widely, with no clear pattern to the data. Variation in the concentration-time data could be responsible for the wide range of observed values — although, taking deactivation into account, a similar dependence of the reaction rate on the concentration could be observed. If deactivation of the catalyst takes place rapidly, with the catalyst activity reaching some steady-state value, this would also correspond with a similar profile. This profile would exhibit a rapid decrease in concentration at the start of the experiment while the concentration of phenol is high. Once the steady-state value is attained, the reaction rate will decrease, becoming independent of the activity of the catalyst, and so reflecting a lower dependence of the reaction rate on the concentration.

**Table 3.13: Reaction orders determined from the differential method**

| Concentration | Potential (nickel)<br>Potential (titanium) | |
|---|---|---|
| [ppm] | [V] | [V] |
| 40 | 15.4 | 11.2 |
| 50 | 7.27 | 5.05 |
| 60 | 2.92 | 4.22 |

Earlier in this chapter, the reaction was assumed to be influenced by both charge transfer and mass transfer. This implies that the effect of mass transfer on the reaction rate is comparable to the effect of charge transfer. External mass transfer effects always exhibit a first-order dependence of the reaction rate on concentration and therefore assuming a first-order dependence of the apparent reaction rate on concentration can be accurate. Regardless, the exponential curves that were fitted to the data presented good statistical properties, with the calculated 95% confidence intervals being smaller than the coefficient in the exponent in all cases. Once again, the number of contributing factors complicated the accurate modelling of the system and, therefore, some simplifications, such as these, had to be made.

## 3.4 Conclusions

From the results obtained in the various experimental sections a number of conclusions were drawn:

1. Too little information is available to make any assumptions about the limiting process.
2. The reaction is first-order with respect to phenol.
3. Passivation effects are negligible.
4. An economical evaluation is required to determine in which mode to operate an envisaged industrial scale plant.

The results discussed in both section 3.3.2 and section 3.3.4 showed that the reaction rate is dependent on current density and flow rate. Due to this interaction, no conclusions will be made here about the exact electrode processes. The effects of the various processes in the reactor are evaluated in greater detail in chapter 6.

The hypothesis that the reaction is first-order with respect to phenol is derived from the statistical data of the various functions fitted against the data. Both the second and third-order polynomials gave 95% confidence intervals greater than the respective polynomial coefficients. This was not the case with the exponential fit, implying that the exponential curve resulted in a stable model of the data. This, in turn, means that the coefficient would not change markedly with the removal of one or two data points.

From these results it can also be said that the effect of passivation is negligible. The catalyst may undergo a brief period of catalytic deactivation until some steady-state level is reached, thereby accounting for the higher reaction rates at the start of the experiments. Often, the first two or three data points are found to be significantly higher than the exponential fit — a trend that supports this hypothesis.

A factor that must be taken into consideration is that the surface where the oxidation is then taking place is not the metal oxide surface any more, but rather the polyphenol film, which would then act as the catalyst.

Everything said, it seems that the above-mentioned statements adequately explain the experimental data sufficiently. However, it must be said that in this particular system there are too many interactions to be able to separately investigate one single aspect of the process.

Simply by determining the reaction rate constants do not give information that is necessary in the design of an industrial unit. Although potentiostatic operation showed high efficiencies, the reaction rate constants were lower than that observed for galvanostatic operation. Further analysis was carried out to determine the most suitable mode of operation as described in chapter 5.

# 4 Disinfection

## 4.1 Introduction

The desired reactor system, besides the requirement of being able to purify selected industrial waste waters, also needs to be capable of disinfecting rural water supplies. Since the catalysts used in electrochemical combustion of organic materials form highly reactive hydroxyl radicals similar to the reactive intermediates formed in ozonation systems, it was realised that the same system could probably be very effective in the treatment of contaminated water sources. In response to this, some basic experiments were conducted to test the efficiency of the reactor with selected contaminated samples.

## 4.2 Experimental

### 4.2.1 Pathogen selection

With the help of the Department of Microbiology at the University of Stellenbosch, three of the more commonly occurring pathogenic micro-organisms were chosen, based on their doubling times. These pathogens included the following:

- *Enterococcus faecallis* (strain 92) — an opportunistic pathogen with a doubling time of approximately 35-40 minutes that is generally found in most types of faecal matter. It causes diarrhoea and nausea when excessive quantities are present in the human body.
- *Salmonella choleraesius* (strain 10398) — a pathogen with a doubling time of approximately 20-30 minutes that originally comes from the digestive tracks of birds and can be found in raw meat (especially chicken and eggs). It causes abdominal pains, diarrhoea, vomiting and fever. It has an incubation period of 48 hours.
- *Escerishia coli* (strain k88) — a pathogen with a doubling time of approximately 20 minutes that is generally found in contaminated water and food (especially beef). It causes severe diarrhoeal diseases, vomiting and fever, and has an incubation period of 24 hours.

The main reason for which the three above mentioned micro-organisms were chosen was: availability, safety and ease of analysis. Experiments were carried out to determine whether the SPE reactor could be used in the destruction of these and similar micro-organisms.

### 4.2.2 Experimental method

In an attempt to imitate typical contaminated water from water sources, a dilute solution of tryptone soy broth (TSB) was used. This is simply a solution of a specific sugar (tryptone), peptones and NaCl that is used by the above-mentioned micro-organisms to sustain life and multiply. A 1% solution of TSB was used, which equates to 0.05 g/l NaCl and 0.25 g/l of other agents such as peptone and sugar. Chemical oxygen demand (COD) measurements of the solution were taken and a value of 850 mg $O_2/l$ was found.

The experiments themselves entailed the initial setting up of growth curves for the corresponding micro-organisms to determine the required minimum duration of the experiments. It was decided that the experiments would be run until the microorganisms reached their respective stationary phases. Once a certain species of microorganism reached its stationary phase its rate of death and rate of multiplication becomes the same due to toxins formed by the microorganism and availability of nutrients. This will correspond to the maximum 'concentration' of microorganisms that can possibly survive in a certain growth medium. If the reactor has not decreased the numbers of the micro-organisms by this stage, it is most likely inefficient in the treatment of water supplies containing these micro-organisms.

A 10 m*l* 100% solution of the growth medium was made up and inoculated with the pathogens. It was then left for a period of time, which corresponded with the specific pathogens' time to reach stationary phase. 1 m*l* of this inoculum was then used to infect the test and control volume, which consisted of 1 *l* of the 1% growth medium. The control volumes were used to compare the efficiency of the reactor on disinfecting the test volume.

In all the experimental results reference is made to the 'concentration' of the solution. This is a very loose term and refers here to the number of living cells per unit volume. This must not be confused with chemical concentration. In the case of a solution containing these living organisms, the organisms form colonies that tend to clump together. This often causes spatial inconsistencies in the cells per unit volume. Due to this characteristic, obtaining accurate representations of the cell count at any given time in the experiment is difficult. In an effort to negate this effect the solutions were always well stirred.

Initially highly concentrated samples were used which created unrealistic test environments. The concentration of cells was then reduced to typical contamination levels found in the literature (typically between $10^2$ and $10^4$ cells per 100 m*l*). At these low concentrations, analysis of the samples became difficult and a different technique had to be used. This involved filtering the entire test volume and therefore only initial and final sample points were available. One option would have been to increase the test volume, but then the risk of flooding the electrodes with too many cells was higher.

Even with this method, inaccurate results were obtained. Eventually, it was decided to use the plate count method to determine the cell count. Usually 100 $\mu l$ was taken as a representative sample. If only this quantity was plated out, it would correspond to a maximum cell count resolution of 1000 cells per 100 m*l*, which was in the middle of the typical contaminated range. It was therefore decided to increase the sample size being plated out to 1 m*l*. This would correspond to a maximum resolution of 100 cells per 100 m*l*, generally the maximum cell count that uncontaminated water may have [31, 32].

Since this was still fairly inaccurate, it was decided to let the final reaction volume grow for 24 hours. If there were any living organisms left in the solution after disinfection, they would grow to a significant measurable quantity. Another sample was therefore taken 24 hours after the experiment was completed and plated out to determine if any micro-organisms were present.

Two types of electrodes were tested in the disinfection experiments: the metal oxide catalyst and graphite electrodes. The graphite electrodes are inert — they do not produce the active hydroxyl radicals, and are ideal to use to test for any other possible influences accounting for the disinfection of the test volume. The graphite electrodes were obtained from LeCarbone (Cape Town, South Africa) and had the same dimensions as the titanium substrate (85 mm diameter, 1 mm thick). The graphite of grade 2112 was chosen for high conductivity and mechanical strength.

## 4.3 Results

As mentioned earlier, the response of the electrochemical combustion system towards three different species of pathogens was investigated. Two sets of experiments were conducted using different levels of contamination. The first experiment was done using very high concentrations of organisms. The results of these experiments are discussed in section 4.3.1. More realistic levels of contamination were also tested and the results of these experiments are presented in section 4.3.2.

### 4.3.1 High–concentration experiments

The results of the experiments conducted with a high concentration ($20 \times 10^6$) of cells are given in Figure 4.1. The reactor system effectively removed the micro-organisms from the test volume to a significantly lower concentration. The reactor rapidly removed the cells up to a certain concentration of about $1 \times 10^6$ cells and then steadily continued decreasing the cells.

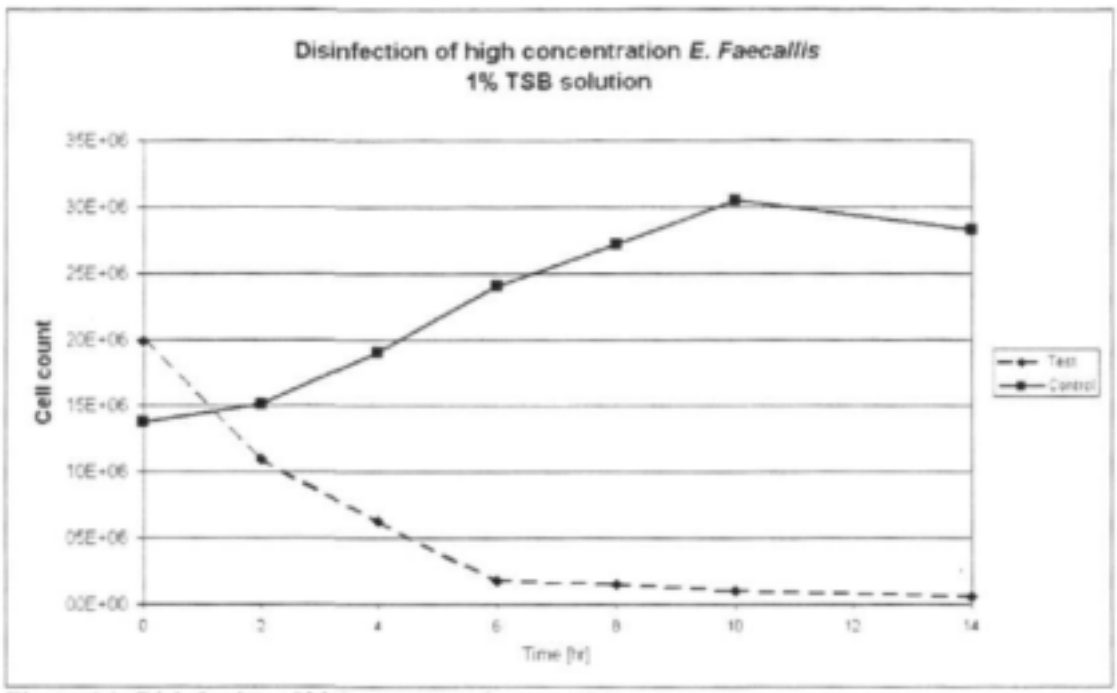


**Figure 4.1: Disinfection of high concentration samples.**

It was noted during the experimental runs that gas was being developed in the anodic compartment. This may have been carbon dioxide resulting from the high organic carbon content of the solution being combusted, or chlorine from dissolved NaCl. Thus the question arose as to whether it was the reactor itself killing the organisms or the chlorine gas acting as disinfectant. It must also be noted that for these experiments 100% TSB solutions were used which contained high levels of chlorine ions. This was later adjusted to the level stated in the experimental method (section 4.2.2).

On completion of the experiment, the test volume was removed from the reactor system and left for a period of 24 hours, after which the cell count was observed. It was found that the cell count had returned to its initial value. Thus, no residual effect was obtained from the reactor itself. It is therefore vital that the reactor system decreases the number of micro-organisms to a significant level, at which no growth will be observed for a period of at least one week, to ensure that stored water remains uncontaminated.

### 4.3.2 Low–concentration experiments

Additional experiments with initial concentrations of micro-organisms closer to realistic values (section 4.2) were conducted. Despite the precautions taken in the preparation of the inoculum, variations of up to two orders of magnitude in the initial concentration were still obtained. In all cases the initial concentration was higher than the maximum observed contamination levels stated in the literature.

Despite these slightly higher concentrations, the reactor system still successfully removed all the micro-organisms. As discussed in section 4.2, the samples were left for an additional period of time, corresponding with the times of the individual micro-organisms exponential growth phase. After this period of time no living organisms were detected in the samples. The cell counts of these experiments are given in Figure 4.2. Note that a period of only four hours was required for the elimination of all living cells.

Although the time required to obtain the stated disinfection was only four hours, it compared unfavourably with water treatment methods such as ozonation, chlorination and UV radiation. These processes are virtually instantaneous when their disinfection capabilities are considered. Also, treatment with chlorine has the added benefit of introducing residual disinfectant agents, ensuring that water that has been treated does not become contaminated for a period of days after treatment.

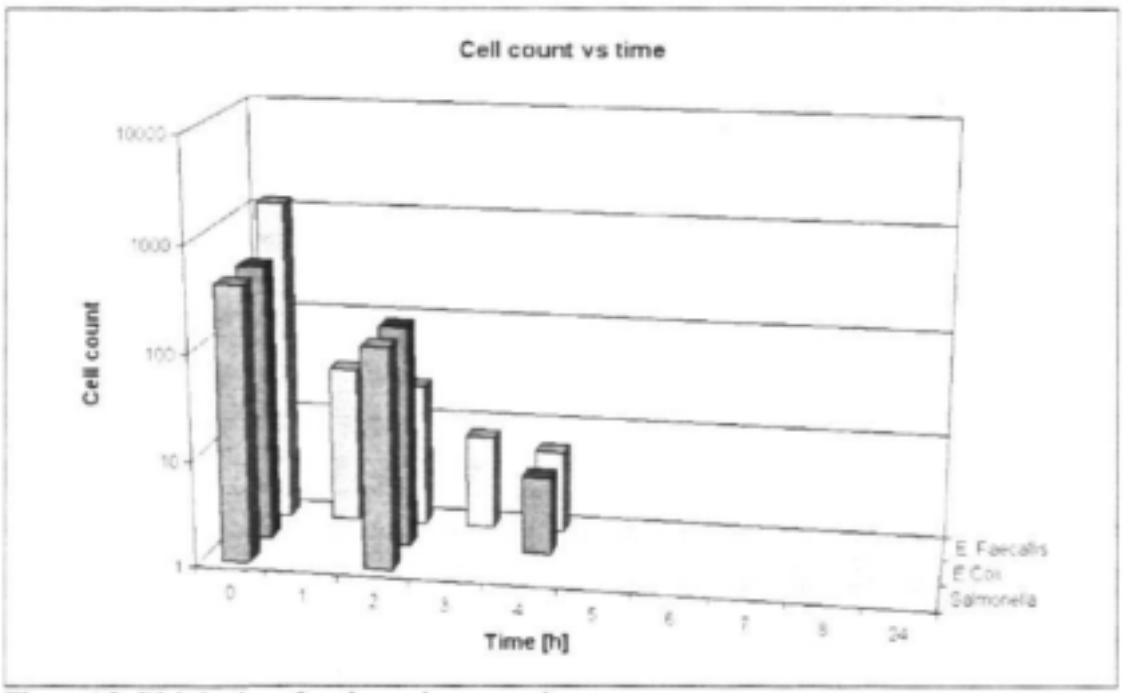


**Figure 4.2: Disinfection of various micro-organisms.**

Additional experiments were carried out to assign a pseudo-rate constant to the disinfection of the samples. The same approach as that used for phenol was used for the determination of pseudo-reaction rate constants in the disinfection experiments. Unfortunately, the results obtained from the *E. coli* experiments were contaminated and the results could not be used. The results for *Salmonella* and *Enterococcus faecallis* are given in Figure 4.3 and 4.4.

The individual values obtained for the coefficient of regression, $\beta$, together with the respective $R^2$ values and 95% confidence interval values, are given in Table 4.1

**Table 4.1: Reaction rate constants for microbiological experiments**

| Species | $-\beta$ [$s^{-1}$] | $k$ [m/s] | $R^2$ % | 95% conf. interval |
|---|---|---|---|---|
| *E. Faecallis* | $2.09 \times 10^{-4}$ | $9.65 \times 10^{-5}$ | 89.7 | $5.02 \times 10^{-5}$ |
| *Salmonella* | $8.17 \times 10^{-4}$ | $3.88 \times 10^{-4}$ | 93.4 | $2.49 \times 10^{-4}$ |

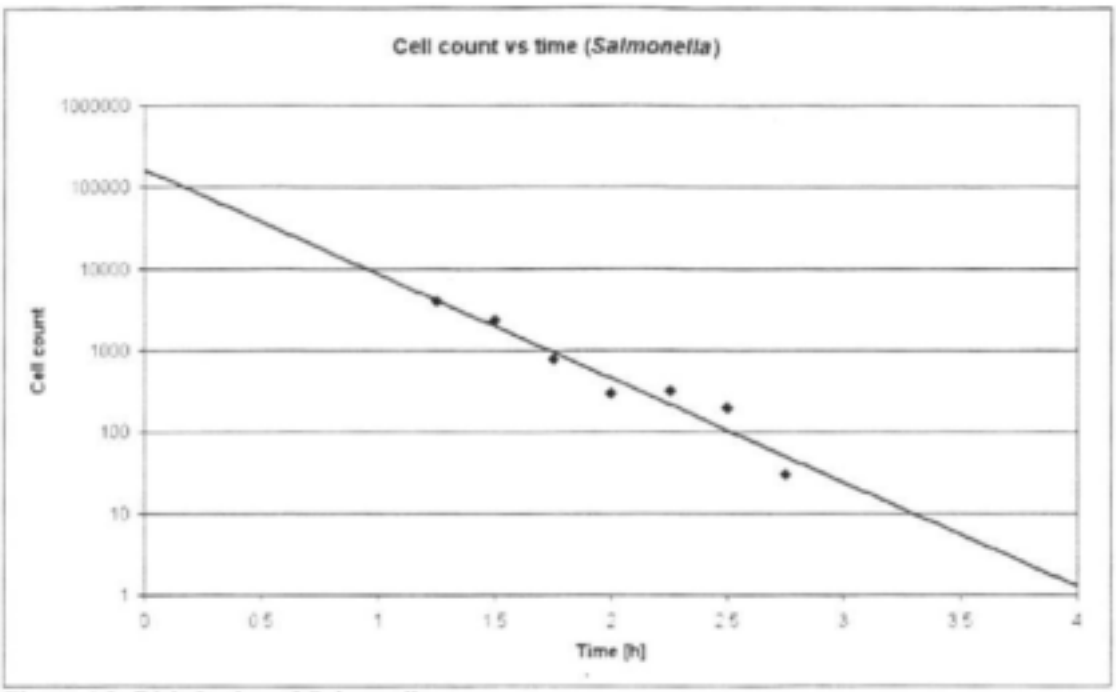


**Figure 4.3: Disinfection of *Salmonella*.**

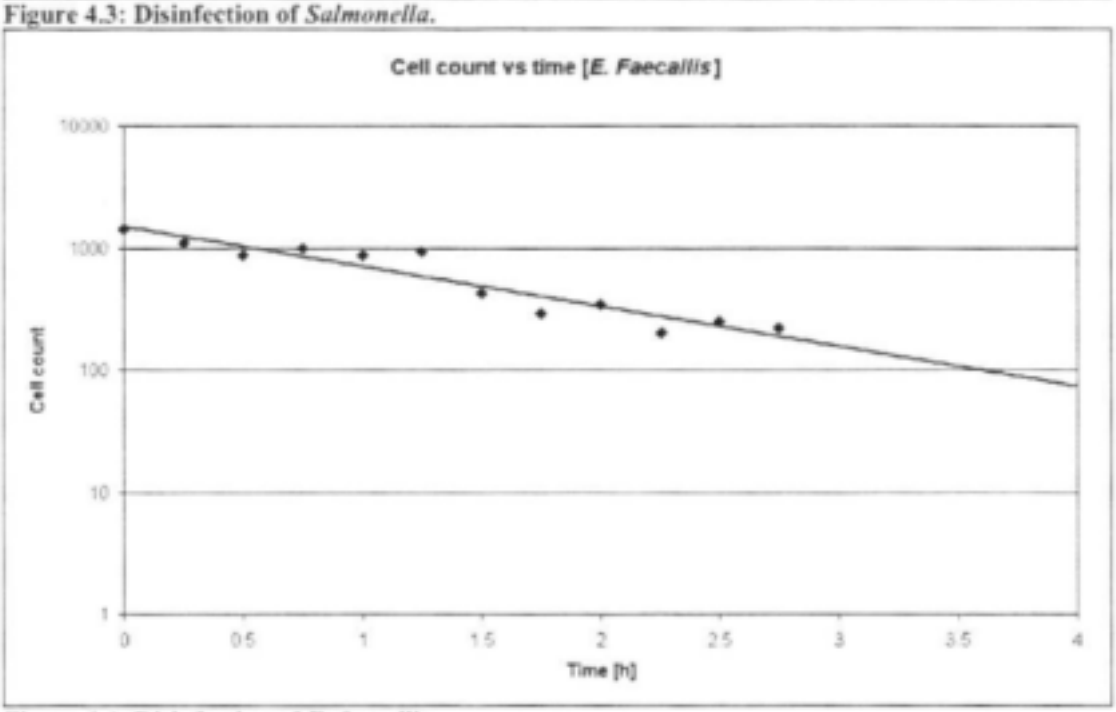


**Figure 4.4: Disinfection of *E. faecallis*.**

The coefficients obtained for the disinfection of the above micro-organisms were, on average, two orders of magnitude greater than those obtained for the oxidation of phenol. These coefficients are used in chapter 5 as comparison when the lengths of the reactors are considered.

It was suspected that the formation of the hydroxyl radicals might not be directly involved in the destruction of the micro-organisms, and that the potential difference in the reactor might disrupt the functioning of the cell membranes, thereby killing the micro-organisms. To determine which of these two processes were responsible, inert electrodes (electrodes that do not produce hydroxyl radicals) were tested with *E. coli*. The inert electrodes were graphite electrodes (see section 4.2).

Experimentation times and conditions were identical to those used in the previous experiments. Analysis of the samples showed that the concentrations of organisms in all of the samples exceeded the top limit of the resolution of the analysis method. This meant that during the entire experiment the cell count in the solution was higher than 300 000 cells per 100 ml. This is 30 times greater than the acceptable limit. Therefore the disinfection could be directly attributed to the action of the catalyst.

## 4.4 Conclusions

The results show that the electrochemical system can be successfully used for the removal of microorganisms. The three organisms were chosen in such a way that it could be considered that if the reactor system could successfully remove them from water, the system should be capable of removing most harmful microorganisms. Prokaryotes, such as *Giardia* and their cysts, were not included. These organisms are most often effectively removed by the proper use of filters.

The removal of the microorganisms can be attributed to the formation of the hydroxyl radicals. These radicals, due to their reactive nature, are short-lived, and therefore it is possible that no residual agents are created in the water to prevent regrowth. Although no regrowth was observed after 24 hours, this does not necessarily mean that introduction of microorganisms after treatment will ensure that the water remains uncontaminated. Additional experiments must still be conducted to determine whether any residual agents are created by this method.

# 5 Application of Experimental Data

## 5.1 Introduction

In this chapter the experimental data presented in the previous sections are used in the derivation of a simple model for the oxidation process. This model is then used to design a hypothetical pilot plant to test the viability of the reactor system. The detailed derivation of the model is shown in Appendix C. The experimental data is discussed in greater detail in section 5.2 and used to design a scaled up version of the reactor, described in section 5.3. This will be followed by a brief economic evaluation of the reactor system in section 5.4.

## 5.2 Discussion of Experimental Work

A simple relationship between the phenol concentration at any time, $t$, and the initial phenol concentration was obtained, as mentioned in section 3.3.1. This relationship was then used to determine the rate constants for the various experiments, which in turn could be used to determine typical reactor lengths. A detailed derivation of the appropriate expressions has been provided in Appendix C, together with an example of the calculations involved in appendix D. The final equation used to extract the reaction rate constants from the experimental data is:

$$k = -\frac{v_R}{WL}\ln(\beta\tau + 1) \tag{3.3}$$

For a description of the symbols in equation 3.3, please refer to section 3.3.1.

The lowest and highest rate constants for the various experimental sections were calculated and are provided here for comparison, followed by the implication of the results for the design of a pilot plant. The current efficiencies presented here were calculated for the complete combustion of phenol to carbon dioxide. A total of 28 electrons need to be supplied by the external power source to completely convert a phenol molecule to carbon dioxide. In the case of the disinfection experiments, the exact number of electrons required to eliminate one cell is not known and possibly varies from cell to cell. Therefore the current efficiencies for the microbiological experiments were omitted. The disinfection experiments were all conducted with the same values for the experimental parameters and therefore only one value for $k_m$ is listed.

**Table 5.1: Comparison of experimental reaction rate constants for different experiments**

| | Lowest value | | Highest value | |
|---|---|---|---|---|
| Experiment | $k_m$ [m/s] | $\varepsilon$ % | $k_m$ [m/s] | $\varepsilon$ % |
| Oxidation – Nickel-plated current collectors | | | | |
| Galvanostatic | $7.16 \times 10^{-7}$ | 5.33 | $2.47 \times 10^{-6}$ | 14.0 |
| Potentiostatic | $4.93 \times 10^{-7}$ | 32.4 | $6.98 \times 10^{-7}$ | 54.3 |
| Oxidation – titanium current collectors | | | | |
| Galvanostatic | $1.56 \times 10^{-6}$ | 17.2 | $3.16 \times 10^{-6}$ | 30.1 |
| Microbiological – titanium current collectors | | | | |
| *E. Faecallis* | — | — | $9.65 \times 10^{-5}$ | ? |
| *Salmonella* | — | — | $3.88 \times 10^{-5}$ | ? |

Table 5.1 shows that potentiostatic operation corresponded with significantly higher current efficiencies — thus, on the surface, it seemed that potentiostatic operation would be the best mode of operation. The titanium current collectors were all operated galvanostatically and yielded significantly higher current efficiencies, the highest of which almost equalled those obtained for potentiostatic operation.

Due to the complexity of the system and the many factors influencing the reaction rate constants, it would be the best course of action at this stage to find some empirical correlation between the reaction rate constant and the main parameters. Therefore, some relationship of the following form could be fitted to the data.

$$k^* = \text{fn}(i, v_R) \tag{5.1}$$

This expression states that the apparent reaction rate constant is some unknown function of the current density, $i$, and the flow rate through the reactor, $v_R$.

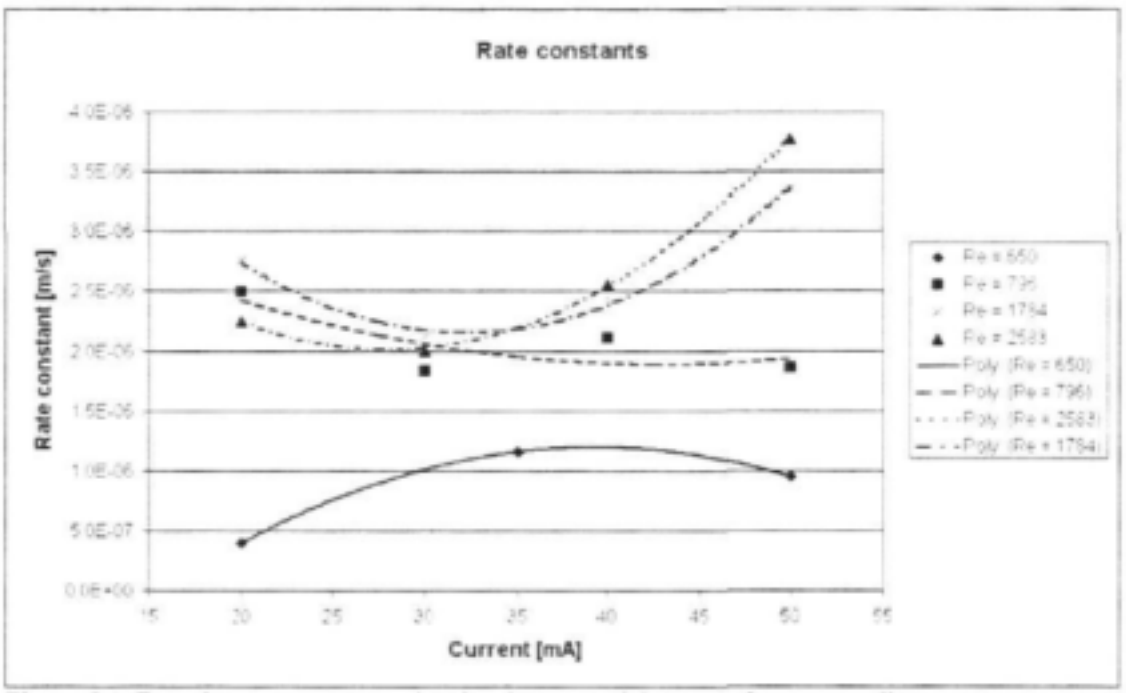


**Figure 5.1: Reaction rate constants for titanium and nickel-plated current collectors.**

The reaction rate constants obtained from the experiments utilising titanium current collectors are shown in graphical format in Figure 5.1. The apparent reaction rate constants were plotted versus current for various values of the flow rate. The exception was the constants obtained for a Reynolds number of 650 that were slightly below the other curves. These constants were obtained using nickel-plated current collectors. Rate constants obtained with the nickel-plated current collectors were lower due to the nickel that was assumed to take part in a separate reaction, thereby lowering current efficiencies.

Nonetheless, a definite trend could be observed in the data. For the low and high current values, the reaction rate constant appeared to have a strong dependency on the flow rate, whereas for the intermediate values almost no change was observed for the reaction rate. In the next section, these values will be used to perform rough scale-up calculations.

## 5.3 Scale-up Calculations

The scale-up calculations were done for a MEA and current collector set-up similar to that used in the experimental reactors. This prevented any errors that could possibly be introduced due to changes in the flow channel dimensions. The cross-sectional area available to flow was changed, to accommodate larger flows.

In order to quantify this scale-up, practical sizes for the substrate were obtained. The largest porous titanium sheets obtained were from Mott Corporation in America. The maximum dimensions of these porous titanium sheets were 0.5 m by 0.25 m. The length of the reactor directly influences the conversion obtained in the reactor (as shown in appendix D), whereas the width of the electrode merely determines the output of the reactor. Due to this, the length of the reactor was chosen to be 0.5 m long. As mentioned, the flow channels in the reactor would have the same dimensions as those in the experimental reactors, and thus a total of 30 flow channels could be fitted onto one electrode. This value was used consistently throughout the rest of the scale-up calculations.

To determine the length of the reactor required to obtain a certain conversion $X$, the same approach was used as in section 5.2. The only difference was that $L$ in this case was the unknown, and $k$ was known or could be calculated. The expression for $L$ then becomes

$$L = -\frac{v_R}{Wk}\ln(1-X) \tag{5.2}$$

The detailed derivation of this equation is once again provided in appendix C. The predicted reactor lengths were calculated for all of the experimental values, and are given in Table 5.2 (nickel-plated current collectors) and 5.3 (titanium current collectors) for the highest and lowest conversions. In comparison, reactor lengths for the potentiostatic and microbiological experiments are given in Table 5.4.

**Table 5.2: Calculated reactor lengths – nickel-plated current collectors**

| Re | $I$ [mA] | Separated electrolyte | $L_{X=0.99}$ [m] | $L_{X=0.5}$ |
|---|---|---|---|---|
| 650 | 20 | No | 6159 | 927.0 |
| 650 | 35 | No | 2878 | 433.2 |
| 650 | 50 | No | 3606 | 542.8 |
| 650 | 50 | Yes | 1803 | 271.4 |
| 1516 | 50 | Yes | 3011 | 453.2 |

**Table 5.3: Calculated reactor lengths – titanium current collectors**

| Re | $I$ [mA] | $L_{X=0.99}$ [m] | $L_{X=0.5}$ |
|---|---|---|---|
| 796 | 20 | 6124 | 921.8 |
| 796 | 30 | 7623 | 1147 |
| 796 | 40 | 5406 | 813.7 |
| 796 | 50 | 6130 | 922.7 |
| 1784 | 20 | 2945 | 443.2 |
| 1784 | 30 | 4067 | 612.2 |
| 1784 | 40 | 3994 | 601.2 |
| 1784 | 50 | 2987 | 449.7 |
| 2583 | 20 | 1160 | 174.5 |
| 2583 | 30 | 1929 | 290.3 |
| 2583 | 40 | 1745 | 262.7 |

**Table 5.4: Calculated reactor lengths - potentiostatic and microbiological experiments**

| Potentiostatic experiments | | |
|---|---|---|
| | $L_{X=0.99}$ [m] | $L_{X=0.5}$ [m] |
| No polarity change | 17044 | 2565 |
| Polarity change | 24131 | 3632 |
| Microbiological experiments | | |
| | $L_{X=0.99}$ [m] | $L_{X=0.5}$ [m] |
| *Salmonella* | 123.3 | 18.6 |
| *E. Faecallis* | 30.7 | 4.6 |

The values given in the table were calculated using the flow rate at which the experiments were conducted, since no expression had yet been obtained to express the reaction rate constant in terms of the flow rate. Also note that the flow rate as calculated here was 30 times that of the experiments. This factor of 30 was introduced because of the number of flow channels that the larger reactor had. The Reynolds number in the individual flow channels was still the same as in the experiments.

The reactor lengths calculated for the potentiostatic experiments, compared to those for the galvanostatic experiments, showed that the mode of operation for the pilot reactor would be galvanostatic. Despite the lower current efficiencies observed for galvanostatic operation, the lengths were more than an order of a magnitude less compared to the lengths obtained for potentiostatic operation.

It was seen that the reactor lengths for the oxidation of phenol were unrealistic, especially if a large volumetric flow rate of waste needed to be treated in a single-pass reactor system. Therefore, introducing a recycle stream that returned a fraction of the effluent to the inlet could reduce the required length of the reactor. The proposed flow diagram for such a pilot plant reactor is given in Figure 5.2.

For a desired flow rate, an economical evaluation of the reactor system could be performed. This is described in the next section where the results are presented in graphical form.

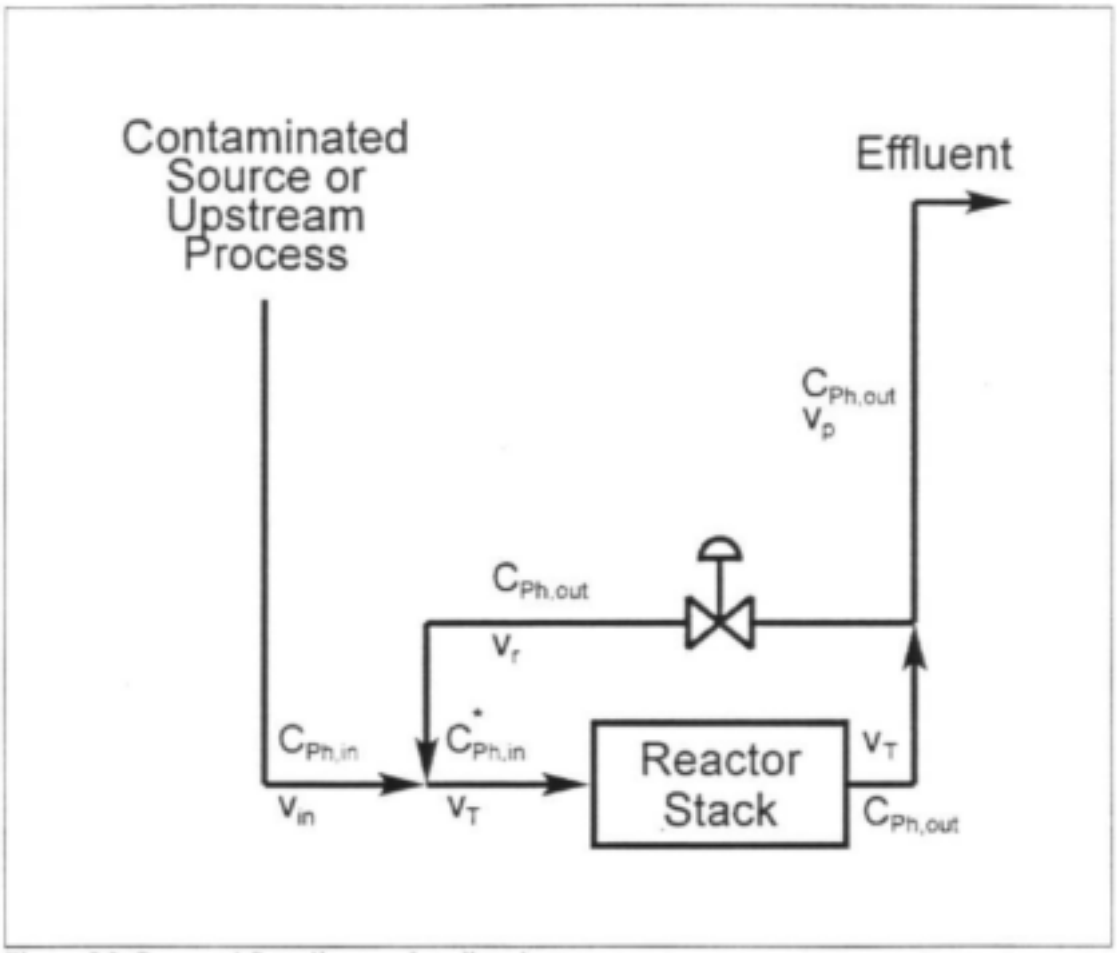


**Figure 5.2: Proposed flow diagram for pilot plant.**

## 5.4 Economic Evaluation

For a practical reactor, the most important factors that contribute to the overall cost involved in building and operating the reactor are the following:

1. **Capital cost** – the price of the materials, cost of construction and installation.
2. **Operating cost** – the cost involved in keeping the reactor running. This includes electricity costs, and any chemicals required on a continuous basis.
3. **Maintenance cost** – the cost involved in maintaining the final reactor. This includes cost of training personnel, paying salaries, general maintenance, etc.

The maintenance cost will not be evaluated at this stage since it requires more information on the practical lifetimes of the membrane and catalyst. No long-term experiments have yet been done to determine the long-term response of the catalyst and membrane under electrolysis conditions.

The major contributing factors to the capital cost are the porous titanium support, titanium current collectors and membrane. To determine the cost of a typical small pilot scale reactor, quotes were obtained in June 2003. It was found that a reactor consisting of 20 units in series would require porous titanium substrates that would amount to approximately R80 000.

The cost of such a reactor was evaluated per meter length of reactor. Pressure drop through the reactor was an important consideration due to the small flow channels in the current

collectors. The pressure drop in the reactor will determine the pump size required, and therefore influence the pumping costs involved and also the initial capital cost.

The final capital cost of the reactor is therefore mainly dependant on the reactor length and the selected recycle ratio. The recycle ratio in this case is the ratio between the volumetric flow rate of the recycle stream and volumetric flow rate of the product stream. Two possible extremes exist in the selection of values for the length and recycle ratio. A high recycle ratio would correspond with a decrease in reactor length and vice versa. This principle is demonstrated graphically in Figure 5.3. In the figure a conversion of 75% was chosen.

High recycle ratios correspond to an increase in the pumping cost since larger pumps would be required. The capital cost associated with the materials of construction for the reactor itself would be reduced though. Low recycle would introduce a reduction in pumping costs, but the increased reactor length required would raise the capital cost of the reactor. Therefore, some trade-off can be found between the two parameters where the total cost is a minimum. The capital cost of the reactor based on a meter length is shown in Table 5.5.

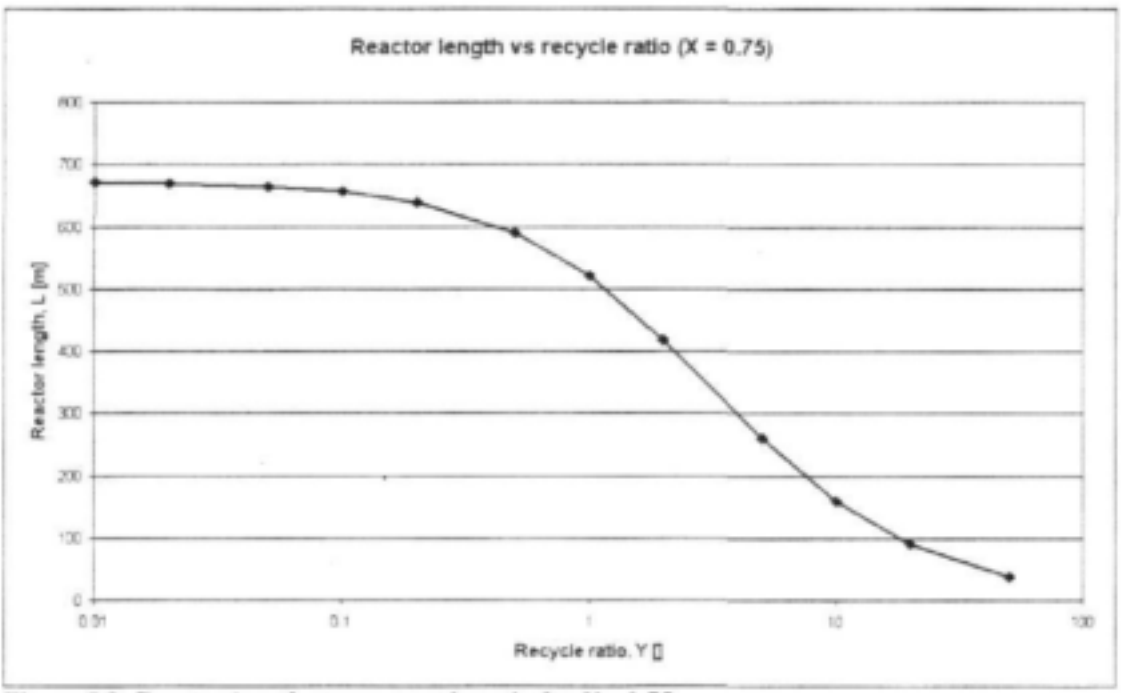


**Figure 5.3: Reactor length versus recycle ratio for $X = 0.75$.**

**Table 5.5: Estimated capital costs of reactor per meter length (June 2003)**

| Part | Cost [R/m] |
|---|---|
| Electrode | 5 860 |
| Membrane | 930 |
| Materials | 1 650 |
| **Total** | **8 440** |

Other factors contributing to the total capital and operating cost were also calculated. The exact expressions for these factors can be found in Appendix C. The overall cost of the reactor can be expressed in terms of these factors. This is shown in equation 5.3.

$$C_{total} = C_{reactor} + C_{pump} + C_{reactor,running} \qquad (5.3)$$

The total cost is dependent on the applied current (electricity required for operation), the total flow through the reactor (and therefore the recycle ratio) and the length of the reactor. The costs involved in the reactor are graphically presented in Figure 5.4.

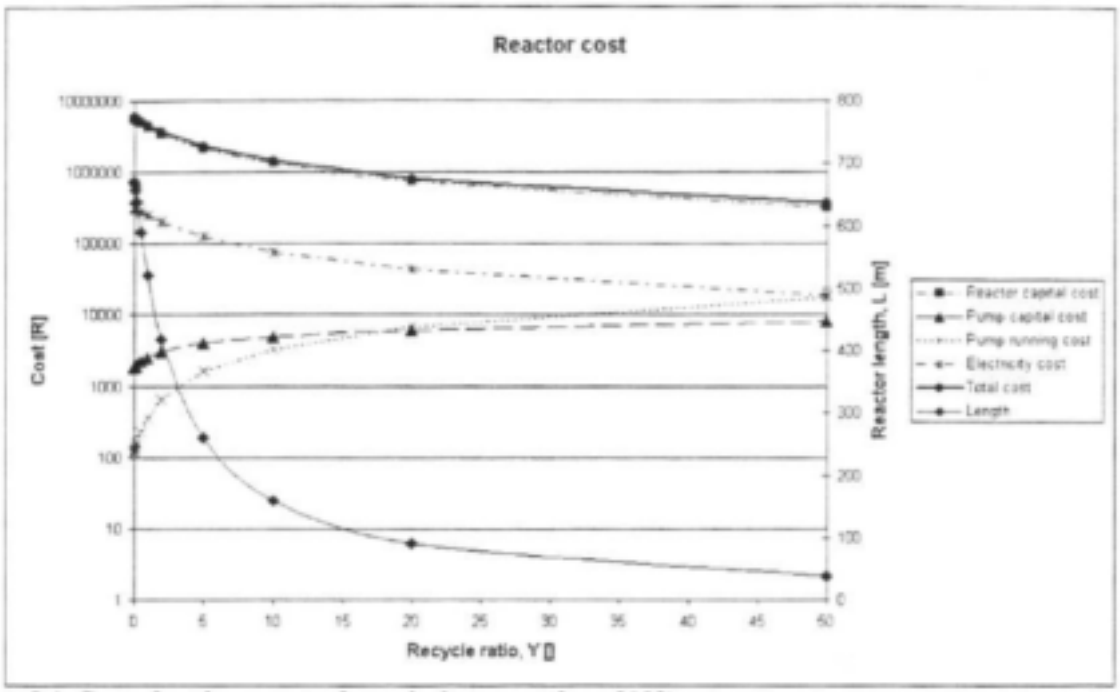


**Figure 5.4: Cost of various parts of a typical reactor (June 2003).**

It can be seen that for the current costs of the reactor parts, the running cost and capital cost of the reactor overshadow the pumping costs. This implies that the minimum cost mentioned earlier can be found at very high recycle ratios and therefore at the moment it is more cost effective to have a very large pumping system and a short reactor.

In future, as more research is done on materials, and the prices of the construction materials are reduced, the reactor capital and running cost will become comparable to that of the pumping cost. The minimum cost will then shift to lower recycle ratios, and some intermediate recycle ratio will give the minimum cost for the reactor system.

This analysis was performed for a flow rate of 186 *l*/h. Although this may be high enough to supply a small rural community with water, it must be remembered that the analysis was done for a conversion of 0.75 and therefore not all of the harmful chemicals will be destroyed. Fortunately, the system is very efficient in the destruction of the micro-organisms, and therefore no pathogens will be present in a reactor of that length.

Increasing the conversion to 99% will increase the length of the reactor significantly, and thus increase both the capital cost and running cost of the reactor significantly. Therefore, it can be said that the reactor system using the current technology available for this kind of water treatment is not economically viable. Other water treatment methods exist that are currently more efficient at disinfecting and purifying water (such as UV treatment and the use of ozone).

## 5.5 Conclusions

The reactor lengths calculated in this section must not be thought to be impossible to attain. A thousand metre reactor is probably difficult to realise, but in the case of this reactor system such a length can be compacted into a small reactor since the flow channels are only 4 × 4 mm. The pressure drop through the reactor must be taken into account though. For the typical flowrates calculated in the cost evaluation, pressure drops varying from 140 kPa to 900 kPa were obtained.

The current state of the technology and the associated cost puts the process at a disadvantage when compared to current methods of water treatment. The main disadvantage is the capital cost requirement of the reactor — the main contributing factor. Selecting a typical recycle ratio, the average cost of treated water per person per day can be calculated. This cost is based on an allowance of 20 *l* per person per day, the minimum recommended quantity as specified by the World Health Organisation. This cost amounts to approximately R2.50 per day (R75 per month). The water provided as such will be completely disinfected with up to 75% removal of organic content.

Considering the cost analysis that has been performed, it can be said that this technology is too expensive. There are other alternatives available that can yield the same quality of water at a lower cost.

# 6 System Requirements for Future Applications

## 6.1 Introduction

In the previous chapters, the electrochemical oxidation process was discussed and analysed, and it was shown that the process is not yet economically competitive with current water treatment techniques. This lead to the next consideration: Determining what would be required of such a system in order for such a system to compete with existing techniques.

The chapter will begin with a detailed sensitivity analysis which will include:

- calculations determining the influence of individual parameters, as well as
- a more fundamental approach to determining the rate-limiting step in the reaction.

Results of the sensitivity analysis are summarised in the subsequent section, which will discuss the actual requirements of the system to make it economically feasible. Finally, the major conclusions drawn from the information that was gathered are made.

## 6.2 Sensitivity Analysis

### 6.2.1 Reactor model revisited

The reactor model had to be modified slightly to take the specific surface area into account. This was necessary because the effect of the specific surface area would be investigated in the sensitivity analysis. The model was changed (the detailed derivation can be found in section C.4 in appendix C) and the final form of the expression relating the conversion to the major parameters could be written as:

$$1-X=\frac{\exp\left\{-\dfrac{k^{*}A_{i}W\delta L}{v_{p}(Y+1)}\right\}}{Y+1-Y\exp\left\{-\dfrac{k^{*}A_{i}W\delta L}{v_{p}(Y+1)}\right\}} \qquad (6.1)$$

The symbols in equation 6.1 are based on the diagram of the pilot plant shown in Figure 5.2. The major parameters in the equation are shown in Table 6.1:

**Table 6.1: Major parameters for sensitivity analysis**

| Symbol | Parameter |
|---|---|
| $k^{*}$ | The apparent reaction rate constant |
| $A_i$ | Specific surface area of the catalyst substrate |
| $Y$ | The recycle ratio defined as $Y \equiv \frac{v_r}{v_p}$ |

The other variables that appear in equation 6.1 are constants and will be specified in the next section.

### 6.2.2 Effect of parameters

The effect of the most important parameters on the operation of a pilot plant (described in chapter 5) can be determined. In this section, the influence of the following parameters was investigated:

- Recycle ratio – strictly speaking, it was the effect of an increase in the flow rate through the reactor that was determined here, since the recycle ratio is directly dependant on the flow rate,
- Reaction rate constant – both the current density and the flow rate influenced the apparent reaction rate constant, therefore the change in conversion was determined for a change in the apparent reaction rate constant.
- Specific substrate surface area.

In this section, when reference is made to the reaction rate constant it is the "apparent" reaction rate constant that is implied.

### Effect of the apparent reaction rate constant

The effect of a change in the apparent reaction rate constant is shown in Figure 6.1. The data points were calculated using the following values for the constant parameters:

**Table 6.2: Constant values used to determine other parameters (effect of apparent reaction rate constant)**

| Parameter | Symbol | Value |
|---|---|---|
| Specific surface area | $S_a$ | 0.7 [m$^2$/g cat.] |
| Reactor length | $L$ | 10 [m] |
| Recycle ratio | $Y$ | 1 |
| Flow rate | $v_p$ | 186 [l/h] |

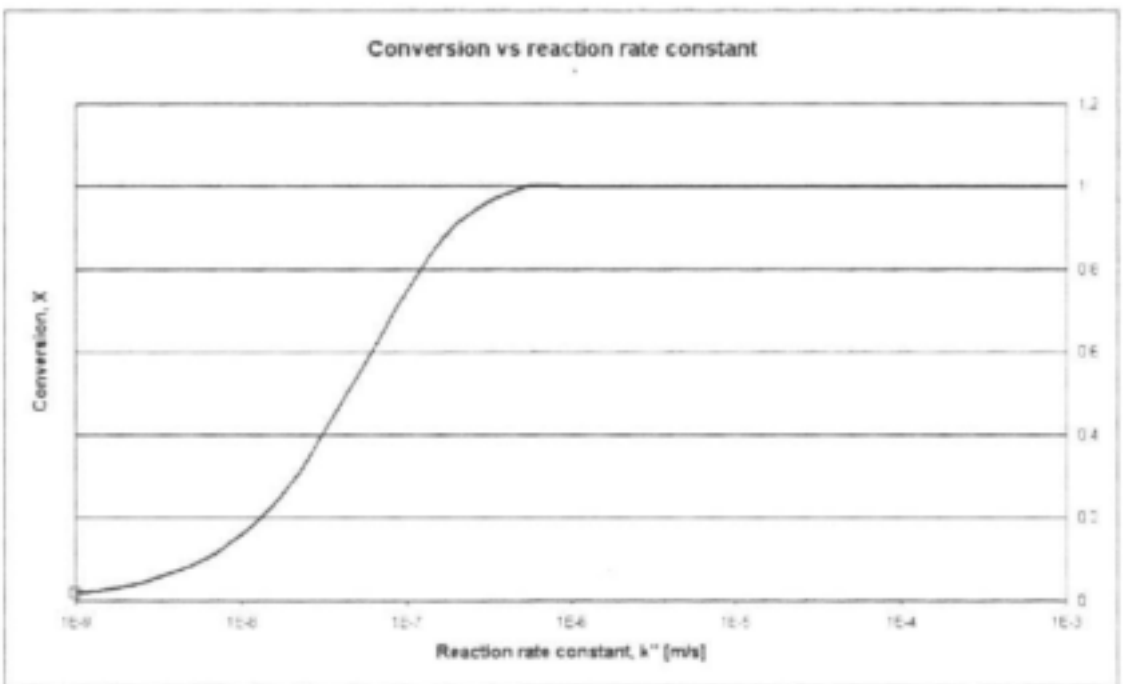


**Figure 6.1: Effect of reaction rate constant on conversion.**

The data point indicated by a square in the graph corresponded to the experimental value of the reaction rate constant that was observed for the experiments with the titanium current collectors. Notice the two asymptotical values of the conversion for two limiting conditions. As the apparent reaction rate constant approaches zero ($k'' \rightarrow 0$), $X \rightarrow 0$. This value for the conversion was obtained by considering equation 6.1. The recycle ratio appears in the denominator of the right-hand side of the equation, so that for a recycle ratio of one ($Y = 1$) and an apparent reaction rate constant of zero ($k'' = 0$), equation 6.1 reduces to:

$$1 - X = \frac{\exp\{0\}}{Y + 1 - Y\exp\{0\}} = \frac{1}{Y + 1 - Y}$$

Or

$$X = 1 - 1 = 0$$

This result is what one would expect if the reaction rate constant approached zero, since no phenol would have reacted.

The other limiting condition was where the apparent reaction rate constant was very high ($\bar{k} \to \infty$), in which case the conversion became unity ($X \to 1$). A conversion of unity means that all of the phenol is combusted in a reactor with a length of 10 metres. The reactor length could then be reduced up to a point where sufficient combustion is obtained (e.g. $X = 0.999$).

It should be noted from the graph however, that the apparent reaction rate constant corresponding to such a value fell just under $1 \times 10^{-6}$ [m/s], almost three orders of magnitude greater than the measured experimental values. This was a significant increase, which in all likelihood is not physically attainable.

There are a couple of ways in which to improve the reaction rate constant. The first method is the development of new and improved catalysts, more suited to the electrochemical oxidation of phenol in aqueous media. The second way would be to increase the current density since the reaction rate is dependant thereon (section 3.3.2).

Both ways have associated disadvantages. An increase in the current density, although improving the reaction rate constant, increases the running cost of the reactor due to increased electricity consumption. The increased reaction rate constant will shorten the required reactor length, but the reduction in cost for a shorter reactor may not be greater than the increase in running costs.

Physical limitations also prevent an indefinite increase in the current density. The proton exchange membrane can only be operated up to a maximum current density before sustaining damage, hence eliminating proton conduction. Also, high current density ensures high operating potentials, which promotes the oxygen-evolution side reaction, introducing an additional inefficiency.

Alternative catalysts therefore show the most promise in increasing the reaction rate constant, but the effectiveness of the catalyst is normally proportional to the cost of the catalyst. For instance, although the tin dioxide catalysts are capable of oxidising phenol, iridium oxide catalysts reputedly show greater effectivity in the combustion of phenol. The trade-off is the cost, which in the case of iridium is significantly higher.

Thus, although improved catalysts can be used and the current density can be optimised for a particular system, an increase of even one order of magnitude in the reaction rate constant seems unlikely. One may observe an improvement of a factor of two to three.

**Effect of specific surface area**

The same analysis as in the previous section can be done for the specific surface area of the catalyst substrate. Before the calculations are done, it should be clear that the curves will have exactly the same shape. Both variables occur only in the numerator of the exponential term in equation 6.1. Conversion was calculated for a range of likely surface areas and the resulting curve is presented in Figure 6.2.

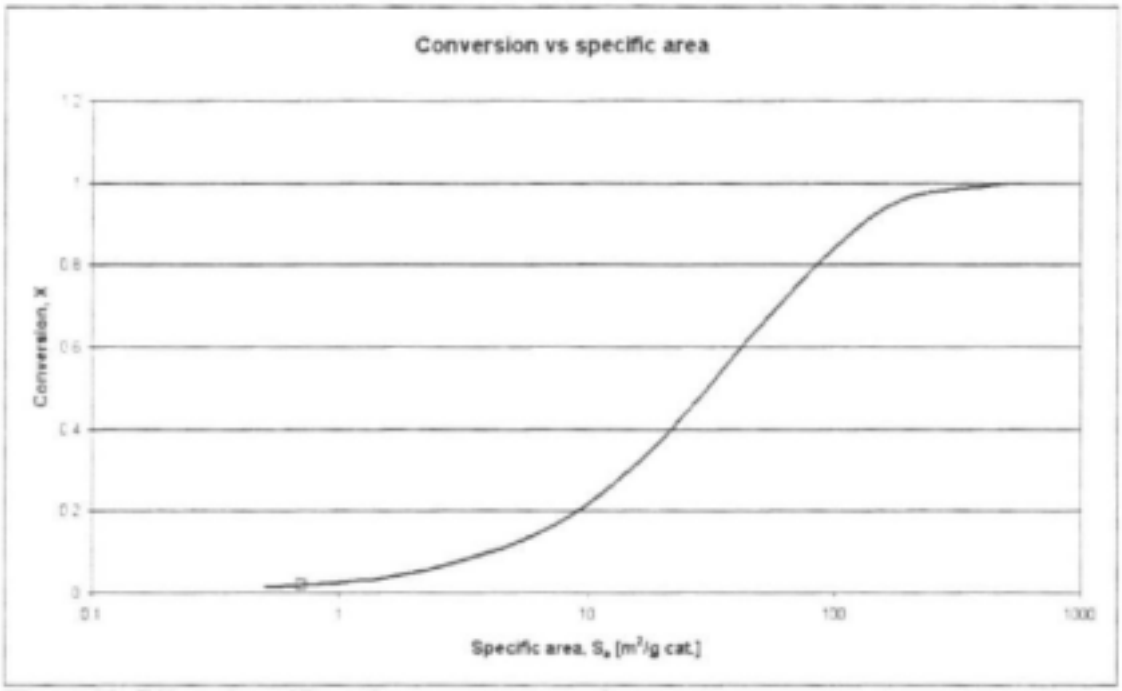


**Figure 6.2: Effect of specific surface area on conversion.**

The constants that were used for the determination of the curve are presented in Table 6.3. The conversion corresponding to the specific surface area as measured for the substrates used in the experimental work is indicated with a square. The same is observed in this case as compared to the effect of the reaction rate constant. The surface area is clearly insufficient to significantly reduce the phenol concentration, with hardly any conversion.

**Table 6.3: Constant values specific for other parameters (effect of specific surface area)**

| Parameter | Symbol | Value |
|---|---|---|
| Apparent rate constant | $k$ | $1 \times 10^{-9}$ [m/s] |
| Reactor length | $L$ | 10 [m] |
| Recycle ratio | $Y$ | 1 |
| Flow rate | $v_0$ | 186 [l/h] |

Again, some improvements are possible if the catalyst properties can be altered. The graph shows that a conversion of almost 90% can be attained if the surface area of the catalyst can be increased to 100 $m^2$/g cat. This is perhaps not unreasonable, since the specific surface area of industrial catalysts typically fall within this range. Once again, it must be stressed that a change in the substrate could increase the cost of the catalyst, eliminating any reduction in cost saved by effectively reducing the reactor size.

### Effect of recycle ratio

Equation 6.1 shows that the recycle ratio appears in most of the terms in the right-hand side of the equation. The same approach to determine the limiting conditions can be followed here. If the recycle ratio is very high ($Y \to \infty$) the conversion approaches some asymptotical value that seems to be dependant on the reaction rate constant. If none of the outlet stream is recycled ($Y = 0$) equation 6.1 reduces to

$$X = 1 - \exp\left\{-\frac{k^{''} A_s W \delta L}{v_0 (Y+1)}\right\} \qquad (6.2)$$

in which case the conversion is only dependant on the parameters discussed earlier in this section.

This can be clearly seen in graphical form in Figure 6.3 and Figure 6.4. The constant values substituted for the other parameters are presented in Table 6.4.

**Table 6.4: Constant values for other parameters (effect of recycle ratio)**

| Parameter | Symbol | Value |
|---|---|---|
| Apparent rate constant | $k$ | $1 \times 10^{-6}$ [m/s] |
| Specific surface area | $S_w$ | 0.7 [$m^2$/g cat.] |
| Recycle ratio | $Y$ | 1 |
| Flow rate | $v_p$ | 186 [$l$/h] |

Notice that the recycle ratio does not play such an important role on the conversions obtained for different reaction rate constants. In all of the cases, however, an increase in the recycle ratio decreases the overall conversion. This is undesirable, and therefore, the optimum value for the recycle ratio is zero. In chapter 5, the results show that the lowest cost can be obtained by maximising the recycle ratio. This contradicts the previous statement. The reason for this contradiction is the inherent assumptions made in both analyses.

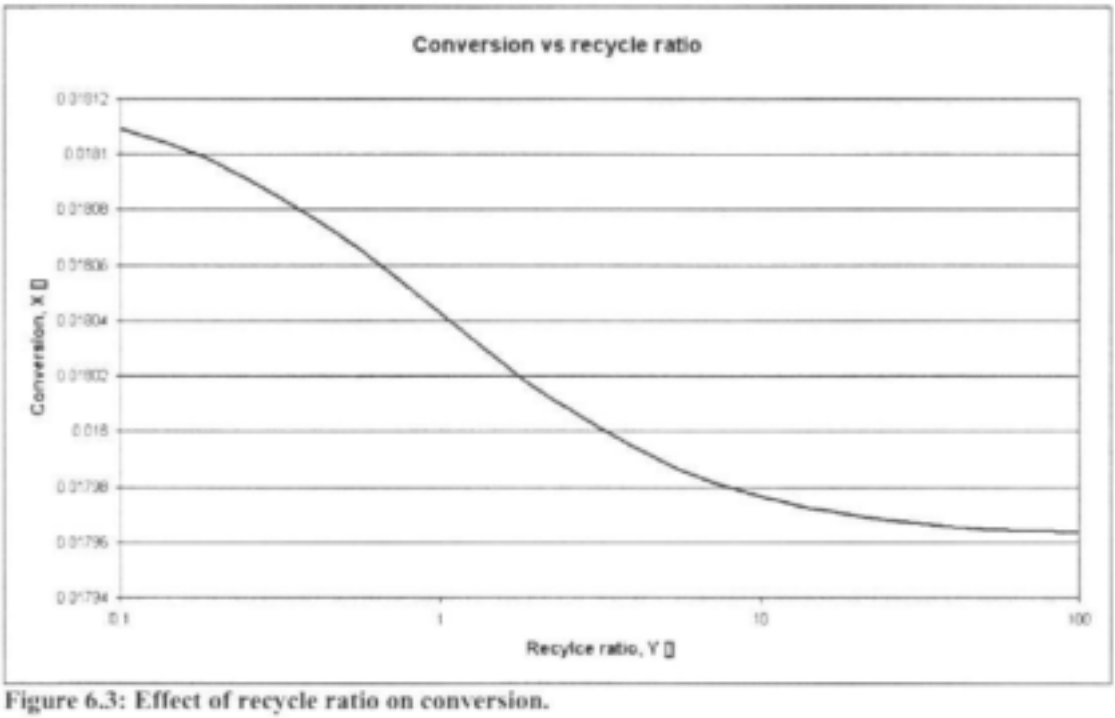


**Figure 6.3: Effect of recycle ratio on conversion.**

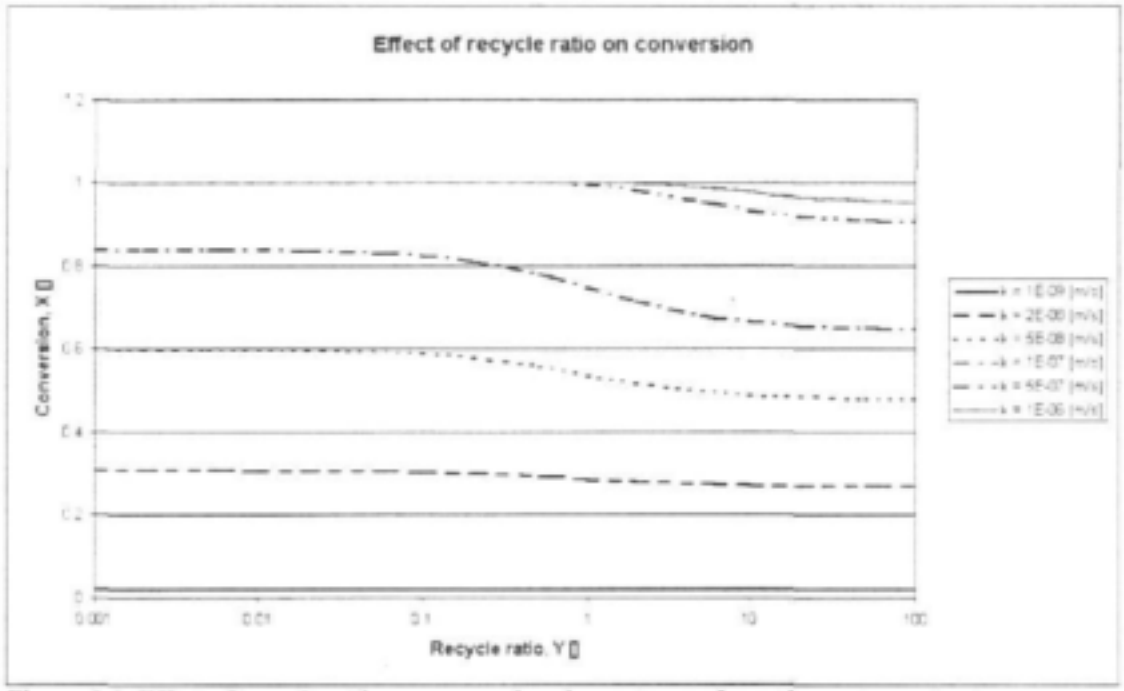


**Figure 6.4: Effect of recycle ratio on conversion: importance of reaction rate constant.**

In chapter 5, the rate constant increased as the recycle ratio increased (as observed in the experimental results, chapter 3). Therefore, the cost reduction gained by an increase in the recycle ratio and the associated reduction in reactor length decreased the overall cost of the reactor.

In this section, it was assumed that the current density was reduced when the recycle ratio increased (constant reaction rate constant) and in such a case an increase in the recycle ratio does not benefit the reaction rate and thus the conversion as in the previous case.

### 6.2.3 Mass transfer effects

Up to this point no information could be extracted from the experimental data to determine exactly what the rate-limiting step is. Therefore, a closer look was taken at the exact processes taking place in the reactor and which of these processes may pose restrictions on the reaction rate. This is reported on here.

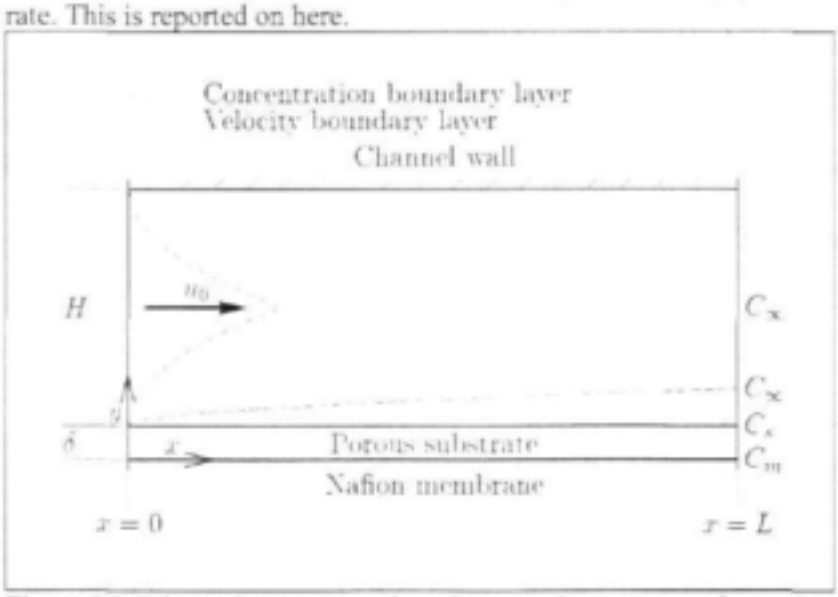


**Figure 6.5: Schematic representation of reactor for mass transfer study.**

A schematic representation of the flow in the reactor is shown in Figure 6.5. Normally, to determine the exact concentration profiles within the bulk flow and the substrate one needs to solve the differential form of the species balance. This equation takes the following form for some infinitesimally small volume element:

$$\frac{\partial C_A}{\partial t} + v_x \frac{\partial C_A}{\partial x} + v_y \frac{\partial C_A}{\partial y} + v_z \frac{\partial C_A}{\partial z} = D_e \left( \frac{\partial^2 C_A}{\partial x^2} + \frac{\partial^2 C_A}{\partial y^2} + \frac{\partial^2 C_A}{\partial z^2} \right) + R_A \qquad (6.3)$$

This expression cannot be solved analytically without simplification and generally computational techniques are employed to find a solution. The area of particular interest in this case is the catalyst substrate. A number of assumptions can be made to simplify equation 6.3. Since the reactor under consideration is a flow-through reactor, it is not unreasonable to assume that it is operating at steady-state. Therefore, the transient term in equation 6.3 can be set to zero:

$$\frac{\partial C_A}{\partial t} = 0 \qquad (6.4)$$

Since the element under consideration is inside the catalyst substrate, it is generally safe to assume that the primary means of mass transfer is due to diffusion. In such a case

$$v_x \approx 0 \qquad v_y \approx 0 \qquad v_z \approx 0 \qquad (6.5)$$

From the discussion in chapter 3, the apparent reaction rate constant was measured and found to be in the order of $1 \times 10^{-6}$ [m/s]. This implies that the rate of phenol removal is slow. In such a case, one may assume that the change in concentration in the $x$-direction is negligible compared to that in the $y$-direction. Also, if for the moment the concentration change in the $z$-direction is also assumed to be negligible compared to that in the $y$-direction, one may write

$$\frac{\partial^2 C_A}{\partial x^2} << \frac{\partial^2 C_A}{\partial y^2}$$

$$\text{and } \frac{\partial^2 C_A}{\partial z^2} << \frac{\partial^2 C_A}{\partial y^2} \qquad (6.6)$$

Taking these simplifications into account, the working form of the differential equation can be written as:

$$D_e \frac{d^2 C_A}{dy^2} + R_A = 0 \qquad (6.7)$$

The generation term, $R_A$, is present to account for any generation of species A per unit volume. In this case, the reaction takes place on the interface between the membrane and the substrate material. Therefore, the generation of species A can be specified as a boundary condition rather than accounting for it in the differential equation. Rewriting equation 6.7 and specifying the boundary conditions, yields:

$$D_e \frac{d^2 C_A}{dy^2} = 0 \qquad (6.8)$$

and boundary conditions:

$$C_{Ph} = C_{Ph,s} \text{ at } y = \delta$$

$$-D_e \left.\frac{dC_A}{dy}\right|_{y=0} = -k'' C_{Ph,m}$$

where $C_{Ph,s}$ refers to the phenol concentration on the surface of the substrate exposed to the bulk fluid flow and $C_{Ph,m}$ refers to the phenol concentration on the surface of the membrane. The negative sign in front of the term on the right-hand side implies that phenol is being removed at the membrane.

In all of the equations, the "effective diffusivity" is used instead of the binary diffusivity, $D_{AB}$ (where A refers to phenol and B to water). In catalysts, it is often observed that the apparent diffusivity is less than the binary diffusivity. This is due to the reduced area available normal to the mass flux of the species under consideration (phenol in this case). Fogler [33] defines the effective diffusivity as:

$$D_e = \frac{D_A \varepsilon_p \sigma}{\tau} \tag{6.9}$$

$\varepsilon_p$ is the substrate porosity
$\sigma$ is the constriction factor
$\tau$ is the tortuosity

and proposed typical values for the three properties. These values are 0.8 for the constriction factor, 3 for the tortuosity and 0.4 for the porosity. The minimum value for the tortuosity is 1 and the maximum value for the constriction factor and the porosity is 1. Therefore, note that the effective diffusivity is always less than or equal to the binary diffusivity.

Equation 6.8 can be readily solved to produce an expression for the concentration profile in the substrate. The detail of the derivation is given in section 0. The expression reads:

$$\frac{C_{Ph}(y)}{C_{Ph,s}} = \frac{1 + \frac{k''}{D_e} y}{1 + \frac{k''}{D_e} \delta} \tag{6.10}$$

This implies that the concentration profile in the substrate is a straight line that is only dependant on the surface concentration, reaction rate constant and effective diffusivity. The concentration at the surface can be found by letting $y = 0$:

$$C_{Ph,m} = \frac{C_{Ph,s}}{1 + \frac{k'' \delta}{D_e}} \tag{6.11}$$

The molar flux at the surface of the membrane can be written as:

$$N''_{Ph}(0) = -D_e \left.\frac{dC_A}{dy}\right|_{y=0} = -k'' C_m$$

$$= -\frac{k'' C_{A,s}}{1 + \frac{k'' \delta}{D_e}} \tag{6.12}$$

Two limiting conditions commonly observed in catalytic reactions can be investigated with the use of equation 6.12. The first is the case when the rate of diffusion to the surface is significantly faster than the rate of reaction, or

$$\frac{\delta k^{*}}{D_e} << 1 \tag{6.13}$$

in which case equation 6.12 becomes:

$$N^{*}_{Ph}(0) = -k^{*} C_{Ph,s} \tag{6.14}$$

This means that the rate of diffusion is so fast that the concentration at the surface of the membrane is the same as the concentration at the surface of the substrate.

On the other hand, if the surface reaction is significantly faster than the rate of mass transfer to the surface, or

$$\frac{\delta k^{*}}{D_e} >> 1 \tag{6.15}$$

then equation 6.12 becomes:

$$N^{*}_{Ph}(0) = -\frac{D_e C_{Ph,s}}{\delta} \tag{6.16}$$

which implies that the concentration at the membrane is zero (all phenol transported is combusted) and that the molar flux to the surface is only dependant on the effective diffusivity and surface concentration. This is a very important observation, because if one considers the measured apparent reaction rate constants, they correspond closely to the factor $\frac{D_e}{\delta}$ which, in this case, can be seen as a sort of an internal mass transfer coefficient. The two values are compared below in Table 6.5. The 'direction column' refers to the direction in which the calculation was made. This means that for the theoretical value, the diffusivity was approximated and the value of $k$ was calculated.

**Table 6.5: Practical vs theoretical reaction rate coefficients**

| | $D_e$ [m$^2$/s] | Direction | $k \equiv \frac{D_e}{\delta}$ [m/s] |
|---|---|---|---|
| Theoretical maximum | $9.415 \times 10^{-10}$ | → | $9.415 \times 10^{-7}$ |
| Practical (best) | $3.77 \times 10^{-9}$ | ← | $3.77 \times 10^{-6}$ |
| Practical (worst) | $4.87 \times 10^{-10}$ | ← | $4.87 \times 10^{-7}$ |

The values presented in Table 6.5 show that the measured values for the apparent reaction rate constant are very close to the internal mass transfer coefficient as discussed. This most likely implies that the limiting step of the reaction is internal diffusion in the substrate. The practical values shown in the table were based on the experimental values measured in the oxidation experiments, described in chapter 3.

In order for the external mass transfer to the substrate surface to be limiting, the measured mass transfer coefficient would, in the first place, be dependant only on the flow rate. Secondly, the measured coefficient would be close to the theoretical determined values for the mass transfer coefficients, as determined by the mass transfer correlation (equation A.46). In all of the cases the measured mass transfer coefficient is less than the theoretical mass transfer coefficient. In some cases this difference is greater than an order of magnitude (see chapter 3).

The difference between the experimentally measured values and the theoretical values as well as the dependency on the current density can be explained by the gas evolution side reaction as well as the water hydrolysis reaction. The formation of gas bubbles in the pores may clear the pores of liquid. Once a bubble escapes into the bulk flow, the void is replaced with fresh fluid, thereby increasing the effective mass transfer coefficient (section A.1.4).

The reduced mass transfer coefficient can be explained at the hand of the effective diffusivity. In the case where the additional mass transfer due to bubble formation is negligible, the internal mass transfer is dependant only on the effective diffusivity. The effective diffusivity is always less than the liquid phase binary diffusion as shown earlier in this section (equation 6.9). Typical values for the constriction factor and tortuosity (Fogler [33]) were used to calculate the effective diffusivity. These values, together with the effective diffusivity are presented in Table 6.6.

**Table 6.6: Typical values for the effective diffusivity**

| Quantity | Value |
|---|---|
| $D_{AB}$ | $9.415 \times 10^{-10}$ |
| $\sigma$ | 0.8 |
| $\tau$ | 3.0 |
| $\varepsilon_p$ | 0.45 |
| $D_e$ | $1.13 \times 10^{-10}$ |

Although the value for the effective diffusivity calculated in Table 6.6 is less than the worst value shown in Table 6.5, the effect of the mass transfer due to bubble formation must still be taken into account, thereby altering the mass transfer.

It is unlikely that the external mass transfer to the surface of the substrate is the limiting step since the calculated mass transfer coefficients must still be adjusted with the additional mass transfer due to the gas evolution. This would place the theoretical values (which lie in the $1 \times 10^{-6}$ range) up to one order of magnitude greater than the internal mass transfer coefficient.

The possibility exists that the surface reaction itself may be limiting. However, at this stage no experimental set-up can be constructed with which the surface reaction rate constant can be measured accurately. Reactions involving radical species generally tend to be rapid due to the reactivity of radical species and therefore it is not expected that the surface reaction is the limiting step. This is purely speculative, and experimental data need to be obtained before such an assumption can be verified.

## 6.3 Requirements for a Practical Application

The effect that a change in a specific parameter can have on the overall conversion in the reactor was discussed in section 6.2. Now the actual physical requirements of a successful system will be compared with what is believed by the author to be physically attainable.

### 6.3.1 Reactor specifications

This section focuses on the capital cost associated with the reactor itself. The entire cost will not be evaluated because of the dependency of the reaction rate constant on the flow rate as well as the current density — two factors that influence the overall cost. The second reason can be justified if one considers Figure 5.4. Notice that the capital cost for the reactor is the main contributing factor to the overall cost of the reactor.

Thus, the capital cost for the reactor will be calculated for various flow rates and values of the different parameters. This analysis therefore assumes the following:

- The cost of the reactor, being the major factor, will have the greatest impact on the overall cost if it can be changed.
- The current density can be altered to such an extent that it compensates for any change in the reaction rate constant induced by a change in the flow rate (which the reaction rate constant is also dependant on).
- The analysis will be based on an overall conversion of 99%.
- The effect of the recycle ratio will not be taken into account. This is based on the discussion in shown in section 6.2.2 that showed that the optimum value for the recycle ratio is zero.
- The capital cost of the reactor is only dependant on the length of the reactor and the flow rate

The final assumption above needs to be clarified somewhat. It should be apparent that the cost of the reactor will be dependent on the length of the reactor alone. The cost analysis in chapter 5 was based on a fixed-width reactor (30 flow channels). In order to reduce the effect that an increase in flow rate will have on the pumping cost, a constant linear velocity in the flow channels will be maintained. This will require the width of the reactor to change, which in turn influence the size of the catalyst substrate (and hence the cost).

The estimated capital costs for various recycle ratios were calculated based on a flow rate of 100 *l*/h. The results are presented in Figure 6.6. Note that the label on the *x*-axis refers only to a "transfer coefficient". The reason for this is the lack of information about the exact limiting process at the specific value. It merely reflects the required value of the coefficient for the limiting process.

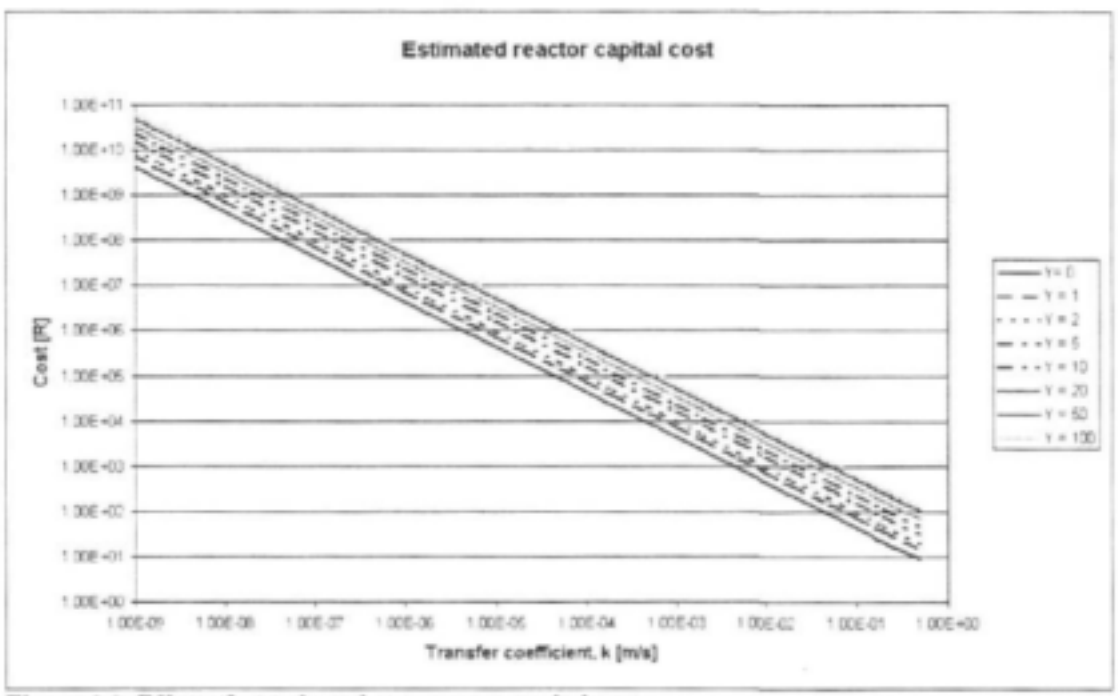


**Figure 6.6: Effect of recycle ratio on reactor capital cost.**

Notice that the lowest cost is obtained for no recycle. Increasing the recycle ratio effectively increases the flow rate through the reactor. In order to maintain a linear velocity of 2 m/s in the flow channels, the width of the reactor needs to be increased, thereby increasing the cost per unit length. This trend was observed for all product flow rates and therefore only the results corresponding to a recycle ratio of zero will be considered in the rest of the discussion.

The effect of an increase in the product flow rate on the cost was also investigated. The capital cost for the reactor was estimated for various product flow rates and the results are presented in Figure 6.7. As seen from the graph, an increase in the flow rate causes a proportional increase in the reactor cost. This is due to the necessary increase in the width of the reactor.

Typical values for the capital cost of water treatment plants were obtained. It was found that water treatment, on average, costs US$ 0.5 per cubic meter per day for municipal water treatment plants and US$ 1.5 per cubic meter per day for water treatment plants utilising ozone [34, 35, 36]. For the flow rates chosen in this analysis, the typical capital cost of these plants would range from about R 10 to R2 000. These values may seem unrealistic, but this reflects the low cost for the already well-established conventional water treatment methods. As a conservative estimate for the rest of this analysis a base capital cost for a water treatment plant was chosen as R 10 000 for a flow rate of 100 *l*/h.

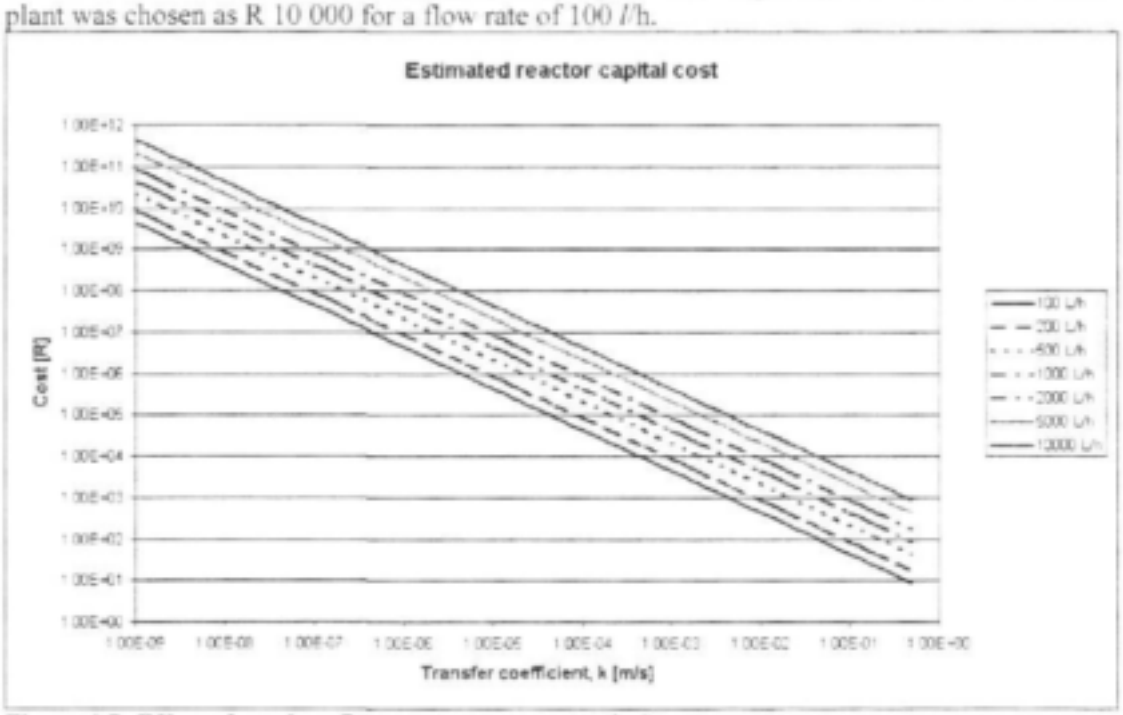


**Figure 6.7: Effect of product flow rate on reactor capital cost.**

Figure 6.7 shows that for a reactor cost in the order of R 10 000, the transfer coefficient must be between $5 \times 10^{-4}$ and $5 \times 10^{-2}$ [m/s]. Assuming that the effective diffusivity cannot be altered significantly, these values require the values of $\delta$ to be 1.88 $\mu$m and 18.83 nm respectively.

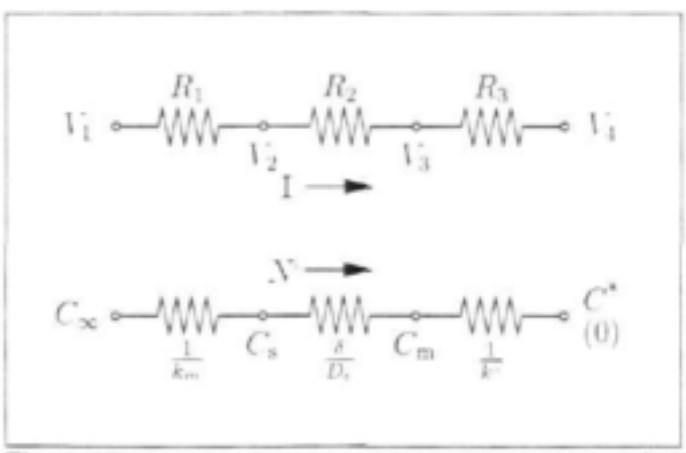


**Figure 6.8: Analogy of mass transfer resistance to electrical systems**

At this point, consider Figure 6.8, representing the analogy between electrical circuits and the main processes in the reactor. These processes, from left to right, are:

- External mass transfer
- Internal mass transfer
- Surface reaction

For an electrical circuit, the total resistance to the electrical current, $I$, between point $V_1$ and $V_4$ is:

$$R_T = R_1 + R_2 + R_3 \tag{6.17}$$

In the case of the mass transfer in the reactor, the mass transfer coefficient is equivalent to conductivity in the electrical system. By definition, the conductivity is the reciprocal of resistance and therefore the overall resistance to mass transfer can be approximated by

$$\frac{1}{k_{apparent}} = \frac{1}{k_m} + \frac{\delta}{D_e} + \frac{1}{k''} \tag{6.18}$$

Values have been estimated for the first two terms of equation 6.18 earlier in this chapter. However, the experimental data did not give any information regarding the actual surface reaction rate constant. Murphy et al. [28] performed a set of experiments under ideal conditions using sulphuric acid as supporting electrolyte. In the experiments they measured the reaction rate constants for a cocktail of cyclic organic molecules, which included phenol. They reported typical reaction rate constants in the order of $1 \times 10^{-4}$ [m/s]. This can be taken as a practical upper limit for the reaction rate constant. Thus, the typically observed values for the various mass transfer resistances are summarised below:

**Table 6.7: Typical values for the resistance to mass transfer in the reactor**

| Process | Resistance [s/m] |
|---|---|
| External mass transfer | $10^{-6}$ |
| Internal mass transfer | $10^{-7}$ |
| Surface reaction | $10^{-4}$ |

Table 6.7 shows that the main factor contributing to the overall resistance to mass transfer is the internal mass transfer. The other two processes only contribute 9.2% to the overall resistance. According to the previous analysis, the overall resistance must be less than $\frac{1}{5\times10^{-4}} = 2000$.

Suppose that the resistance corresponding to the internal mass transfer can in some way be decreased to this value. This still leaves the overall resistance at $1 \times 10^{6} + 2\,000 + 1 \times 10^{4} = 1\,012\,000$. The reason for this is that even though an improvement has been made in the coefficient for one of the steps, one of the other steps now becomes the limiting step. In this case, external mass transfer now limits overall mass transfer.

Therefore, all three steps need to be improved up to the point where the sum of their resistances equal 2 000. Thus, on average, each resistance must equal 666.7 or, in terms of the coefficients, $1 \times 10^{-3}$ [m/s]. Considering that the reaction rate constant, according to the literature, can only be in the order of $1 \times 10^{-5}$ [m/s], the type of improvement that is required to make the process work is impossible with present technology.

### 6.3.2 Reactor capability

The following table summarises the maximum expected improvements in the various parameters.

**Table 6.8: Expected improvements in the various parameter values**

| Parameter | Unit | Old value | New value |
|---|---|---|---|
| Effective diffusivity, $D_e$ | [m²/s] | $1.13 \times 10^{-10}$ | $2.5 \times 10^{-10}$ |
| Substrate thickness, $\delta$ | [m] | 0.001 | 0.0002 |
| Linear velocity, $u$ | [m/s] | 2.0 | 3.0 |
| Internal mass transfer coefficient | [m/s] | $1.13 \times 10^{-7}$ | $1.25 \times 10^{-6}$ |
| External mass transfer coefficient | [m/s] | $1.95 \times 10^{-7}$ | $2.39 \times 10^{-7}$ |

Thus, it can be seen that even with the expected improvements, the external mass transfer is predicted to become the limiting factor. The transfer coefficient of $2.39 \times 10^{-7}$ corresponds with a reactor cost of R 18.1m for a flow rate of only 100 ℓ/h. An increase of the product flow rate to 1000 ℓ/h increases the capital cost of the reactor to R 181m. This is unacceptable and therefore it can be said that even with the expected improvements in the various parameters, the reactor system will still cost far more than existing water treatment methods. For interest sake, if the conversion in the reactor was reduced to 75%, the reactor length reduces to 25 500 m (R 2.99m).

The previous analysis was based on several assumptions that may not be entirely accurate. However, the analysis was done to obtain an order of magnitude estimate of the required and current values of the various parameters. This has been done and it has been shown that far greater improvements than physically possible must be achieved before the reactor cost becomes reasonable.

## 6.4 Conclusions

The following conclusions can be drawn from the results obtained in this chapter:

- The sensitivity analysis showed the dependency of the conversion on the various parameters in the initial model. However, a more fundamental approach to determining the rate-limiting step in the reactor showed that the internal mass transfer from the bulk flow to the surface of the membrane is likely to be the limiting step.
- The consideration of possible improvements in the important parameters of the reactor performance showed that with possible improvements, the achieved improvement will not even approach the required improvement in the reactor cost. A small reactor (delivering only 100 ℓ/h of clean water, 99% removal) will still cost R 18.1 million. Therefore, it can be said that the technology is too expensive compared to other treatment options.

# 7 Overall Conclusions and Recommendations

## 7.1 Conclusions

The following conclusions can be drawn from this study:

- The SPE reactor system is only partially successful in removing organic content from waste water. It does however, completely destroy all living organisms present in the samples.
- Due to the complex interactions in the reactor system, the experimental data cannot give any indication as to what the limiting process is. A theoretical evaluation of the system described indicated that internal mass transfer was the limiting factor regarding the reaction rate.
- Despite the higher current efficiencies observed under potentiostatic control, it was found that galvanostatic control, due to the much higher rate of charge transfer, is the better choice for the mode of operation of the reactor. Reductions in the length of the reactor of up to an order of magnitude can be obtained.
- The reactor system, using the current catalyst and reactor set-up, is not economically viable for treating contaminated water due to the high costs of materials and operation.
- The required length for the reactor can be reduced by up to an order of a magnitude when treating waste streams that are contaminated with micro-organisms.
- Titanium must be used for the current collectors. The nickel-plated current collectors showed corrosion, even after the first run. Although nickel may be cheaper initially, maintenance will need to be done more frequently. The presence of nickel ions in the effluent is also undesirable.
- The HPLC analytical method that was developed can be accurately used in the quantitative detection of phenol and its breakdown products. However, there is still a large amount of information that needs to be obtained regarding the exact breakdown products. Only a few of these products have been identified to date. An unidentified peak was observed in the HPLC analysis of aliphatic acids, and may represent some of the as yet unidentified breakdown products.
- The present system is uneconomical compared to other water purification technologies. Also, the projected improvements required in the various properties of the reactor, such as catalyst substrate, reaction rate constant and mass transfer coefficients are not physically possible. For example, the rate of the limiting step in the process needs to be improved from the current value of approximately $1.1 \times 10^{-7}$ [m/s] to at least $5 \times 10^{-4}$ [m/s].

## 7.2 Recommendations

The following recommendations are made for future research in this field of research:

- High overpotentials are observed for the electrode reactions. One of the main reasons for the high overpotential may be the contacting provided between the electrode and the membrane. If the catalyst and membrane can be combined into one unit, two contacting surfaces would be removed.
- It is not possible to identify and quantitatively analyse all of the intermediates. Accurate measurement of the oxygen generated in the reaction will however give an indication of the extent of the reaction. Measurement of carbon dioxide will indicate the extent of the full reaction. If reliable methods can be obtained to measure the concentrations of these gases, more accurate assumptions can be made about the mechanisms involved. Hence such methods should be investigated.

- When considering future work, the results in chapter 6 should be taken into account. These results show what type of improvements are necessary before this type of technology would be economically feasible.

**References**


1. Droste, R.L. *Theory and practice of water and wastewater treatment.* John Wiley & Sons, Inc., 1997.
2. Comninellis, Ch. Electrocatalysis in the conversion/combustion of organic pollutants for waste water treatment. *Electrochim. Acta*, **39**:1857 – 1862, 1994.
3. Fòti, G., Didier, G., Comninellis, Ch., Perret, A. and Haenni, W. Oxidation of organics by intermediates of water discharge in $IrO_2$ and synthetic diamond anodes. *Electrochemical and Solid State Letters*, **2**:228 – 230, 1999.
4. Stucki, S., Kötz, R., Carcer, B., and Suter, W. Electrochemical waste water treatment using high overvoltage anodes. Part II: Anode performance and applications. *J. Appl. Electrochem.*, **21**:99 – 104, 1991.
5. Comninellis, Ch. and Pulgarin, C. Electrochemical oxidation of phenol for wastewater treatment using $SnO_2$ anodes. *J. Appl. Electrochem.*, **23**:108 – 112, 1993.
6. Petrov, K.M., Kaba, L.M., Srinivasan, S. and Appleby, A.J. Water post-treatment without expendables — proton exchange membrane based electrolysis system. *J. Hydrogen Energy*, **18**:377 – 382, 1993.
7. Comninellis, Ch. Electrochemical oxidation of organic pollutants for wastewater treatment. In C.A.C. Sequira, editor, *Environmental oriented electrochemistry*, Amsterdam, Elsevier, 1994.
8. Polcaro, A.M., Palmas, S., Renoldi, F. and Mascia, M. On the performance of $Ti/SnO_2$ and $Ti/PbO_2$ anodes in electrochemical degradation of 2-chlorophenol for wastewater treatment. *J. Appl. Electrochem.*, **29**:147 – 151, 1999.
9. Kötz, R., Stucki, S. and Carcer, B. Electrochemical waste water treatment using high overvoltage anodes. Part I: Physical and electrochemical properties of $SnO_2$ anodes. *J. Appl. Electrochem.*, **21**:14 – 20, 1991.
10. Kirk, D.W., Sharifian, H. and Foulkes, F.R. Anodic oxidation of aniline for waste water treatment. *J. Appl. Electrochem.*, **15**:285 – 292, 1985.
11. Sharifian, H. and Kirk, D.W. Electrochemical oxidation of phenol. *J. Electrochem. Soc.*, **133**:921 – 924, 1986.
12. Tahar, N.B. and Savall, A. Mechanistic aspects of phenol electrochemical degradation by oxidation on a $Ta/PbO_2$ anode. *J. Electrochem. Soc.*, **145**:3427 – 3434, 1998.
13. Grimm, J. *Electrochemical purification of hazardous organic compounds from wastewater by means of novel electrode materials and a solid-polymer-electrolyte-reactor system.* PhD thesis, University of Stellenbosch, South Africa, 1999.
14. Fang, G., Liu, Z., Zhang, Z., Hu, Y., Ashur, I.A. and Yao, K.L. Preparation of $SnO_2$–CuO nanocrystalline powders in two different ways by the sol–gel method. *Phys. Stat. Sol. A*, **156**:15 – 22, 1996.
15. Casey, V. and Stephenson, M.I. A study of undoped and molybdenum doped, polycrystalline, tin oxide thin films produced by a simple reactive evaporation technique. *J. Phys. D: Appl. Phys.*, **23**:1212 – 1215, 1990.
16. Gouvea, D., Varela, J.-A., Longo, E., Smith, A. and Bonnet, J.-P. Chemical synthesis of homogenous $SnO_2$ powders doped with manganese. *Eur. J. Solid State Inorg. Chem.*, **30**:915 – 927, 1993.
17. Correa-Lozano, B., Comninellis, Ch. and De Battisti, A. Physicochemical properties of $Ti/SnO_2$-$Sb_2O_5$ films prepared by the spray pyrolysis technique. *J. Electrochem. Soc.*, **143**:203 – 209, 1996.
18. Baker, P.G.L. *Sol–gel preparation, characterisation and electrochemistry of mixed metal tin oxide electrodes.* PhD thesis, University of Stellenbosch, South Africa, to be submitted, 2004.
19. Comninellis, Ch. and Nerini, A. Anodic oxidation of phenol in the presence of NaCl for wastewater treatment. *J. Appl. Electrochem.*, **25**:23 – 28, 1995.
20. Duprez, D., Delanoë, F., Barbier Jr, B., Isnard, P. and Blanchard, G. Catalytic oxidation of organic compounds in aqueous media. *Catalysis Today*, **29**:317 – 322, 1996.

21. Comninellis, Ch. and De Battisti, A. Electrocatalysis in anodic oxidation of organics with simultaneous oxygen evolution. *J. Chim. Phys.*, **93**:673 – 679, 1996.
22. Gattrell, M. and Kirk, D.W. A Fourier transform infrared spectroscopy study of the passive film produced during aqueous acidic phenol electro-oxidation. *J. Electrochem. Soc.*, **139**:2736 – 2744, 1992.
23. Gattrell, M. and Kirk, D.W. A study of the oxidation of phenol at platinum and preoxidized platinum surfaces. *J. Electrochem. Soc.*, **140**:903 – 911, 1993.
24. Valendo, A. Ya, Norikov, Yu. D. and Blyumberg, E.A. *Neftekhimiya*, **9**:866, 1969.
25. Gattrell, M. and Kirk, D.W. A study of the oxidation of phenol at platinum and preoxidized platinum surfaces. *J. Electrochem. Soc.*, **140**:1534 – 1540, 1993.
26. Koile, R.C. and Johnson, D.C. *Anal. Chem.*, **51**:741, 1979.
27. Comninellis, Ch. Electrochemical treatment of wastewater containing organic pollutants. In E.E. Eckenfelder, A.R. Bowers, and J.A. Roth, editors, *Proceedings of the 3rd International Symposium on Chemical Oxidation, Chemical Oxidation: Technology for the Nineties*. Technomic Publishing, 1994.
28. Murphy, O.J., Hitchens, G.D., Kaba, L. and Verostko, C.E. Direct electrochemical oxidation of organics for wastewater treatment. *Wat. Res.*, **26**:443 – 451, 1992.
29. Sax, N.I. *Dangerous Properties of Industrial Materials*. Van Nostrand Reinhold Company Inc., 6th edition, 1984.
30. Wendt, H. and Kreysa, G. *Electrochemical engineering – science and technology in chemical and other industries*. Springer-Verlag, Berlin, Heidelberg, 1999.
31. http://www.obf.on.ca/watertest2002.htm.
32. http://www.nature.ca/rideau/c/c2.e.htm.
33. Fogler, H.S. *Elements of chemical reaction engineering*. Prentice-Hall, 2nd edition, 1992.
34. http://www.city.kamloops.bc.ca/water/treatment/wtp_faqs.html.
35. http://www.sannet.gov/water/cip/miramar.shtml.
36. http://www.signonsandiego.com/news/metro/20021115_999_2m15nosalt.html.
37. Pickett, D.J. *Electrochemical reactor design*. Elsevier Scientific Publishing Company, Amsterdam, 2nd edition, 1979.
38. Kortüm, G. *Treatise on Electrochemistry*. Elsevier, Amsterdam, 2nd edition, 1965.
39. Fahidy, T.Z. *Principles of Electrochemical Reactor Analysis*. Elsevier, 1985.
40. Vicent, F., Morallón, E., Quijada, C., Vázquez, J.L. and Aldaz, A. Characterization and stability of doped $SnO_2$ anodes. *J. Appl. Electrochem.*, **28**:607 – 612, 1998.
41. Correa-Lozano, B., Comninellis, Ch. and De Battisti, A. Preparation of $SnO_2$-$Sb_2O_5$ films by the spray pyrolysis technique. *J. Appl. Electrochem.*, **26**:83 – 89, 1996.
42. Correa-Lozano, B., Comninellis, Ch. and De Battisti, A. Electrochemical properties of Ti/$SnO_2$-$Sb_2O_5$ electrodes prepared by the spray pyrolysis technique. *J. Appl. Electrochem.*, **26**:683 – 688, 1996.
43. Burke, L.D. and Murphy, O.J. Surface area – voltammetric charge correlation for $RuO_2$/$TiO_2$-based anodes. *J. Electroanal. Chem.*, **112**:39 – 50, 1980.
44. Comninellis, Ch. and Vercesi, G.P. Problems in DSA coating deposition by thermal decomposition. *J. Appl. Electrochem.*, **21**:136 – 142, 1991.
45. Park, S. and Mackenzie, J.D. Sol-gel-derived tin oxide thin films. *Thin Solid Films*, **258**:268 – 273, 1995.
46. Hench, L.L. and West, J.K. The sol-gel process. *Chem. Rev.*, **90**:33 – 72, 1990.
47. Lu, F., Chen, S. and Peng, S. Ultrafine $SnO_2$ prepared by supercritical fluid drying technique (SCFDT) for gas sensors. *Catalysis Today*, **30**:183 – 188, 1996.
48. Ward, D.A. and Ko, E.I. Preparing catalytic materials by the sol-gel method. *Ind. Eng. Chem. Res.*, **34**:421 – 433, 1995.
49. Maddalena, A., Dal Maschio, R., Diré, S. and Raccanelli, A. Electrical conductivity of tin oxide films prepared by the sol–gel method. *J. Non-Cryst. Solids*, **121**:365 – 369, 1990.
50. Chatelon, J.P., Terrier, C., Bernstein, E., Berjoan, R. and Roger, J.A. Morphology of $SnO_2$ thin films obtained by the sol – gel technique. *Thin Solid Films*, **247**:162 – 168, 1994.

51. Terrier, C., Chatelon, J.P., Berjoan, R. and Roger, J.A. Sb-doped $SnO_2$ transparent conducting oxide from the sol–gel dip–coating technique. *Thin Solid Films*, **263**:37 – 41, 1995.
52. Grimm, J., Bessarabov, D., Maier, W., Storck, S. and Sanderson, R.D. Sol – gel film – preparation of novel electrodes for the electrocatalytic oxidation of organic pollutants in water. *Desalination*, **115**:295 – 302, 1998.
53. Fang, G., Liu, Z., Zhang, Z., et al. Preparation of $ZrO_2$-$SnO_2$ thin films by the sol-gel technique and their gas sensitivity. *Phys. Stat. Sol. A*, **156**:81 – 85, 1996.
54. Qadri, S.B., Kim, H., Khan, H.R., Skelton, E.F., et al. Transparent conducting films of $In_2O_3$-$ZrO_2$, $SnO_2$-$ZrO_2$ and ZnO-$ZrO_2$. *Thin Solid Films*, **377-378**:750 – 754, 2000.
55. Yu, J.J. and Boyd, I.W. XRD and electrical characterization of photo-CVD zirconium oxide layers. *Applied Surface Science*, **208-209**:374 – 377, 2003.
56. Fortuny, A., Bengoa, C., Font, J. and Fabregat, A. Bimetallic catalysts for continuous catalytic wet air oxidation of phenol. *Journal of Hazardous Materials* 181 – 193, 1999.
57. Sauti, G. and McLachlan, D.S. AC conductivity based microstructural characterization of Ytria stabilized zirconia. *Mat. Res. Soc.Symp. Proc.* **699**:69 – 74, 2002.
58. Mizsei, J., Pirttiaho, L., Karppinen, M. and Lanto, V. Nanocatalyst sensitisers by agglomeration of nanfilms. *Sensors and Actuators B* **65**:195 – 198, 2000.
59. Ratcheva, T., Stambolova, I. and Konstantinov, K. *Sensors and Actuators B*, **21**:199 – 204, 1994.
60. Zhou, R., Yu, T., Jiang, X., Chen, F., and Zheng, X. Temperature programmed reduction and desorption studies of $CuO/ZrO_2$ catalysts. *Applied Surface Science*, **148**:263 – 270, 1999.
61. Shah, R.K. and London, A.L. *Laminar flow forced convection in ducts*. Academic Press, 1978.
62. Economic indicators. *Chemical Engineering*, **109**:122, 2002.
63. Perry, R.H. and Green, D.W. *Perry's chemical engineers' handbook*. McGraw-Hill, 7th edition, 1997.
64. Water quality — Determination of phenol index — 4-Aminoantipyrine spectrometric methods after distillation, SABS SM 211:1992. (equivalent to ISO 6439:1990).

# A Additional Theory and Literature

Some of the theory required for the understanding of the technical aspects of the report were deemed as too detailed for the main body of the report. The information does however need to be added to support some of the assumptions and derivations made. Therefore, the additional theory and literature excluded from the main report is added here.

The first section (0) in the appendix address all of the theory pertaining to electrochemical reactors. This includes a general description of electrochemical reactors and a discussion of electrode processes and phenomena. Additional background regarding alternative catalyst preparation techniques, as well as a detail discussion of the sol–gel technique is provided in section A.2.

## A.1 Electrochemical Reactors

An electrochemical reactor is defined as any device in which chemical reactions occur directly due to the input of electrical energy [37]. A schematic representation of an electrochemical cell is given in Figure A.1. A typical electrochemical reactor consists of two electronic conductors or electrodes immersed in some conducting liquid, namely the electrolyte. The electrodes are connected externally to a d.c. power supply. When a suitable electro-motive force (emf) is applied, current flows in the external circuit and chemical reactions take place at each electrode. This process is termed electrolysis.

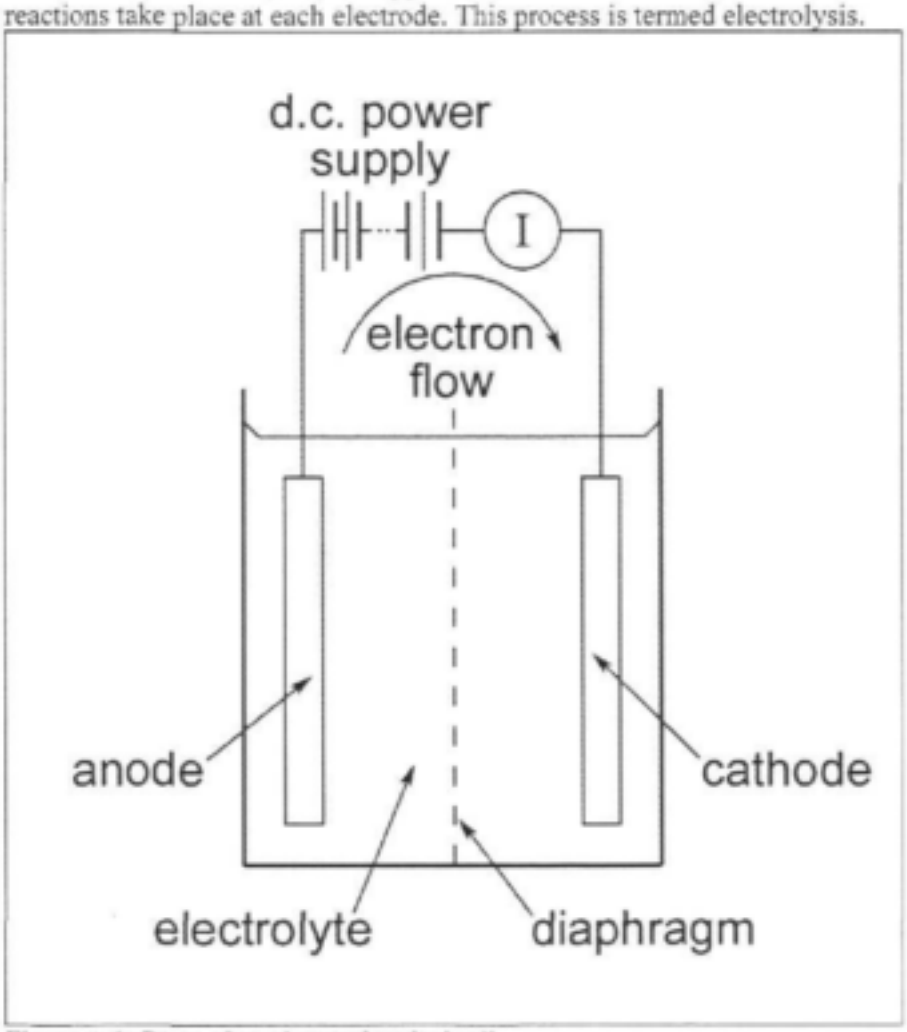


**Figure A.1: Parts of an electrochemical cell.**

Electrical conduction in the electrolyte is mainly due to the movement of charged species. The charged species or ions are made available from the chemical components — either by melting them or dissolving them in a suitable solvent, most commonly water. The application of a potential difference between the two electrodes causes the negatively charged species (anions) in solution to migrate towards the positive electrode (anode). Similarly, the positive ions (cations) move towards the negative electrode or cathode.

According to Pickett [37], the predominant factor in the movement of ions in an electrochemical cell can almost always be attributed to mass transfer. Since chemical reactions take place at the surfaces of the electrodes, concentration differences are caused between the bulk of the solution and the solution surrounding the electrode. This concentration difference then supplies the main driving force for the movement of the ions.

The discharge of ions at the electrodes results in chemical changes and causes electricity to flow in the external circuit. In this circuit, electrons flow from the anode to the cathode. In a chemical sense this implies that oxidation takes place at the anode and reduction at the cathode.

There are normally two different modes of operation for electrochemical cells. The mode of operation generally depends on the reactions taking place. Under galvanostatic operation, the cell is operated under constant current. In this case, the potential is adjusted in order to keep the applied current in the cell equal to the set value. In certain cases, especially where one or more side reactions take place, this may cause the selectivity to shift towards the unwanted side reaction. The advantage of this mode of operation is that the current density can be set to any required value.

Under potentiostatic operation, the electrochemical cell is operated under constant applied voltage. This mode of operation is sometimes necessary to force only some reactions to take place, for instance in the electrowinning of metals from a solution of several metal ions. This way, the metals can be extracted one at a time to obtain high purity metals. The disadvantage is that there is basically no control over the current — therefore, kinetically hindered reactions can give very low currents.

### A.1.1 Electrochemical Reaction Rates

In a homogenous redox reaction the electrons are directly transferred from a donor molecule to an acceptor molecule. This can be summarised by the following set of equations:

$$A + D \rightarrow A^{\nu_e^-} + D^{\nu_e^+} \tag{A.1}$$

$$D \rightarrow D^{\nu_e^+} + \nu_e e^- \tag{A.1a}$$

$$A + \nu_e e^- \rightarrow A^{\nu_e^-} \tag{A.1b}$$

In an electrochemical reaction however, the reactions are heterogeneous and occur at different sites (anode and cathode), and the electrons are transferred via the external circuit.

In equation (A.1) one can see that for one mole of product to form, a number of electrons equal to $\nu_e$ must be consumed. Faraday discovered two laws that relate the amount of product formed during electrolysis to the amount of electricity passed. These two laws can be expressed in the following statement [37] (p. 7):

The passage of 96487 coulombs through an electrochemical reactor produces in total one gram equivalent of products at an electrode.

This quantity can be calculated by taking the charge of one electron ($e_0 = 1.602 \times 10^{-19}$ C) and Avogadro's number ($N_A = 6.022 \times 10^{23}$ mol$^{-1}$) to give the charge of one mole of electrons (F = 96486.69 C/mol) — known as the Faraday. If only one reaction takes place at the electrode and the current is constant, the following simplified relationship gives the moles of product, $n$, formed in an electrochemical reaction applies:

$$n = \frac{Q}{\nu_e F} = \frac{It}{\nu_e F} \tag{2.14}$$

If the mass of product formed is required, equation 2.14 can be multiplied by the molar mass of the product to give:

$$m = \frac{M_R Q}{\nu_e F} = \frac{M_R \int I\mathrm{d}t}{\nu_e F} \tag{A.2}$$

Here, the term $Q$ is replaced with the integral of current over time. This is typically used if the current is not constant for the duration of the electrolysis.

According to Wendt and Kreysa [30], for the more general reaction scheme,

$$\nu_r \mathrm{R} + \nu_e e^- \rightarrow \nu_p \mathrm{P} \tag{A.3}$$

Faraday's law can be written as

$$m_p = \frac{\nu_p M_{R,p}}{\nu_e F} \int I\mathrm{d}t \tag{A.4}$$

with respect to the product, or with respect to the reactant:

$$m_r = \frac{\nu_r M_{R,r}}{\nu_e F} \int I\mathrm{d}t \tag{A.5}$$

The differential form of equation A.4 can be obtained by differentiation with respect to $t$:

$$\frac{\mathrm{d}n_p}{\mathrm{d}t} = \frac{\nu_p I}{\nu_e F} \tag{A.6}$$

Normally, for heterogeneous electrochemical reactions, the reaction rate is proportional to the surface area of the electrode, and therefore equation A.6 can be normalised,

$$\frac{1}{A_e}\frac{\mathrm{d}n_p}{\mathrm{d}t} = \frac{1}{A_e}\frac{\nu_p I}{\nu_e F} = \frac{\nu_p i}{\nu_e F} \tag{A.7}$$

where $i$ is the current density. In practical applications, conditions are rarely this simple. Often several reactions take place simultaneously at the same electrode. For instance, in the electrowinning of metals the following reactions may take place:

$$M^{n+} + ne^- \rightarrow M$$
$$2H^+ + 2e^- \rightarrow H_2 \qquad (A.8)$$

In such a case, each reaction's contribution to the overall current flowing through the external circuit is given by the specific reaction's current efficiency, $\varepsilon_j$. By definition, the sum of all the current efficiencies must be one:

$$\sum_j \varepsilon_j = 1 \qquad (A.9)$$

Using Faraday's law, the expression for an individual reaction can be determined as

$$\varepsilon_p = \frac{n_p \cdot \nu_e F}{\nu_p Q} \qquad (A.10)$$

with

$$Q = A_e \int_0^t i\,dt \qquad (A.11)$$

### A.1.2 Cell Potential

In the case of fuel cells, which are electrochemical reactors that produce electrical energy from chemical energy, some spontaneous reaction ($\Delta G < 0$) takes place at both electrodes and an electrical current is produced in the external circuit. In the case of electrolysers, the process is non-spontaneous, and an applied potential is required to force the reaction to take place. In this case the Gibbs free energy change is positive ($\Delta G > 0$). The applied potential is supplied by the external power supply and is termed the electro-motive force.

In order to quantify this emf, the approach as used by Pickett will be discussed [37] (p. 10). Consider a single reaction taking place at an electrode under constant temperature and pressure:

$$\nu_A A + \nu_B B \rightarrow \nu_C C + \nu_D D \qquad (A.12)$$

Since the reaction does not take place naturally, the free energy change, $\Delta G$, of the reaction is positive:

$$\Delta G = \nu_C \mu_C + \nu_D \mu_D - \nu_A \mu_A - \nu_B \mu_B \qquad (A.13)$$

where $\mu_A$, $\mu_B$, $\mu_C$ and $\mu_D$ are the chemical potentials for species A, B, C and D. The purpose of applying the external potential is to increase the free energies of A and B in order to reverse the sign of $\Delta G$.

According to convention, the applied voltage is given by

$$V = V_+ - V_- \qquad (A.14)$$

where $V_+$ and $V_-$ are the electrical potentials of the positive and negative terminals of the power source. If the potential drop due to the resistance in the external circuit is ignored, the

voltage can be separated into three potential drops — two that occur at the solution/electrode interface (to be discussed later) and the other due to resistance to ion transfer in the solution.

This is schematically represented in Figure A.2(a).

If this voltage is decreased until the solution potential drop becomes zero, this condition of zero current leaves the system in a state of equilibrium. The interfacial potentials are still present although they are reduced in magnitude. This voltage is known as the minimum electrolysing voltage or equilibrium cell potential, and is represented by Figure A.2(b). To determine this voltage, we rewrite equation A.12 to account for the electrons taking part in the separate electrode reactions:

$$\nu_c e_c + \nu_A A + \nu_B B \rightarrow \nu_c e_a + \nu_C C + \nu_D D \qquad (A.15)$$

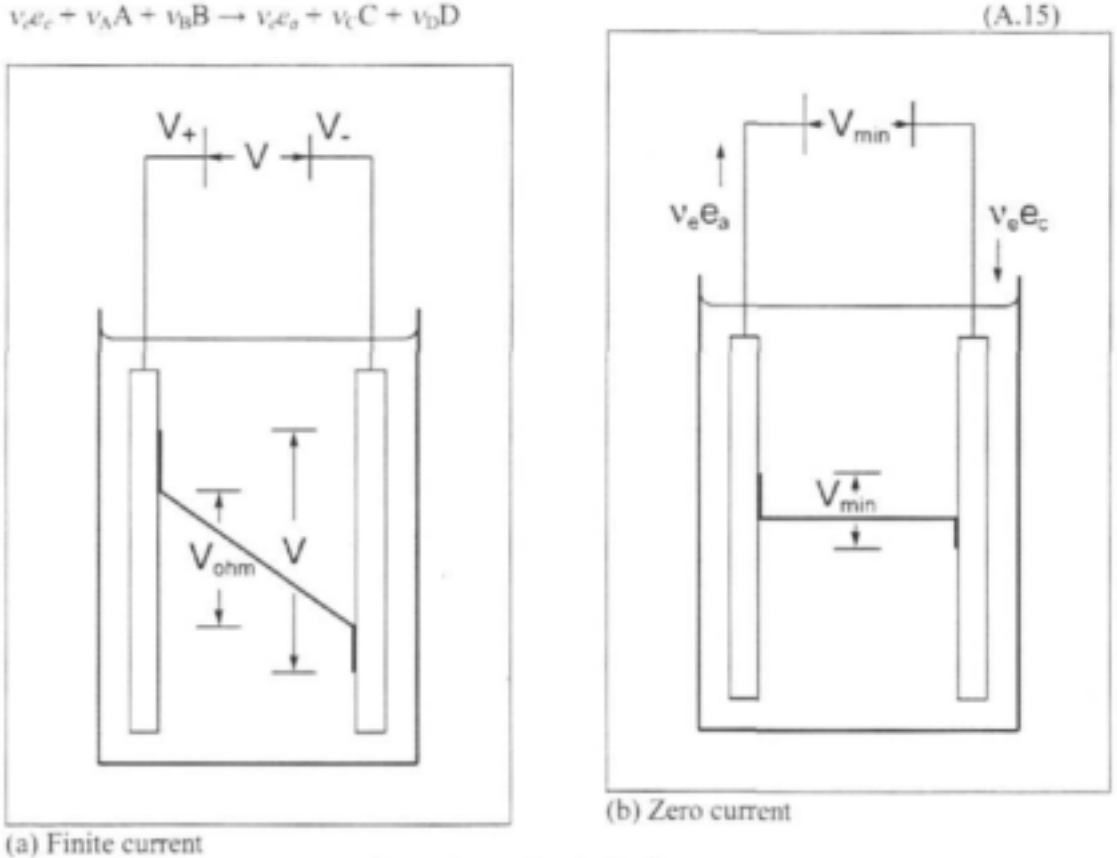


(a) Finite current

(b) Zero current

**Figure A.2. Voltage components in an electrochemical cell.**

($e_c$ and $e_a$ being the electrons involved in the cathodic and anodic half-reactions respectively).

Since the system is in equilibrium, the free energy is at a minimum and therefore

$$\nu_c \mu_{e_c} + \nu_A \mu_A + \nu_B \mu_B = \nu_c \mu_{e_a} + \nu_C \mu_C + \nu_D \mu_D \qquad (A.16)$$

Substitution of equation A.13 into equation A.16 then yields

$$\nu_e \left( \mu_{e_c} - \mu_{e_a} \right) = \Delta G \qquad (A.17)$$

At equilibrium, the chemical potential of an electron is equal to the chemical potential of an electron in the adjacent power supply terminal, thus

$$\mu_{e_c} = \mu_{e'}$$

And

$$\mu_{e_-} = \mu_{e^-} \tag{A.18}$$

According to Pickett [37], the difference between the chemical potentials of electrons in the two terminals can be given by

$$\mu_{e^-} - \mu_{e^-} = -F(V_- - V_-) \tag{A.19}$$

Substituting equation A.18 and equation A.19 into equation A.17, one can obtain an expression for the minimum electrolysing voltage, $V_{min}$:

$$\Delta G = \nu_e F(V_- - V_-)$$
$$\Delta G = \nu_e F V_{min} \tag{A.20}$$

or, in terms of $V_{min}$

$$V_{min} = \frac{\Delta G}{\nu_e F} \tag{A.21}$$

The Gibbs free energy of any chemical reaction depends on the reaction temperature, the concentrations of dissolved species and the partial pressures of the gaseous reactants. The equations derived here should only be used at standard temperature and pressure. Concentration-related activities and fugacities are derived from actual concentrations and partial pressures, as shown in the following set of equations [30]:

$$a_i = C_i \gamma_i \tag{A.22}$$
$$p_i^* = p_i f_i \tag{A.23}$$

These coefficients account for deviations from ideal behaviour, which is described by the two limiting equations and which, in turn describes chemical potentials at low concentrations and pressures

$$\mu_i = \mu_i^0 + RT \ln\left(\frac{p_i}{p^0}\right) \tag{A.24}$$

$$\mu_j = \mu_j^0 + RT \ln\left(\frac{C_j}{C^0}\right) \tag{A.25}$$

with $p^0$ being the standard fugacity (0.1 MPa) and $C^0$ being the standard activity (1 mol/dm$^3$). The reduced quantities $\frac{p}{p^0}$ and $\frac{C}{C^0}$ are used to make the logarithm dimensionless and are often omitted in the literature. For higher concentrations and pressures, the corrected equations read

$$\mu_i = \mu_i^0 + RT \ln(p_i f_i) \tag{A.26}$$
$$\mu_j = \mu_j^0 + RT \ln(C_j \gamma_j) \tag{A.27}$$

Substituting equations A.26 and A.27 into equations A.13 and A.20 and ignoring deviations from ideality, one obtains

$$V_{min} = \frac{\left\{\sum \nu_{i,j}\mu_{i,j} + RT\ln\left(\prod_{i,j} C_j^{\nu_j} p_i^{\nu_i}\right)\right\}}{\nu_e F} \qquad (A.28)$$

or, for the species A, B, C and D in equation A.13,

$$V_{min} = V_{min}^{0} - \frac{RT}{\nu_e F}\ln\frac{a_A^{\nu_A} a_B^{\nu_B}}{a_C^{\nu_C} a_D^{\nu_D}} \qquad (A.29)$$

where the activities are given by equation A.22 or equation A.23 depending on the phase of the reactants and products. Often it is assumed that the activity and fugacity coefficients are one, especially at low concentrations. It then follows that the concentrations and partial pressures can replace the activities.

Now that the minimum voltage required to run an electrochemical process has been defined, a brief discussion of the elements of practical voltage requirements will be given. The equilibrium voltage in a typical electrochemical cell is given by the relationship

$$V_{min} = V_a - (-V_c) \qquad (A.30)$$

During non-equilibrium operation, the potential drop due to the solution resistance becomes important. Also, the electrode potentials start to deviate from their respective equilibrium values. If the electrode processes were thermodynamically reversible, one would be able to pass a large current through the solution without these potentials varying notably. The solution drop would then be

$$V = V_{min} + V_{ohm} \qquad (A.31)$$

where $V_{ohm}$ is the solution potential drop. Such electrodes are referred to as "non-polarizable". Most practical electrodes exhibit polarisation and this deviation in potential is referred to as the overpotential. In such a case, the electrolysing voltage can be represented by

$$V = V_a^* - (-V_c^*) + V_{ohm} \qquad (A.32)$$

$V_a^*$ and $V_c^*$ are the non-equilibrium electrode potentials.

To obtain an expression for the practical voltage drop in the case of polarizable electrodes, equation A.30 is subtracted from equation A.32, giving

$$V = V_{min} + (V_a^* - V_a) - \{(-V_c^*) - (-V_c)\} + V_{ohm}$$
$$V = V_{min} + \eta_a - \eta_c + V_{ohm} \qquad (A.33)$$

where $\eta_a$ and $\eta_c$ are known as the anodic and cathodic overpotential. These values are defined as the difference between the electrode potential at non-equilibrium and equilibrium operation:

$$\eta_a = V_a^* - V_a \tag{A.34}$$

$$\eta_c = \left(-V_c^*\right) - \left(V_c\right) \tag{A.35}$$

According to convention, the cathodic overpotential is generally negative, but causes an increase in the total operating voltage. Therefore, equation (A.33) is often written as

$$V = V_{min} + \eta_a + \left|\eta_c\right| + V_{ohm} \tag{A.33a}$$

Many phenomena may be associated with the overpotential. Up to five different effects may cause this overpotential according to Kortüm [38]. The most important of these phenomena may be associated with the solution (concentration overpotential); and processes taking place at the actual site of the reaction on the electrode surface (activation overpotential).

Concentration overpotential is caused by the depletion or accumulation of species taking part in the reaction close to the surface of the electrode. The electrode is thus surrounded by a solution with a different concentration than that of the bulk solution, causing a shift in the potential away from the equilibrium value. Keeping the solution concentration as close as possible to the bulk concentration will thus reduce the overpotential. This is typically done by increasing the mass transfer from the bulk to the electrode surface by stirring or increased flow of the solution.

Activation potential on the other hand, arises due to the phenomena associated with the electrode reaction. In any electrochemical reaction electrons are transferred across the electrode interface to the reactant molecule. This normally takes place in a sequence of steps of which adsorption and desorption of the reactants, intermediates and products, surface diffusion and surface reactions are all a part. Only one of these steps is the rate-limiting step — it is this step that requires a certain input of energy, the activation energy, to take place. This step represents the state of maximum energy of the system and is necessarily higher than the original state of the system. Once the system has accumulated enough energy it proceeds to the final state of energy which is greater than the original state, but lower than the maximum. A portion of the original activation energy is thus lost and this irreversibility gives rise to the activation overpotential. This energy is lost at the expense of a higher potential.

### A.1.3 Electrode Kinetics

The rate of an electrochemical reaction

$$A + v_e e^- \Leftrightarrow B \tag{A.36}$$

has been shown in section A.1.1 to be determined by the applied current. Differentiation of equation 2.14 gives

$$r = -\frac{dn_j}{dt} = \frac{\varepsilon_j I}{v_e F} \qquad (j = A) \tag{A.37}$$

with $\varepsilon_j$ being the current efficiency for the considered reaction. As is convention, the rate can be normalised with respect to surface area, and current density can be used to represent the reaction rate:

$$-\frac{1}{A_e}\frac{dn_j}{dt} = \frac{1}{A_e}\frac{\varepsilon_j I}{v_e F} = \frac{\varepsilon_j i}{v_e F} \tag{A.7a}$$

According to Wendt [30] (p. 41), it is an experimental fact that if mass transfer limitations are eliminated, the rate of charge transfer varies exponentially with the overpotential. For reactions that have both a forward and a backward reaction, such as the one in equation A.36, both are changed in an opposite sense by the applied overpotential. Thus, according to the Butler-Volmer equation, one obtains the effective current density as the difference between the cathodic and anodic partial current densities:

$$i = i_0\left(\exp\left\{\frac{\alpha_a F\eta}{RT}\right\} - \exp\left\{\frac{-\alpha_c F\eta}{RT}\right\}\right) \tag{A.38}$$

where $i_0$ is called the "exchange current density" and basically equals the current that is exchanged back and forth between the two electrodes under equilibrium. $\alpha_a$ and $\alpha_c$ are the anodic and cathodic charge transfer coefficients and determine the response of the partial current densities towards a change in overpotential. The sum of these two charge transfer reactions must always equal the stoichiometric electrons, $\nu_e$, of the potential-determining electrode reaction, but even this only hold for conditions close to equilibrium.

If the overpotential is high enough for one of the reactions, equation A.38 can be simplified as follows:

$$i = i_0 \exp\left\{\frac{\alpha_a F\eta}{RT}\right\} \qquad \text{for} \qquad \frac{\alpha_a F\eta}{RT} >> 1 \tag{A.39}$$

or

$$i = i_0 \exp\left\{\frac{-\alpha_c F\eta}{RT}\right\} \qquad \text{for} \qquad \frac{-\alpha_c F\eta}{RT} >> 1 \tag{A.40}$$

Normally the Tafel equation is derived from these equations:

$$\eta = a + b\log i \tag{A.41}$$

with

$$a = -2.302\left(\frac{RT}{\alpha F}\right)\log i_0 \tag{A.42}$$

$$b = 2.302\left(\frac{RT}{\alpha F}\right) \tag{A.43}$$

with $b$ known as the Tafel slope. The graphical determination of these values is schematically represented in Figure A.3.

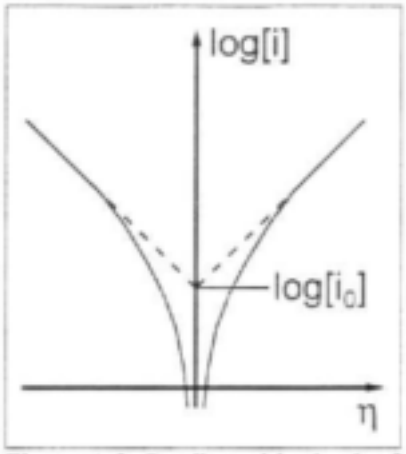


**Figure A.3: Semilogarithmic plot for determination of $i_0$ and the Tafel slope.**

For the system used in this study, the use of a membrane makes the system too complex to accurately derive values from the Tafel slope. The use of a membrane to separate the electrolyte in an electrochemical cell makes the system irreversible, and therefore conventional methods cannot always be used to accurately determine Tafel values in such a system. Also, due to all the breakdown products formed in the oxidation of phenol, the accuracy of the values will be suspect.

Often it is found that the value $i_0$ is dependent on the concentration of species in the reaction solution [30] (p. 49). Therefore $i_0$ can be expressed as a function of the concentration of different reactants and their respective reaction orders.

$$i_0 = i_0^0 \prod_i c_i^n \tag{A.44}$$

This approach is similar to that followed by Pickett [37] (p. 52), where the reaction rate can be directly related to current density and often assumed to have similar kinetics to chemical kinetic equations:

$$r = \frac{i}{v_e F} = kC^n \tag{A.45}$$

This methodology will also be assumed in this work, since very little information is available on the exact current-potential relationship. The derivation of the exact equation used in the reactor model is discussed in chapter 5.

### A.1.4 Electrode Mass Transfer Phenomena

In chapter 5, a simple model is derived that takes into account the reaction taking place at the membrane-electrode interface. This reaction is quantified in terms of a reaction rate constant that is determined from the experimental results in chapter 3. Generally, there are two desired types of limiting conditions in chemical reactors: mass-transfer limited and reaction rate limited operation.

In the experimental work, in order to determine which limiting condition prevails, one needs to have some idea of the mass transfer from the bulk of the solution in the flow channel to the surface of the electrode. Several mass transfer correlations exist in the literature that describes the mass transfer coefficient in dimensionless form (Sherwood number) for a variety of electrode configurations [39]. The mass transfer coefficient for a parallel plate electrode of finite width can be calculated from the following correlation [39] (p. 80):

$$\mathrm{Sh} = \frac{k_m d_e}{D} = 1.467\left(\frac{2}{1+\gamma}\right)^{1/3}\left(\mathrm{Re}\cdot\mathrm{Sc}\frac{d_e}{L}\right)^{1/3} \qquad \text{(A.46)}$$

This correlation can then be used to determine the coefficient for external mass transfer.

Another important process that often takes place at electrodes in aqueous solutions is gas evolution. According to Wendt and Kreysa [30] (p. 103), it has been proven that an additional mass transfer element is introduced due to bubble formation. The effective mass transfer is quantitatively described by the following equation:

$$k_m = \left(k_{m,\mathrm{macro}}^2 + k_{m,\mathrm{bubble}}^2\right)^{0.5} \qquad \text{(A.47)}$$

with the mass transfer element attributed to bubble formation given by

$$\frac{k_{m,\mathrm{bubble}}\cdot d_b}{D} = \frac{2.76}{C}(\mathrm{ReSc})^{0.5}(1-\Theta)^{0.5} \qquad \text{(A.48)}$$

where $\Theta$ is the degree of gas bubble coverage of the electrode and $d_b$ is the average bubble diameter. The Reynolds number as given in equation A.48 is proportional to the volumetric flow rate of gas evolution per unit electrode surface area, i.e.

$$\mathrm{Re} = \frac{\dot{V}_{\mathrm{surface}}\, d_b}{\nu} \qquad \text{(A.49)}$$

$C$ is a factor that accounts for the bubble shape. $C$ = 1.59 for hemispheres and $C$ = 2 for spheres.

### A.1.5 Analogy to Chemical Kinetics

As mentioned in section A.1.3, one can make the general assumption that an electrochemical reaction follows kinetics analogous to those observed in chemical reactors [37]. In such a case, the rate of the reaction is given by equation A.45.

$$r = \frac{i}{\nu_e F} = kC^n \qquad \text{(A.45)}$$

In order for this equation to be used in the final model of the process, values for the reaction rate constant, $k$, and the reaction order, $n$, must be obtained. A number of methods exist that can be used to obtain these values from concentration-time data.

A method that is often used in the extraction of the reaction order is the differential method of rate analysis, as described by Fogler [33]. For a given reaction

A → products

the rate law is given by

$$-r_A = kC_A^n \qquad \text{(A.50)}$$

For a constant-volume batch reactor, performing the appropriate mass balance and combining it with the rate law, one obtains

$$-\frac{dC_A}{dt} = kC_A^n \tag{A.51}$$

After taking the natural logarithms on each side of equation A.51, one obtains

$$\ln\left(-\frac{dC_A}{dt}\right) = \ln k + n \ln C_A \tag{A.52}$$

Notice that the slope of a plot of $\ln\left(-\frac{dC_A}{dt}\right)$ versus $\ln C_A$ is the reaction order. Therefore, the concentration-time data must be differentiated, either graphically or numerically. Graphical methods can be iterative and prone to error, and thus only the numerical methods will be discussed here.

The rate of change of the concentration-time data can be obtained in two ways. The first is the three-point differentiation formulae for equally spaced data points. For a set of data containing $N$ points:

| Time | $t_0$ | ... | $t_m$ | ... | $t_N$ |
|---|---|---|---|---|---|
| Concentration | $C_{A0}$ | ... | $C_{Am}$ | ... | $C_{AN}$ |

where $m$ is some intermediate value ($0 < m < N$). The formulae to determine the rate of change of the concentration at various points are:

$$\left(\frac{dC_A}{dt}\right)_{t_0} = \frac{-3C_{A0} + 4C_{A1} - C_{A2}}{2\Delta t} \tag{A.53}$$

$$\left(\frac{dC_A}{dt}\right)_{t_i} = \frac{C_{A,i+1} - C_{A,i-1}}{2\Delta t} \tag{A.54}$$

$$\left(\frac{dC_A}{dt}\right)_{t_N} = \frac{C_{A,N-2} - 4C_{A,N-1} + C_{AN}}{2\Delta t} \tag{A.55}$$

The other popular method used is to fit a polynomial expression through the data points:

$$C_{Ph} = a_0 + a_1 t + a_2 t^2 + \cdots + a_n t^n \tag{A.56}$$

and then finding appropriate values for the constants $a_i$. Once this has been done equation A.56 can be differentiated with respect to time

$$\frac{dC_{Ph}}{dt} = a_1 + 2a_2 t + 3a_3 t^2 \cdots + na_n t^{n-1} \tag{A.57}$$

and used to obtain the rate of change of the concentration at any time $t$. The logarithm of the rate of change of concentration can then be plotted against the logarithm of concentration. The slope of a straight line fitted through the data will give the order of the reaction.

Another method is to assume a value for the reaction order. The concentration-time data is then linearised according to the assumed reaction order and a straight line is fitted through this data. If the fit is statistically sound, the correct reaction order has been assumed. This method will be described shortly with reference to typical graphs that can be obtained for each reaction order. One rarely finds reaction orders higher than two and therefore the discussion will only be extended to reaction orders of two.

With this method, one does not have to have only constant-volume batch reactor data and the kinetic expression can be directly incorporated into the reactor model, thereby accounting for other possible effects playing a role in the reactor.

If one assumes 0-th order kinetics, equation A.51 can be written as

$$-\frac{dC_{Ph}}{dt} = k \tag{A.58}$$

integrating yields

$$C_{Ph} = kt + K \tag{A.59}$$

In this case, one would plot values of the concentration versus time, and fit a straight-line through the data points. If the straight line fits the data well in a statistical sense of the word, the order of the reaction is zero. The slope of this line is equal to the reaction rate constant, $k$. $K$ in equation A.59 equals the intercept of the straight line at time $t = 0$. This would correspond with a calculated value for the initial concentration $C_{Ph,0}$. The procedure for obtaining the parameter values for 0-th order kinetics is shown in Figure A.4(a).

The same can be done for first and second order kinetics. The quantity used for the $y$-axis and the integrated equations are summarised in Table A.1.

**Table A.1: Summary of method for determining reaction order**

| $x$-axis | $y$-axis | Slope | Intercept | Equation |
|---|---|---|---|---|
| $t$ | $C_A$ | $k$ | $C_{A0}$ | $C_A = C_{A0} - kt$ |
| $t$ | $\ln(C_A)$ | $k$ | $\ln(C_{A0})$ | $C_A = C_{A0}\exp(-kt)$ |
| $t$ | $\frac{1}{C_A}$ | $k$ | $\frac{1}{C_{A0}}$ | $C_A = \frac{C_{A0}}{1+C_{A0}kt}$ |

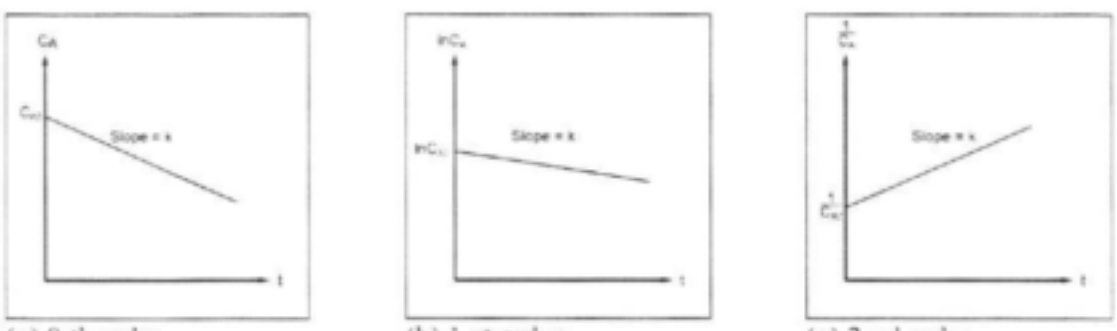


(a) 0-th order (b) 1-st order (c) 2-nd order

**Figure A.4: Determination of reaction rate constants for different reaction orders.**

If none of the plots based on these three reaction orders are statistically valid, some other effect is taking place in the reaction and a more sophisticated approach must be tried. Especially in the case of reactions on a catalytic surface, adsorption and desorption often influences the reaction kinetics.

## A.2 Electrode Preparation

In general, the preparation of the electrode involves the deposition of a metal oxide layer onto a substrate material. In most cases the substrate material used is titanium, because of its excellent resistance to corrosion. Another reason is that the metal oxide catalysts often lack the mechanical strength to be used as electrodes. Titanium therefore serves as the backbone for these types of electrodes. Titanium has been the substrate material most widely used and described in the literature [40].

Various methods have been developed for the formation of the oxide layer such as chemical vapour deposition, thermal decomposition, reactive sputtering, spray pyrolysis and the sol-gel technique. Since the sol-gel technique is employed for the preparation of the catalysts in this project, it is discussed in detail in section A.2.3, while short discussions of the other techniques are given in sections A.2.1 and A.2.2 as background.

### A.2.1 Spray Pyrolysis

With this technique [40, 9, 41, 17, 42], an appropriate solution is made with suitable precursors (exclusively inorganic salts) and solvents (typically ethanol). The solution is then sprayed through a nozzle from a fixed distance onto the pre-heated substrate. Typical temperatures of the substrate at this stage of catalyst preparation are about 400-700°C. This is sometimes followed by a heating period of about 10 minutes after which additional coatings of the solution are applied to the substrate. After all the necessary coatings are completed, a final heat treatment is applied in some cases. It appears that 550°C resulted in films with the best electrical conductivity.

### A.2.2 Thermal Decomposition

In this technique [43, 44], a paste or solution containing the desired ratios of precursor salts are prepared. When using the paste, a brush is used to apply the mixture onto the substrates, whereas in the case of a solution the coating film can be applied by brush, spray or dipping onto the substrate. This process is followed by an initial drying step at low temperature (50°C), followed by the annealing stage, which typically takes place at 400-550°C.

### A.2.3 Sol-gel Dip-coating

The sol-gel method of catalyst preparation is claimed to have several advantages over the aforementioned methods. Excellent homogeneity, easy control of film thickness, ability to coat large surfaces and simple and low-cost processing are some of the most important advantages [46]. The sol-gel process has been studied extensively and has been used to prepare a wide variety of metal oxide catalysts.

According to Hench and West [46], three approaches are used to make sol-gel monoliths:

- gelation of a solution of colloidal powders,
- hydrolysis and polycondensation of alkoxide or nitrate precursors, followed by supercritical drying, and
- hydrolysis and polycondensation of alkoxide precursors, followed by ageing and drying under ambient atmospheres.

In this project, the third approach was used for the preparation of the doped tin dioxide catalyst. The first method requires the use of colloidal powders. This can be difficult to obtain in some cases, especially where the more exotic dopants are used. The second method requires the use of supercritical fluid drying, which utilises high pressure and temperature

vessels. The third method is relatively easy when compared to the first two and was chosen for this reason. The precursor salts are very easy to obtain (Merck, Sigma-Aldrich) and no complicated instruments or machinery are required in the process.

Firstly, important terms in the sol-gel process need to be defined. A *sol* is defined as a dispersion of colloidal particles in liquid; *colloids* being solid particles with diameters of 1-100nm. A *gel* is an interconnected, rigid network, containing submicrometer size pores and polymeric chains with average lengths greater than a micrometer [46].

Once simultaneous hydrolysis and polycondensation form the interconnected 3-D network of the gel, the pore liquid must be removed as a vapour phase to leave behind the gel. Supercritical drying of the gel may be employed to remove the excess pore liquid [47]. Due to the supercritical conditions, the network does not collapse and a low-density *aerogel* is formed. Pore volumes as high as 98% and densities as low as 80 $kg/m^3$ have been reported.

When conventional drying at ambient pressure is used to remove the pore liquid, the network collapses due to shrinkage and a *xerogel* is formed. These xerogels have been termed *alcogels* if the pore liquid is primarily alcohol based. A dried gel can be obtained by removing all physically adsorbed water. This occurs between 100-180°C.

Due to the very large surface concentration of chemisorbed hydroxyls on the surface of the pores, heat treatment in the range 500-800°C is used to desorb these hydroxyls. This reduces the number of pores and connectivity substantially, due to viscous-phase sintering (*densification*). This results in a *stabilized gel*. Complete densification results in the elimination of all pores and takes place at temperatures between 1000-1500°C — it is dependent on the surface area and pore size of the gel.

In the preparation of a gel, up to seven steps may have to be followed to form a gel with the desired properties. Only the most important steps for the preparation of the tin dioxide catalysts will be presented here.

Step 1: *Mixing*. Generally a liquid alkoxide precursor is used to prepare the sol, but according to Ward and Ko [48] a wide variety of precursors may be used. The liquid alkoxide precursor ($M(OR)_n$) is hydrolysed by mixing with water. Hydrolysis and condensation reactions then take place in the solution (according to Ward and Ko [48]) as follows:

hydrolysis:

$$-MOR + H_2O \rightarrow -MOH + ROH \qquad (A.60)$$

condensation:

$$-MOH + ROM- \rightarrow -MOM- + ROH \qquad (A.60a)$$

or

$$-MOH + HOM- \rightarrow -MOM- + H_2O \qquad (A.60b)$$

These hydrolysis and condensation reactions continue until sufficient interconnected M–O–M bonds are formed, at which time they begin responding as a sol. The size of the sol particles depends on the pH and the ratio of alkoxide to water in the initial solution.

Step 2: *Gelation*. Given enough time, the colloidal particles will link together and form the 3-D network. The size of the particles and the extent of cross-linking before the gelation step determine the physical properties of the network. At this stage, the viscosity increases greatly.

Step 3: *Ageing*. Also known as *syneresis*, ageing involves the continuation of polycondensation. Localised solution and reprecipitation of the gel network also takes place, increasing the strength of the gel. Porosity of the gel network decreases with increased ageing time.

Step 4: *Drying*. During drying, whether by the conventional or supercritical technique, the pore liquid is removed from the interconnected network.

Step 5: *Densification*. Through the heating of the porous gel at high temperatures, the pores in the network are eliminated and, in the case of coated substrates, the catalyst is fused to the substrate.

Ward and Ko [48] suggest several parameters that are responsible for the final properties of the layer. Of these, the type of precursor, type of solvent, water content, acid or base content, precursor concentration and temperature are important.

In the literature, preparation of $SnO_2$ films has almost exclusively been done using inorganic precursor salts. These salts were always hydrated salts, i.e. $SnCl_4{\cdot}5H_2O$ [47] or $SnCl_2{\cdot}2H_2O$ [49, 50, 51, 52]. In one instance Tin(IV)-ethylhexano-isopropoxide ($Sn(OOC_8H_{15})_2(OC_3H_7{}^i)_2$) was used as precursor [45]. It is assumed that the water required for the hydrolysis reaction comes from the adsorbed water in the precursor salt, since no water is added at any stage of the process. The precursor salts are then dissolved in a suitable solvent (ethanol or isopropanol) and heated under reflux at temperatures up to 80°C in a closed vessel.

Different steps are followed at this stage of the process. In some cases the solvent was evaporated until a fine powder was left behind, while some researchers allowed the solution to undergo gelation for up to 5 days. The same procedure was followed for any dopants that were to be added to the tin solution. In the case of the powders, the desired level of dopant was added and the mixture was redissolved in the solvent. This solution was then heated under reflux, in an open vessel, for 2 hours.

The substrates were then immersed in the solution and withdrawn slowly at a constant rate. This rate varied from 3 to 11 cm/min. These films were then dried in air at 60 to 110°C for between 1 and 2 hours. This process was repeated for each coating of the catalyst. The substrates were then subjected to a final heat treatment at temperatures ranging between 500 and 600°C for 10 minutes to 1 h, at a heating rate of 2°C per minute.

# B Catalyst Development

by Priscilla G.L. Baker

## B.1 Preparation of Mixed Metal Oxide Catalysts

### B.1.1 Sol-gel preparation of mixed metal oxide electrodes

Sol-gel involves hydrolysis of organic or inorganic precursors, followed by condensation and ageing. A schematic representation of the sol-gel process is given below (Figure B.1). The cationic precursors in sol-gel preparation were either chloride salts (Sb, Pd) or organic derivatives (Cu, Zr). In the case of manganese doping, citrate derivatives of manganese and tin were preferred. The manganese citrate derivative was freshly prepared before sol-gel synthesis, from $MnCO_3$ by precipitation and filtration. The organic solvent in all cases was absolute ethanol, except for zirconium doping, where the solvent was methanol.

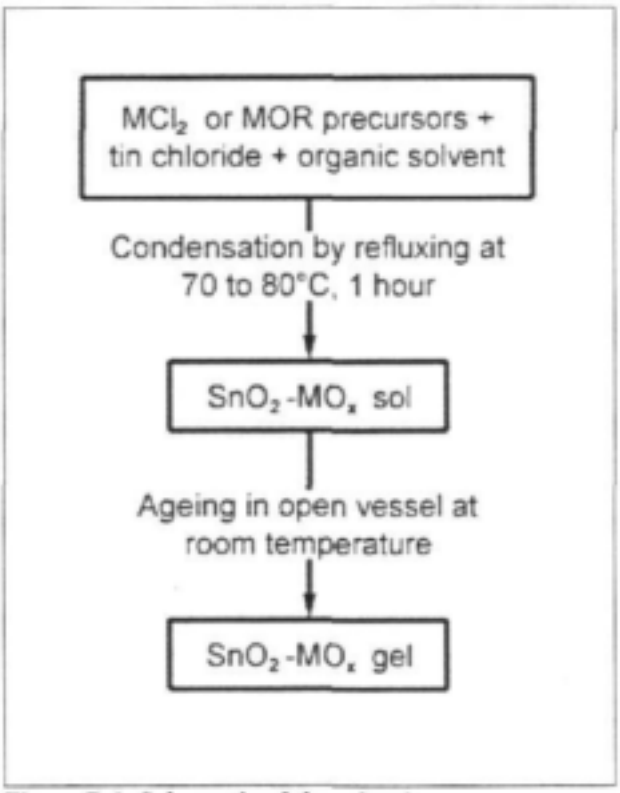


**Figure B.1: Schematic of the sol–gel process.**

The doping ratios were kept as low as possible, using literature references as a guideline (Table B.1). The doping ratio was determined according to the following formula:

$$\text{Doping ratio} = \frac{n_i}{\sum n} \qquad \text{(B.1)}$$

Where $n_i$ is the number moles of dopant atom and n is the total number of moles ($SnO_2$ + dopant)

**Table B.1: Doping ratios for mixed metal tin oxides**

| Starting materials | Dopant | Ratio |
|---|---|---|
| $SnCl_4 \cdot 5H_2O$; $Cu(CH_3COO)_2 \cdot H_2O$ | CuO | 2.5 wt. % |
| $SnCl_2 \cdot 2H_2O$; $Zr(OC_4H_9)_4$ | $ZrO_2$ | 1 mol % |
| $SnCl_2 \cdot 2H_2O$; $PdCl_2$ | Pd | 1 mol % |
| citric acid, tin citrate, ethylene glycol, nitric acid, manganese citrate | $MnO_2$ | 5 mol % |
| $SnCl_2 \cdot 2H_2O$; $SbCl_3$ | $Sb_2O_5$ | 10 mol % |

In all cases the solutions were well stirred and refluxed before being left to age at room temperature for the respective amount of time (12 to 24 h). The obtained gel was evaporated to dryness to produce a powder. The powder samples were submitted for XRD analysis. For the purpose of casting the thin films, the gels were retained in the liquid form. They were found to be stable at room temperature for up to 6 months when stored in the absence of direct light.

### B.1.2 Preparation of thin-film electrodes

Thin films were prepared by dip coating sol-gel techniques. The major advantages of this technique over other techniques such as spray pyrolysis, chemical vapour deposition and RF sputtering (radio frequency electromagnetic wave energy (e.g., 13.65 MHz, etc.) is utilised to energise the sputtering operation) are: high purity starting material, easy coating of large and complex shaped substrates and low cost [50].

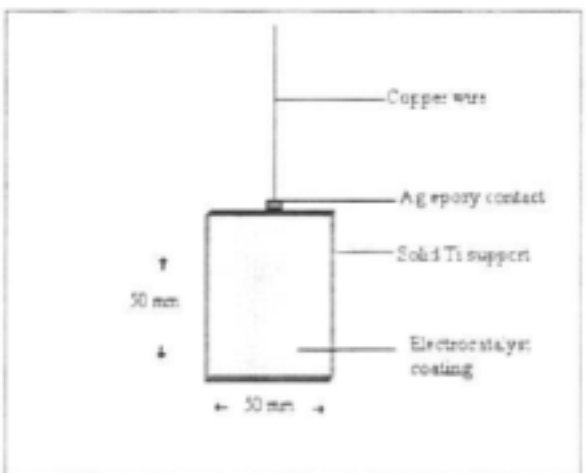


**Figure B.2: Design of mixed metal tin oxide coated electrode.**

This technique produces high quality mixed metal $SnO_2$ thin films as far as structure and morphology are concerned. Experimental conditions can be readily controlled to ensure reproducibility. The dip coating mechanism is similar to that described by Grimm et al [52]. The effect of spin coating the mixed metal oxides onto the titanium substrates, as opposed to dip coating, was also investigated. The films were coated once, allowed to dry at 100°C for 30 minutes in a standard laboratory oven, before the second coating was applied. All the films prepared by dip coating and spin coating were annealed in a tube furnace (LABOFURN, quartz tube) with a model 7 temperature controller. The samples were heated at a ramp rate of 60°C per hour and kept at 600°C for one hour, before being allowed to cool again to room temperature.

## B.2 Characterisation of catalysts

The mixed metal tin oxide materials prepared via the sol-gel route were extensively characterised. TGA analysis was performed to confirm that at 600°C (the calcination temperature) no further structural changes due to mass loss occur. UV spectroscopy of the gels allowed the determination of the band gap energy. The surfaces of the thin film electrodes were characterised by X-ray diffraction (XRD), atomic force microscopy (AFM), scanning electron microscopy (SEM), Rutherford backscattering (RBS) and particle induced X-ray emission (PIXE) analysis provided some insight into the chemical composition of the mixed metal tin oxides.

### B.2.1 Experimental

#### Thermogravimetric analysis

Small sample masses are used in TGA to ensure uniform heating of sample and to reduce exchange of gas with the surrounding atmosphere. A concentrated gel material was prepared for TGA by evaporating the solvent of a small volume of the original gel. The sample was analysed on a Perkin Elmer TGA (7 series). The heating rate was 1°C/min up to a maximum of 600°C and nitrogen was used as purging gas.

#### UV/vis spectroscopy

A Unicam, Helios Gamma, UV spectrophotometer and Aurora 1.1 scanning software version was used for the collection of the data. The instrument was used in single beam mode. Absolute ethanol (solvent used in preparation of mixed metal oxide gels) was used as a reference. The gel samples were diluted 1:1 with absolute ethanol to obtain absorbance readings on an appropriate scale. The band gap energy (eV) was measured by extrapolation of the first absorbance peak, usually observed between 300 to 400 nm.

#### X-ray diffraction

Samples of the mixed metal tin oxide gels were evaporated to dryness and the resulting powders were analysed by X-Ray diffraction (XRD). Measurements were made on a Siemens advanced D8 diffractometer (Bruker AXS) with primary (Cu tube, variable divergent slit) and secondary (NaI(Th)) scintillation, variable anti-scatter slit) detectors. The incident angle was set as 2°, for all measurements. Energy dispersive X-ray flourescence (EDXRF) was useful in the quantitative analysis of the Cu doped thin film composition, in particular.

#### Scanning electron microscopy

SEM pictures of the surfaces were obtained at 500× and 5000× magnification using a Topcon scanning electron microscope, model ABT60. The microscope was operated in secondary electron detection (SED) mode at an accelerating voltage of 20 kV. The working distance was 10 mm, the samples were tilted 20° and they were not coated for viewing.

#### Atomic force microscopy

AFM micrographs were taken at two different positions on each film that was prepared using a Topometrix Explorer TMX 2000. Two measurements on the same sample were done to improve representation of the entire surface morphology, since the sample surface is not homogeneous. The samples were scanned in non-contact mode (i.e. the probe is oscillated in the attractive regime). A low resonance frequency cantilever was used and the force spring constant was 35-65 N/m.

**Particle induced X-ray emission/ Rutherford backscattering**

Compositional analyses of the mixed metal oxides cast as thin films were obtained by the combination PIXE/RBS technique. The sample was bombarded with protons and the energy of the beam was kept at 3 eV. A selected section of the surface (5 $\mu$m × 5 $\mu$m) was bombarded with protons and taken to be representative of the total surface composition (5 mm × 5 mm). The backscattered energy was recorded using an X-ray detector. Semi-quantitative on-line imaging was made possible by the use of the GEO-PIXE suite of programmes. Compositional analysis (ppm of element) is based on matrix determination and depth profiling (film thickness) provided by RBS. PIXE/RBS and XRD analyses were done at the nuclear microprobe facility at Ithemba Labs, Faure, South Africa.

## B.2.2 Results and discussion

**Thermogravimetric analysis**

The TGA profiles obtained for the synthesized gels are in good agreement with published TGA profiles for Zr, Pd and CuO doped $SnO_2$ [53, 54, 55]. In all cases, an initial 10 to 20% weight loss was assigned to the evaporation of the organic solvent. Subsequent major weight loss between 100 to 200°C is ascribed to evaporation of water, ions and organic compounds. The most stable phase of all transition metal doped tin oxides is formed by $PdO_2/SnO_2$ at around 180°C. CuO, $ZrO_2$ and $Sb_2O_5$ doped tin oxide show very gradual weight losses (±10%) between 180 to 400°C, where after a stable phase is reached (Figure B.3). CuO and $MnO_x$ doped tin oxide follow a similar pattern, but there is slightly more weight loss. All mixed metal tin oxides form stable phases before the calcination temperature used in the preparation of thin films, i.e. 600°C.

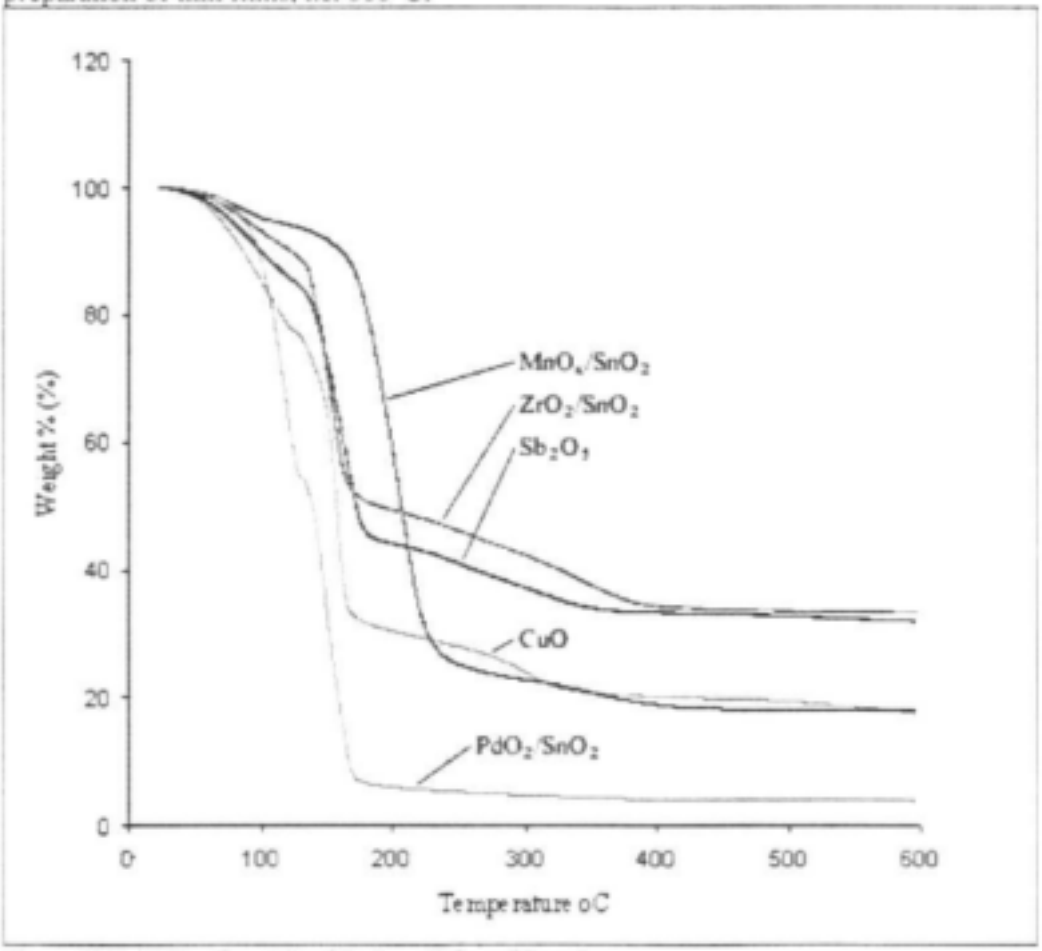


**Figure B.3: TGA of metal oxide doped tin oxide gels.**

**UV/vis spectroscopy**

The band gap energies for all mixed metal tin oxides were determined to be between 2.37 to 3.37 eV (Table B.2).

The band gap energy (eV) for each mixed metal oxide was determined from the onset of the absorption in the UV region, as illustrated in Figure B.4. $PdO_2/SnO_2$ was the only mixed metal tin oxide which gave a band gap energy lower than that of undoped tin oxide. The $MnO_x/SnO_2$ sample was in the form of a dispersion, rather than a clear solution and this complicated the absorbance measurements, even after dilution. It was therefore not possible to determine the band gap energy for this composition.

**Table B.2: Band gap energy values of the mixed metal tin oxide gels prepared**

| Gel composition | $E_{bg}$ [eV] |
|---|---|
| $SnO_2$ | 3.30 |
| $SnO_2/CuO$ | 3.03 |
| $SnO_2/PdO_2$ | 2.37–2.47 |
| $SnO_2/Sb_2O$ | 3.34 |
| $SnO_2/ZrO_2$ (2002) | 3.30 |
| $SnO_2/ZrO_2$ (2003) | 3.37 |
| $SnO_2/MnO_x$ | — |

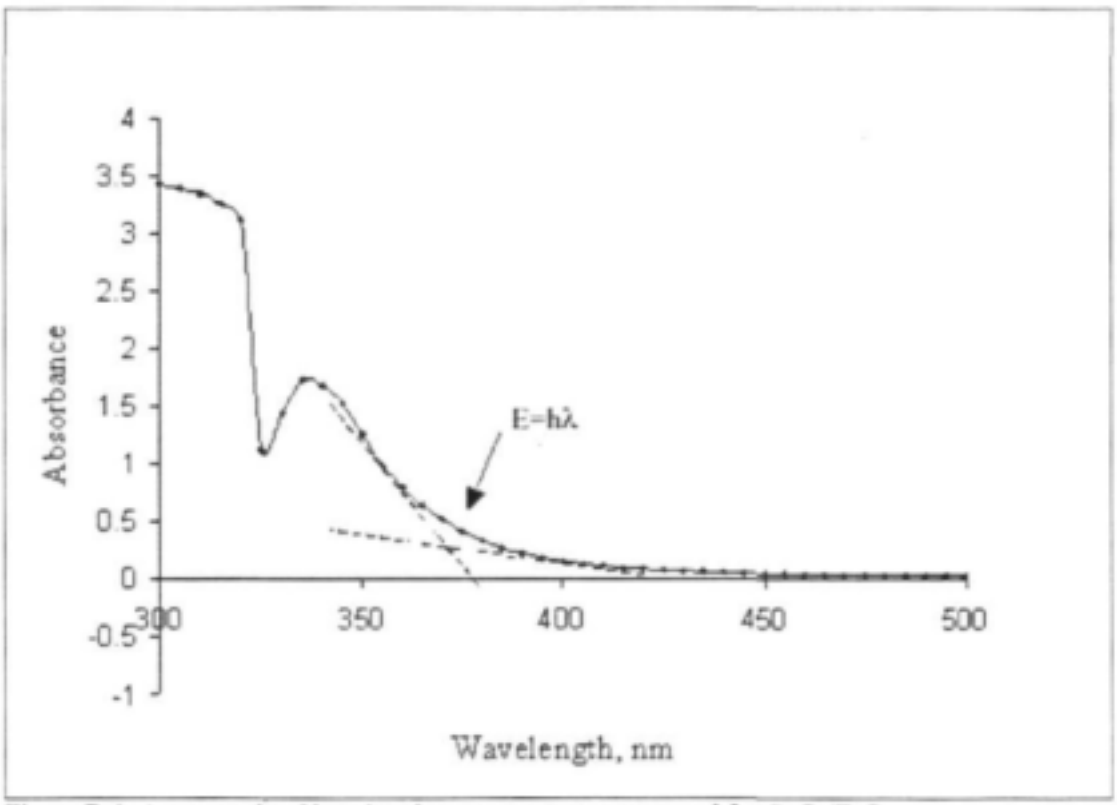


**Figure B.4: An example of how band gap energy was measured for $SnO_2/ZrO_2$.**

Three samples of $ZrO_2/SnO_2$ gels were collected over time to observe the effect of long term ageing on the absorbance response of the gels. Two samples of the zirconium doped tin oxide which were prepared a year apart (March, 2002 and September, 2003) showed distinctly different absorptions at 340 nm (Figure B.5). The absorption peak for the 2002 sample was at least 1 absorbance unit bigger than that of the 2003 sample. As the sample ages with time the extent of cross-linking increases and the gel becomes more dense or crystalline. This increase in cross-linking of the sample due to the ageing process is reflected in the larger absorbance for the aged samples.

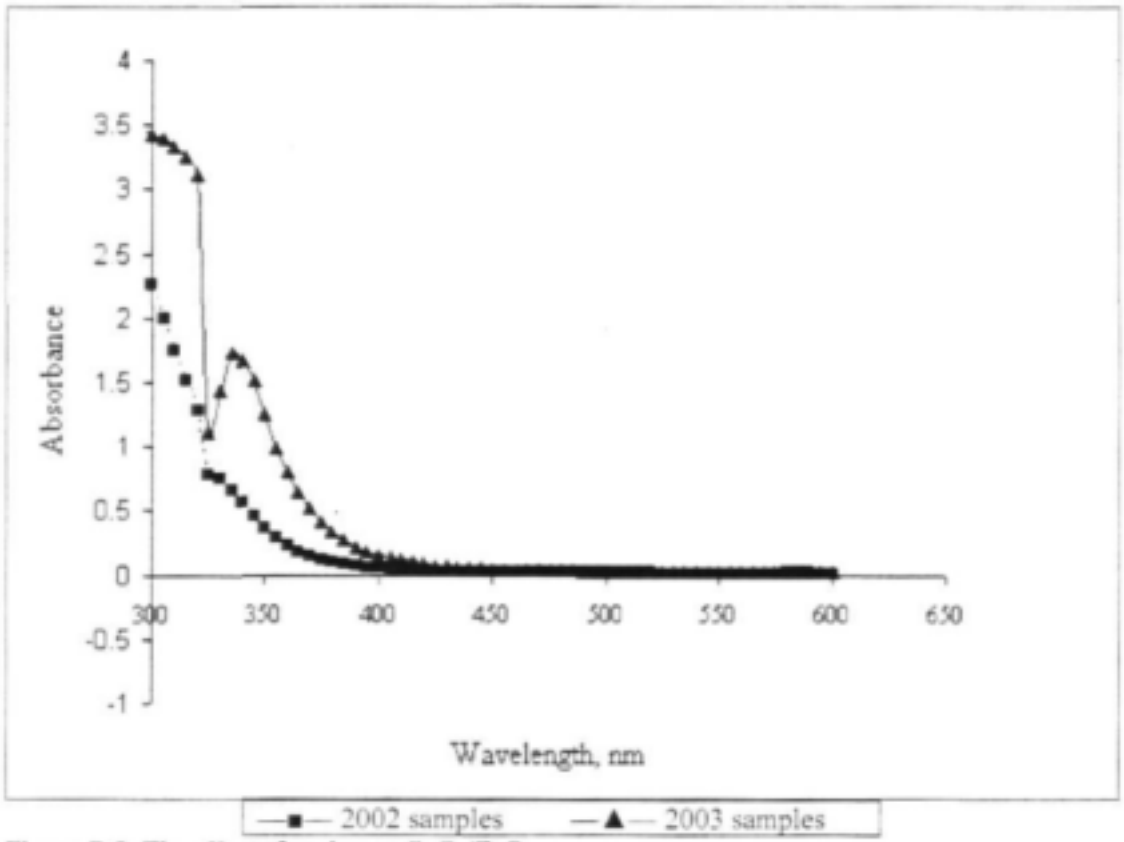


**Figure B.5: The effect of ageing on $SnO_2/ZrO_2$.**

### B.2.3 X-ray methods

XRD was able to confirm the characteristic peaks for $SnO_2$ when compared to the JCPDS file number 21-1250 (Cassiterite syn $SnO_2$) for the mixed metal oxide powders (Figure B.6). Peaks for the identification of the dopant atom were however not always observed since the very low dopant ratio of 1 mol% is beyond the capability of the instrument used. In a study of $SnO_2/ZrO_2$ prepared as 95:5 wt% composition, XRD could only confirm the crystalline cassiterite structure. Thus at 5 wt% $ZrO_2$ doping the refinement of the lattice parameters were in good agreement with that of bulk $SnO_2$ [56]. XRD of $ZrO_2$ thin films grown by photo-induced chemical vapour deposition, showed weak intensity bands at 30.4 Å and 35 Å, which could be assigned to the tetragonal and monoclinic phases respectively. This confirmed that $ZrO_2$ layers grown in this manner start to crystallize at a deposition temperature of 250°C [57]. Energy dispersive X-ray fluorescence (EDXRF) was able to positively identify the copper in $CuO/SnO_2$. XRD could not confirm the presence of the dopant atoms.

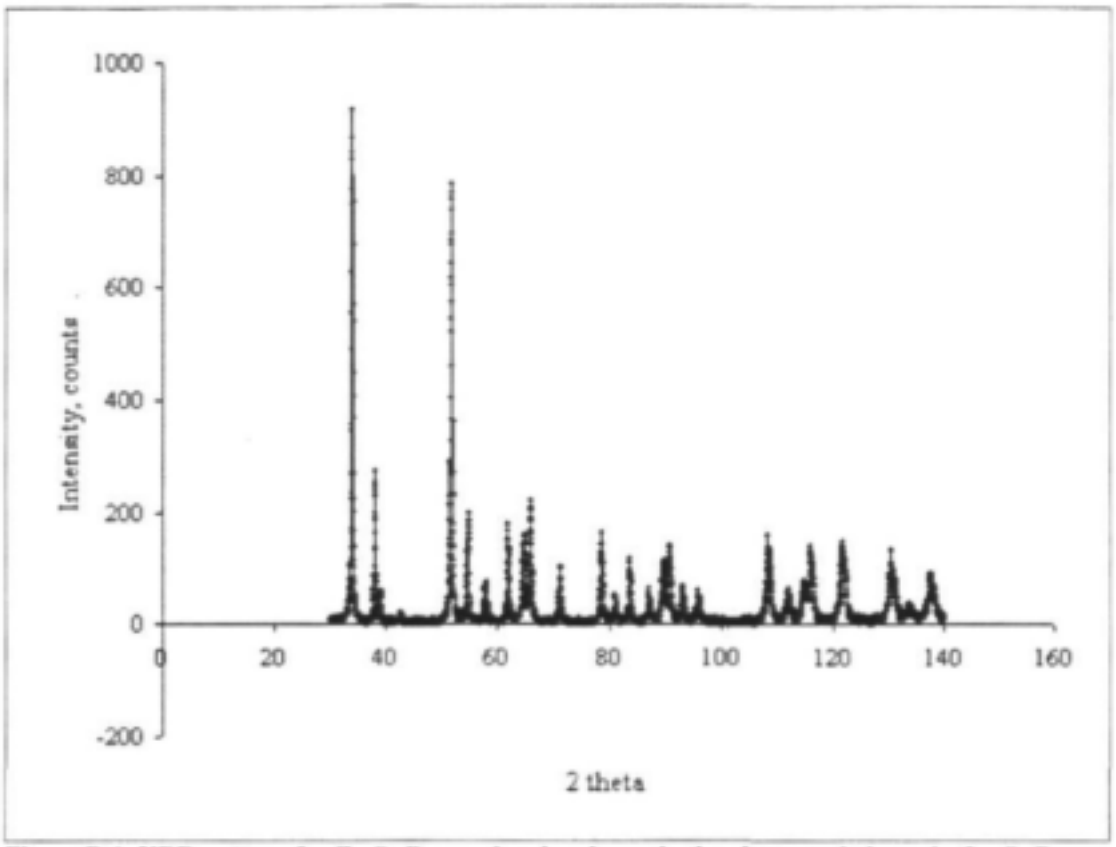


**Figure B.6: XRD pattern for Zr-$SnO_2$ powder showing only the characteristic peaks for $SnO_2$.**

**Scanning electron microscopy**

Scanning electron micrographs reflected well coated surfaces in most cases for spin coating as well as dip coating. The Cu-doped surfaces (spin coated) showed a lighter and a darker area at 500× magnification which could be due to an uneven concentration distribution (Figure B.7a).

The Zr-doped spin coated surface showed dramatic fragmentation at 500× magnification. Increase in the doping level of Zr in the tin oxide host material gave rise to clusters or island formation as a result of exclusion (Figure B.7b). Pd-doped spin coated surface produced a cauliflower like surface as a result of agglomeration of metal oxide particles (Figure B.7c). Noble metals like palladium, readily oxides in air forming a layer of touching oxide particles. These oxide particles can be reduced back to metallic palladium by further heating (up to 500°C) in a reducing atmosphere, giving rise to the agglomeration of metal oxide and metallic particles observed [58].

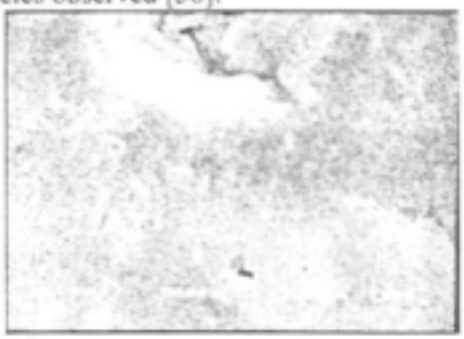

(a)

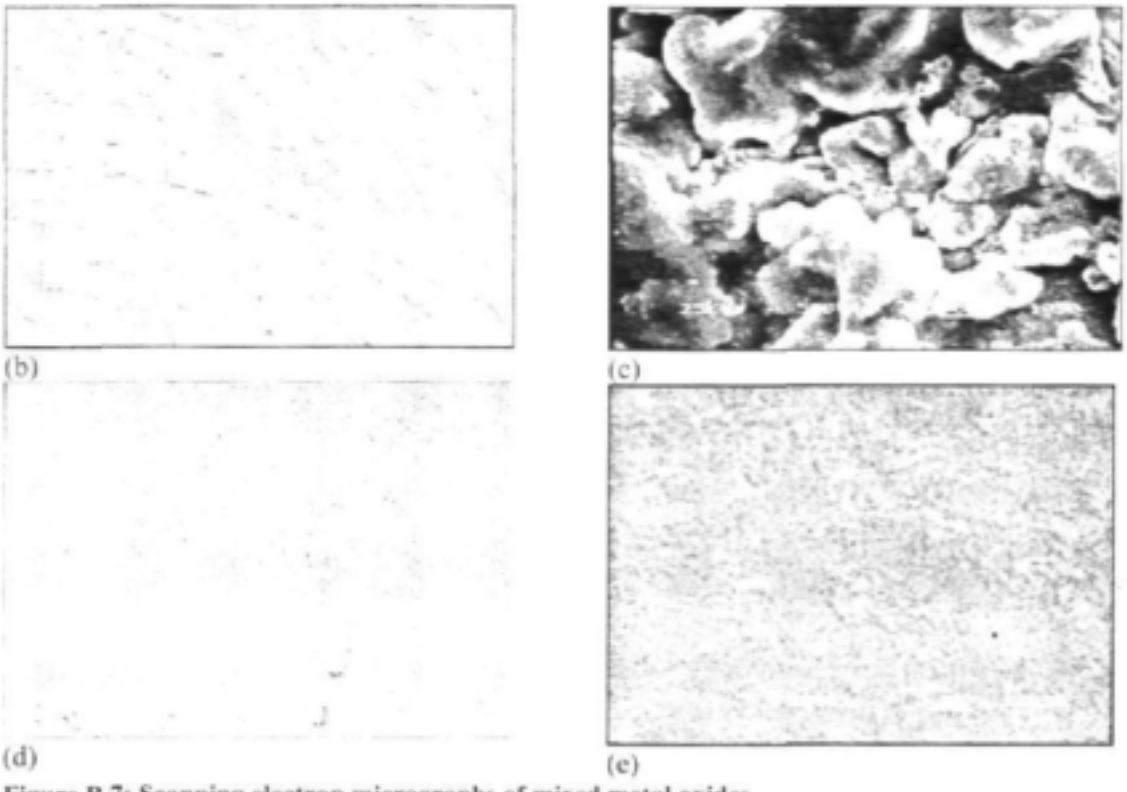


**Figure B.7: Scanning electron micrographs of mixed metal oxides.**

The agglomeration observed for zirconium and palladium doped tin oxide, was confirmed by repeat coatings and is therefore characteristic of the coating composition. The spin coated thin films showed greatly enhanced surface roughness compared to dip coated films of the same composition.

The scanning electron micrographs of manganese and antimony doped tin oxide also confirm good surface coatings (Figure B.7d, e).

**Atomic force microscopy**

Atomic force micrographs of $Sb_2O_5$ doped thin films showed greater surface roughness for the dip coated than the spin coated surfaces. The dipping process leads to the formation of regularly repeating triangular patterns on the thin film electrode surfaces. These regularly repeating surface patterns confirm that the dopant atoms are included in an interstitial fashion so that the octahedral arrangement of the host material is maintained i.e. cassiterite syn $SnO_2$ (Figure B.8 a,b,c,d,e). The difference in surface roughness between spin and dip coated thin films observed, is as a result of the forces that act upon the film during the coating process i.e the drag during the dipping process and centrifugal forces during spin coating. The spin coated surfaces showed less surface roughness and appear smoother. The atomic force microscope that was used, was not able to detect much more than surface morphology. It was possible to get pictures at atomic level and investigate molecular or atomic bond structure using a more advanced AFM instrument than the one used in these experiments. Information of this nature would enable structural analysis of thin film surface composition.

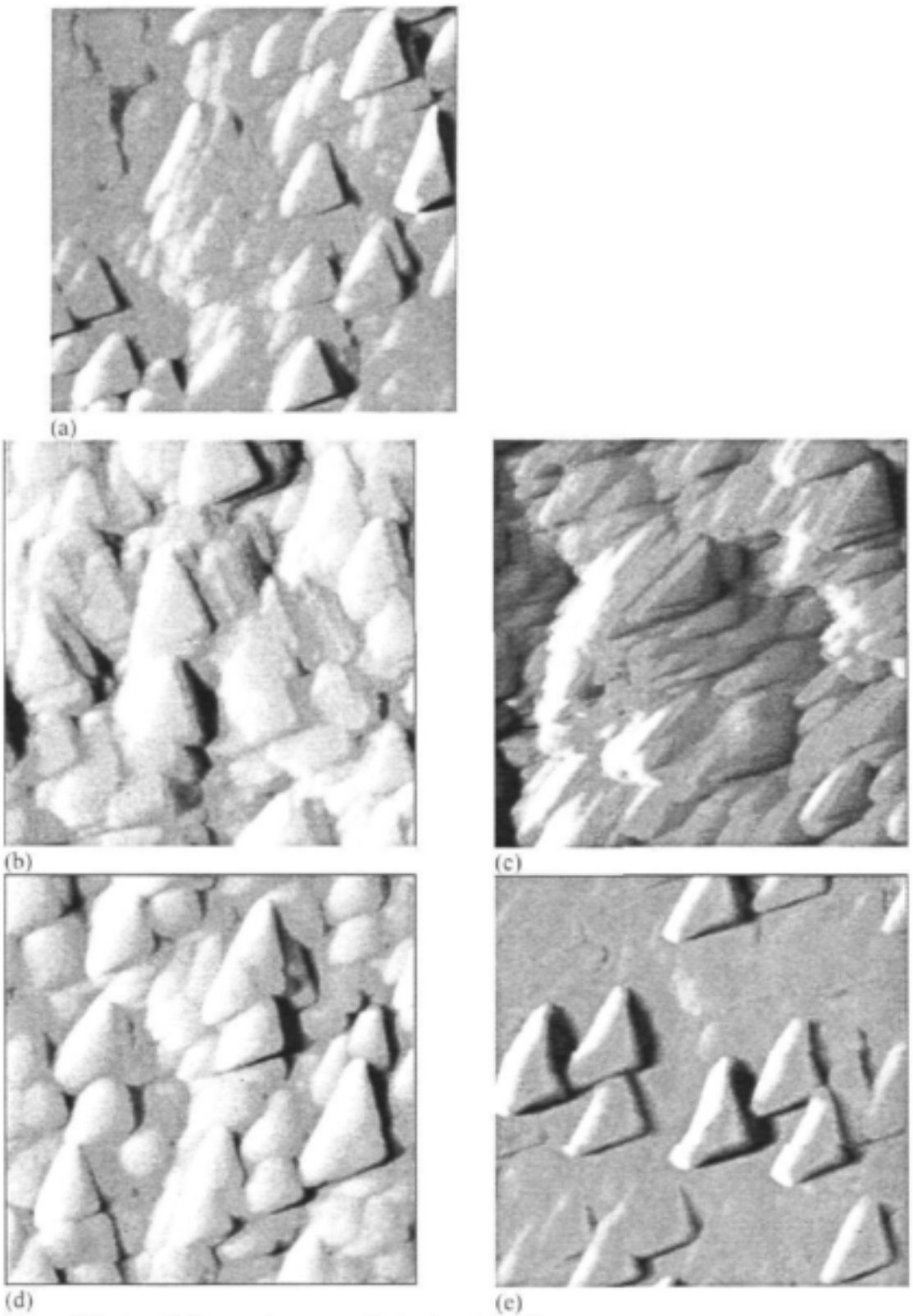


**Figure B.8: Atomic Force microscopy of mixed metal oxides.**

**Rutherford backscattering**

The RBS spectra show that the substrate that was used (solid titanium) and the coated metal oxide thin films give well separated peaks for simulation and fitting purposes. This confirms the suitability of RBS as an analytical tool for compositional analysis. Simulation was done using the Rutherford Universal Manipulation Programme (RUMP).

Comparing the spin and dip coated surfaces, it appears that in most cases the elements were more abundant in the spin coated surfaces than in the dip coated surfaces. This is reflected in the larger peak areas obtained by RBS for spin coated versus dip coated samples (Figure B.9 and B.10).

It should be noted however that the surfaces were not homogeneous in composition and hence compositional analysis of the thin films as presented in the data is subject to the composition of the specific surface area that was bombarded with $\alpha$-particles (RBS) and protons (PIXE). Usually an area $5\mu m \times 5\mu m$ near the centre of the samples was selected for characterization and taken as representative of the entire sample.

The thickness of films determined by RBS was in the order of 20 to 40 nm for spin coated films and less for dip coated films. The only exception was the Zr spin coated film which had a film thickness of 140 nm.

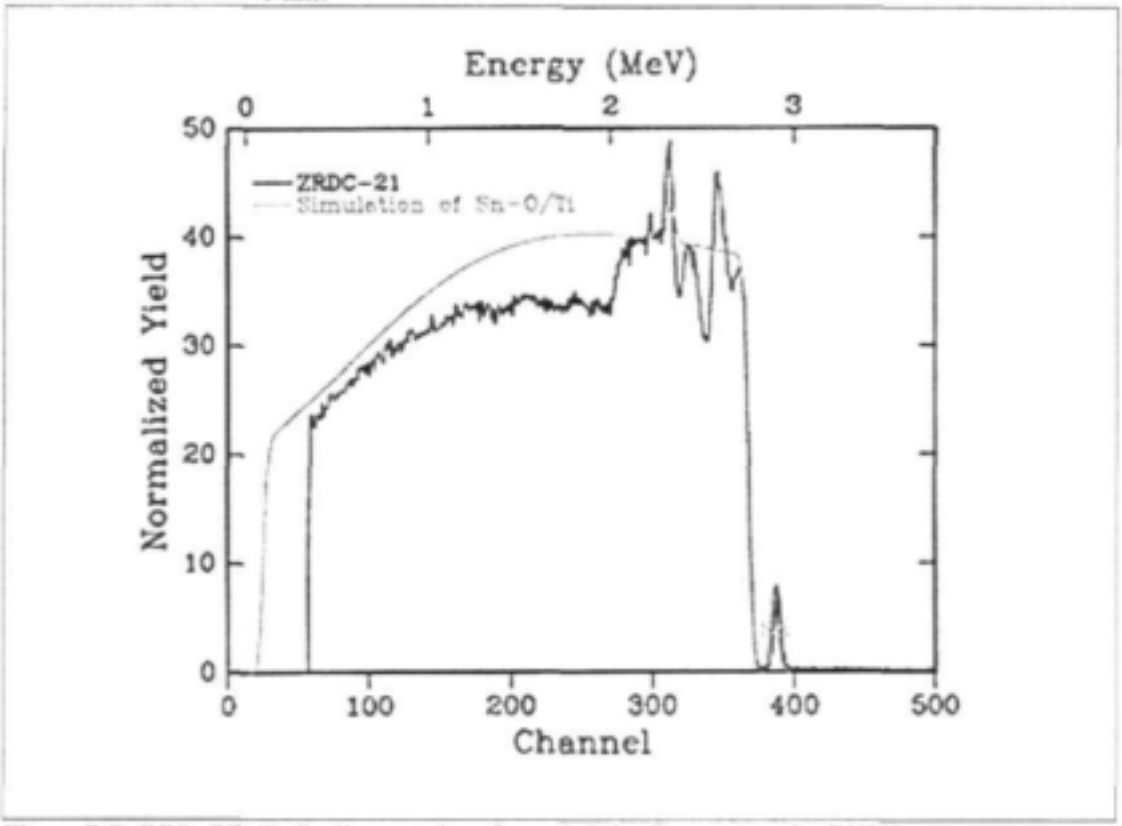


**Figure B.9: RBS of $Zr/SnO_2$ dip coated surfaces and the fit spectrum by RUMP.**

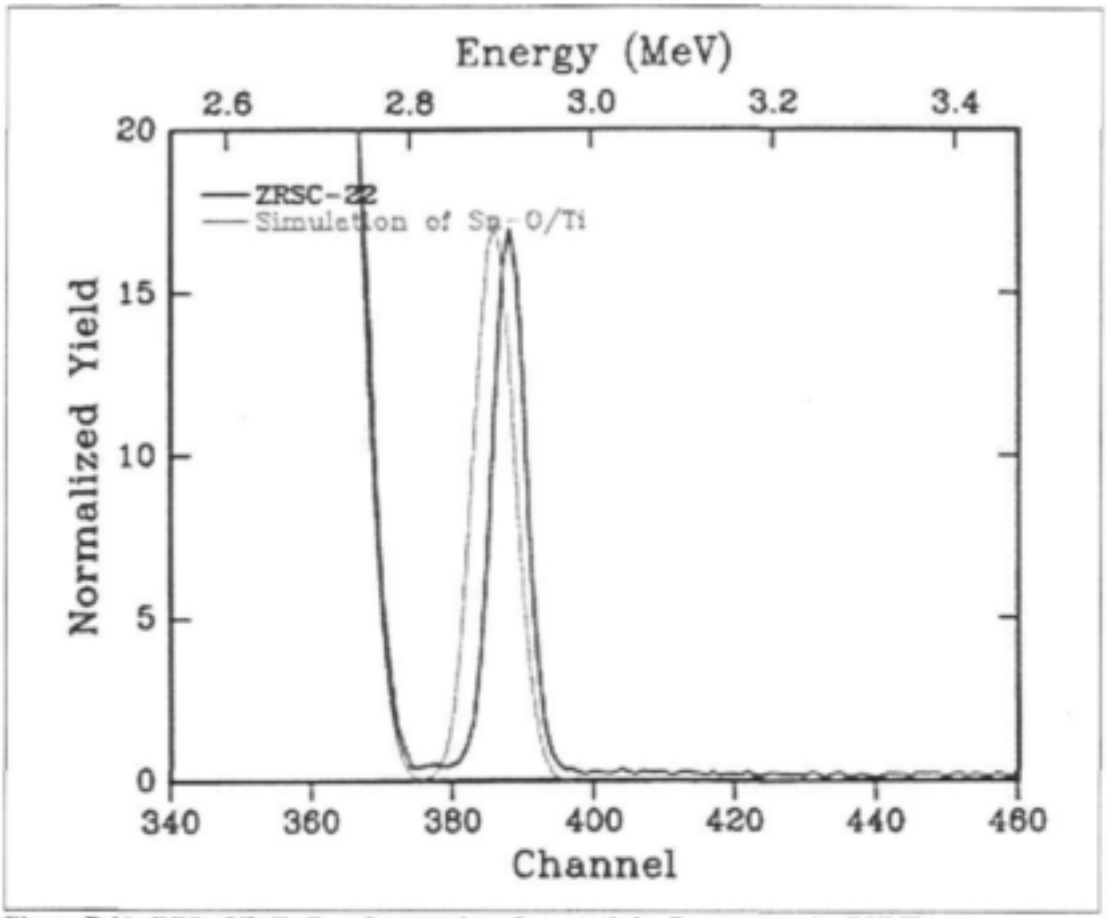


**Figure B.10: RBS of $Zr/SnO_2$ spin coated surfaces and the fit spectrum by RUMP.**

**Particle induced X-ray emission**

Three sets of prepared thin films were analysed. In all cases the dopant element was positively identified. The spin coated samples generally gave thicker films than the dip coated samples did. The detection of the dopant element was consequently also more successful for spin coated samples than for dip coated samples. For the third set of samples, detection of the dopant element in the dip coated samples was generally so low that no quantitative evaluation of the dopant element was performed.

Tungsten (W) was identified as a contaminant in all samples, as determined by performing a blank run on an uncoated titanium sample. Further tests with blank samples and standards eliminated the detection chamber as the source of contamination. The W is thought to be introduced at some as yet undefined stage in the preparation. Fe and Ag contaminants were introduced as part of the composition of the starting materials and were therefore unavoidable. None of the contaminants however showed any interference with the catalytic behaviour of the thin film electrodes.

By using intrinsic doping during sol-gel synthesis, a fusion of the dopant atom with the $SnO_2$ host material is obtained after annealing the thin films. The surface composition of mixed metal oxide thin films (expressed as a %) based on ppm quantification, will therefore not necessarily reflect the calculated composition (Table B.3). Consistency in the estimations for Pd, Zr, Sb and Cu is observed, at their respective levels of doping.

For detailed structural analysis, tools such as X-ray crystallography could assist in identifying the exact location of the dopant molecules within the $SnO_2$ host structure. This would involve the growth of good quality crystals which is time consuming and a specialized skill in its own right.

**Table B.3: Typical compositional analysis of mixed metal tin oxide thin films (% composition based on ppm analysis) as determined by PIXE/RBS**

| Dopant | Coat | Fe | Cu | Ag | Sn | Sb | W | Mn | Co | Zr | Pd | Zn |
|---|---|---|---|---|---|---|---|---|---|---|---|---|
| Sb | Dip | 2.79 | 0.47 | — | 60.1 | 26.9 | 9.68 | — | — | — | — | — |
| Sb | Spin | 3.38 | 1.14 | — | 55.1 | 12.2 | 28.2 | — | — | — | — | — |
| Mn | Dip | 2.57 | 0.94 | 2.71 | 72.1 | 0.00 | 19.5 | 0.92 | 1.24 | — | — | — |
| Mn | Spin | 0.33 | 0.20 | 0.09 | 94.0 | 1.30 | 3.41 | 0.38 | 0.27 | — | — | — |
| Zr | Dip | 0.47 | 0.11 | 0.10 | 95.4 | 0.54 | 2.49 | 0.13 | 0.12 | 0.65 | — | — |
| Zr | Spin | 0.13 | 0.05 | — | 98.0 | 0.07 | 1.01 | 0.03 | 0.04 | 0.68 | — | — |
| Pd | Spin | 0.35 | 0.21 | 0.33 | 94.8 | — | 3.12 | 0.28 | 0.28 | — | 0.67 | — |
| Pd | Dip | 0.33 | 0.24 | 0.04 | 54.1 | — | 4.13 | 0.08 | 0.12 | — | 0.27 | 40.7 |
| Cu | Dip | 4.72 | 5.16 | — | 41.0 | 0.43 | 48.7 | — | — | — | — | — |
| Cu | Spin | 0.47 | 9.34 | 0.66 | 86.4 | — | 3.16 | — | — | — | — | — |

## B.3 Conclusions and Recommendations

The following conclusions can be drawn from the work done on the catalyst performance:

- Intrinsically doped transition metal tin oxide gels have been prepared successfully using the sol-gel method. $Sb_2O_5$, $PdO_2$, CuO, $MnO_2$ and $ZrO_2$ have been introduced successfully into a $SnO_2$ host, at very low dopant levels to produce mixed metal oxide electrodes. Sol-gel synthesis of mixed metal oxides was established as an efficient yet simple way to produce intrinsically doped mixed metal tin oxide gels, reproducibly. Thin film electrodes were produced by dip coating the gels onto solid titanium substrates, which were then annealed to produce dimensionally stable electrodes.
- In an attempt to produce electrodes with increased surface area, surfactants were added to the mixed metal oxide gels. However, the thin films electrodes produced from these modified gels were not reproducible and not suitable for electrochemical evaluation. Dip coating the mixed metal tin oxide gels onto porous titanium substrates gave the desired thin film electrode with increased surface area.
- TGA analysis showed that $PdO_2/SnO_2$ formed the most stable phase. It also confirmed that the calcination temperature of 600°C, was high enough to ensure that all mixed metal oxides form stable phases. UV/vis measurements were able to confirm the band gap energies for all mixed metal oxides to be in the range 2.37 to 3.37 eV. These values are not significantly different from the band gap energy of undoped $SnO_2$.
- XRD analysis was not able to characterise the chemical composition of the thin films, since the catalytic metal oxide element was introduced at very low concentration. XRD analysis of each mixed metal oxide system, only gave confirmation of the syn cassiterite $SnO_2$ host material.
- Morphological characterisation of the thin film electrode surfaces, using SEM confirmed that the coatings were free from cracks and other surface imperfections. AFM was useful in differentiating between thin film preparation techniques. The spin coated samples consistently appeared smoother with lower surface roughness estimates. The morphology of all mixed metal oxide surfaces showed regularly repeating triangular units. It was not possible to relate these patterns to any structural parameters due to limitations of the instrument used.
- The PIXE/RBS combination was used to confirm the presence of the dopant atom in the thin film mixed metal tin oxide samples, but quantitative determination was not in good agreement with calculated values. The mixed metal oxide samples did however provide a challenge for the application for this combined technique. Good separation between the titanium (substrate) signal and the signal of the thin film elements was observed. Therefore, quantification as performed, is reliable.

The following recommendations can be made based on the results obtained in this appendix:

- The electrodes evaluated in this study represents only a sample of the transition metal oxide doped tin oxide electrodes family. Further evaluation of this class of electrodes should include (a) varying the dopant ratio to find the most effective electrocatalyst within a given combination. It has been demonstrated that the conductivity of $SnO_2/ZrO_2$ thin films increases up to a doping level of 5 wt%, after which they become insulating [54]. Combinations of different dopant elements in order to obtain the best possible combination for anodic oxidation, should also be investigated further. In phosphine sensing experiments, $SnO_2$ doped with PdO only or $ZrO_2$ only, have shown weaker sensitivity towards phosphine detection than a Pd activated $SnO_2/ZrO_2$ thin film [59]. $CuO/ZrO_2$ catalysts were shown to be effective for low temperature CO oxidation [60].
- Mixed metal oxide electrodes have been and will be the focus of electrocatalyst development and the evaluation of its applications. The control over sensitivity and selectivity that can be achieved by the (i) combinations of metal oxides and (ii) the thin film preparation methods, leaves this field wide open for development in future work. We have demonstrated how these mixed metal oxides can be synthesised at relatively low cost and characterised fully (depending on the sophistication of the characterisation tools used).

# C Model derivations

The expressions used for the determination of reactor length and cost were omitted from the main body of the report because they were not required for the presentation of the results. They have been included here for parties interested in the detail of the calculations. They are also necessary for Appendix D, where typical calculations are shown for the various parts of the report.

## C.1 Reactor Model

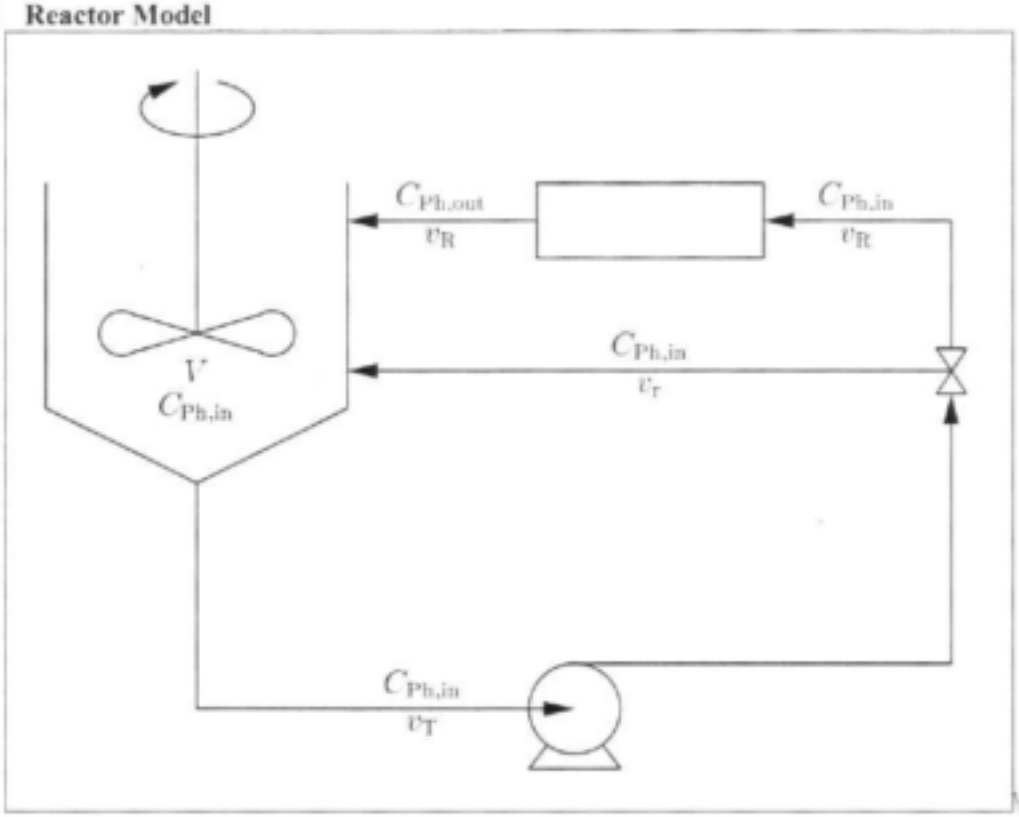


**Figure C.1: Nomenclature used in model derivation.**

An overall mass balance can be performed on the reservoir as shown in Figure C.1.

| | | | |
|---|---|---|---|
| IN: | | $\rho_{out} v_R + \rho_{in} v_r$ | |
| OUT: | – | $\rho_{in} v_T$ | |
| GENERATION: | + | 0 | |
| ACCUMULATION: | = | 0 | (C.1) |

From the assumption that the physical properties of the inlet and outlet are the same, i.e. $\rho_{in} = \rho_{out}$, the following relationship is obtained

$$v_T = v_R + v_r \qquad \text{(C.2)}$$

Performing a component mass balance on the reservoir using phenol as compound, one obtains

| | | | |
|---|---|---|---|
| IN: | | $(C_{Ph,out} v_R + C_{Ph,in} v_r) M_{R,Ph} \Delta t$ | |
| OUT: | – | $C_{Ph,in} v_T M_{R,Ph} \Delta t$ | |
| GENERATION: | + | 0 | |
| ACCUMULATION: | = | $M_{R,Ph} V \left( C_{Ph,in}\big\|_{t+\Delta t} - C_{Ph,in}\big\|_{t} \right)$ | (C.3) |

Dividing equation C.3 by $M_{R,Ph}\Delta t$ and letting $\Delta t \to 0$ one obtains the differential form of the defining equation for the reservoir:

$$V\frac{dC_{Ph,in}}{dt} = v_1\left(C_{Ph,out} - C_{Ph,in}\right) \qquad (C.4)$$

Replacing $\frac{V}{v_1}$ with $\tau$, the residence time, the final form of the differential equation can be obtained as shown in equation C.5.

$$\frac{dC_{Ph,in}}{dt} = \frac{\left(C_{Ph,out} - C_{Ph,in}\right)}{\tau} \qquad (C.5)$$

The same mass balances can be done for an infinitesimally small length element in the reactor. The component mass balance based on phenol gives:

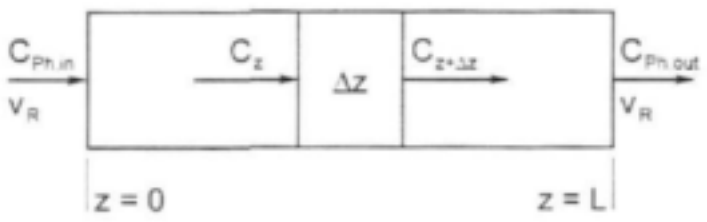


**Figure C.2: Nomenclature used for reactor.**

| | | |
|---|---|---|
| IN: | | $C_{Ph}\big\|_z M_{R,Ph} v_R$ |
| OUT: | – | $C_{Ph}\big\|_{z+\Delta z} M_{R,Ph} v_R$ |
| GENERATION: | + | $r_{Ph}^{*} a(t) M_{R,Ph} W \Delta z$ |
| ACCUMULATION: | = | 0 |

(C.6)

Dividing by $\Delta z M_{R,Ph}$ and letting $\Delta z \to 0$ gives the differential form of the mass balance for the reactor:

$$\frac{dC_{Ph,z}}{dz} = \frac{r_{Ph}^{*} a(t) W}{v_R} \qquad (C.7)$$

Replacing $r_{Ph}^{*}$ with an appropriate form, one obtains the general form of the mass balance in differential form:

$$\frac{dC_{Ph,z}}{dz} = \frac{-kC_{Ph}^{n} a(t) W}{v_R} \qquad (C.8)$$

It was assumed that the reaction rate has an SnSth-order dependence on the concentration.

This can then be integrated for two different cases of $n$. For $n \neq 1$:

$$\int_{C_{Ph,in}\big|_z}^{C_{Ph,out}\big|_z} \frac{dC_{Ph,z}}{C_{Ph}^{n}} = -\frac{ka(t)W}{v_R}\int_0^L dz$$

$$\frac{1}{1-n} C_{Ph}^{1-n}\Big|_{C_{Ph,in}\big|_z}^{C_{Ph,out}\big|_z} = -\frac{ka(t)W}{v_R} L$$

giving

$$C_{\mathrm{Ph,out,}J}^{1-n} - C_{\mathrm{Ph,in,}J}^{1-n} = -\frac{(1-n)ka(t)W}{v_R} L$$

$$C_{\mathrm{Ph,out,}J} = \left\{ C_{\mathrm{Ph,in,}J}^{1-n} - \frac{(1-n)ka(t)W}{v_R} L \right\}^{\frac{1}{1-n}} \tag{C.9}$$

Assuming a reaction order of 1:

$$\int_{C_{\mathrm{Ph,in}}|_{z=0}}^{C_{\mathrm{Ph,out}}|_{z=L}} \frac{\mathrm{d}C_{\mathrm{Ph},z}}{C_{\mathrm{Ph}}} = -\frac{ka(t)W}{v_R} \int_0^L \mathrm{d}z$$

$$\ln C_{\mathrm{Ph}} \Big|_{C_{\mathrm{Ph,in}}|_{z=0}}^{C_{\mathrm{Ph,out}}|_{z=L}} = -\frac{ka(t)W}{v_R} L$$

giving

$$C_{\mathrm{Ph,out,}J} = C_{\mathrm{Ph,in,}J} \exp\left\{ -\frac{ka(t)W}{v_R} L \right\} \tag{C.10}$$

This expression must be substituted into equation C.5 to yield:

$$\frac{\mathrm{d}C_{\mathrm{Ph,in}}}{\mathrm{d}t} = \frac{C_{\mathrm{Ph,in}}}{\tau} \left( \exp\left\{ -\frac{ka(t)W}{v_R} L \right\} - 1 \right) \tag{C.11}$$

No experiments were done to determine the effect of catalyst deactivation and therefore the activity of the catalyst with respect to time is always one (1). Therefore, equation C.11 can be solved producing the final expression for the concentration at a time $t$ in terms of the initial concentration:

$$C_{\mathrm{Ph,in,}J} = C_{\mathrm{Ph,in,0}} \exp\left( \frac{t}{\tau} \left\{ \exp\left( -\frac{kWL}{v_R} \right) - 1 \right\} \right) \tag{3.2}$$

In all of the experimental work, an exponential curve of the form

$$C_{\mathrm{Ph,}J} = C_{\mathrm{Ph,0}} e^{\beta t} \tag{3.1}$$

with $\beta$ being the one of the coefficients of the linear regression. Comparing this equation to equation 3.2 one may find $\beta$ in terms of the reactor parameters:

$$\beta = \frac{1}{\tau} \left( \exp^{-\frac{kWL}{v_R}} - 1 \right) \tag{C.12}$$

Some mathematical manipulation yields the expression relating the apparent reaction rate constant, $k$, to $\beta$:

$$k = -\frac{v_R}{WL} \ln(\beta\tau + 1) \tag{3.3}$$

## C.2 Scale-up Calculation

Performing an overall mass balance on the system, assuming that the difference between the physical properties of the inlet and outlet is negligible, one obtains:

$$v_{in} = v_p \tag{C.13}$$

Performing the same mass balance on the T-junction (see Figure 5.2) just before the inlet of the reactor where the recycle and inlet streams meet, an expression for the total flow rate through the reactor is found

$$v_T = v_r + v_p \tag{C.14}$$

An expression can be obtained for the concentration of the stream entering the reactor. This can be done by performing a component mass balance at the same junction:

$$C_{Ph,in} v_{in} + C_{Ph,out} v_r = v_T C^*_{Ph,in} \tag{C.15}$$

$$C^*_{Ph,in} = \frac{C_{Ph,in} v_{in} + C_{Ph,out} v_r}{v_T} \tag{C.16}$$

Performing a component mass balance on the reactor, assuming first order reaction kinetics, the expression for the outlet concentration can be obtained in terms of the inlet concentration:

$$v_T C_{Ph,z} - v_T C_{Ph,z+\Delta z} + r_{Ph} W \Delta z = 0$$

$$-v_T \frac{dC_{Ph,z}}{dz} = k C_{Ph,z} W$$

$$\frac{dC_{Ph,z}}{C_{Ph,z}} = -\frac{kW}{v_T} dz$$

$$C_{Ph,out} = C^*_{Ph,in} \exp\left(-\frac{kWL}{v_T}\right) \tag{C.17}$$

Substituting equation C.16 into equation C.17, the final form of the expression giving $C_{Ph,out}$ in terms of $C_{Ph,in}$ is obtained:

$$C_{Ph,out} = \frac{C_{Ph,in} v_{in} + C_{Ph,out} v_r}{v_T} \exp\left(-\frac{kWL}{v_T}\right)$$

$$C_{Ph,out}\left[1 - \frac{v_r}{v_T}\exp\left(-\frac{kWL}{v_T}\right)\right] = C_{Ph,in}\frac{v_{in}}{v_T}\exp\left(-\frac{kWL}{v_T}\right)$$

If $Y$, the recycle ratio, is defined as $\frac{v_r}{v_p}$

$$C_{Ph,out}\left[Y + 1 - Y\exp\left(-\frac{kWL}{v_T}\right)\right] = C_{Ph,in}\exp\left(-\frac{kWL}{v_T}\right)$$

and $v_T$ is written as $v_p(Y+1)$,

$$\frac{C_{Ph,out}}{C_{Ph,in}} = 1 - X = \frac{\exp\left(-\frac{kWL}{v_p(Y+1)}\right)}{Y + 1 - Y\exp\left(-\frac{kWL}{v_p(Y+1)}\right)} \tag{C.18}$$

Notice that the only independent variables in the expression are $L$ and $Y$. $v_p$ is a set variable, and will be determined by the specific application of the reactor system. The applied current does not feature as a variable in the expression, but determines the rate constant, $k$, that will be used.

In order to demonstrate the steps involved in the optimisation based on economic considerations of the reactor system, a simple expression for the rate constant will be derived for a fixed current value of 50 mA. This current value corresponds with the highest reaction rate constants for all of the flow rates except one (Re = 650). As an approximation, a straight line is fitted through the rate constant versus Reynolds number data to yield:

$$k = 1.4621\times10^{-9}\,\mathrm{Re} + 3.9402\times10^{-8} \qquad \text{(C.19)}$$

The Reynolds number in equation C.19 can be converted to a product flow rate. Equation C.19 will then have the following form:

$$k = 1.4621\times10^{-9}\cdot 8.33\times10^{5}(Y+1)v_p + 3.9402\times10^{-8}$$

$$k = 0.01218\cdot(Y+1)v_p + 3.9402\times10^{-8} \qquad \text{(C.20)}$$

Equation C.20 can then be substituted into equation C.18, in order to obtain an expression in which conversion is only dependant on reactor length, recycle ratio and product flow rate. The conversion was calculated for various values of the recycle ratio and plotted versus reactor length. The graph hereof is presented in figure C.3.

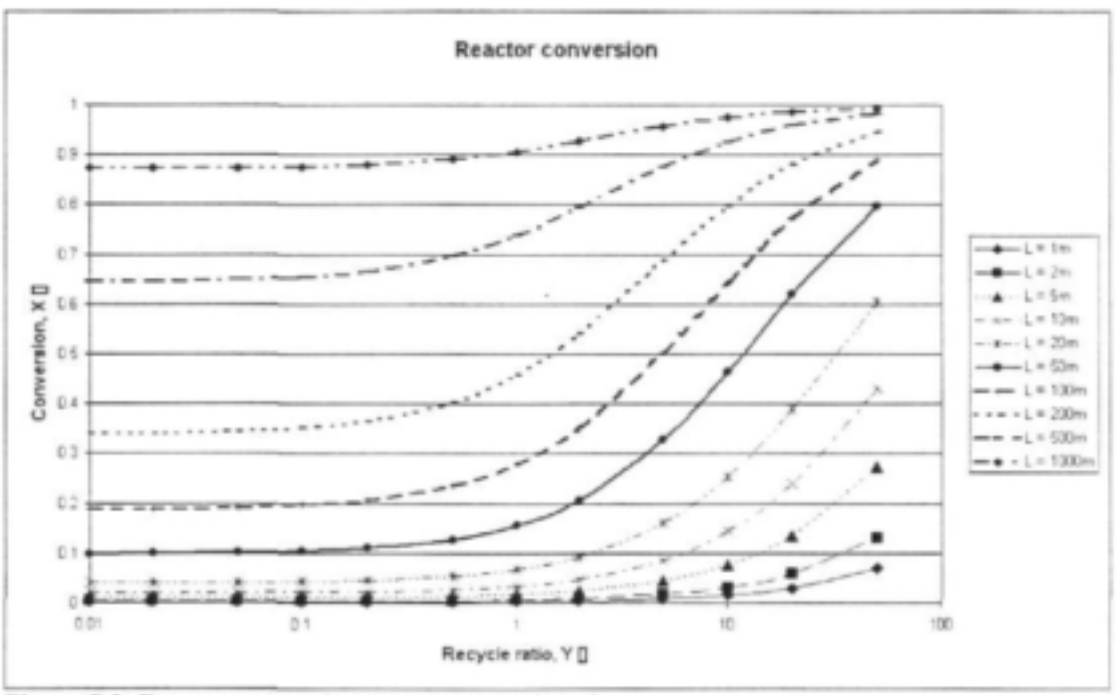


**Figure C.3: Reactor conversion versus reactor length.**

Now that the conversion has been expressed in terms of the major variables of the reactor, an economic evaluation can be performed to find optimum values for these variables.

## C.3 Economic Evaluation

The expressions for the capital cost of the reactor, in terms of the reflux ratio and reactor length, can be derived considering the following simplifying assumptions:

1. Only the pressure drop due to friction in the flow channels will be considered. This assumes that the friction losses due to pipe fittings are negligible, relative to the reactor.
2. Only phenol will be considered as compound taking part in the reaction. This assumes that the phenol is directly converted to carbon dioxide. This is not unreasonable considering the low concentrations observed for the intermediate organics.

The expression relating conversion to reactor length, recycle ratio and product flow rate was derived in the previous section. In order to obtain optimum values for the recycle ratio and reactor length, economic values must be assigned. The prices calculated in this section relate only to the reactor and do not reflect installed prices of such a unit.

All of the major costs involved are linked to both variables (reactor length and recycle ratio). This will become clear as the cost of each major part of the reactor is evaluated. The total cost can therefore be subdivided into the following elements:

$$C_{total} = C_{reactor} + C_{pump} + C_{reactor,running} \tag{C.21}$$

Each term in equation 5.3 will now be discussed and expanded upon. The first element of the total cost is the capital cost of the reactor itself. This can be expressed as:

$$C_{reactor} = (C_{substrate} + C_{membrane} + C_{materials})L \tag{C.22}$$

The values supplied in Table 5.5 can be used directly in the above equation. The equation merely states that the capital cost is the cost (per meter) of the titanium substrate, membrane and construction materials, multiplied by the length of the reactor.

Next, the cost of the reactor pump must be evaluated. Based on the assumption that the major pressure drop in the system is due to the reactor, the energy balance can be simplified to express the pump's power requirement in terms of the friction losses:

$$P_{pump} = v_T \rho_T \left( \frac{2 f u_1^2 L}{d_c} \right) \tag{C.23}$$

The friction losses were calculated using [61] (p. 199):

$$f\mathrm{Re} = 24\left[1 - 1.3553\gamma + 1.9467\gamma^2 - 1.7012\gamma^3 + 0.9564\gamma^4 - 0.2537\gamma^5\right] \tag{C.24}$$

From this the electricity cost of the pump can be calculated:

$$C_{pump,running} = \frac{P_{pump} \cdot t_{life} \cdot C_{electricity}}{1000\eta_{pump}} \tag{C.25}$$

The factor 1000 in the denominator was introduced to convert the pump power to kW. If the lifetime of the reactor is measured in hours, an expression for the required power in terms of kWh is obtained. $C_{electricity}$ is the unit price for electricity. Equation C.25 only accounts for the running cost of the pump — the actual capital cost of the pump can also be significant relative to the other costs.

The capital cost of the pump was calculated using the Marshall and Swift index as published in *Chemical Engineering* [62]. The pump cost was calculated using an exponential method [63] (p. 9–67) and a Marshall and Swift index of 1000. Thus, the cost of the pump was calculated by

$$C_{pump,capital} = C^*_{pump,capital} \left( \frac{q_2}{q_1} \right)^n \tag{C.26}$$

where $C^*_{pump,capital}$ is the published cost for a pump of capacity $q_1$. $q_2$ is the desired capacity of the pump. $n$ is the exponent used to determine the new cost. The calculated value was then adjusted using the Marshall and Swift index published in [62]:

$$\text{Cost in year A} = \text{Cost in year B} \frac{\text{Index in year A}}{\text{Index in year B}} \tag{C.27}$$

Since the values calculated by equation C.26 were based on an index of 1000, and the most recent index was 1089.0 in 2000, the capital cost could be calculated. The total pump cost is the sum of the pump capital and running cost.

$$C_{pump} = C_{pump,capital} + C_{pump,running} \tag{C.28}$$

The running cost of the reactor itself can be calculated based on the applied current density.

$$C_{reactor,running} = \frac{iWLVt_{life}C_{electricity}}{1000} \tag{C.29}$$

From the various equations contributing to the total cost, it can be seen that the cost is dependent on the applied current, the total flow through the reactor (and therefore the recycle ratio) and the length of the reactor.

If for an arbitrary conversion, and various values of the recycle ratio, the required reactor lengths are calculated using equation C.18; a plot of reactor length versus recycle ratio for a fixed conversion can be obtained such as the on presented in Figure 5.3. Here a conversion of 75% was chosen.

The various costs can now be calculated for the two values of $Y$ and $L$ and plotted. This has been done for typical values, with the exception of the pump costs, since no information was available regarding this aspect of the cost at the time of the evaluation. The graph of cost versus recycle ratio is presented in Figure 5.4.

## C.4 Sensitivity Analysis

The original form of the reactor model only accounts for the reaction rate constant $k$. In the sensitivity analysis, the specific reaction rate constant $k^{"}$ as well as the specific surface area of the catalyst must be taken into account. In the first case, the generation term in the mass balance can be written as:

$$\text{GENERATION} = -kC_{Pb}W\Delta z \tag{C.30}$$

However, once the specific surface area is taken into account, equation C.30 becomes:

$$\text{GENERATION} = -k^{"}C_{Pb}A_{s}W\delta\Delta z \tag{C.31}$$

This term can be substituted into equation C.7 and the same integration can be done to obtain the final form of the expression which gives the concentration at time $t$ in terms of the initial concentration:

$$\frac{1}{C_{Ph,in}}\frac{dC_{Ph,in}}{dt} = \frac{1-\exp\left\{-\frac{k^{*}AW\delta L}{v_R}\right\}}{\tau}$$

$$\int_{C_{Ph,in,0}}^{C_{Ph,in,t}} \frac{dC_{Ph,in}}{C_{Ph,in}} = \frac{1-\exp\left\{-\frac{k^{*}AW\delta L}{v_R}\right\}}{\tau}\int_0^t dt$$

$$\ln C_{Ph,in}\Big|_{C_{Ph,in,0}}^{C_{Ph,in,t}} = \left(\frac{1-\exp\left\{-\frac{k^{*}AW\delta L}{v_R}\right\}}{\tau}\right)t$$

$$\frac{C_{Ph,in,t}}{C_{Ph,in,0}} = \exp\left\{\left(\frac{1-\exp\left\{-\frac{k^{*}AW\delta L}{v_R}\right\}}{\tau}\right)t\right\}$$

$$C_{Ph,in,t} = C_{Ph,in,0}\exp\left\{\left(\frac{1-\exp\left\{-\frac{k^{*}AW\delta L}{v_R}\right\}}{\tau}\right)t\right\} \qquad (C.32)$$

In order for a sensitivity analysis to be performed, the calculations will be based on the conversion, not the concentration. Since the conversion is defined as

$$X = \frac{C_{Ph,in,0} - C_{Ph,in,t}}{C_{Ph,in,0}} \qquad (C.33)$$

equation C.32 can be rewritten as

$$1 - X = \exp\left\{\left(\frac{1-\exp\left\{-\frac{k^{*}AW\delta L}{v_R}\right\}}{\tau}\right)t\right\}$$

or

$$X = 1 - \exp\left\{\left(\frac{1-\exp\left\{-\frac{k^{*}AW\delta L}{v_R}\right\}}{\tau}\right)t\right\} \qquad (C.34)$$

The expression for the outlet concentration of the reactor in terms of the inlet concentration and the parameters is given by equation C.35. Note that the flow rate through the reactor is now replaced with the symbol $v_T$, the total flow rate through the reactor.

$$C_{Ph,in,t} = C^{*}_{Ph,in,0}\exp\left\{-\frac{k^{*}AW\delta L}{v_T}\right\} \qquad (C.35)$$

However, in the pilot plant, some of the effluent is recycled to reduce the required reactor length. Therefore, assigning $v_r$ to the recycle stream flow rate and $v_T$ to the reactor stream flow rate, the recycle ratio can be defined as

$$\text{Recycle ratio} = Y = \frac{v_r}{v_T} \qquad (C.36)$$

Performing a component mass balance on the T-junction yields

$$v_1 C^*_{\text{Ph,in}} = C_{\text{Ph,in}} v_{\text{in}} + C_{\text{Ph,out}} v_r$$

$$C_{\text{Ph,out}} = \frac{C_{\text{Ph,in}} v_{\text{in}} + C_{\text{Ph,out}} v_r}{v_1} \exp\left\{-\frac{k^* A_j W \delta L}{v_T}\right\}$$

$$C_{\text{Ph,out}}\left(v_T - v_r \exp\left\{-\frac{k^* A_j W \delta L}{v_T}\right\}\right) = C_{\text{Ph,in}} v_{\text{in}} \exp\left\{-\frac{k^* A_j W \delta L}{v_T}\right\}$$

$$1 - X = \frac{v_{\text{in}} \exp\left\{-\frac{k^* A_j W \delta L}{v_T}\right\}}{v_T - v_r \exp\left\{-\frac{k^* A_j W \delta L}{v_T}\right\}}$$

Writing the flow rates in terms of the recycle ratio can be achieved with the following substitutions

$$v_r = Y v_{\text{in}}$$

$$v_1 = (Y+1) v_{\text{in}}$$

producing

$$1 - X = \frac{\exp\left\{-\frac{k^* A_j W \delta L}{v_{\text{in}}(Y+1)}\right\}}{Y + 1 - Y \exp\left\{-\frac{k^* A_j W \delta L}{v_{\text{in}}(Y+1)}\right\}} \qquad (6.1)$$

## C.5 Internal Mass Transfer

$$D_e \int \mathrm{d}\frac{\mathrm{d}C_A}{\mathrm{d}y} = 0$$

$$\frac{\mathrm{d}C_A}{\mathrm{d}y} = \frac{C_1}{D_e}$$

$$C_A = \frac{C_1}{D_e} y + C_2$$

Using the boundary conditions:

$$\frac{C_1}{D_e} = \frac{k^*}{D_e} C_m$$

$$\therefore C_1 = k^* C_m$$

and

$$C_{A,\delta} = \frac{C_1}{D_e}\delta + C_2$$

$$C_2 = C_{A,\delta} - \frac{k^* C_m}{D_e}\delta$$

Thus,

$$C_A = \frac{k^{''} C_m}{D_e} y + C_{A,s} - \frac{k^{''} C_m}{D_e} \delta \qquad \text{(C.37)}$$

Eliminating for $C_m$:

$$C_A(0) = C_m = C_{A,s} - \frac{k^{''} C_m}{D_e} \delta$$

$$C_m \left( 1 + \frac{k^{''}}{D_e} \delta \right) = C_{A,s}$$

$$C_m = \frac{C_{A,s}}{1 + \frac{k^{''}}{D_e} \delta}$$

Substituting for $C_m$ in equation C.43 one finds:

$$\frac{C_A(y) - C_{A,s}}{C_m} = \frac{k^{''}}{D_e} y - \frac{k^{''}}{D_e} \delta$$

$$\left( \frac{C_A(y) - C_{A,s}}{C_{A,s}} \right) \left( 1 + \frac{k^{''}}{D_e} \delta \right) = \frac{k^{''}}{D_e} y - \frac{k^{''}}{D_e} \delta$$

$$\frac{C_A(y)}{C_{A,s}} - 1 = \frac{\frac{k^{''}}{D_e} y - \frac{k^{''}}{D_e} \delta}{1 + \frac{k^{''}}{D_e} \delta}$$

$$\frac{C_A(y)}{C_{A,s}} = \frac{\frac{k^{''}}{D_e} y - \frac{k^{''}}{D_e} \delta + 1 + \frac{k^{''}}{D_e} \delta}{1 + \frac{k^{''}}{D_e} \delta}$$

$$\frac{C_A(y)}{C_{A,s}} = \frac{1 + \frac{k^{''}}{D_e} y}{1 + \frac{k^{''}}{D_e} \delta} \qquad \text{(C.38)}$$

# D Miscellaneous Calculations

## D.1 Reaction Rate Constants

Equation 3.3 will be used in the calculation of the reaction rate constants. As an example, the constant will be calculated for one of the experiments conducted with the nickel-plated current collectors (50 mA, Re = 650, 15 lb-in, not separated). In this case, the flow rate is 2.6 $\times 10^{-6}$ $m^3/s$. Thus,

$$\tau = \frac{V}{v} = \frac{0.001}{2.6\times10^{-6}} = 384.6\,s \qquad (D.1)$$

The constant obtained in the exponential fit for the specific experiment was $-1.82 \times 10^{-6}$. Substituting the appropriate values into equation 3.3:

$$k = -\frac{2.6\times10^{-6}}{0.004\cdot0.548}\ln\left(-1.82\times10^{-6}\cdot384.6+1\right) = 8.30\times10^{-7}\ m/s \qquad (D.2)$$

## D.2 Differential Method of Rate Analysis

As an example of this method, the determination of the reaction order for the 60 ppm phenol experiment will be shown here using the technique described in section A.1.5. The first step is the fitting of the polynomial to the experimental data. The data points are shown in Table D.1. Both a 2nd and 3rd order polynomial was fitted to the data.

The coefficients obtained for the polynomials, together with the appropriate statistical data, are given in Table D.2. Note that in all cases (except $a_0$) the 95% confidence interval is greater than the corresponding coefficient, indicating an unstable fit to the data. This means that the removal or addition of a point can cause large changes in these coefficients.

The logarithmic plots of the rate of change in concentration vs the concentration are given in Figure D.1.

**Table D.1: Data for the derivation of reaction orders**

| $t$ [s] | $C_{Ph}$ [mM] | $\left(\frac{dC_{Ph}}{dt}\right)_2$ $\left[\frac{mmol}{dm^3\cdot s}\right]$ | $\left(\frac{dC_{Ph}}{dt}\right)_3$ $\left[\frac{mmol}{dm^3\cdot s}\right]$ | $\ln(C_{Ph})$ | $\ln\left(-\frac{dC_{Ph}}{dt}\right)$ 2nd-order | $\ln\left(-\frac{dC_{Ph}}{dt}\right)$ 3rd-order |
|---|---|---|---|---|---|---|
| 0 | 0.6189 | $-4.38\times10^{-6}$ | $-2.50\times10^{-6}$ | -0.4797 | -12.34 | -12.90 |
| 900 | 0.6309 | $-4.29\times10^{-6}$ | $-2.98\times10^{-6}$ | -0.4606 | -12.36 | -12.72 |
| 1800 | 0.6305 | $-4.21\times10^{-6}$ | $-3.39\times10^{-6}$ | -0.4612 | -12.38 | -12.59 |
| 2700 | 0.6223 | $-4.12\times10^{-6}$ | $-3.72\times10^{-6}$ | -0.4743 | -12.40 | -12.50 |
| 3600 | 0.6128 | $-4.04\times10^{-6}$ | $-3.98\times10^{-6}$ | -0.4898 | -12.42 | -12.43 |
| 4500 | 0.6321 | $-3.95\times10^{-6}$ | $-4.15\times10^{-6}$ | -0.4587 | -12.44 | -12.39 |
| 5400 | 0.5963 | $-3.87\times10^{-6}$ | $-4.26\times10^{-6}$ | -0.5170 | -12.46 | -12.37 |
| 6300 | 0.5812 | $-3.78\times10^{-6}$ | $-4.29\times10^{-6}$ | -0.5427 | -12.49 | -12.36 |
| 7200 | 0.6049 | $-3.70\times10^{-6}$ | $-4.24\times10^{-6}$ | -0.5027 | -12.51 | -12.37 |
| 8100 | 0.6038 | $-3.61\times10^{-6}$ | $-4.12\times10^{-6}$ | -0.5045 | -12.53 | -12.40 |
| 9000 | 0.5846 | $-3.53\times10^{-6}$ | $-3.92\times10^{-6}$ | -0.5368 | -12.56 | -12.45 |
| 9900 | 0.5924 | $-3.44\times10^{-6}$ | $-3.65\times10^{-6}$ | -0.5236 | -12.58 | -12.52 |
| 10800 | 0.6065 | $-3.36\times10^{-6}$ | $-3.30\times10^{-6}$ | -0.5001 | -12.60 | -12.62 |
| 11700 | 0.5850 | $-3.27\times10^{-6}$ | $-2.87\times10^{-6}$ | -0.5361 | -12.63 | -12.76 |
| 12600 | 0.5786 | $-3.19\times10^{-6}$ | $-2.37\times10^{-6}$ | -0.5471 | -12.66 | -12.95 |
| 13500 | 0.5702 | $-3.10\times10^{-6}$ | $-1.80\times10^{-6}$ | -0.5619 | -12.68 | -13.23 |
| 14400 | 0.5827 | $-3.02\times10^{-6}$ | $-1.14\times10^{-6}$ | -0.5401 | -12.71 | -13.68 |

**Table D.2: Statistical data for polynomial fits**

| | 2nd-order | | 3rd-order | |
|---|---|---|---|---|
| | Coefficient | 95% c.i. | Coefficient | 95% c.i. |
| $a_0$ | 0.6301 | 0.01645 | 0.6282 | 0.02081 |
| $a_1$ | $-4.38 \times 10^{-6}$ | $5.30 \times 10^{-6}$ | $-2.50 \times 10^{-6}$ | $1.29 \times 10^{-5}$ |
| $a_2$ | $-4.72 \times 10^{-11}$ | $3.55 \times 10^{-10}$ | $-2.89 \times 10^{-10}$ | $2.12 \times 10^{-9}$ |
| $a_3$ | — | — | $1.55 \times 10^{-14}$ | $9.67 \times 10^{-14}$ |
| $R^2$ | 69.9% | | 70.2% | |

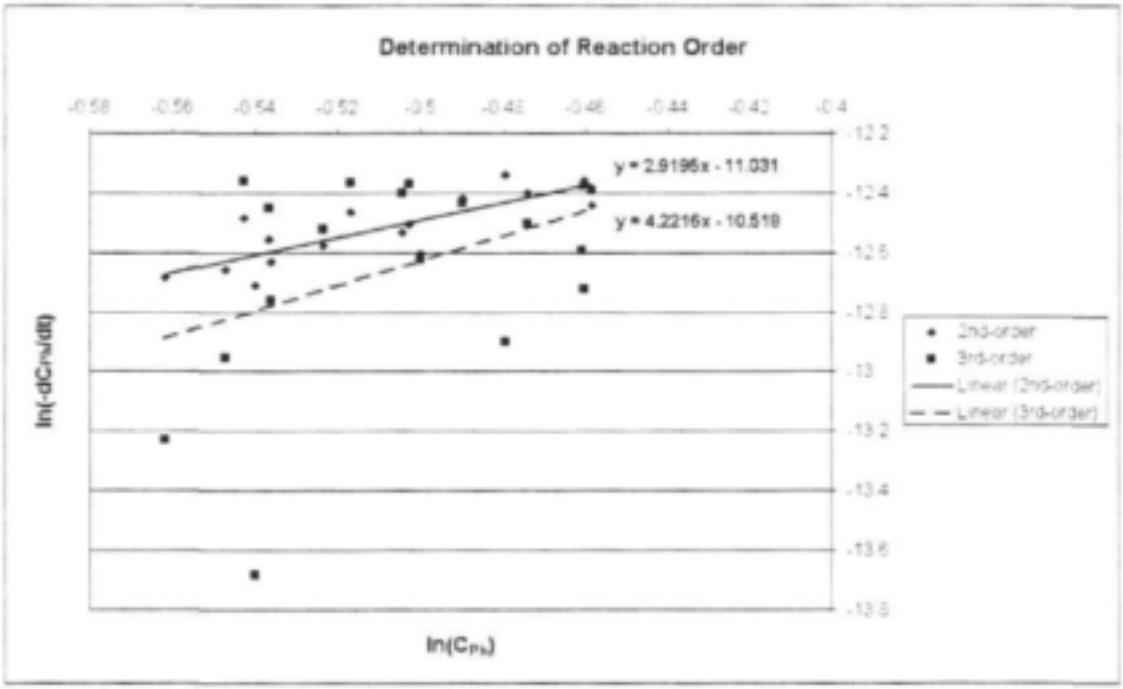


**Figure D.1: Determination of reaction order – example.**

## D.3 Reactor Cost

The economic evaluation was based on a conversion of 75%. An example of the reactor cost calculation will be shown for a recycle ratio of 1. The first step is to determine the reactor length that, together with a recycle ratio of 1, will result in a conversion of 0.75. This can be done by solving equation C.18; yielding a value of 520.7 for the reactor length. The capital cost of the reactor is only dependant on the length, and can therefore be calculated using R 8440 as the cost per unit length:

$$C_{reactor} = 8440 \cdot 520.7 = \text{R}4\,394\,591 \qquad \text{(D.3)}$$

To determine the pressure drop required for the pump, the linear velocity of the water needs to be determined. A product flow rate of $5.17 \times 10^{-5}$ was chosen, since this would ensure that the estimation of the $k$ values are relatively accurate. Thus, the total flow rate can be calculated using the recycle ratio:

$$v_T = (Y+1)v_p = 2v_p = 1.03 \times 10^{-4}\,[\text{m}^3/\text{s}] \qquad \text{(D.4)}$$

Taking into consideration that there are 30 flow channels in the current collectors, the linear velocity can be calculated:

$$u_T = \frac{v_T}{A_c} = \frac{1.03\times10^{-4}}{30\cdot0.004\cdot0.004} = 0.215\,[\text{m/s}] \qquad (D.5)$$

corresponding to a Reynolds number of

$$\text{Re}_T = \frac{1000\cdot0.004\cdot0.215}{0.001} = 861.1 \qquad (D.6)$$

Using equation C.24, and an aspect ratio of one, the friction factor can be determined as 0.0165. This can then be substituted into equation C.23 to obtain the power requirement of the pump (assuming a pump efficiency of 50%).

$$P_{\text{pump}} = 1.03\times10^{-4}\cdot1000\left(\frac{2\cdot0.0165\cdot0.215^2 520.7}{0.004}\right) = 41.2\,[\text{W}] \qquad (D.7)$$

This can be used to calculate the capital cost of the pump. The prices listed in [63] were for North America, but a reasonable estimate of the contribution of the pump to the cost can be obtained in this way. Assuming an exchange rate of R 7.00 to the dollar, the capital cost can be calculated as

$$C_{\text{pump,capital}} = 1600\left(\frac{41.2}{7500}\right)^{0.3} = \text{R}2\,350 \qquad (D.8)$$

Taking into account the Marshall and Swift index, the total cost amounts to

$$C_{\text{pump,capital}} = 2350\frac{1089}{1000} = \text{R}2\,560 \qquad (D.9)$$

To determine the running cost of the reactor, a lifetime needs to be determined for the reactor system. Since no experiments were done involving catalyst and membrane lifetime, no information is available regarding the lifetime. Thus, a lifetime of 5 years was chosen for the reactor. The pump running cost can therefore be calculated using equation C.25. The electricity cost was approximately R 0.20 per kWh.

$$C_{\text{pump,running}} = \frac{41.2\cdot43800\cdot0.20}{1000} = \text{R}361 \qquad (D.10)$$

Equation C.29 can be used to calculate the electricity cost of the power source. The width used in this case, must be the width of the reactor, which is 0.25 m. A current density of 0.88 A/cm$^2$ was selected.

$$C_{\text{reactor,running}} = \frac{8.811\cdot0.25\cdot520.7\cdot25\cdot43800\cdot0.20}{1000} = \text{R}251\,180 \qquad (D.11)$$

All of the individual elements of the cost can now be added up:

$$C_{\text{total}} = 4394591 + 2560 + 361 + 251180 = \text{R}4\,648\,692 \qquad (D.12)$$

# E Initial Work

## E.1 Introduction

The research regarding the electrochemical oxidation of organic molecules in the literature tests a wide range of catalytic metal oxides for their suitability as catalyst. All of the information presented, with the exception of one group of researchers [28], present no information regarding the kinetic performance of the catalyst with regard to reaction rate constants.

In most cases these experiments were conducted with the addition of a supporting electrolyte. This changes the conductivity of the electrolyte completely and would therefore also affect the kinetic parameters involved. Therefore, it was decided to perform experiments in a reactor similar to that used by Grimm to determine the kinetics of the electrochemical oxidation reaction. Once this has been done, the process could be compared to an analysis of the data found in the literature.

A larger reactor was therefore designed in order to perform a bench-scale analysis of the process. This work will give additional information regarding scale-up that will be used in the design and construction of a pilot plant.

## E.2 Experimental

### E.2.1 Instruments and specifications

Although both set-ups mentioned were similar in design, the scale of the two separate systems was different. In the first work with the initial set-up, the scale was significantly larger compared to the SPE reactors in the literature. It was presumed that most of the work done in the literature could be scaled up directly to make a working bench-scale reactor. A schematic of the first reactor flow system is given in Figure E.1.

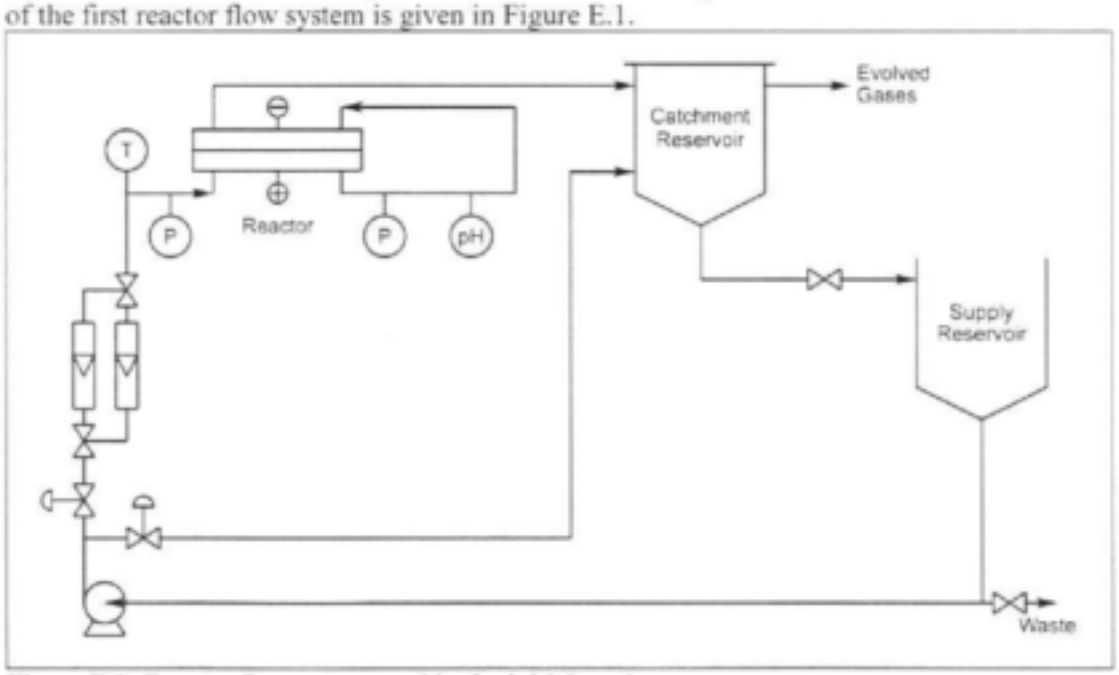


**Figure E.1: Reactor flow system used in the initial work.**

The initial set-up consisted of two 50 *l* tanks, constructed from 1.6mm stainless steel 316. Only the bottom-most tank was filled at the beginning of each experiment. The other tank was situated directly above this source tank. The purpose of this set-up was twofold. Firstly, the

second tank was sealed from the environment so that any gases generated in the process could be recovered and measured. Secondly, the process could be run in both semi-batch and continuous fashion.

After a number of experimental runs were performed, the two tanks were replaced with a single 10 *l* tank. These runs showed no conversion at all and therefore the volume to electrode area ratio was reduced. Also, no gas evolution was observed and therefore the need for the sealed tank was deemed unnecessary.

A magnetically driven centrifugal pump (Brubin, Magflo M6.1 SS 316) was used to circulate the reaction solution through the system. Downstream from the pump, the solution could be pumped through two different rotameters, depending on the desired flow. A flow range of between 60 and 2400 *l*/h could be monitored by the two rotameters. Both the reactor and the recycle line had a diaphragm control valve so that the desired flow rate could be obtained.

Other instruments included a temperature gauge situated on the inlet of the reactor, two pressure gauges (before and after the reactor) and a pH sensor capable of measuring the temperature on the outlet line. All of the instruments, including the rotameters were obtained from Indecx, Cape Town, South Africa. All of the tubing, fittings and valves were PVC products obtained from Astore Africa, Cape Town, South Africa. The electrical current was supplied by a d.c. power source (GW Laboratory DC Power Supply GPR-3520H).

### E.2.2 Experimental reactor

In the design of the experimental reactor, the material of construction was a very important factor to consider. At this stage of the design it was still not known exactly what processes took place at the electrode/membrane interface. An important unknown in the design was exactly what sort of conditions was present in the reactor, especially close to the current collectors. From the general reaction mechanism given in section 2.2.1 it is seen that protons were being generated. This meant that the pH in at least the anodic compartment of the reactor should be less than 7. It was also possible that the adsorbed hydroxyl radicals could interact with one another to form hydrogen peroxide which would give a pH higher than 7.

Thus, the choice of current collector material had to be made very carefully so that the reactor would show excellent corrosion resistance over a wide pH range. Titanium was therefore chosen as the construction material for the current collectors. Titanium, upon exposure to water, forms an insoluble oxide layer that is highly resistant to chemical attack, but still allows electrical conductivity.

Straight, rectangular flow channels were then machined into the current collectors to allow fluid flow past the electrodes. The choice in length of the flow channel was unfortunately fixed due to the limited availability of the porous titanium substrates. The porous substrates used in the study were only 85mm in diameter. Larger substrates could be obtained from manufacturers in America (Mott Corporation), but the variation in the flatness of these larger substrates could lead to local variations in the current density. Since the reactor used square current collectors, the circular discs were cut to fit the current collector, which measured 66mm on a side.

Each current collector was machined with nine square flow channels, each flow channel measuring 4×4mm in size. The titanium machining was done commercially by Allweld Marine Industrial cc. (Cape Town, South Africa). The electrode membrane assembly was then sandwiched and fitted into a PVC frame (Cape Plastics, Cape Town, South Africa). Diverging channels were machined into the PVC frame on each side of the current collector housing to attempt to reduce pressure drop in the reactor. Schematic drawings of the reactor are given in Appendix G.

Electrical contact was supplied to the current collector through five stainless steel bolts. The cathodic side was fixed to prevent the flow channels from shifting too far from being flush with the PVC frame flow channel. This was done by welding five M6 bolts onto a flat stainless steel plate. This served as the secondary cathodic current collector. The EMA (electro-membrane-assembly) rested on this plate. The anodic current collector was then pressed onto the cathodic current collector plate by fastening five M8 stainless steel 316 bolts that passed through the PVC frame and connected directly with the anodic current collector.

The reactor was sealed using a 3mm Viton o-ring that fitted in a groove around the flow channels and EMA. A total of 16 M6 galvanised mild steel bolts were used to provide the required compression to seal the reactor.

### E.2.3 Analysis

Grimm used a standard method [64] to determine what is referred to as a "phenol-index". The process entails the pre-treatment (basically distillation) and subsequent dyeing of the cyclic organic molecules in the sample. The pre-treatment step is done to ensure that the dye reacts only with organic molecules. The resultant dye is then measured photospectrometrically and the concentration of the phenol is calculated by comparison with a standard curve.

The method is applicable for a variety of applications, especially where a great number of cyclic intermediates are present and a rough estimation of the organic content of a sample is desired. The problem with the system in this project was the formation of the cyclic intermediate quinone and dihydroxy-benzene structures which would also react to form a dye. Thus, the results would not accurately represent the organic content in the sample and a different analysis method was required.

Total organic carbon analysis were chosen to determine the organic content in the sample since it would accurately represent to what extent the original phenol was broken down to carbon dioxide. The total organic carbon sample analyses were carried out at the CSIR in Stellenbosch, South Africa.

### E.2.4 Method

Each experiment was conducted over a period of 12 hours, with samples taken every 2 hours. The samples were refrigerated to preserve the samples until analyses could be carried out. Distilled water and reagent grade phenol (Aldrich puris, > 99%) were used to prepare the feed solution (initial concentration = 5 mM).

## E.3 Results and Discussion

In the initial experiments, only the effect of flow rate on the reaction rate of the organic oxidation was investigated as all of the experiments were run galvanostatically. Due to the high overpotential of the reaction, relatively high current densities (230 mA/cm$^2$) had to be maintained in order for the potential to be high enough. This corresponded with the maximum output for the power source and could therefore not be varied.

A 5 mM solution of phenol is used as stock solution in the experiments. This corresponds with a concentration of about 360 ppm total organic carbon (TOC). Samples were taken according to the method described in section E.2.4 and analysed. The experimental results obtained for the initial reactor are shown in Figures E.2 to E.4. In these graphs, the TOC is plotted versus time and an exponential curve is fitted through the data.

The experimental parameters and conditions of the initial experiments are summarised in Table E.1. These conversions based on the difference between the initial and final values are also given. The conversion in this case is defined as

$$X = \frac{\mathrm{TOC}|_{t=t_x} - \mathrm{TOC}|_{t=0}}{\mathrm{TOC}|_{t=0}} \qquad \text{(E.1)}$$

Both the initial concentration as well as the calculated initial TOC is given. In all the cases the analyses of the initial samples resulted in values close to 250 ppm TOC. This can be attributed to the refractory nature of phenol, which gives a lower predicted value of the TOC, as discussed in section 3.2.3.

**Table E.1: Experimental parameter values for initial experiments**

| Flow rate | Applied current | | Initial concentration | | Volume | Conversion |
|---|---|---|---|---|---|---|
| [$l$ h] | $I$ [A] | $i$ [A cm$^{-2}$] | [mM] | [$TOC_{calc}$] | [$l$] | |
| 500 | 10 | 230 | 5.0 | 360.3 | 10 | 0.024 |
| 600 | 10 | 230 | 5.0 | 360.3 | 10 | 0.034 |
| 700 | 10 | 230 | 5.0 | 360.3 | 10 | 0.083 |

From the breakdown curves it can be seen that very low conversion of the total organic carbon was obtained. It was only realised at a later stage in the project that passivation of the electrode could have a major influence on the reaction rate. In these experiments, the electrode surface area to reaction volume was much smaller than in the laboratory experiments (4.4 vs 56.7 units). It is therefore possible that due to the passivation reaction, the electrode became completely deactivated before sufficient combustion could take place.

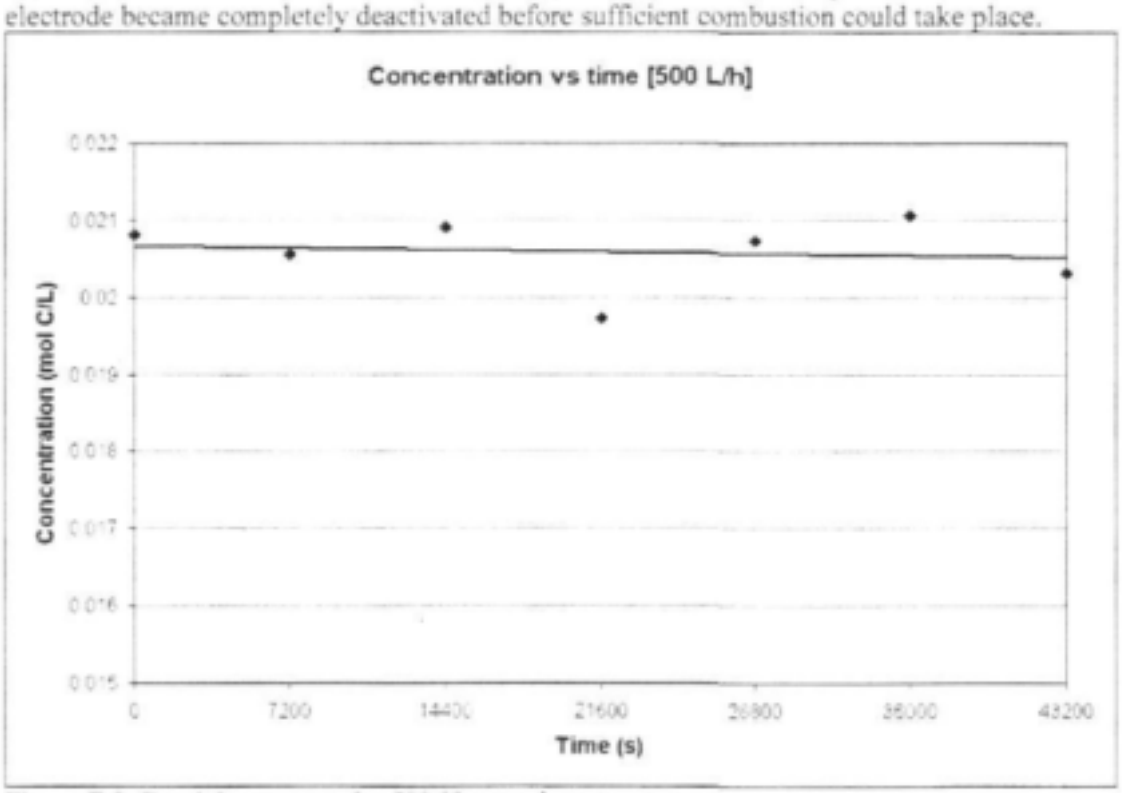


**Figure E.2: Breakdown curve for 500 $l$/h experiment.**

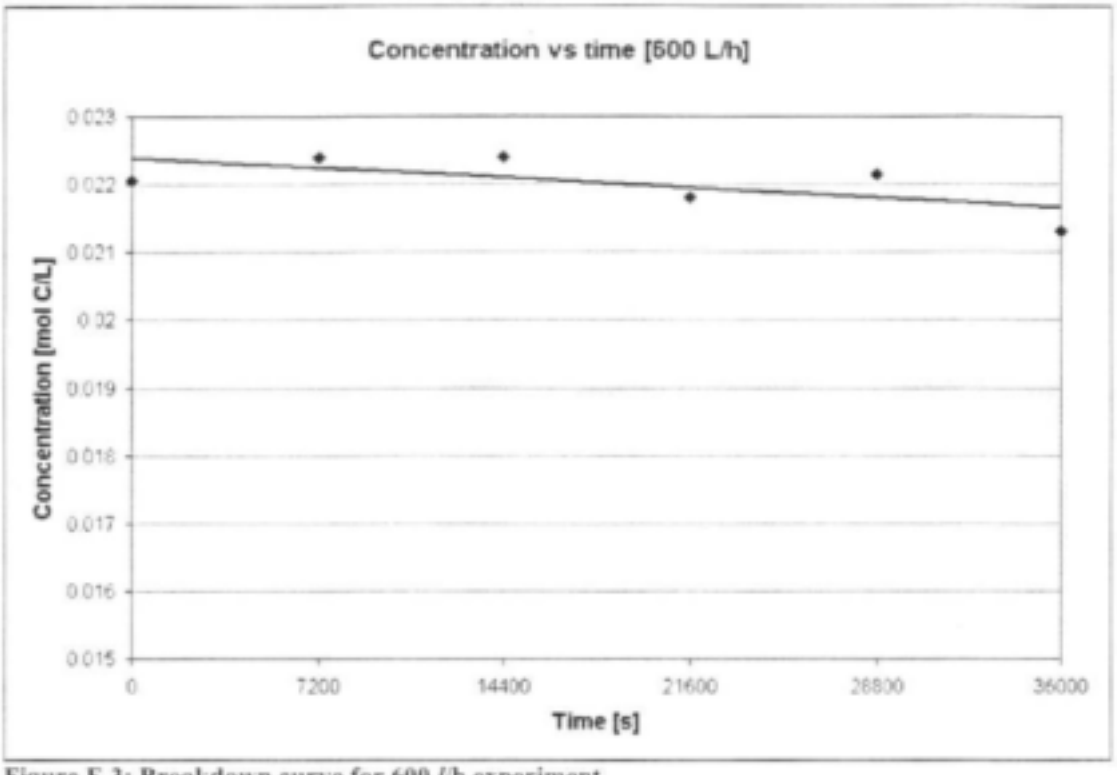


**Figure E.3: Breakdown curve for 600 *l*/h experiment.**

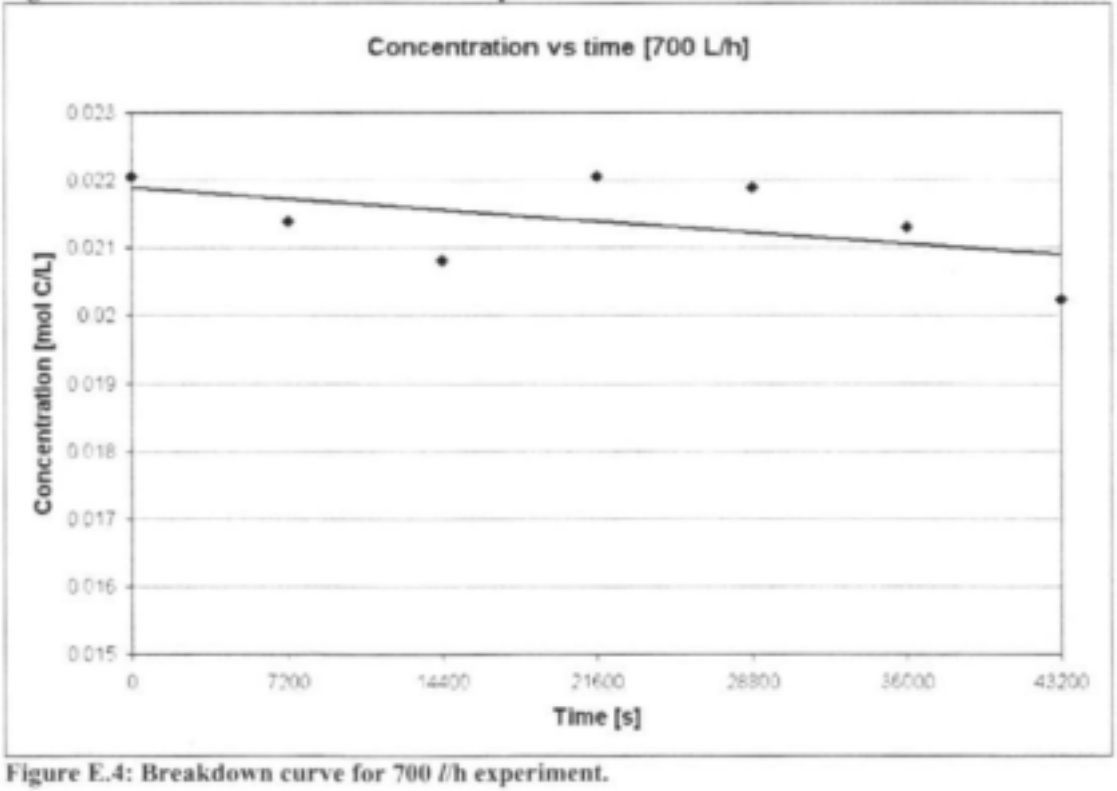


**Figure E.4: Breakdown curve for 700 *l*/h experiment.**

Theoretically, a charge 3.2 times greater than necessary to convert all of the phenol to carbon dioxide was supplied. As discussed in section 0, high current densities tend to damage and dehydrate the membrane and this could also account for the low conversions obtained. In such a case, the proton transfer in the membrane becomes the limiting step, with most of the electricity converted into heat energy due to resistance.

The calculated reaction rate constants are given in Table E.2 with the respective $R^2$ values and the 95% confidence interval values (calculated for $\beta$) . The values for $\beta$ represent the actual coefficients obtained in the exponential fit. $k$ represents the apparent reaction rate constant calculated from $\beta$ as discussed in section C.1 according to the equation:

$$k = -\frac{v_R}{WL}\ln(\beta\tau + 1) \qquad (3.3)$$

Generally, if the coefficient determined by regression is much greater than the 95% confidence interval value, the proposed model or curve estimate the experimental values accurately. At least, the coefficient must be greater than the confidence interval value.

**Table E.2: Rate constants for initial experiments.**

| Flow rate | $\beta$ | $k$ | $R^2$ | 95% confidence |
|---|---|---|---|---|
| [l/h] | [$s^{-1}$] | [m/s] | | interval ($\beta$) |
| 500 | $1.63 \times 10^{-7}$ | $8.27 \times 10^{-8}$ | 0.013 | $1.61 \times 10^{-6}$ |
| 600 | $9.24 \times 10^{-7}$ | $4.68 \times 10^{-7}$ | 0.032 | $1.45 \times 10^{-6}$ |
| 700 | $1.08 \times 10^{-6}$ | $5.46 \times 10^{-7}$ | 0.266 | $2.06 \times 10^{-6}$ |

Results of the experiments showed very poor fits of the exponential curve to the experimental data. In all cases the 95% confidence interval was greater than the absolute value of the coefficient $\beta$, indicating a poor fit. Also, the $R^2$ values were very close to zero, thus showing a significant deviation between the experimental values and the exponential fit.

If the values for the kinetic constants could be taken as is, one would assume that the process is under mass-transfer-limited control due to the increase in the constant with an increase in flow rate. Unfortunately, due to the variation in the results leading to inaccurate constants, one cannot validate this assumption.

## E.4 Conclusions

The following conclusions can be drawn from the experimental results in this chapter:

- The scale-up experiments using the bigger reactor did not work, yielding low phenol conversion (less than 5%).
- With the limited experimental data provided, it is assumed that the specific surface area of the electrode substrate limits the reaction rate. The specific surface area of the catalyst is measured as 0.7 $m^2$/g catalyst. The surface area to volume ratio in the experiments is 287.5 $cm^2/l$. The author believes that an experimental set-up utilizing significantly higher ratios need to be designed in order to improve the conversion.
- The high initial concentration of phenol makes it difficult to extract accurate kinetic data from the experimental results mainly due to the low conversion.

# F Growth Curves

The growth curves for the individual pathogens are given in this Appendix. The growth curves were set up by allowing an innoculated vessel containing various concentrations of TSB to grow for a period of 24 hours. At selected times, samples were taken and the absorbance were measured using a photospectrometer. The absorbance is normally directly proportional to the number of cells in the solution at any time. To prove this, cell counts were obtained for *Enterococcus faecallis* and compared to the absorbance. This is done in Figure F.1. Notice the excellent correlation between the absorbance and cell count. The growth curves for *E. faecallis*, *Salmonella* and *E. coli* are given in Figures F.2, F.3 and F.4 respectively.

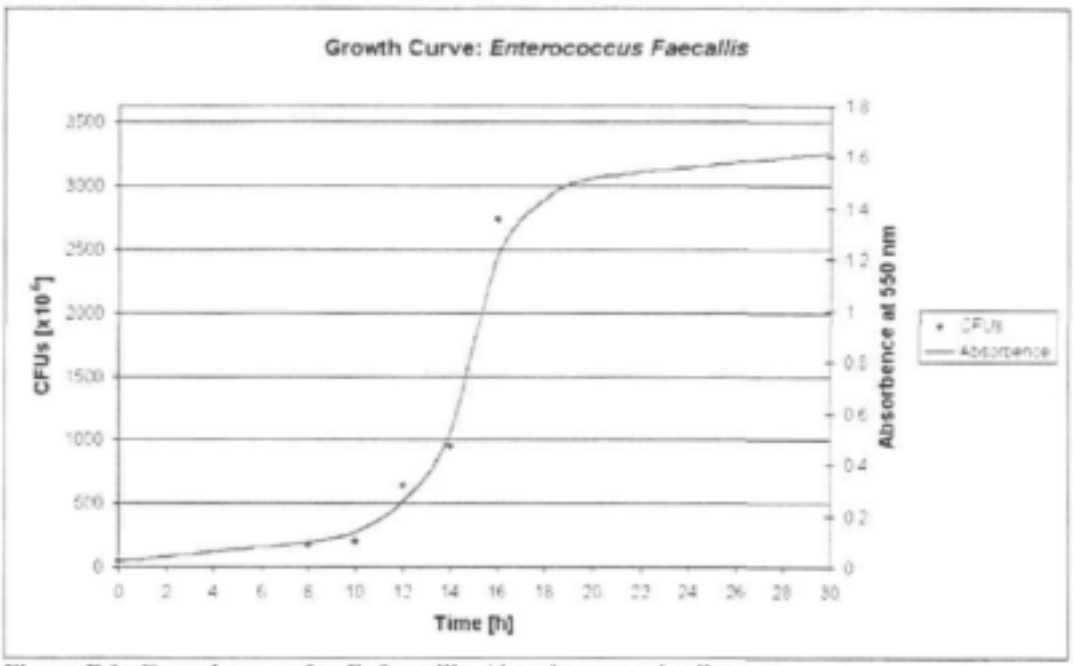


**Figure F.1: Growth curve for *E. faecallis*: Absorbence and cell count.**

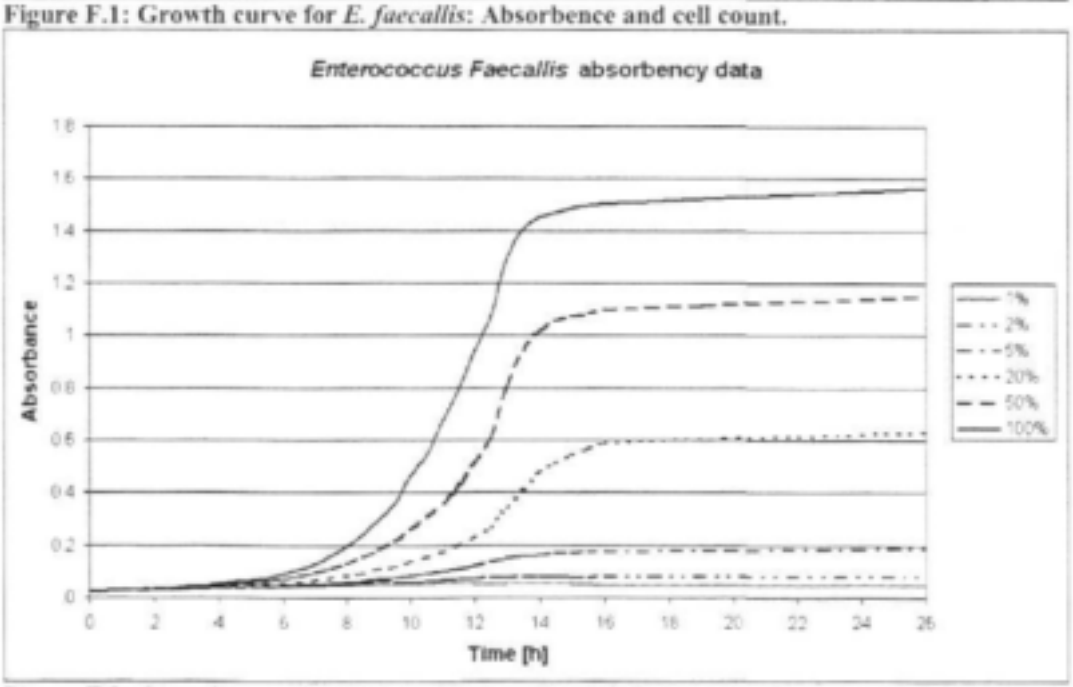


**Figure F.2: Growth curve for *E. faecallis* at various TSB concentrations.**

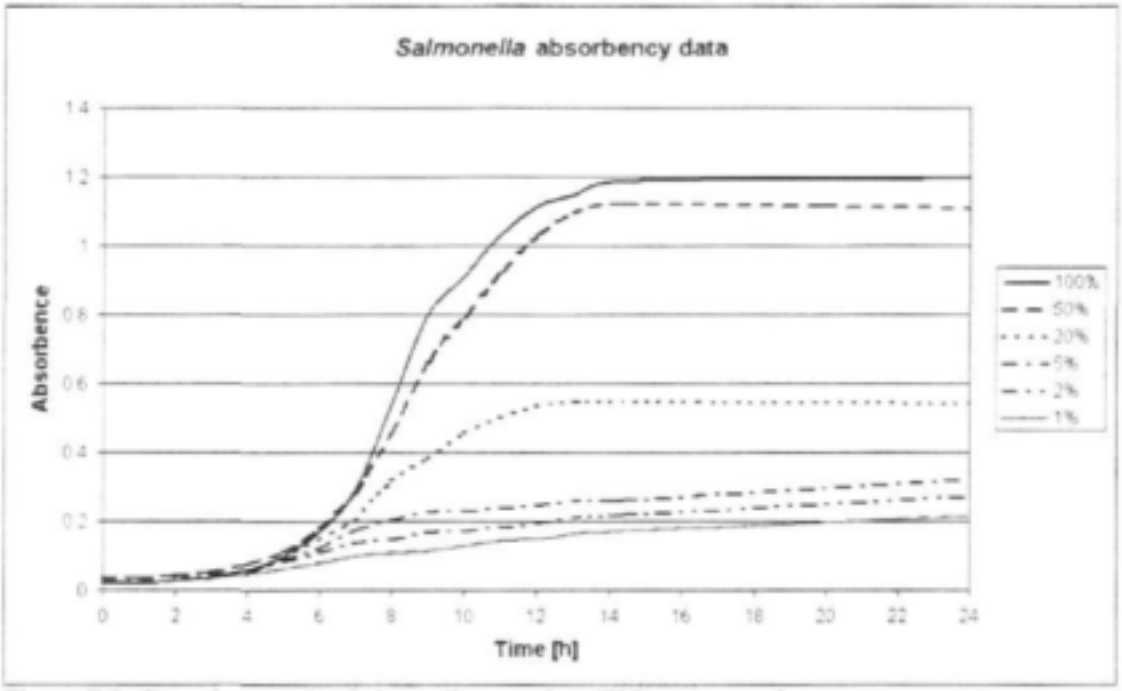


Figure F.3: Growth curve for *Salmonella* at various TSB concentrations.

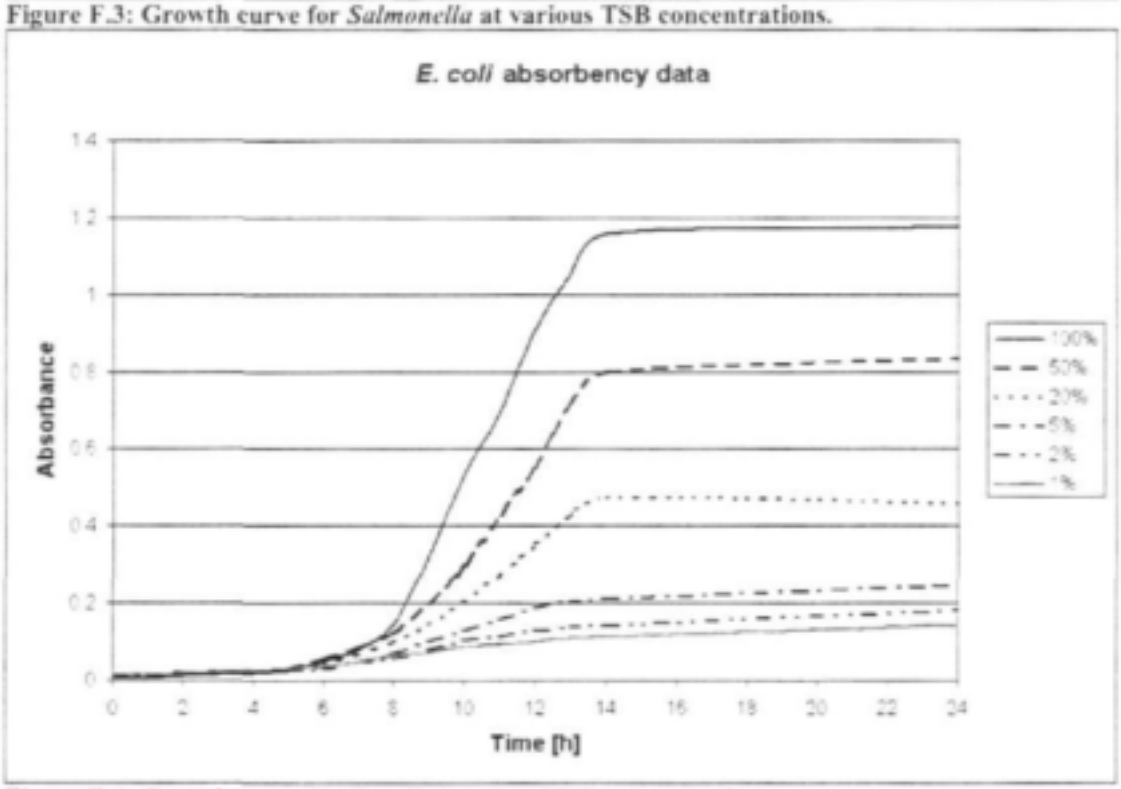


Figure E.4: Growth curve for *E. coli* at various TSB concentrations.

# G Technical Drawings

Drawings of the initial reactor are given in Figures G.1 to G.3. The schematic drawings of the laboratory-scale reactor are given in Figures G.4 to G.6.

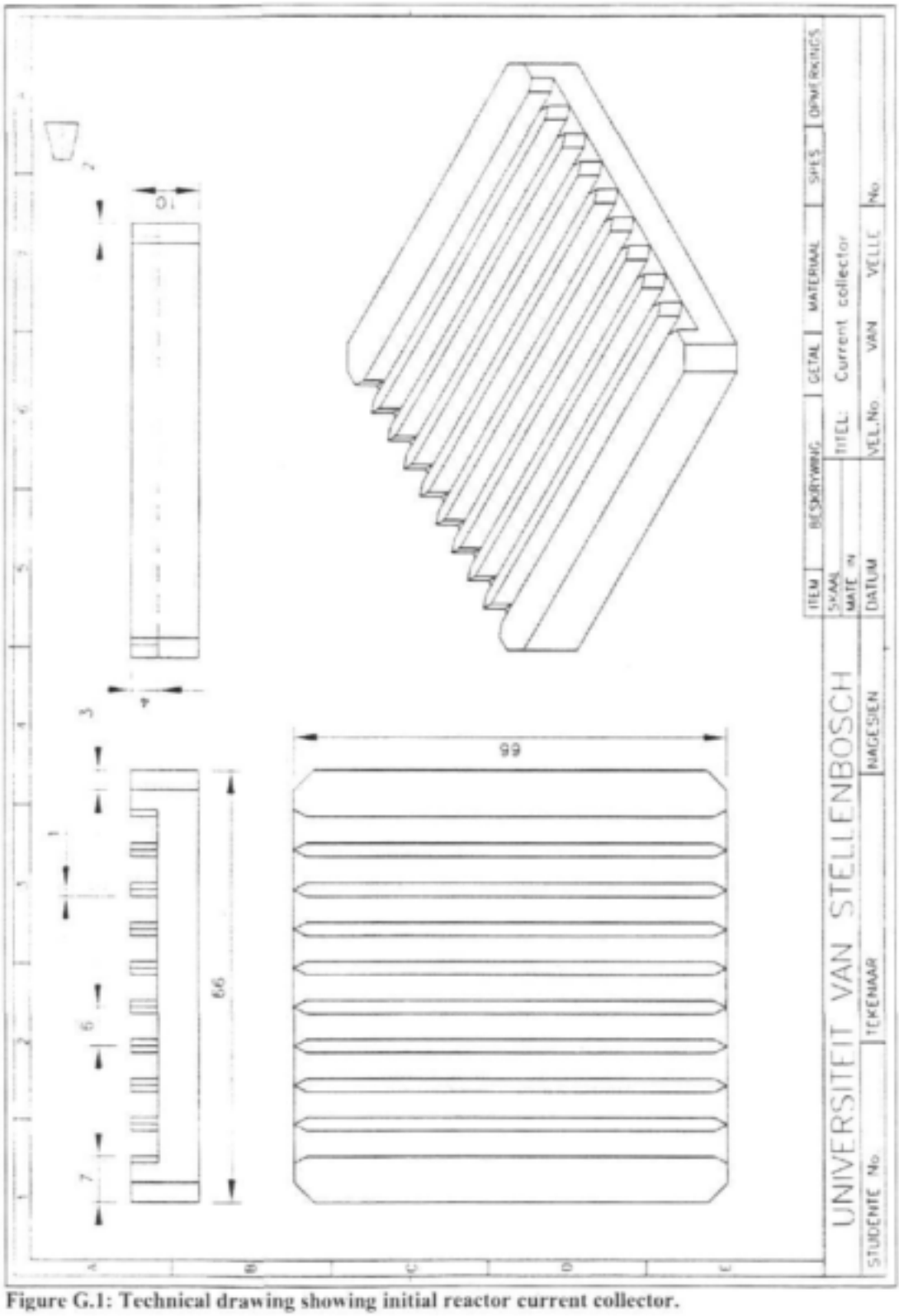


**Figure G.1: Technical drawing showing initial reactor current collector.**

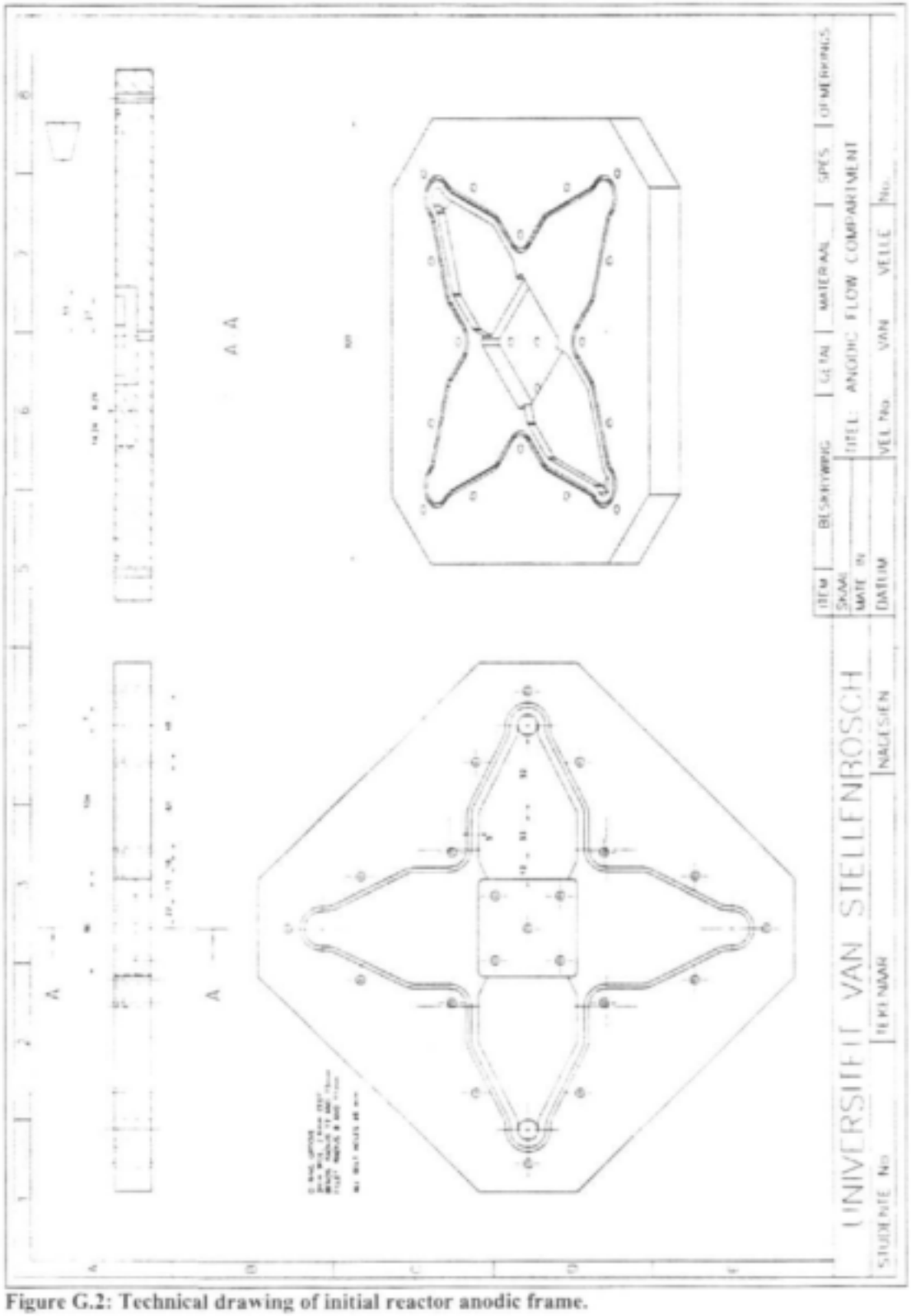


**Figure G.2: Technical drawing of initial reactor anodic frame.**

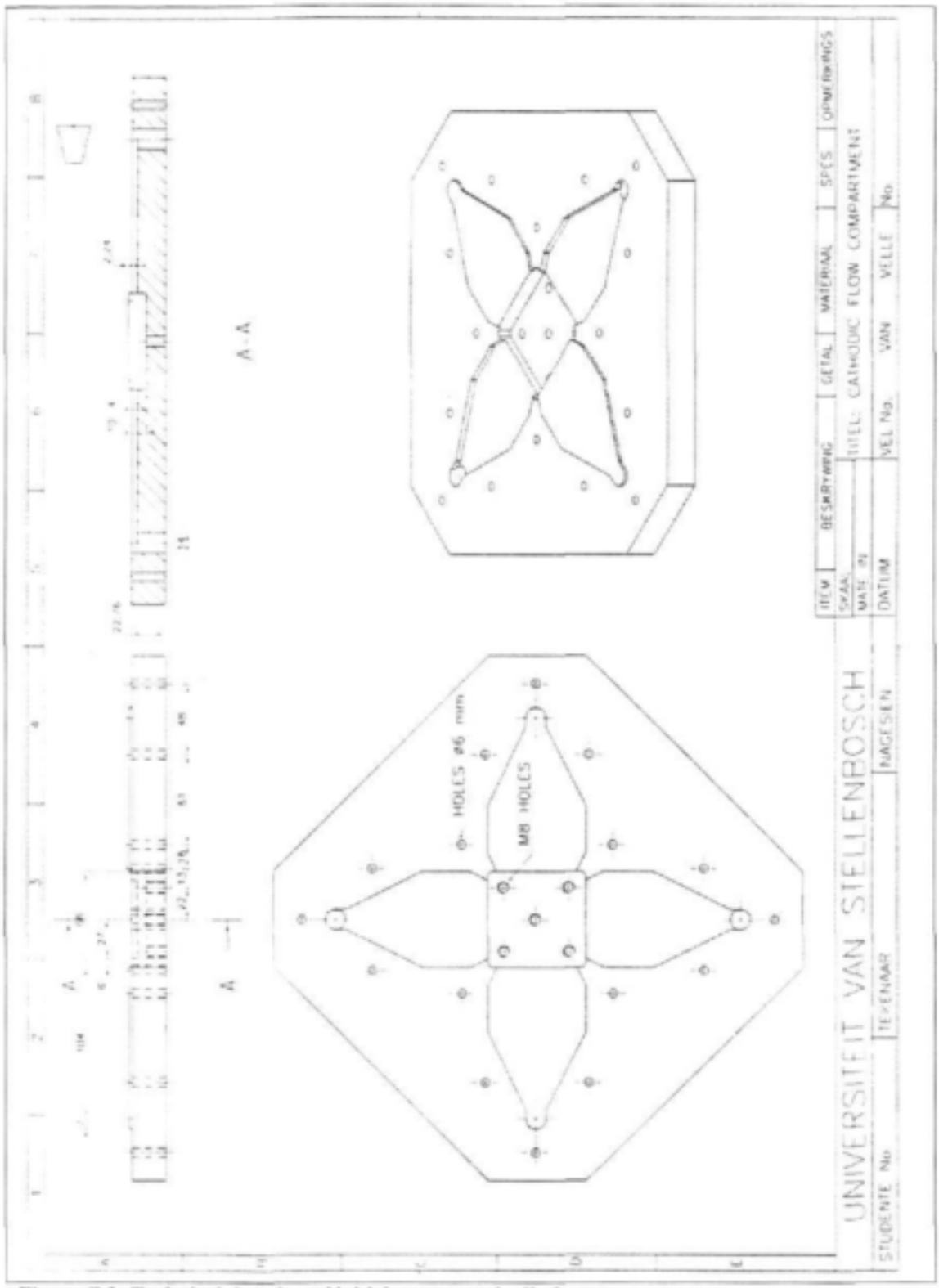


**Figure G.3: Technical drawing of initial reactor cathodic frame.**

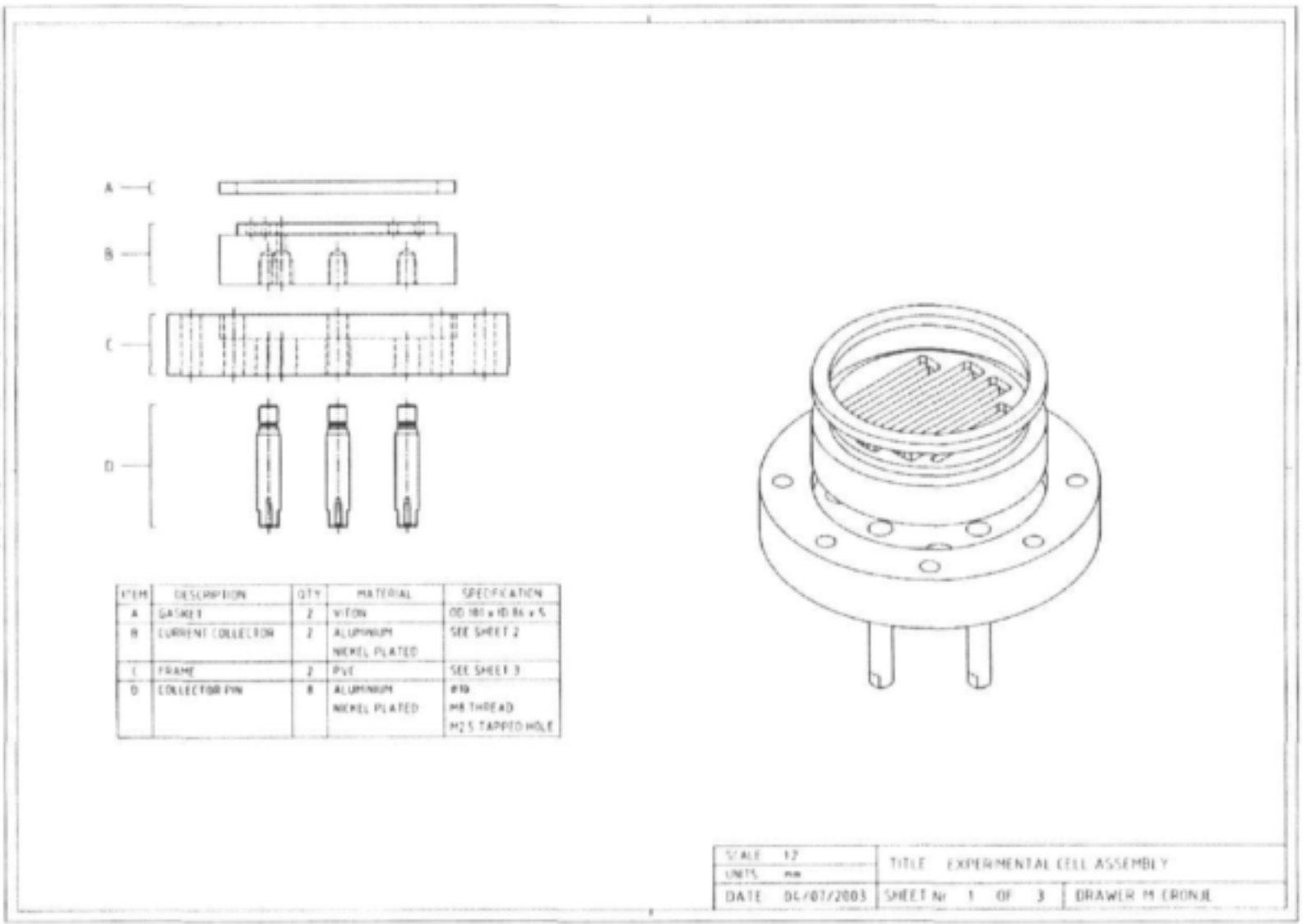


Figure G.4: Technical drawing showing all parts of the laboratory reactor.

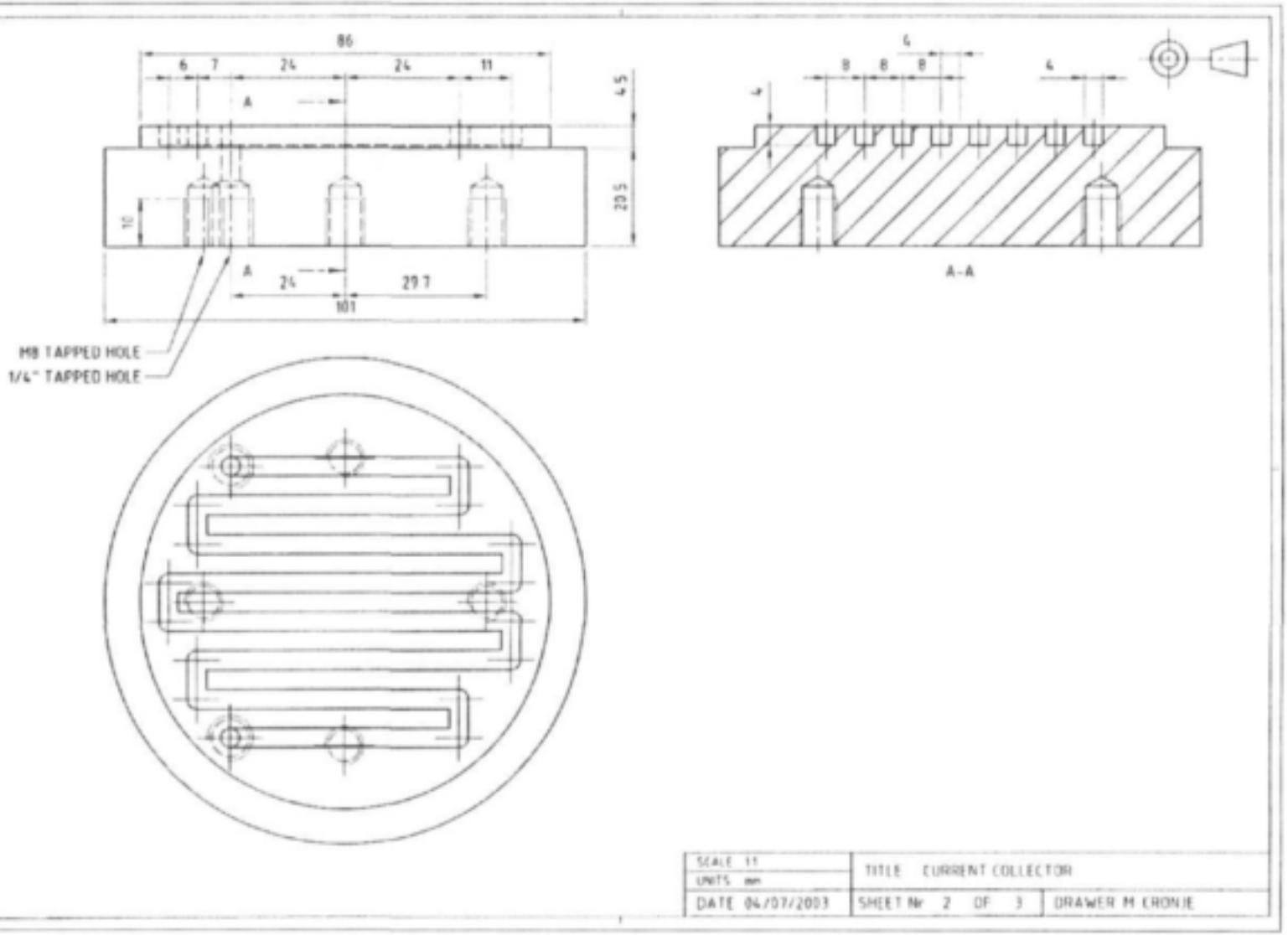


Figure G.5: Technical drawing of laboratory reactor current collector.

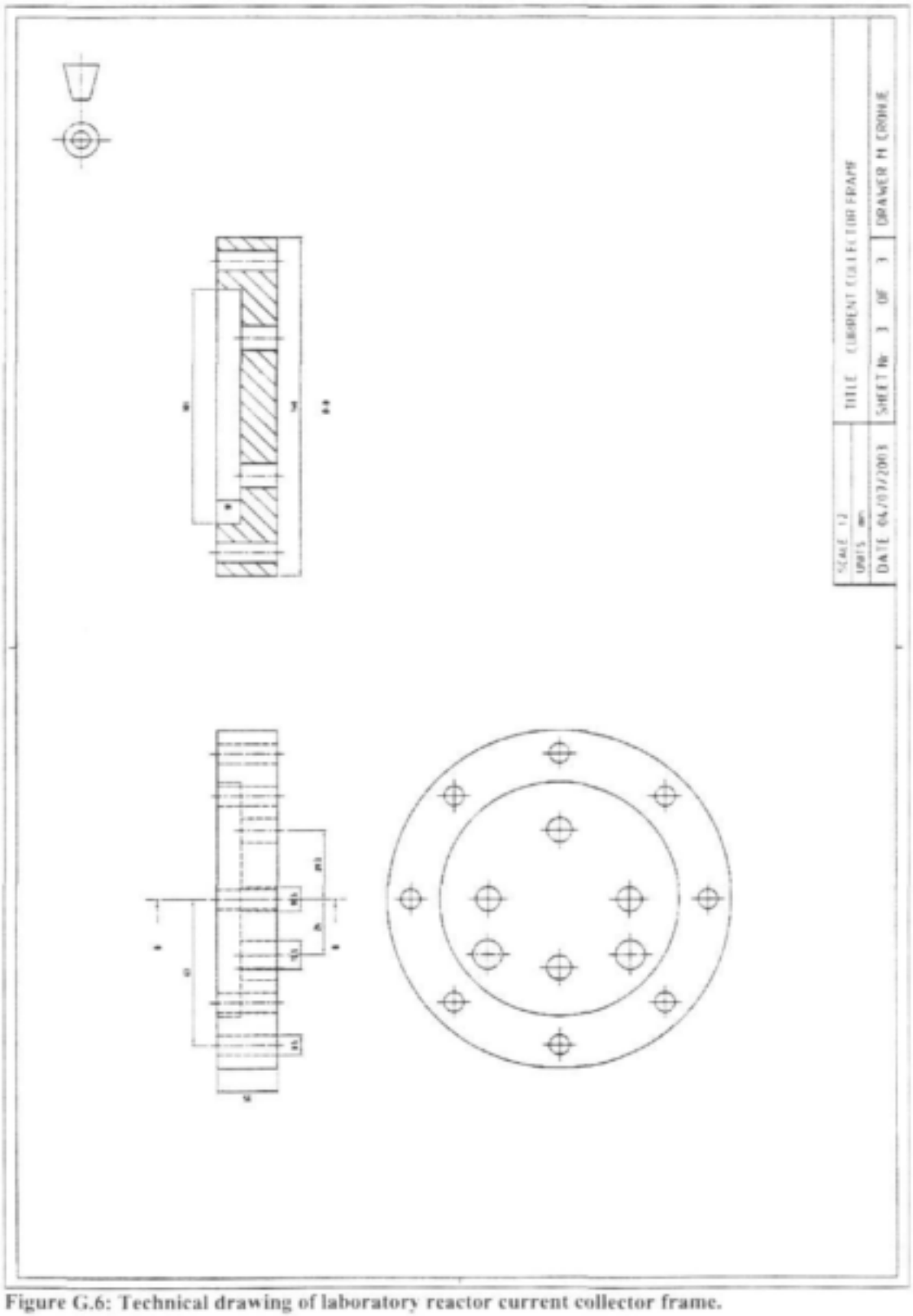


Figure G.6: Technical drawing of laboratory reactor current collector frame.

# Other related WRC reports available:

**Membrane reactor for the electro catalytic minimization of organic matter in water and effluents**

*Linkov VM; Maluleke A*

Novel proton-conducting ceramic membranes for the oxidation of recalcitrant organic material in water have been developed at the University of the Western Cape. Initial laboratory studies show good promise. The aim of this project is the further development and improvement of these membranes. Prototype membranes will be evaluated on organics removal from a selection of possible effluents, such as Cape surface water, textile, power station and petroleum effluents. The scope includes the construction of a small pilot plant from which large plants could be upscaled.

**Report Number: 1231/1/04** **ISBN: 1 77005 201 1**

TO ORDER: Contact **Publications** - Telephone No: 012 330 0340
Fax Number: 012 331 2565
E-mail: publications@wrc.org.za

1770053352

Water Research Commission
Private Bag X03, Gezina, 0031, South Africa
Tel: +27 12 330 0340, Fax: +27 12 331 2565
Web: http://www.wrc.org.za